Universidad de Oviedo

Departamento de Ciencia de los Materiales e Ingeniería Metalúrgica

Programa de Doctorado en Materiales

PREPARACIÓN DE MATERIALES BIDIMENSIONALES PARA APLICACIONES EN ALMACENAMIENTO DE ENERGÍA Y MEDIO AMBIENTE

PREPARATION OF BIDIMENSIONAL MATERIALS FOR ENERGY STORAGE AND ENVIRONMENTAL APPLICATIONS

Doctorando:

Alberto Martínez Jódar

Oviedo, Julio de 2024

Universidad de Oviedo

Departamento de Ciencia de los Materiales e Ingeniería Metalúrgica

Programa de Doctorado en Materiales

PREPARACIÓN DE MATERIALES BIDIMENSIONALES PARA APLICACIONES EN ALMACENAMIENTO DE ENERGÍA Y MEDIO AMBIENTE

PREPARATION OF BIDIMENSIONAL MATERIALS FOR ENERGY STORAGE AND ENVIRONMENTAL APPLICATIONS

Doctorando:

Alberto Martínez Jódar

Directores:

Dr. D. Juan Ignacio Paredes Nachón
Dra. Dña. Silvia María Villar Rodil

Oviedo, Julio de 2024

Universidad de Oviedo

FOR-MAT-VOA-010 (Reg.2018)

RESUMEN DEL CONTENIDO DE TESIS DOCTORAL

1.- Título de la Tesis	
Español: Preparación de materiales bidimensionales para aplicaciones en almacenamiento de energía y medio ambiente.	Inglés: Preparation of bidimensional materials for energy storage and environmental applications.

2.- Autor	
Nombre: Alberto Martínez Jódar	
Programa de Doctorado: Materiales	
Órgano responsable: Centro Internacional de Postgrado	

RESUMEN (en español)

Esta tesis tiene como objetivo la preparación, modificación y procesado de láminas bidimensionales (2D) de los dicalcogenuros de metales de transición MoS$_2$ y MoSe$_2$ usando metodologías descendentes o *top-down* (exfoliación directa en fase líquida y exfoliación electroquímica) para el estudio de sus aplicaciones como material activo en almacenamiento de litio y como catalizador para la reducción de nitroarenos. La exfoliación en fase líquida consistió en la sonicación de los polvos *bulk* de MoS$_2$ y MoSe$_2$ en disolventes orgánicos y la posterior transferencia del producto exfoliado a fase acuosa en ausencia de estabilizantes. La exfoliación electroquímica se realizó en condiciones catódicas con electrolitos acuosos u orgánicos, partiendo de cristales macroscópicos de MoS$_2$. Ambos tipos de exfoliación permitieron preservar la fase cristalina original 2H de los dicalcogenuros tras su transformación en nanoláminas 2D.

Se desarrolló un método de funcionalización superficial con grupos carboxílicos de las nanoláminas de MoS$_2$ mediante tratamiento electroquímico con organoioduros en medio acuoso que mejoró su estabilidad coloidal y su actividad catalítica para la reducción de nitroarenos.

Se realizó un estudio comparativo de la actividad catalítica para la reducción de nitroarenos en fase acuosa de nanoláminas de MoS$_2$ y MoSe$_2$ obtenidas por exfoliación directa en fase líquida, y se encontró una mayor eficiencia de las segundas. Cálculos computacionales permitieron explicar la diferente actividad catalítica mostrada por MoSe$_2$ frente a diferentes isómeros estructurales de nitroarenos.

Se estudió la obtención de nanoláminas mediante exfoliación electroquímica de un cristal *bulk* de MoS$_2$ usando sales de amonio en medio orgánico. Se evaluaron sus prestaciones como ánodo para almacenamiento de litio y se compararon con las de las nanoláminas obtenidas por exfoliación en fase líquida, resultando superiores las primeras tanto en términos de capacidad como de ciclabilidad.

RESUMEN (en inglés)

The present thesis aims for the preparation, modification and processing of bidimensional (2D) nanosheets of the MoS$_2$ and MoSe$_2$ transition metal dichalcogenides by means of *top-down* approaches (direct liquid phase exfoliation and electrochemical exfoliation) for the study of their applications in lithium storage and nitroarene reduction. Direct liquid phase exfoliation

relied on the sonication of *bulk* MoS_2 and $MoSe_2$ powder in organic solvents and the subsequent transfer of the exfoliated products to aqueous medium in the absence of stabilizers. Electrochemical exfoliation was carried out under cathodic conditions using aqueous and organic electrolytes, with macroscopic MoS_2 crystals. Both techniques allowed to preserve the original 2H phase of the dichalcogenides after their transformation into 2D nanosheets.

A method for the surface functionalization of MoS_2 nanosheets with carboxylic groups was developed by electrochemical treatment using organoiodides in aqueous medium. The resulting nanosheets displayed improved colloidal stability as well as enhanced catalytic activity in the reduction of a number of nitroarenes.

A comparative study of the catalytic performance of $MoSe_2$ and MoS_2 nanosheets prepared by direct liquid phase exfoliation in the reduction of nitroarenes in aqueous media was conducted, and a higher efficiency was disclosed for the $MoSe_2$ nanosheets. Computational calculations allowed to rationalize the different catalytic activities exhibited by $MoSe_2$ towards distinct structural isomers of the nitroarenes.

The production of cathodically exfoliated MoS_2 nanosheets using ammonium salts in organic solvent was investigated and their performance for lithium storage evaluated and compared with that of direct liquid phase-exfoliated nanosheets. It was concluded that lithium storage in the cathodically exfoliated MoS_2-based electrodes was more efficient, in terms of capacity and cyclability, than that of its liquid phase-exfoliated counterpart.

SR. PRESIDENTE DE LA COMISIÓN ACADÉMICA DEL PROGRAMA DE DOCTORADO EN MATERIALES

Índice de Contenido

Índice de Contenido 1

Índice de Figuras 4

Índice de Tablas 8

Glosario de términos 9

1 Introducción 13

1.1 Materiales nanoestructurados y materiales bidimensionales (2D) 13

Dicalcogenuros de metales de transición 2D 15

1.2 Métodos de obtención de materiales 2D 21

Métodos *bottom-up* o ascendentes 22

Métodos *top-down* o descendentes 23

Propiedades de las dispersiones coloidales de materiales 2D 30

1.3 Métodos de modificación de materiales 2D 32

a) Ingeniería de fase 32

b) Control morfológico 33

c) Funcionalización superficial covalente y no covalente 33

d) Generación de vacantes atómicas en materiales 2D 34

Referencias 35

2 Objetivos 50

3 Materiales y métodos 52

3.1 Preparación y procesado de dispersiones coloidales de MoS_2 y $MoSe_2$ 52

Exfoliación en fase líquida asistida por ultrasonidos 52

Exfoliación electroquímica catódica de MoS_2 52

Lavado de las dispersiones y transferencia a fase acuosa 55

Determinación de la concentración de las dispersiones coloidales 56

3.2 Modificación superficial de nanoláminas de MoS_2 y $MoSe_2$ 56

Funcionalización superficial de nanoláminas de MoS_2 56

Generación de vacantes superficiales por tratamiento con hidracina 57

Inmovilización de nanoláminas de dicalcogenuro sobre esponjas para aplicaciones catalíticas 57

3.3 Aplicaciones 58

Catálisis 58

Baterías de ion-Litio 60

Referencias 63

4 Técnicas de caracterización 64

4.1 Espectroscopías 64

Espectroscopía de absorción ultravioleta visible (UV-vis) 65

Espectroscopía infrarroja por transformada de Fourier con reflectancia total atenuada (ATR-FTIR) 68

Espectroscopía Raman 69

Espectroscopía fotoelectrónica de rayos X (XPS) 73

Difracción de rayos X (XRD) 76

Espectroscopia de resonancia paramagnética electrónica (EPR) 77

Dispersión de luz dinámica (DLS) 79

4.2 Técnicas cromatográficas 80

Cromatografía líquida de ultra-alta eficacia de fase reversa acoplada a espectrometría de masas (RP-UHPLC/MS) 80

4.3 Microscopías 83

Microscopía electrónica de transmisión (TEM) 83

Microscopía electrónica de barrido (SEM) 88

Microscopía de fuerza atómica (AFM) 91

4.4 Técnicas electroquímicas 94

Potencial de circuito abierto (OCV) 94

Voltamperometría cíclica (CV) 94

Espectroscopia de impedancia electroquímica (EIS) 98

Carga-descarga galvanostática (GCD) con limitación de potencial 101

4.5 Métodos computacionales 103

Teoría del Funcional de la Densidad (DFT) 103

Referencias 105

5 Resúmenes y artículos 108

5.1 Exfoliación electroquímica catódica.. 108

Resumen de Artículo I 108

ARTÍCULO I...110

Supplementary Material 157

Resumen de Artículo II 165

ARTÍCULO II... 167

Supporting Information 209

5.2 Exfoliación en fase líquida 246

Resumen de Artículo III 246

ARTICULO III 247

Supplementary Material 300

6 Conclusiones 327

Índice de Figuras

Figura 1. Ejemplos de materiales nanoestructurados derivados del carbono. 13

Figura 2. Esquema ilustrativo del grupo de los materiales 2D. Grafeno (*Graphene*), hidróxidos de capa doble (*layered double hydroxides*, LDHs), dicalcogenuros de metales de transición (*transition metal dichalcogenides*, TMDs), redes orgánicas covalentes (*covalent organic frameworks*, COFs), perovskitas (*perovskites*), nitruro de carbono grafitico (*graphitic carbon nitrides*, GCN), óxidos (*oxides*), redes metalorgánicas (*metal-organic frameworks*, MOFs), metales (*metals*), MXenos (*MXenes*), fósforo negro (*black phosphorous*, BP), nitruros de boro hexagonal (*hexagonal boron nitrides*, h-BNs). 15

Figura 3. **(a)** Esquema de la celda unidad de las fases más frecuentes de MoS_2, con indicación de su grupo espacial y tipo de coordinación del metal, también aplicable al caso del $MoSe_2$. **(b)** Visión cenital de la coordinación trigonal prismática **(izquierda)** y octaédrica **(derecha)** del $MoSe_2$, también aplicable al caso del MoS_2........................... 17

Figura 4. Esquema de la distribución electrónica de valencia para una coordinación **(a)** trigonal prismática y **(b)** octaédrica de los átomos de Mo^{4+}.. 17

Figura 5. Representación de una monocapa de MoS_2 con vacantes de S y átomos de H adsorbidos (esferas blancas). 20

Figura 6. Esquema de los métodos de preparación de materiales nanoestructurados. .. 21

Figura 7. Esquema de la formación de monocapas, bicapas y tricapas de MoS_2 mediante CVD.. 22

Figura 8. Esquema de la síntesis solvotérmica para la obtención de TMDs 2D (MoS_2, $MoSe_2$, WS_2, WSe_2, etc.)... 23

Figura 9. Esquema de las etapas de la exfoliación micromecánica de materiales laminares usando cita adhesiva. 24

Figura 10. **(a)** Esquema del mecanismo de exfoliación en ultrasonidos mediado por burbujas de cavitación. **(b)** Dispersión de grafeno obtenida usando un rotor de cizalla. 25

Figura 11. Esquema del mecanismo de la exfoliación asistida por intercalación química de Li^+.. 27

Figura 12. Montaje experimental típico de una celda electrolítica en un sistema de dos electrodos para exfoliación electroquímica y proceso general de exfoliación anódica y catódica. 28

Figura 13. (a) Esquema del efecto Tyndall. **(b)** Efecto Tyndall sobre una dispersión de nanoláminas de MoS_2 en agua. 31

Figura 14. **(a)** Esquema de algunos de los tipos de interacción entre partículas coloidales en suspensión. **(b)** Esquema ilustrativo de la definición del potencial Zeta en una partícula coloidal cargada. 32

Figura 15. Imágenes de nanoestructuras de MoS_2, con diferentes morfologías, obtenidas mediante microscopía electrónica. 33

Figura 16. Esquema del montaje de una pila de botón. 61

Figura 17. (a) Esquema de funcionamiento de un espectrofotómetro de doble haz. Espectros UV-vis de una dispersión de nanoláminas de **(b)** ee-MoS_2, preparadas por EE con HTMABr; y **(c)** $MoSe_2$, preparadas por LPE... 67

Figura 18. Esquema del funcionamiento de **(a)** un espectrómetro FTIR acoplado a **(b)** un accesorio con modalidad de ATR. 69

Figura 19. (a) Esquema del mecanismo de dispersión de la energía. **(b)** Diagrama de los mecanismos de excitación/relajación entre estados energéticos que originan la dispersión Rayleigh y Raman. Espectros Raman de nanoláminas de **(c)** MoS_2 modificadas con ácido iodoacético; y **(d)** nanoláminas de $MoSe_2$ preparadas mediante LPE. 71

Figura 20. Esquema de los componentes de un espectrofotómetro Raman, con indicación de su funcionamiento. 72

Figura 21. **(a)** Diagrama del mecanismo de emisión de un fotoelectrón y de un electrón Auger en XPS. Espectros XPS de **(b)** una muestra de HOPG donde se muestra la banda CKLL (electrones Auger) y C1s (fotoelectrones). Espectros XPS de alta resolución y con el fondo sustraído para **(b)** Mo 3d y **(c)** Se 3d de nanoláminas de $MoSe_2$ preparadas por LPE. 74

Figura 22. Esquema de los componentes, con indicación de su funcionamiento, de un espectrofotómetro XPS. 75

Figura 23. **(a)** Esquema del funcionamiento de un difractómetro de rayos X. **(b)** Diagrama de aplicación de la Ley de Bragg. Difractogramas de una muestra de nanoláminas de **(c)** $MoSe_2$ y **(d)** MoS_2, preparadas ambas mediante LPE. 76

Figura 24. Espectro EPR del polvo *bulk* de $MoSe_2$ (línea negra) y de las nanoláminas de $MoSe_2$ exfoliadas mediante LPE sin vacantes (línea roja) y tras la generación de vacantes (línea azul). 78

Figura 25. **(a)** Esquema de la fluctuación de la intensidad de la luz dispersada en función del tamaño de partícula. **(b)** Distribución del tamaño de partícula (obtenida del diámetro hidrodinámico) para una dispersión de nanoláminas de $MoSe_2$. 79

Figura 26. Esquema de la separación y determinación de compuestos mediante HPLC/MS. 82

Figura 27. **(a)** Esquema del funcionamiento de un microscopio de transmisión. Imágenes de HR-TEM, a diferentes aumentos, de **(b)** nanoláminas de $MoSe_2$ preparadas por LPE y **(c)** nanoláminas de ee-MoS_2 preparadas mediante exfoliación catódica en medio orgánico. 84

Figura 28. **(a)** Esquema del funcionamiento de un equipo STEM. Imagen HAADF de **(b)** una nanolámina de $MoSe_2$ y **(c)** una nanolámina de MoS_2, ambas preparadas mediante LPE. 85

Figura 29. Patrón de SAED de **(a)** nanoláminas de $MoSe_2$ y **(b)** nanoláminas de MoS_2, ambas exfoliadas mediante LPE, incluyendo la familia de planos implicados en las difracciones. 86

Figura 30. Mapeo EDX **(derecha)** para la determinación elemental de Mo (rojo) y Se (azul) de la correspondiente nanolámina de $MoSe_2$ **(izquierda)** obtenida mediante LPE. 87

Figura 31. **(a)** Esquema del funcionamiento de un microscopio SEM. **(b)** Imagen SEM de MoS_2 expandido en medio orgánico. **(c)** Imagen FE-SEM de un electrodo inicial de $MoSe_2$. 90

Figura 32. **(a)** Esquema de operación de un microscopio AFM. **(b)** Perfil típico de la interacción punta-muestra en función de la distancia de separación. 91

Figura 33. Imágenes de AFM de **(a)** una nanolámina de MoS_2 preparada mediante EE con KCl y **(b)** nanoláminas de ee-MoS_2, preparado mediante EE con HTMABr. 93

Figura 34. **(a)** Representación del barrido lineal de potencial frente al tiempo empleado en CV. **(b)** Esquema de un voltamograma típico, indicando las reacciones que ocurren en función del potencial aplicado. 95

Figura 35. **(a, b, d, e, g, h)** Voltamogramas cíclicos de materiales con diferentes mecanismos de almacenamiento de energía y **(c, f, i)** dependencia del potencial eléctrico vs tiempo en función del tipo de almacenamiento de energía. 96

Figura 36. **(a)** Principales picos redox de un electrodo de MoS_2, registrados por CV a diferentes velocidades de barrido. **(b)** Valores de *b* calculados aplicando el método de Dunn, a partir de los datos de (a). 97

Figura 37. Ejemplos de la proporción de contribución faradaica (no sombreado) y pseudocapacitiva (sombreado) para un electrodo de MoS_2, registradas a 1 $mV \cdot s^{-1}$....... 98

Figura 38. Esquema del mecanismo de perturbación sinusoidal de un sistema electroquímico para la medición de impedancia. 99

Figura 39. Diagrama de Nyquist que muestra **(a)** la correlación entre la Z medida y los fenómenos físicos de los que depende, y un ejemplo de circuito equivalente (*inset*). **(b)** Relación entre la Z de un sistema y el tipo de mecanismo de almacenamiento de carga. 100

Figura 40. Diferentes perfiles de curvas GCD según el mecanismo de almacenamiento de energía (indicado debajo).. 102

Figura 41. Curva de polarización donde se representa la variación del potencial en función de la capacidad gravimétrica de carga y descarga para un electrodo de ee-MoS_2, a 0.2 $A \cdot g^{-1}$. 103

Índice de Tablas

Tabla 1. Electrolitos empleados para la EE en fase orgánica. 54

Tabla 2. Sustratos empleados para la reacción de reducción durante los ensayos catalíticos. 58

Glosario de términos

0D: cerodimensional

1D: monodimensional

2D: bidimensional

2-NA: 2-nitroanilina

2-NP: 2-nitrofenol

3D: tridimensional

3-NA: 3-nitroanilina

3-NP: 3-nitrofenil

4-NA: 4-nitroanilina

4-NP: 4-nitrofenol

ACN: acetonitrilo

AFM: microscopía de fuerza atómica

AMP: adenosín monofosfato

BE: energía de ligadura

BP: fósforo negro

CB: negro de carbono

CE: contraelectrodo

CTAB: bromuro de cetiltrimetilamonio

CV: voltametría cíclica

CVD: depósito químico en fase vapor

DFT: teoría del funcional de densidad

DLS: dispersión dinámica de luz

DMF: N,N-dimetilformamida

DMSO: dimetil sulfóxido

EC: eficiencia culómbica

EDL: doble capa eléctrica

EDLC: condensador de doble capa eléctrica

EE: exfoliación electroquímica

ee-MoS$_2$: nanoláminas de MoS$_2$ obtenidas mediante EE en fase orgánica.

EIS: espectroscopía de impedancia electroquímica

EPR: resonancia paramagnética electrónica

ESI: ionizador de electrospray

FE-SEM: microscopía electrónica de barrido de emisión de campo

FTIR-ATR: espectroscopia infrarroja con transformada de Fourier de reflectancia total atenuada.

g: fuerza centrífuga relativa (*relative centrifugal force,* rcf)

GCD: carga/descarga galvanostática con limitación de potencial.

GMP: guanosín monofosfato

HAADF: detector de campo anular de alto ángulo

h-BN: nitruro de boro hexagonal

HER: reacción de evolución de hidrógeno

HOPG: grafito pirolítico altamente orientado

HPLC: cromatografía líquida de alta eficacia

HR-TEM: microscopía electrónica de transmisión de alta resolución

HTMABr: bromuro de hexiltrimetilamonio

HTMACl: cloruro de hexiltrimetilamonio

KE: energía cinética

LPE: exfoliación en fase líquida

lpe-MoS$_2$: nanoláminas de MoS$_2$ obtenidas mediante LPE

LSV: voltametría de barrido lineal

MB: azul de metileno

MO: naranja de metilo

MS: espectrometría de masas

MWCNTs: nanotubos de carbono de pared múltiple

NMP: N-metil-2-pirrolidona

OCV: potencial de circuito abierto

PC: carbonato de propileno

PVDF: fluoruro de polivinilideno

QTOF: cuadrupolo-tiempo de vuelo

R_{CT}: resistencia a la transferencia de carga

RP-UHPLC: cromatografía líquida de ultra-alta eficacia de fase reversa

SAED: difracción electrónica en área seleccionada

SEM: microscopía electrónica de barrido

STEM: microscopía electrónica de transmisión de barrido

TBACl: cloruro de tetrabutilamonio

TEACl: cloruro de tetraetilamonio

TEM: microscopía electrónica de transmisión

$THABF_4$: tetrafluoroborato de tetrahexilamonio

THACl: cloruro de tetrahexilamonio

TMACl: cloruro de tetrametilamonio

TMDs: dicalcogenuros de metales de transición

TMOABr: bromuro de octiltrimetilamonio

TPACl: cloruro de tetrapropilamonio

UHPLC: cromatografía líquida de ultra-alta eficacia

UV-vis: ultravioleta-visible

WE: electrodo de trabajo

XPS: espectroscopía de fotoelectrónica de rayos X

XRD: difracción de rayos X

1 Introducción

1.1 Materiales nanoestructurados y materiales bidimensionales (2D)

Los materiales nanoestructurados o nanomateriales son aquellos sólidos que presentan al menos una de sus dimensiones espaciales en la escala de los nanómetros (1-100 nm). De esta manera, los nanomateriales se pueden clasificar como cero-dimensionales (0D, como los puntos cuánticos), si poseen tres dimensiones en la escala nanométrica; unidimensionales (1D, como los nanotubos), cuando dos de sus dimensiones están en esta escala; bidimensionales (2D, como las nanoláminas) si tan solo una de sus dimensiones es del orden de los nanómetros; y tridimensionales (3D, como los materiales *bulk* formados por nanogranos), si presentan dimensiones macroscópicas en las tres direcciones espaciales junto con una estructura interna de unidades nanométricas (Figura 1) [1,2].

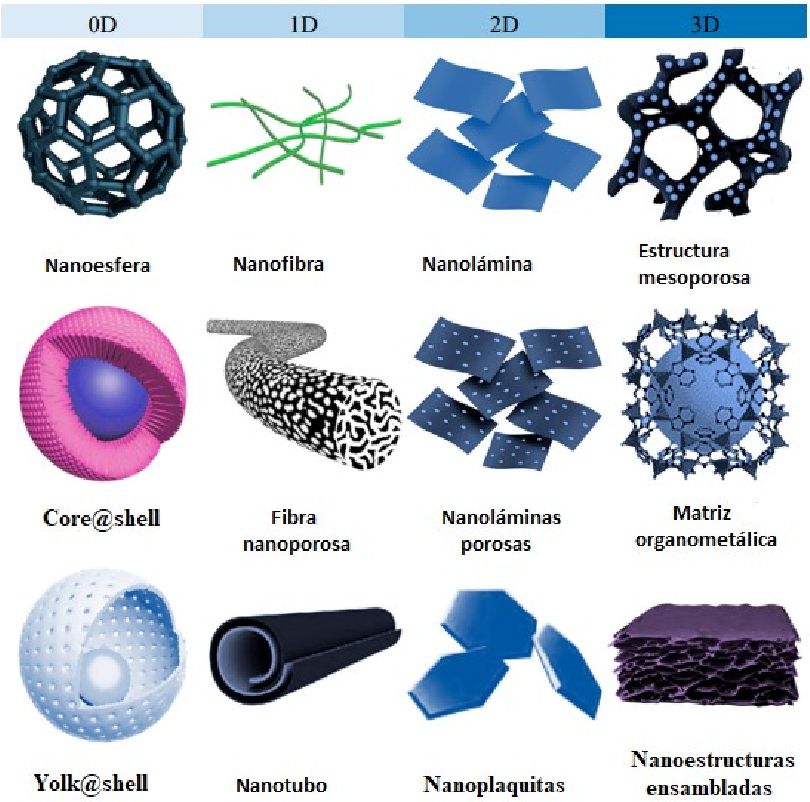

Figura 1. Ejemplos de materiales nanoestructurados derivados del carbono. Adaptado de [3].

El inicio de la era de los materiales 2D vino marcado por el aislamiento y posterior estudio de las propiedades del grafeno. Estrictamente hablando, el término grafeno hace referencia a una monocapa de grafito, aunque también se usa para referirse a nanoláminas de grafito formadas por unas pocas o varias monocapas (< 10) [4]. Las propiedades de los materiales 2D son, en general, diferentes de las observadas en sus equivalentes *bulk*, debido principalmente al incremento de la superficie específica (relación superficie/masa) y al confinamiento de los electrones en dos dimensiones, lo que altera muchas de sus propiedades (electrónicas y otras) [5]. Un ejemplo de ello es la fotoluminiscencia detectada en las nanoláminas de MoS_2, ausente en su forma *bulk*, o la transición de semiconductor de *gap* indirecto a directo del MoS_2 *bulk* a medida que su grosor se aproxima a la monocapa [6]. La mayoría de los materiales 2D estudiados proceden de sólidos laminares (Figura 2), es decir, de sólidos constituidos por monocapas apiladas. Dentro de cada monocapa, los átomos están unidos por enlaces covalentes, mientras que los apilamientos de unas monocapas sobre otras están generalmente basados en interacciones interlaminares débiles de tipo van der Waals. Los materiales 2D derivados de compuestos laminares están formados por un número limitado de monocapas apiladas, típicamente menor de 10, aunque el número depende del sólido en cuestión. Es más, el número concreto de monocapas apiladas del material 2D permite modular en muchos casos sus propiedades, de manera que un material 2D monocapa suele presentar propiedades diferenciadas de las de sus equivalentes de pocas o varias monocapas [7]. Aunque los equivalentes *bulk* 3D de la mayor parte de los materiales 2D estudiados hasta el presente poseen una estructura laminar, también existen materiales 2D cuyos equivalentes *bulk* 3D no son laminares.

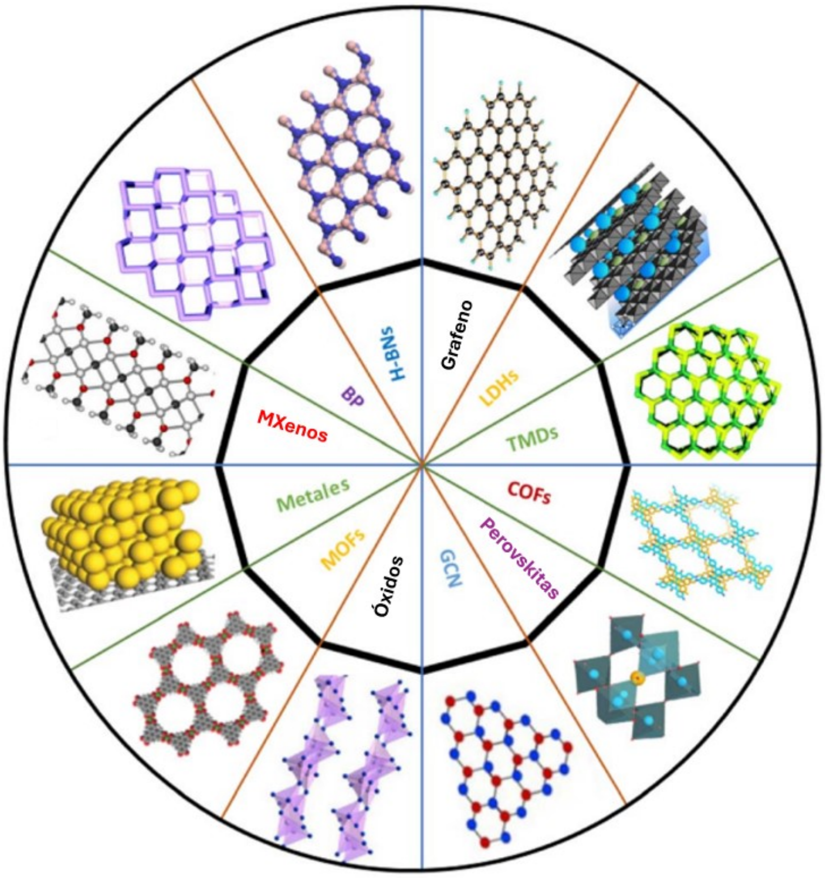

Figura 2. Esquema ilustrativo del grupo de los materiales 2D. Grafeno (*Graphene*), hidróxidos de capa doble (*layered double hydroxides*, LDHs), dicalcogenuros de metales de transición (*transition metal dichalcogenides*, TMDs), redes orgánicas covalentes (*covalent organic frameworks*, COFs), perovskitas (*perovskites*), nitruro de carbono grafitico (*graphitic carbon nitrides*, GCN), óxidos (*oxides*), redes metalorgánicas (*metal-organic frameworks*, MOFs), metales (*metals*), MXenos (*MXenes*), fósforo negro (*black phosphorous*, BP), nitruros de boro hexagonal (*hexagonal boron nitrides*, h-BNs). Adaptado de [8].

Dicalcogenuros de metales de transición 2D

Los dicalcogenuros de metales de transición (*transition metal dichalcogenides,* TMDs) son un conjunto de compuestos que en su mayoría pertenecen a la familia de los sólidos laminares, de fórmula genérica MX_2 y cuya estructura consiste en una capa de un metal de transición M (Mo, W, Ti, V, etc.) empaquetada entre dos capas de calcógeno X (S, Se, Te) [8]. Los TMDs presentan una gran variedad de combinaciones y diferentes características, y se han descrito más de 40 compuestos laminares formados por la combinación de diferentes metales de transición y calcógenos. Dependiendo del número de electrones *d* del átomo metálico, es posible encontrar TMDs semiconductores (p.e., MoS_2 y WS_2), metálicos (p.e., NbS_2 y VSe_2), semimetálicos (p.e., WTe_2 y $TiSe_2$), magnéticos ($CrSe_2$) e incluso superconductores (p.e., $NbSe_2$ y $PdTe_2$). En los TMDs, el metal puede adoptar una coordinación trigonal prismática de simetría hexagonal (fase 2H) o romboédrica (fase 3R); o una coordinación octaédrica de simetría tetragonal (fase 1T) [9,10]. El creciente interés en las formas bidimensionales de los TMDs se explica tanto por el perfeccionamiento de los métodos de preparación como por el amplio potencial de aplicación que presentan en campos como la (opto)electrónica, sensores, (electro/foto)catálisis, remediación ambiental o almacenamiento de energía, derivado de sus atractivas propiedades físicas [10]. Si bien el compuesto más estudiado de la familia de los TMDs 2D es el MoS_2, debido a su mayor disponibilidad práctica frente a otros TMDs, existe un interés creciente en otros compuestos de este grupo, como $MoSe_2$, $NbSe_2$, $MoTe_2$ o WS_2, cuyas prestaciones en diferentes aplicaciones podrían ser superiores a las del MoS_2 [11].

MoS_2 y $MoSe_2$ 2D

Principalmente, en esta tesis se ha trabajado con nanoláminas de MoS_2 y $MoSe_2$.

a) Estructuras atómica y cristalina

Tanto el MoS_2 (presente en la naturaleza en forma de cristales de molibdenita) como el $MoSe_2$ (encontrado en la drisdalita, mineral extremadamente raro en el que los átomos de S de la molibdenita se sustituyen por Se) tienen, en sus formas *bulk,* una estructura laminar consistente en el empaquetamiento denso de un plano de átomos de Mo entre dos planos hexagonales de átomos de calcógeno X (X=S o Se). Cada monocapa del dicalcogenuro responde a la fórmula S-Mo-S o Se-Mo-Se, respectivamente, y presenta fuertes enlaces covalentes Mo-X, mientras que las monocapas están unidas entre sí mediante interacciones débiles de tipo van der Waals (~6.2 Å de espaciado interlaminar para MoS_2 y ~6.5 Å para $MoSe_2$). Estos dicalcogenuros pueden encontrarse en tres fases cristalinas distintas, asociadas al correspondiente grupo espacial de su celda unidad (Figura 3): fase 1T (trigonal), fase 2H (hexagonal) y fase 3R (romboédrica) [9,12]. La fase 2H es la más estable termodinámicamente en condiciones ambientales tanto para MoS_2 como para $MoSe_2$. Las fases 3R y 1T son metaestables y se obtienen de manera sintética [12,13].

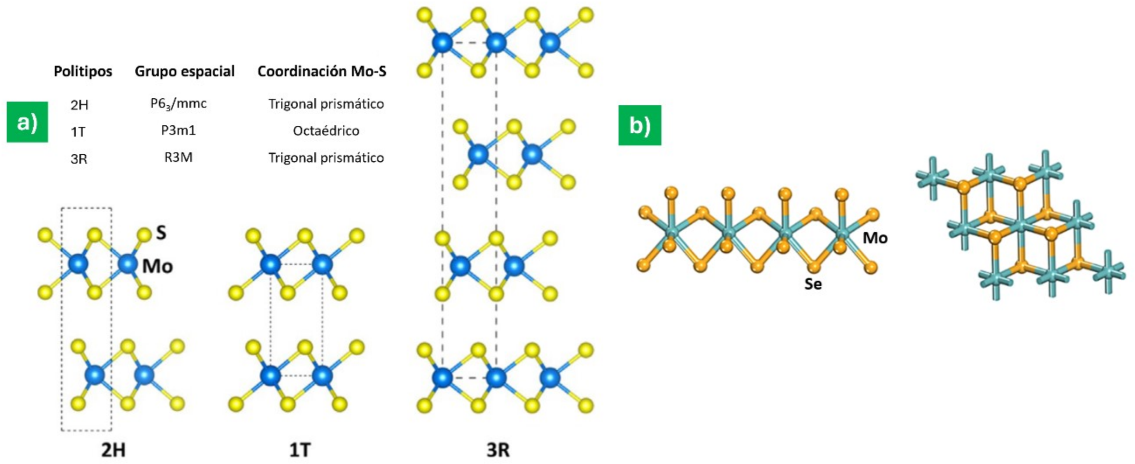

Figura 3. (a) Esquema de la celda unidad de las fases más frecuentes de MoS_2, con indicación de su grupo espacial y tipo de coordinación del metal, también aplicable al caso del $MoSe_2$. Adaptado de [9]. **(b)** Visión cenital de la coordinación trigonal prismática **(izquierda)** y octaédrica **(derecha)** del $MoSe_2$, también aplicable al caso del MoS_2. Adaptado de [14].

b) *Propiedades electrónicas*

Las propiedades electrónicas del MoS_2 y del $MoSe_2$ dependen de la coordinación de los átomos de Mo y de la interacción entre los electrones de sus orbitales *d* (Figura 4). La coordinación trigonal prismática, característica de la fase 2H y 3R, da lugar al llenado completo del orbital d_{z^2}, pero deja vacíos los orbitales d_{xy} y $d_{x^2-y^2}$. A causa de la configuración electrónica de valencia resultante del orbital $4d^2$ del Mo^{4+}, las fases 2H y 3R tienen carácter semiconductor. Sin embargo, en la coordinación octaédrica típica de la fase 1T, la degeneración de los orbitales d_{xz}, d_{yz} y d_{xy} provoca una distribución electrónica diferente. En este caso, la ausencia de un *gap* de banda y la deslocalización de los electrones entre los orbitales *d* isoenergéticos confiere carácter metálico a la fase 1T [9].

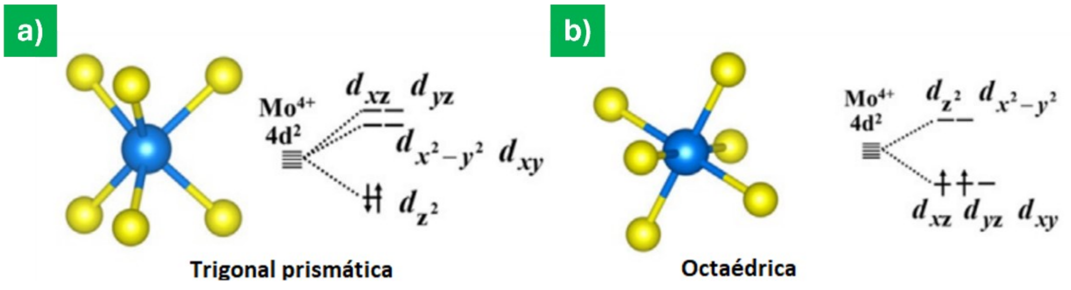

Figura 4. Esquema de la distribución electrónica de valencia para una coordinación **(a)** trigonal prismática y **(b)** octaédrica de los átomos de Mo^{4+}. Adaptado de [9].

La distribución electrónica específica y la energía de las bandas de conducción y valencia confieren a los materiales nanoestructurados, incluidos los materiales 2D, sus singulares propiedades. El 2H-MoS_2 *bulk* es un semiconductor indirecto (*gap* de banda ~1.2 eV), aunque al disminuir progresivamente el número de monocapas de este material (por debajo de las 10), el *gap* de banda aumenta. Finalmente, en el límite de una única monocapa el 2H-MoS_2 es un semiconductor de *gap* de banda directo (~1.9 eV). El 2H-$MoSe_2$ también pasa de ser semiconductor indirecto en su forma *bulk* (*gap* de banda de ~1.1 eV) a directo en su versión monocapa (~1.55 eV). Ello hace que las formas 2D de ambos compuestos, especialmente las monocapas, exhiban propiedades fotoluminiscentes. No obstante, la fase 1T del $MoSe_2$ es más estable termodinámicamente que la del MoS_2 [12]. Además, aunque el 2H-$MoSe_2$ es también un sólido semiconductor, presenta una conductividad eléctrica mucho mayor que la del 2H-MoS_2 ($1 \cdot 10^{-3}$ $S \cdot m^{-1}$ frente a $5 \cdot 10^{-28}$ $S \cdot m^{-1}$, respectivamente) debido al mayor carácter metálico del átomo de Se [15].

A diferencia del grafeno, que no posee *gap* de banda al ser un semimetal, la presencia de un *gap* de banda en 2H-MoS_2 y $MoSe_2$ permite una amplia modulación de sus propiedades eléctricas mediante dopaje y funcionalización molecular [9,13], propiedad que sitúa al MoS_2 y al $MoSe_2$ como posibles sustitutos del silicio en transistores de efecto de campo [16,17]. La gran similitud entre las propiedades electrónicas del 2H-MoS_2 y el $MoSe_2$ permite que ambos encuentren aplicaciones en el campo de los (bio)sensores [18-20], dispositivos (bio)electrónicos [21,22], (electro)catálisis [23,24] generación de H_2 verde [25].

c) Propiedades mecánicas y tribológicas

Debido a su reducido coeficiente de fricción, consecuencia de la exposición de planos basales de baja energía superficial y carentes de enlaces no saturados, el MoS_2 es frecuentemente utilizado como lubricante seco y como aditivo en materiales compuestos que requieren una baja fricción [26,27]. Por la misma razón, el $MoSe_2$ también presenta un bajo coeficiente de fricción, pero además posee una mayor estabilidad térmica y menor sensibilidad a la humedad que el MoS_2 y disulfuros análogos [28], con lo que resulta más adecuado como aditivo en lubricantes para usos en entornos húmedos [29].

El módulo de Young o de tracción de las nanoláminas de MoS_2 (~270 GPa) es comparable al del acero (~200-250 GPa) y al del óxido de grafeno (~250 GPa) [30,31], lo que permite su uso como refuerzo de materiales compuestos [32]. También se han conseguido preparar filmes de MoS_2 (5-25 capas de espesor) con un alto coeficiente de elasticidad, lo que señala a este material como un buen candidato para aplicaciones en el campo de los semiconductores flexibles [30]. Por otro lado, se ha determinado que el módulo de Young para monocapas de $MoSe_2$ es de ~130 GPa [33], aproximadamente la mitad de los valores publicados para MoS_2 y óxido de grafeno [30,31].

d) Propiedades térmicas

En los materiales semiconductores, parece que el mecanismo de transporte térmico a lo largo de la red cristalina está controlado por la transmisión de fonones (vibraciones atómicas cuantizadas). Para una nanolámina, formada por el apilamiento de una o más monocapas, el transporte de fonones a lo largo de la red cristalina se produce longitudinalmente al plano basal, ya que la dirección transversal incluye espacios interlaminares que dispersan los fonones y, por tanto, dificultan el transporte fonónico [34].

En el caso del MoS_2 *bulk*, la gran cantidad de capas apiladas contribuye la baja conductividad térmica en el plano transversal (~18 $W \cdot m^{-1} \cdot K^{-1}$) [35]. Sin embargo, se ha determinado que el valor de la conductividad térmica longitudinal para una monocapa suspendida de MoS_2 es de ~34.5 $W \cdot m^{-1} \cdot K^{-1}$ [36], mientras que para monocapas y bicapas soportadas oscila entre 35 y 62 $W \cdot m^{-1} \cdot K^{-1}$ [37]. La gran conductividad térmica de las nanoláminas de MoS_2 posibilita su aplicación en dispositivos electrónicos, por su rápida disipación del calor, que contribuye a evitar sobrecalentamientos [38]; y en nanocomposites, ya que la buena compatibilidad del MoS_2 con otros materiales permite mejorar sus propiedades térmicas [39].

En el caso del $MoSe_2$, se ha encontrado que, para muestras de un grosor comprendido entre 5 y 80 nm, la conductividad térmica en el plano longitudinal aumenta desde 6.2 a ~30 $W \cdot m^{-1} \cdot K^{-1}$ [40]. Las propiedades térmicas del $MoSe_2$ permiten su aplicación en el desarrollo de dispositivos termoeléctricos (que permiten la conversión directa de calor residual en energía eléctrica), por su buena conductividad térmica, durabilidad y bajo coeficiente de Seebeck (relación entre la capacidad de generación de electricidad y la diferencia de temperatura empleada) [41].

e) Propiedades químicas

De forma análoga al grafeno, tanto el MoS_2 como el $MoSe_2$ prístino poseen un marcado carácter hidrófobo debido a su baja energía superficial (ausencia de enlaces no saturados en su plano basal) [42], lo que dificulta su dispersión coloidal directa en agua en ausencia de agentes estabilizantes [43] o de funcionalización superficial adecuada [44].

El MoS_2 *bulk* presenta una significativa inercia química, y solamente se disuelve en ácidos oxidantes fuertes, como el agua regia, para dar Mo^{6+}. Su calentamiento a 500 ºC a temperatura ambiente provoca su oxidación a MoO_3, y su calentamiento a vacío por encima de 1200 ºC provoca su descomposición en Mo_2S_3 y Mo metálico [45]. Sin embargo, los derivados 2D del MoS_2 y del $MoSe_2$ tienden a ser más reactivos y pueden experimentar procesos de oxidación superficial simplemente por exposición prolongada a condiciones ambientales [46,47].

Asimismo, si bien el plano basal de las nanoláminas es generalmente inerte, la relativa abundancia de vacantes de S y Se (debido a su moderada energía de formación) en los planos basales y la existencia de los bordes dejan expuestos átomos insaturados que pueden reaccionar con facilidad (Figura 5). Por tanto, los bordes y vacantes constituyen centros de alta reactividad [15] y poseen actividad catalítica en procesos como la reacción de evolución de hidrógeno (*hidrogen evolution reaction*, HER*)* [48,49], la hidrodesulfuración [50], la reducción de compuestos nitrogenados [51,52] y la reducción de nitroarenos [53,54].

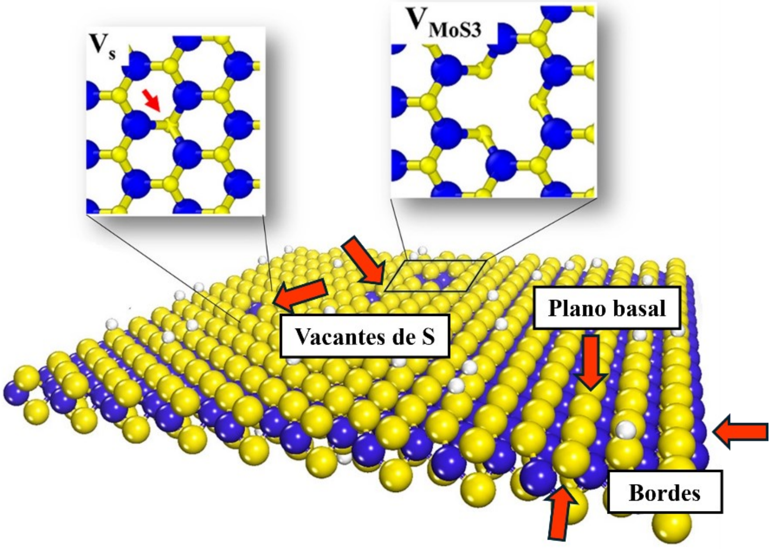

Figura 5. Representación de una monocapa de MoS_2 con vacantes de S y átomos de H adsorbidos (esferas blancas). Adaptado de [55].

1.2 Métodos de obtención de materiales 2D

Las propiedades de los materiales 2D son sustancialmente diferentes a las de sus correspondientes formas *bulk.* Aunque sus características puedan verse afectadas por factores como el dopaje atómico o molecular, la generación de defectos estructurales como vacantes atómicas o su combinación con otros (nano)materiales para formar heteroestructuras, éstas dependen en gran medida del grosor (o número de capas) del material 2D. Por tanto, controlar el grado de exfoliación de los compuestos *bulk* laminares precursores es de gran importancia para el diseño y control de las propiedades finales de los materiales 2D. Actualmente, existe una gran variedad de métodos de preparación de materiales 2D, basados en distintas estrategias, y que poseen diferentes características en términos de coste de producción, cantidad de material obtenido, rendimiento, escalabilidad del proceso, grado de control sobre las propiedades finales del producto (espesor, tamaño lateral, oxidación, defectos, funcionalización, morfología, etc.), eficiencia y cantidad de subproductos generados. Por ello, es importante considerar previamente la aplicación concreta que se persigue para un material 2D, la cual determinará las características que este ha de poseer y, por tanto, el método o métodos de preparación más adecuados.

Los métodos de preparación de materiales nanoestructurados, incluidos los materiales 2D, pueden clasificarse en dos grandes grupos: métodos ascendentes o *bottom-up* y descendentes o *top-down* (Figura 6) [56]. A continuación, se describen los métodos ascendentes y descendentes más usados para la preparación de materiales 2D, con especial énfasis en TMDs 2D.

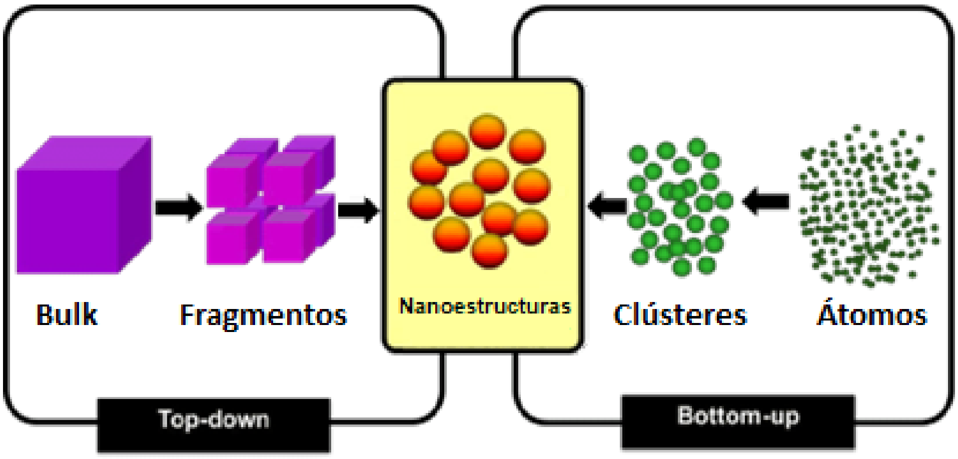

Figura 6. Esquema de los métodos de preparación de materiales nanoestructurados. Adaptado de [57].

Métodos *bottom-up* o ascendentes

Se basan en el empleo de precursores atómicos o moleculares que, tras una serie de reacciones químicas, se ensamblan para dar lugar a estructuras finales con morfología 2D. En la síntesis de TMDs 2D, destacan el depósito químico en fase vapor (*chemical vapor deposition,* CVD) y la síntesis solvotérmica.

a) Depósito químico en fase vapor (CVD)

Se basa en la descomposición y reacción química en fase vapor de un precursor del metal M (p. ej. MO_3 o MCl_5) con otro del calcógeno sobre la superficie de un sustrato (generalmente metálico), dando lugar al crecimiento de un depósito 2D del TMD correspondiente (Figura 7). El CVD se realiza en el interior de cámaras de reacción adecuadas que requieren de temperaturas elevadas para permitir la síntesis del TMD. Esta técnica permite un control bastante preciso del grosor de las nanoláminas (monocapas, bicapas, etc.) y suele dar lugar a productos de muy alta calidad estructural. Sin embargo, requiere de equipos muy específicos y de tiempos de reacción largos [11]. Por sus características, los TMDs 2D preparados por CVD encuentran aplicaciones como componentes en transistores de efecto de campo, contraelectrodos de celdas fotovoltaicas, fotodetectores y electrocatalizadores para la HER [58].

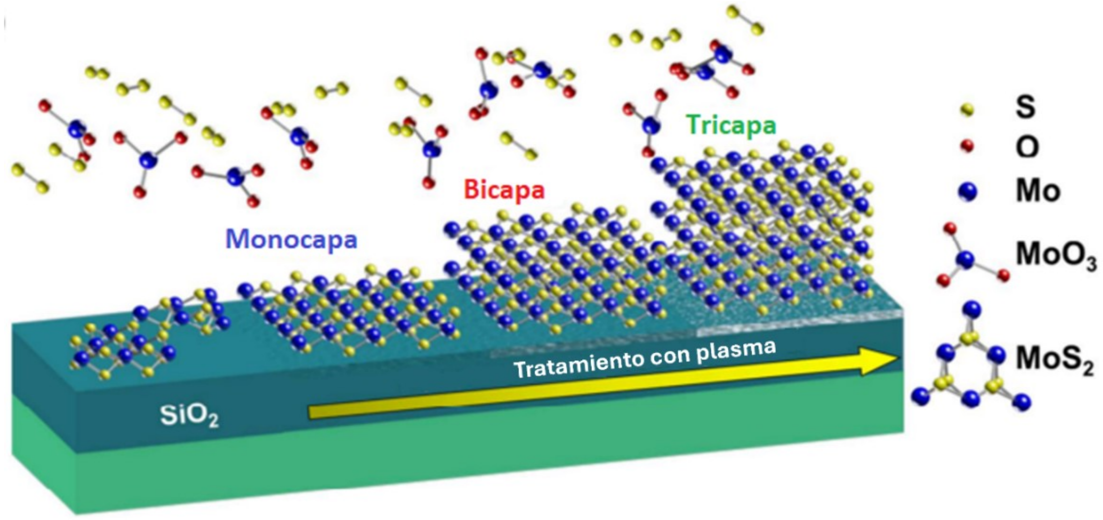

Figura 7. Esquema de la formación de monocapas, bicapas y tricapas de MoS_2 mediante CVD. Adaptado de [11].

b) Síntesis solvotérmica

Consiste en la reacción química en fase líquida (acuosa u orgánica) de precursores que contengan el metal de transición y el calcógeno de interés. Se lleva a cabo en recipientes de presión o autoclaves (Figura 8) y, aunque las temperaturas a las que se trabaja en el autoclave sólo sean moderadamente altas (típicamente 200-300ºC), la presión alcanzada en su interior es muy elevada (usualmente 10-100 bares). Es una técnica muy versátil para la síntesis de un gran número materiales nanoestructurados, entre los que se encuentran muchos TMDs 2D. De hecho, una apropiada optimización de las condiciones de síntesis permite la obtención de TMDs 2D con diversas morfologías y proporción de fases cristalinas (1T, 2H) [11]. Los TMDs 2D obtenidos por el método de síntesis solvotérmica han sido empleados como componentes de sensores electroquímicos y biosensores [59], como electrodos para baterías de Li-S [60] y en aplicaciones optoelectrónicas [61], entre otros usos.

Figura 8. Esquema de la síntesis solvotérmica para la obtención de TMDs 2D (MoS_2, $MoSe_2$, WS_2, WSe_2, etc.). Adaptado de [11].

Métodos *top-down* o descendentes

Se basan en la exfoliación de materiales laminares *bulk* para la obtención de las correspondientes láminas 2D, formadas tanto por una como por varias monocapas. La exfoliación se consigue mediante la introducción de suficiente energía en el sistema (en forma de ondas de ultrasonidos, fuerzas de cizalla o intercalación (electro)química) como para superar las interacciones interlaminares débiles de tipo van der Waals, pero insuficiente para romper de manera generalizada los fuertes enlaces covalentes intralaminares. Este proceso se ve favorecido por el hecho de que las fuerzas de van der

Waals se vuelven despreciables para distancias interlaminares superiores a varios Å, ya que la energía de interacción es proporcional a $1/d^6$ [62].

a) Exfoliación micromecánica

Este método permite extraer nanoláminas de espesor atómico de cristales laminares *bulk* adhiriendo las capas más externas del cristal a materiales adhesivos (incluida cinta adhesiva común). Repitiendo sucesivamente este proceso, se consiguen láminas extremadamente delgadas, incluso de grosor atómico (Figura 9). En 2004, Novoselov y Geim aislaron por primera vez láminas de grafeno de varias monocapas aplicando este método a una pieza de grafito pirolítico altamente orientado (*highly oriented pirolytic graphite*, HOPG) [4] y, posteriormente, obtuvieron nanoláminas de otros sólidos laminares (MoS_2, WS_2, BP, h-BN, etc.) [63]. A pesar de que este método permite la obtención de nanoláminas 2D limpias, de grandes dimensiones laterales y de alta cristalinidad, su rendimiento es extremadamente bajo, y la falta de control sobre el tamaño y el grosor de los objetos obtenidos lleva asociada una escasa reproducibilidad (se suelen obtener láminas monocapa y de varias capas entre una multitud de láminas mucho más gruesas). Por estos motivos, los materiales 2D obtenidos por exfoliación micromecánica suelen ser muy usados en estudios fundamentales, pero no son útiles con vistas a aplicaciones prácticas [64].

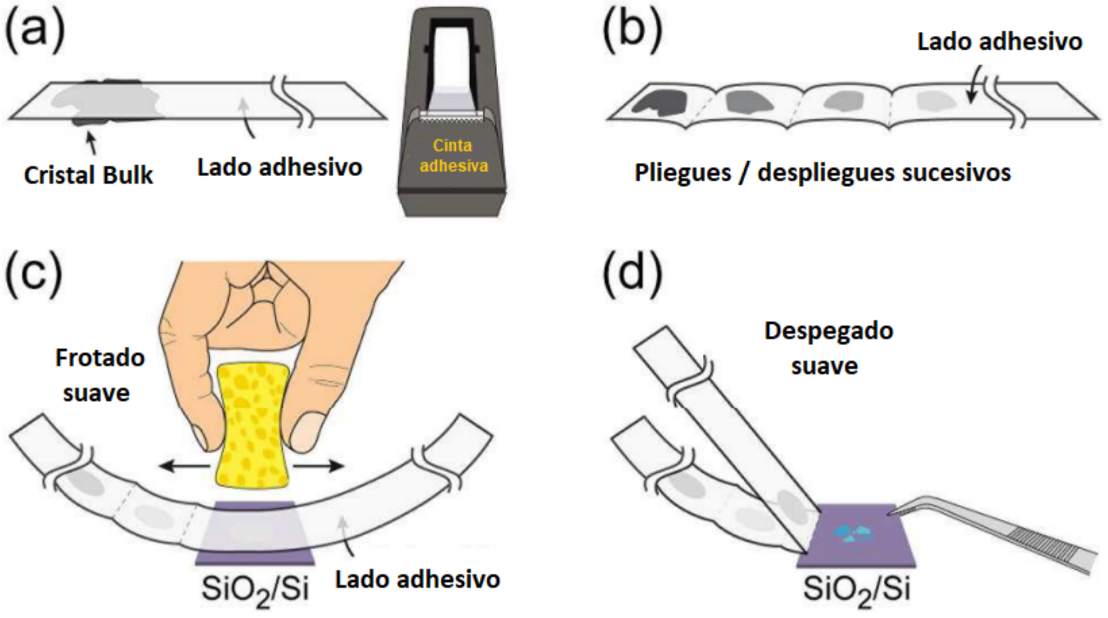

Figura 9. Esquema de las etapas de la exfoliación micromecánica de materiales laminares usando cita adhesiva. Adaptado de [65].

De hecho, el bajo rendimiento y ritmo de producción de la exfoliación micromecánica hizo necesario desarrollar otras estrategias de exfoliación más eficientes para la producción de materiales 2D. Actualmente, muchos de los métodos más comunes de exfoliación se llevan a cabo en medio líquido y permiten la obtención de cantidades considerables de material 2D, facilitando a la vez su procesado.

b) Exfoliación por ultrasonidos y fuerzas de cizalla

La exfoliación directa de compuestos laminares mediante ultrasonidos es una de las opciones más simples y extendidas para la obtención en medio líquido de materiales 2D en cantidades significativas (Figura 10). Para ello, el material laminar *bulk* se transfiere a un disolvente adecuado y se somete a tratamiento por ultrasonidos durante un período determinado. Las ondas de ultrasonidos provocan la aparición en el disolvente de las denominadas burbujas de cavitación. Estas burbujas colapsan y generan fuertes ondas de choque que ejercen tensiones verticales y horizontales sobre el material laminar disperso. Como consecuencia, se produce la deslaminación y fractura de material *bulk*, generando láminas 2D de unas pocas o varias monocapas de espesor junto con fragmentos poco exfoliados o no exfoliados de mayor grosor [64,66]. Como método alternativo de exfoliación directa en medio líquido, se pueden emplear fuerzas de cizalla, aplicadas por medio de un sistema de rotor-estator [67].

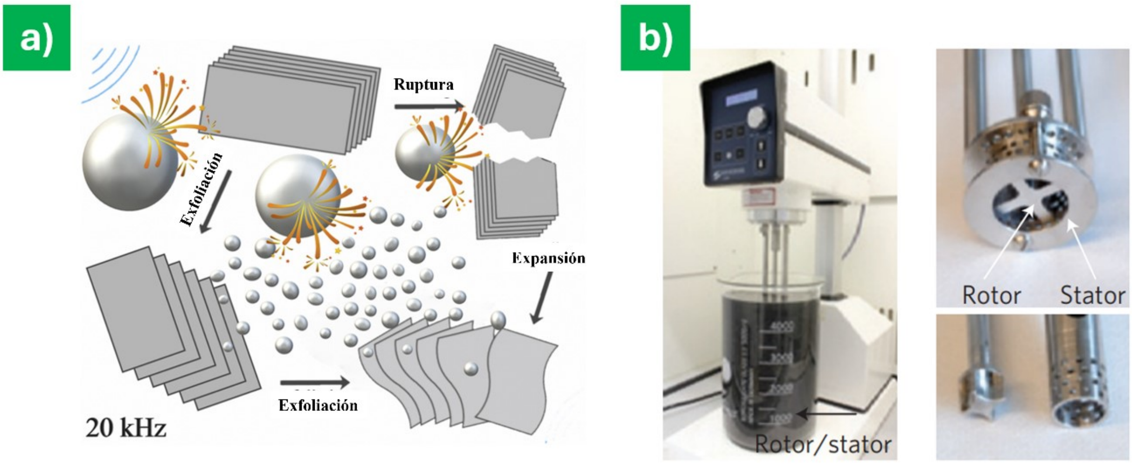

Figura 10. (a) Esquema del mecanismo de exfoliación en ultrasonidos mediado por burbujas de cavitación. Adaptado de [68]. **(b)** Dispersión de grafeno obtenida usando un rotor de cizalla. Adaptado de [67].

Para lograr una óptima exfoliación en fase líquida (*liquid phase exfoliation*, LPE), se ha demostrado que es necesario que la energía superficial del disolvente empleado sea similar a la energía superficial del plano basal del material laminar correspondiente, lo que permite minimizar el coste energético de la estabilización coloidal de las nanoláminas 2D [66]. En esta línea, se ha determinado que disolventes orgánicos tales como la *N*-metil-2-pirrolidona (*N-methyl-2-pyrrolidone*, NMP) y la N,N-dimetilformamida (*N,N-dimethylformamide*, DMF) son efectivos para la exfoliación y dispersión coloidal tanto de grafito [69] como de otros materiales laminares (TMDs, h-BN, fosforeno, etc.) [66]. Como alternativa al uso de disolventes orgánicos, pueden utilizarse mezclas de disolvente orgánico con agua o disoluciones acuosas para ajustar la energía superficial del medio y facilitar así la estabilización coloidal del material 2D. De esta forma, se han descrito mezclas etanol/agua como disolvente [70], así como agua con determinadas concentraciones de surfactantes [71], polímeros [72] y biomoléculas anfifílicas [73]. Estos métodos de exfoliación directa en fase líquida permiten la obtención de dispersiones coloidales relativamente concentradas de materiales 2D que mantienen mayormente su composición química e integridad estructural. No obstante, la proporción de monocapas obtenidas es muy reducida, el proceso puede inducir la aparición de algunos defectos estructurales y el rendimiento de exfoliación es muy bajo (aproximadamente del 1%) [64]. En cualquier caso, los materiales 2D exfoliados por ultrasonidos/fuerzas de cizalla encuentran aplicaciones en la adsorción de contaminantes [74], (foto)catálisis [75], células solares [76] y almacenamiento de energía [77].

c) *Exfoliación por intercalación química*

Esta metodología, también conocida como exfoliación química, se basa en la inserción de cationes de metales alcalinos (Li^+, Na^+, K^+) en los espacios interlaminares de un material laminar *bulk*, para generar un compuesto de intercalación expandido (por ejemplo, Li_xMX_2 en el caso de los TMDs, donde M es el metal y X es el calcógeno). Tras la intercalación, las interacciones interlaminares tipo van der Waals se debilitan, facilitando la exfoliación del material (Figura 11). Generalmente, la intercalación se lleva a cabo empleando compuestos de organolitio, siendo el *n*-butil-litio y el *tert*-butil-litio los más utilizados. Los materiales intercalados se pueden exfoliar fácilmente en disolventes específicos, especialmente en agua, para dar lugar a láminas monocapa o de unas pocas monocapas de espesor. Ello es debido a que los cationes intercalados reaccionan fácilmente con el agua para generar el hidróxido correspondiente (por ejemplo, LiOH) e hidrógeno, lo que favorece la deslaminación del sólido *bulk*. Sin embargo, el proceso requiere largos tiempos de intercalación, típicamente de entre uno y varios días [11,78].

La intercalación del ion alcalino en TMDs como MoS_2 y $MoSe_2$ lleva asociada la transferencia de electrones a los orbitales *d* del metal de transición. Si el número de electrones transferidos es lo suficientemente elevado, se inducirá una transición de la fase 2H (semiconductora) a la fase 1T (metálica) o a fases distorsionadas de ésta última (1T´, 1T´´) en el MoS_2/$MoSe_2$ [79]. Las nanoláminas de fase 1T exfoliadas suelen estar cargadas negativamente debido a la densidad electrónica adicional que poseen. Ello facilita su estabilidad coloidal en medio acuoso en base a las fuertes repulsiones electrostáticas que se establecen entre las láminas, aunque la progresiva pérdida de estos electrones adicionales por reacciones de hidrólisis con el agua conduce a su agregación y precipitación en cuestión de semanas. Cabe mencionar que la fase 1T posee carácter metaestable y, por ello, las nanoláminas tienden a retornar espontáneamente a la fase 2H, termodinámicamente estable. No obstante, es posible incrementar la estabilidad de las las primeras mediante estrategias de funcionalización superficial [80,81]. Los TMDs 2D preparados por intercalación química pueden ser empleados como electrodos para supercondensadores [82], membranas para purificación de agua [83] o catalizadores para la reducción de compuestos orgánicos [84].

Figura 11. Esquema del mecanismo de la exfoliación asistida por intercalación química de Li^+. Adaptado de [85] y [86].

d) Exfoliación por intercalación electroquímica

La intercalación electroquímica o exfoliación electroquímica (EE) se basa en la intercalación de una especie química cargada en los espacios interlaminares de un material laminar *bulk* por efecto de la aplicación de un potencial eléctrico (Figura 12) [87]. Constituye una de las técnicas más prometedoras de exfoliación en medio líquido para la obtención de materiales 2D, ya que no requiere de condiciones experimentales agresivas ni de equipos especializados, es potencialmente escalable, emplea tiempos de exfoliación moderadamente cortos y permite un control de las propiedades finales del material en base a las condiciones electroquímicas, incluyendo la obtención de láminas de buena calidad estructural con rendimientos aceptables [88]. La exfoliación electroquímica ha sido investigada durante más de una década para la producción de grafeno, y desde años más recientes se ha generalizado para la obtención de otros materiales 2D laminares, entre ellos los TMDs [89].

En la exfoliación electroquímica, un electrodo de trabajo (*working electrode*, WE) del material laminar *bulk* y un electrodo inerte que actúa como contraelectrodo (*counter electrode*, CE) se sumergen en un electrolito líquido, que puede ser una disolución (acuosa u orgánica) de una sal adecuada o un líquido iónico. La aplicación de un potencial eléctrico al WE provoca su polarización y la consiguiente migración de especies iónicas solvatadas de carga opuesta hasta su superficie. La posterior intercalación de estas especies en los espacios interlaminares del WE conduce a su expansión, lo que debilita las interacciones de van der Waals que mantienen al sólido *bulk* cohesionado, facilitando su exfoliación a nanoláminas. Generalmente, la existencia de reacciones electrolíticas adicionales en los espacios interlaminares (p.e. generación de H_2 por hidrólisis del agua o descomposición del electrolito) contribuye de manera muy importante al proceso de exfoliación [89].

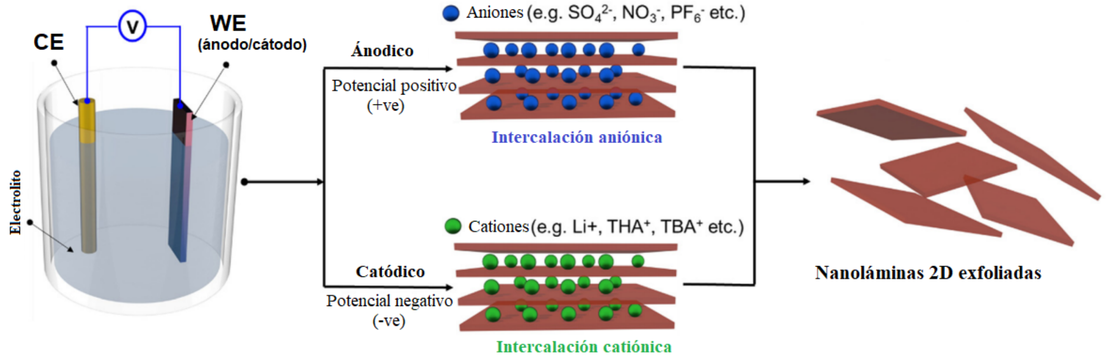

Figura 12. Montaje experimental típico de una celda electrolítica en un sistema de dos electrodos para exfoliación electroquímica y proceso general de exfoliación anódica y catódica. Adaptado de [89].

Dependiendo del signo del potencial aplicado al WE respecto del CE, la exfoliación electroquímica se clasifica en anódica (potencial positivo) y catódica (potencial negativo). En la **exfoliación anódica**, que generalmente emplea agua como disolvente, se aplica un potencial positivo (típicamente entre 5 y 30 V) al WE respecto del CE para inducir la intercalación de especies aniónicas [88]. El anión sulfato (SO_4^{2-}) ha demostrado ser particularmente eficiente para la exfoliación anódica de grafito y también de TMDs como MoS_2, siendo por tanto común el uso de electrolitos basados en ácido sulfúrico [90] y sales de sulfato (Na_2SO_4, $(NH_4)_2SO_4$, etc.) [91], aunque también se han usado sulfonatos orgánicos [92], ácido fosfórico [93] o incluso líquidos iónicos [94]. Sin embargo, la aplicación de potenciales tan elevados provoca la oxidación del agua y la generación de radicales (p. ej., el radical hidroxilo, ·OH) altamente reactivos. Estos radicales tienden a oxidar el plano basal y los bordes de grano del material laminar, donde inducen una apertura del espacio interlaminar que favorece la intercalación progresiva de más aniones y moléculas de agua. Además de oxidar al propio material laminar, la oxidación progresiva de los aniones y los radicales libres en el espacio interlaminar genera especies gaseosas (O_2, CO, CO_2, etc.) que contribuyen a una mayor expansión. Las nanoláminas obtenidas por exfoliación anódica suelen tener espesores muy pequeños (1-5 monocapas), así como un alto contenido en grupos funcionales de oxígeno (~10-20 at.%) en el caso del grafeno y en productos de oxidación (p. ej., MoO_x) en el caso de los TMDs, lo que conlleva la presencia de defectos estructurales en la red cristalina [88]. Aunque mucho menos habitual, también se ha estudiado la exfoliación anódica en medio orgánico usando electrolitos polifluorados [95].

En la **exfoliación catódica** se aplica un potencial negativo (típicamente entre -2 y -10 V) al WE respecto del CE para provocar la intercalación de especies catiónicas. Generalmente se considera que la inserción del catión puede ir acompañada por la co-intercalación de moléculas de disolvente, es decir, se produce la intercalación del catión (parcialmente) solvatado, lo que facilita la exfoliación del material laminar [88]. Este tipo de exfoliación electroquímica se realiza habitualmente en medio orgánico, usando, por ejemplo, carbonato de propileno (*propylene carbonate*, PC), acetonitrilo (*acetonitrile*, ACN) o dimetilsulfóxido (*dimethyl sulfoxide*, DMSO) como disolventes. Respecto a las sales, las de litio han sido muy utilizadas [96,97], aunque los líquidos iónicos [98] y, especialmente, las sales cuaternarias de amonio [22] también han dado buenos resultados (el mayor tamaño del catión de amonio previene una excesiva inyección de electrones en las nanoláminas que derive en una transición de fase 2H a 1T). Asimismo, la exfoliación catódica puede realizarse en fase acuosa usando KCl como electrolito en el caso del MoS_2 [54] o sales cuaternarias de amonio en el caso de algunos grafitos [99]. Aunque las nanoláminas obtenidas mediante exfoliación catódica presentan generalmente un grosor mayor (5-15 monocapas) que las obtenidas mediante exfoliación anódica, su calidad estructural suele ser superior debido a la ausencia de procesos oxidativos [88].

Es destacable que, generalmente, tanto la exfoliación anódica como la catódica no conducen a la obtención directa de nanoláminas aisladas. En su lugar, se obtienen materiales expandidos que habrán de ser sometidos a un tratamiento posterior, típicamente en fase líquida por aplicación de ultrasonidos o fuerzas de cizalladura, para la extracción de las nanoláminas [88].

Propiedades de las dispersiones coloidales de materiales 2D

Una dispersión coloidal o coloide es una mezcla heterogénea de dos fases, en la que una fase está generalmente formada por partículas de tamaño comprendido entre ~1 nm y 1000 μm (fase dispersa), que se encuentran suspendidas en una fase continua mayoritaria (fase dispersante). Si la fase dispersante es un disolvente, sus moléculas forman una esfera de solvatación alrededor de las partículas coloidales para formar una suspensión, pero no las disuelven en términos termodinámicos debido al gran tamaño de estas. Es decir, una dispersión es, por definición, un sistema heterogéneo metaestable y no un sistema termodinámicamente estable (disolución homogénea). Tanto la fase dispersa como la dispersante pueden ser gases, líquidos o sólidos, o una combinación de diferentes fases [100].

En base a lo mencionado en secciones anteriores, muchos métodos descendentes de obtención de materiales 2D dan lugar a dispersiones coloidales en fase líquida de los mismos, generalmente con morfología de nanoláminas [42,84,95,101,102]. La presencia, en estas dispersiones coloidales, de poblaciones de nanoláminas de diferentes tamaños laterales y, por tanto, con diferentes grados de estabilidad coloidal permite su selección por tamaños en base a estrategias como la centrifugación en cascada [103,104]. Además, el relativo gran tamaño de las partículas coloidales causa la aparición del denominado efecto Tyndall, fenómeno óptico de dispersión de la luz provocado por las partículas en suspensión, que no se observa en disoluciones homogéneas (Figura 13).

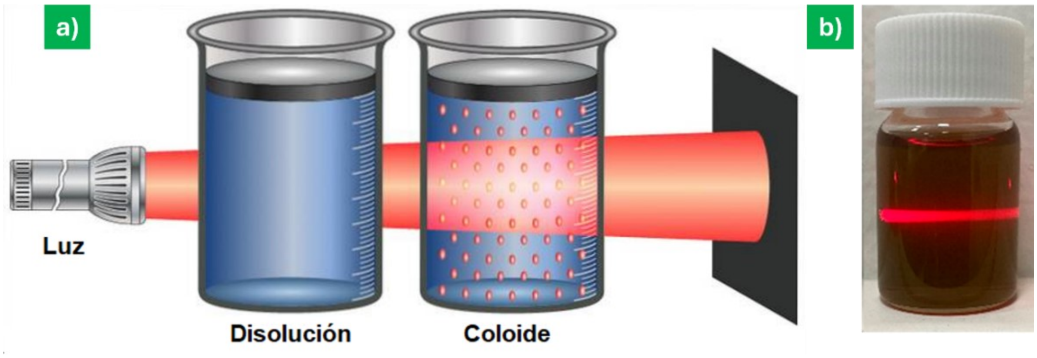

Figura 13. **(a)** Esquema del efecto Tyndall. **(b)** Efecto Tyndall sobre una dispersión de nanoláminas de MoS_2 en agua.

La estabilidad coloidal de partículas sólidas dispersas en fase líquida, incluidas las nanoláminas de materiales 2D, depende de varios factores [100,103]:

- Movimiento browniano: movimiento aleatorio de las partículas provocado por el hecho de que éstas se encuentran en agitación térmica constante. Es un factor esencial para la estabilidad coloidal de las partículas de menor tamaño.

- Tendencia a la agregación: el área superficial expuesta de las partículas coloidales favorece la interacción entre las mismas cuando unas se acercan a otras. En muchos casos, estas interacciones son atractivas de mayor o menor intensidad; por ejemplo, fuerzas de van der Waals (menos intensas) o puentes de hidrógeno (más intensas), lo que provoca la aglomeración de las partículas y su consiguiente sedimentación. Aunque el movimiento browniano contribuye en muchos casos a estabilizar las partículas coloidales, también promueve su interacción al dar lugar a una cierta probabilidad de colisión entre ellas. Por tanto, en determinados casos el movimiento browniano puede favorecer procesos de agregación. Así, las partículas de mayor tamaño y masa tienen una mayor tendencia a la agregación, en muchos casos irreversible.

- Carga eléctrica superficial: las partículas coloidales con carga superficial del mismo signo establecen interacciones electrostáticas repulsivas entre ellas, de mayor magnitud cuanto mayor sea la carga eléctrica que portan, lo que previene su aglomeración e incrementa su estabilidad coloidal (Figura 14a). El potencial Zeta (o electrocinético) es una propiedad de las partículas coloidales en suspensión, y denota la diferencia de potencial eléctrico entre la partícula coloidal solvatada y el medio de dispersión (Figura 14b). El potencial Zeta está directamente relacionado con la estabilidad cinética de las partículas en suspensión y depende del pH del medio dispersante.

- Disolvente utilizado y empleo de surfactantes: las partículas un mismo tipo muestran desigual estabilidad coloidal en diferentes disolventes debido a las interacciones específicas que establecen con sus moléculas. Además, la presencia en el disolvente de moléculas con actividad interfacial, por ejemplo, moléculas anfifílicas en medio acuoso (entre las que se incluyen los surfactantes), puede dotar a las partículas de carga eléctrica superficial o de barreras estéricas, lo que contribuye de manera esencial a prevenir su agregación.

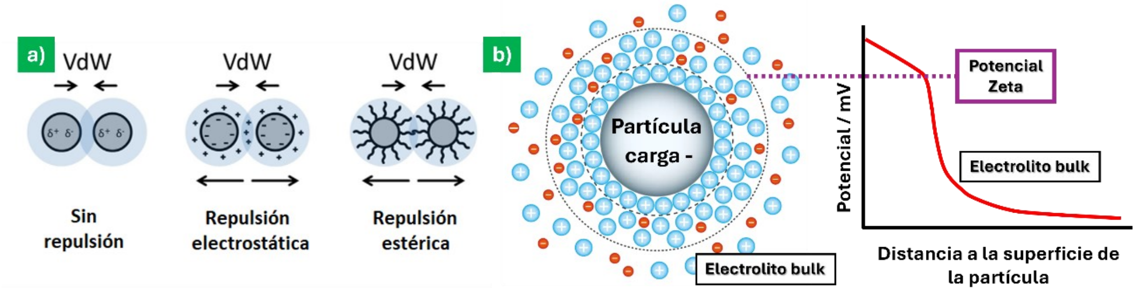

Figura 14. **(a)** Esquema de algunos de los tipos de interacción entre partículas coloidales en suspensión. Adaptado de [103]. **(b)** Esquema ilustrativo de la definición del potencial Zeta en una partícula coloidal cargada. Adaptado de [105].

1.3 Métodos de modificación de materiales 2D

Las propiedades de los materiales 2D dependen de una serie de parámetros (morfología, fase, número de capas, composición química, funcionalización superficial, etc.) que pueden controlarse experimentalmente. El desarrollo de metodologías para la modificación de las propiedades de los materiales 2D ha permitido incrementar su versatilidad y mejorar sus prestaciones en distintos campos de aplicación.

a) Ingeniería de fase

La ingeniería o modulación de fase se aplica a compuestos que presentan polimorfismo (como los TMDs). En el caso de los TMDs 2D, la principal vía para la obtención selectiva de fases cristalinas consiste en la modulación de las condiciones de preparación del material 2D. Por ejemplo, mediante el control de los parámetros de la síntesis solvotérmica (p. ej., la temperatura), se pueden obtener nanoláminas de MoS_2 que se encuentran exclusivamente en la fase 2H o que posean una mezcla de fases 1T y 2H, con utilidad en hidrodesulfurización [106] o almacenamiento de energía [107]. También se han obtenido, mediante exfoliación electroquímica, nanoláminas de WS_2 de fase 1T directamente a partir de la exfoliación electroquímica de WS_2 *bulk* de fase 2H, que se han estudiado en procesos catalíticos [108], así como nanoláminas de MoS_2 con mezcla de fases 1T y 2H a partir de un tratamiento térmico post-síntesis en atmósfera reductora del material *bulk* en fase 2H [109].

b) Control morfológico

La morfología juega un papel importante a la hora de determinar las propiedades y aplicaciones de los materiales nanoestructurados en general y de los materiales 2D en particular, pudiéndose controlar por medio de las condiciones de síntesis (Figura 15) [11]. Por ejemplo, en base a parámetros como tipo y proporción de precursores y disolventes, tiempo y temperatura de reacción, la vía solvotérmica permite la obtención de morfologías de MoS_2 tan variadas como puntos cuánticos [110], nanoláminas [111], nanoesferas [112], nanoflores [106] o nanotubos [113]. Algunos materiales 2D pueden experimentar cambios morfológicos por interacción con estímulos externos, como el caso del $NbSe_2$, cuya morfología puede pasar de nanolámina extendida a nanolámina enrollada (nanorrollo) dependiendo del disolvente en el que se dispersa [114]; o el caso de las nanoláminas de W_xMoS_2, cuya morfología varía con el pH del medio dispersante [115].

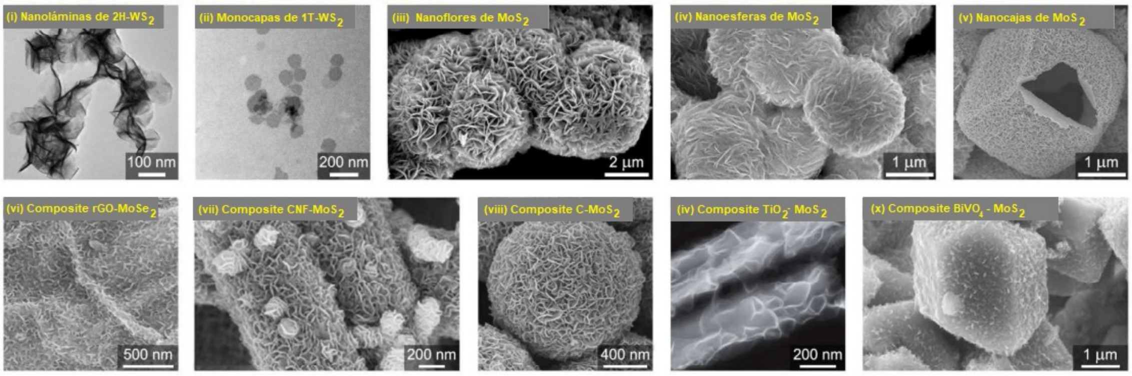

Figura 15. Imágenes de nanoestructuras de TMDs con diferentes morfologías, obtenidas mediante microscopía electrónica. Adaptado de [11].

c) Funcionalización superficial covalente y no covalente

La funcionalización covalente de materiales 2D permite anclar especies moleculares en su superficie mediante la formación de enlaces covalentes (quimisorción), lo que en muchos casos da lugar a una modificación de las propiedades del material. Ejemplos de funcionalización covalente los constituyen la síntesis de nanoláminas de MoS_2, $MoSe_2$, WS_2 y WSe_2 derivatizadas con ácido tiobarbitúrico (interacciones entre el átomo de Mo de las nanoláminas y el átomo de S de la tioamina) [44]; las nanoláminas soportadas de MoS_2 dopadas con Ni para la catálisis de la HER [116]; o la funcionalización de MoS_2 mediante anclaje covalente de maleimidas, por interacción entre el átomo de S nucleofílico y la región aromática electrófila de la maleimida [117].

La funcionalización no covalente hace referencia a la adsorción de especies moleculares sobre la superficie de nanoláminas 2D mediante interacciones débiles (fisisorción), tales como fuerzas dispersivas o puentes de hidrógeno, y por tanto no implica la formación de enlaces covalentes. Por ejemplo, la fisisorción de surfactantes y otras especies (macro)moleculares anfifílicas sobre las láminas 2D es ampliamente utilizada para mejorar su estabilidad coloidal en medio acuoso [118], para favorecer su exfoliación [119] o para incrementar su biocompatibilidad [120].

d) Generación de vacantes atómicas en materiales 2D

Se denomina *vacante atómica* al defecto estructural que se genera en un sólido cristalino tras la eliminación de un átomo o unos pocos átomos contiguos de su estructura. En el caso de los TMDs, las vacantes atómicas pueden involucrar únicamente al metal o al calcógeno, o bien involucrar a ambos [121]. Sin embargo, las vacantes más habituales son las de calcógenos, encontrándose en muestras tanto naturales como sintéticas a concentraciones no despreciables debido a su energía de formación relativamente baja. La presencia de vacantes de calcógeno en la superficie de TMDs 2D se asocia a una mayor reactividad química, lo que es especialmente interesante en (electro)catálisis [48,122] o en almacenamiento de energía [123]. Para generar vacantes atómicas en TMDs 2D se pueden emplear métodos químicos [53], electroquímicos [48] o asistidos por láser [124], entre otros.

Referencias

[1] International Organization for Standardization, ISO/TS 80004:2015 Nanotechnologies- Vocabulary.

[2] Mas-Ballesté, R., Gómez-Navarro, C., Gómez-Herrero, J., Zamora, F. 2D materials: To graphene and beyond. *Nanoscale*, 3 (2011), 20–30.

[3] Goh, P. S., Wong, K. C., Ismail, A. F. Nanocomposite membranes for liquid and gas separations from the perspective of nanostructure dimensions. *Membranes*, 10 (2020), 1–29.

[4] Novoselov, K. S., Geim, A. K., Morozov, S. V., Jiang, D., Dubonos, S. V., Grigorieva, I. V., Firsov, A. A. Electric Field Effect in Atomically Thin Carbon Films. *Science*, 306 (2004), 666-669.

[5] Grayfer, E. D., Kozlova, M. N., Fedorov, V. E. Colloidal 2D nanosheets of MoS_2 and other transition metal dichalcogenides through liquid-phase exfoliation. *Advances in Colloid and Interface Science*, 245 (2017), 40–61.

[6] Huang, Y., Guo, J., Kang, Y., Ai, Y., Li, C. M. Two dimensional atomically thin MoS_2 nanosheets and their sensing applications. *Nanoscale*, 7 (2015), 19358–19376.

[7] Anasori, B., Lukatskaya, M. R., Gogotsi, Y. 2D metal carbides and nitrides (MXenes) for energy storage. *Nature Reviews Materials*, 2 (2017), 16098.

[8] Uddin, M. M., Kabir, M. H., Ali, M. A., Hossain, M. M., Khandaker, M. U., Mandal, S., Arifutzzaman, A., Jana, D. Graphene-like emerging 2D materials: recent progress, challenges and future outlook. *RSC Advances*, 13 (2023), 33336–33375.

[9] Zhao, W., Pan, J., Fang, Y., Che, X., Wang, D., Bu, K., Huang, F. Metastable MoS_2: Crystal Structure, Electronic Band Structure, Synthetic Approach and Intriguing Physical Properties. *Chemistry - A European Journal*, 24 (2018), 15942–15954.

[10] Wang, Q. H., Kalantar-Zadeh, K., Kis, A., Coleman, J. N., Strano, M. S. Electronics and optoelectronics of two-dimensional transition metal dichalcogenides. *Nature Nanotechnology*, 7 (2012), 699–712.

[11] Samadi, M., Sarikhani, N., Zirak, M., Zhang, H., Moshfegh, A. Z. Group 6 transition metal dichalcogenide nanomaterials: synthesis, applications and future perspectives. *Nanoscale Horizons*, 3 (2018), 90–204.

[12] Zhao, Y., Yan, Y., Lee, J. M. Recent progress on transition metal diselenides from formation and modification to applications. *Nanoscale*, 14 (2022), 1075–1095.

[13] Saha, D., Kruse, P. Conductive Forms of MoS_2 and Their Applications in Energy Storage and Conversion. *Journal of the Electrochemical Society,* 167 (2020), 126517.

[14] Banu S, L., Veerapandy, V., Fjellvåg, H., Vajeeston, P. First-Principles Insights into the Relative Stability, Physical Properties, and Chemical Properties of $MoSe_2$. *ACS Omega*, 8 (2023), 13799–13812.

[15] Li, Y., Wang, M., Sun, J. Molecular Engineering Strategies toward Molybdenum Diselenide Design for Energy Storage and Conversion. *Advanced Energy Materials*, 12 (2022), 2202600.

[16] Park, H., Baek, S., Sen, A., Jung, B., Shim, J., Park, Y. C., Lee, L. P., Kim, Y. J., Kim, S. Ultrasensitive and Selective Field-Effect Transistor-Based Biosensor Created by Rings of MoS_2 Nanopores. *ACS Nano*, 16 (2022), 1826–1835.

[17] Sharma, R., Dawar, A., Ojha, S., Laishram, R., Sathe, V. G., Srivastava, R., Sinha, O. P. A Thrifty Liquid-Phase Exfoliation (LPE) of $MoSe_2$ and WSe_2 Nanosheets as Channel Materials for FET Application. *Journal of Electronic Materials*, 52 (2023), 2819–2830.

[18] Jang, J., Kim, J. J. S., Kim, H. J., Kang, M. S., Kim, T. S., Won, J., Lee, J., Cheon, J., Kang, K., Im, W. I., Pak, J. Mechanoluminescent, Air-Dielectric MoS_2 Transistors as Active-Matrix Pressure Sensors for Wide Detection Ranges from Footsteps to Cellular Motions. *Nano Letters*, 20 (2020), 66–74.

[19] Alsalme, A., Alsaeedi, H. Fabrication of Selective and Sensitive Hydrazine Sensor Using Sol-Gel Synthesized $MoSe_2$ as Efficient Electrode Modifier. *Crystals*, 13 (2023), 161.

[20] Liu, K., Zhang, J., Jiang, J., Xu, T., Wang, S., Chang, P., Zhang, Z., Ma, J., Liu, T. $MoSe_2$-Au Based Sensitivity Enhanced Optical Fiber Surface Plasmon Resonance Biosensor for Detection of Goat-Anti-Rabbit IgG. *IEEE Access*, 8 (2020), 660–668.

[21] Kang, P., Wang, M. C., Nam, S. Bioelectronics with two-dimensional materials. *Microelectronic Engineering*, 161 (2016), 18–35.

[22] Lin, Z., Liu, Y., Halim, U., Ding, M., Liu, Y., Wang, Y., Jia, C., Chen, P., Duan, X., Wang, C., Song, F., Li, M., Wan, C., Huang, Y., Duan, X. Solution-processable 2D semiconductors for high-performance large-area electronics. *Nature*, 562 (2018), 254–258.

[23] Guo, Y., Tang, J., Wang, Z., Kang, Y. M., Bando, Y., Yamauchi, Y. Elaborately assembled core-shell structured metal sulfides as a bifunctional catalyst for highly efficient electrochemical overall water splitting. *Nano Energy*, 47 (2018), 494–502.

[24] Zazpe, R., Krumpolec, R., Sopha, H., Rodriguez-Pereira, J., Charvot, J., Hromádko, L., Kolíbalová, E., Michalička, J., Pavliňák, D., Motola, M., Přikryl, J., Krbal, M., Bureš, F., Macak, J. M. Atomic Layer Deposition of $MoSe_2$ Nanosheets on TiO_2 Nanotube Arrays for Photocatalytic Dye Degradation and Electrocatalytic Hydrogen Evolution. *ACS Applied Nano Materials*, 3 (2020), 12034–12045.

[25] Wazir, M. B., Daud, M., Safeer, S., Almarzooqi, F., Qurashi, A. Review on 2D Molybdenum Diselenide ($MoSe_2$) and Its Hybrids for Green Hydrogen (H_2) Generation Applications. *ACS Omega*, 7 (2022), 16856-16865.

[26] Donnet, C., Martin, J. M., Le Mogne, Th., Belin, M. Super-low friction of MoS_2 coatings in various environments. *Tribology International*, 29 (1996), 123–128.

[27] Mukhtar, S. H., Gulzar, A., Saleem, S., Wani, M. F., Sehgal, R., Yakovenko, A. A., Goryacheva, I. G., Sharma, M. D. Advances in development of solid lubricating MoS_2 coatings for space applications: A review of modeling and experimental approaches. *Tribology International*, 192 (2024), 109194.

[28] Zhan, W., Zou, J., Mao, X., Tang, L., Wei, H. Structure and tribological properties of $MoSe_2$ films prepared by two-step process. *Transactions of Nonferrous Metals Society of China*, 33 (2023), 2483–2496.

[29] Chen, Z., Guo, L., Yan, H., Yao, H., Liu, Q. Amino functionalization of graphene/graphene-like $MoSe_2$ hybrids as lubricant additives for bismaleimide composites: Preparation, mechanical and tribological properties. *Composites Part B: Engineering*, 161 (2019), 263–271.

[30] Castellanos-Gomez, A., Poot, M., Steele, G. A., van der Zant, H. S. J., Agraït, N., Rubio-Bollinger, G. Elastic Properties of Freely Suspended MoS_2 Nanosheets. *Advanced Materials*, 24 (2012), 772–775.

[31] Gómez-Navarro, C., Burghard, M., Kern, K. Elastic Properties of Chemically Derived Single Graphene Sheets. *Nano Letters*, 8 (2008), 2045–2049.

[32] Haq, Z. U., Zia-ul-Haq, M., Jiang, Y., Wang, J., Zhang, Y. Preparation and mechanical properties of natural rubber composites reinforced by modified molybdenum disulfide. *Journal of Applied Polymer Science*, 140 (2023).

[33] Piejko, A., Tamulewicz-Szwajkowska, M., Król, K., Ciesiolkiewicz, K., Kudrawiec, R., Serafińczuk, J. Mechanical and Kelvin Probe Force Microscopy Investigations of Ultrathin Membranes Based on MoS_2 and $MoSe_2$. *Physica status solidi (b)*, 261 (2024), 2300352.

[34] Peng, B., Zhang, H., Shao, H., Xu, Y., Zhang, X., Zhu, H. Thermal conductivity of monolayer MoS_2, $MoSe_2$, and WS_2: Interplay of mass effect, interatomic bonding and anharmonicity. *RSC Advances*, 6 (2016), 5767–5773.

[35] Kim, J.-Y., Choi, S.-M., Seo, W.-S., Cho, W.-S. Thermal and Electronic Properties of Exfoliated Metal Chalcogenides. *Bulletin of the Korean Chemical Society*, 31 (2010), 3225–3227.

[36] Yan, R., Simpson, J. R., Bertolazzi, S., Brivio, J., Watson, M., Wu, X., Kis, A., Luo, T., Walker, A. R. H., Xing, H. G. Thermal Conductivity of Monolayer Molybdenum Disulfide Obtained from Temperature-Dependent Raman Spectroscopy. *ACS Nano,* 8 (2014), 986–993.

[37] Goni, M., Yang, J., Schmidt, A. J. Enhanced thermal transport across monolayer MoS_2. *Nano Research*, 11 (2018), 2173–2180.

[38] Zou, L., Sang, D., Ge, S., Yao, Y., Wang, G., Wang, X., Fan, J., Wang, Q. High-temperature optoelectronic transport behavior of n-MoS_2 nanosheets/p-diamond heterojunction. *Journal of Alloys and Compounds*, 972 (2024), 172819.

[39] Riaz, S., Rhee, K. Y., Park, S. J. Enhanced thermal and mechanical properties of epoxy composites at ultra-low loading of functionalized MoS_2 nanosheets. *Steel and Composite Structures,* 41 (2021), 609–624.

[40] Zobeiri, H., Wang, R., Wang, T., Lin, H., Deng, C., Wang, X. Frequency-domain energy transport state-resolved Raman for measuring the thermal conductivity of suspended nm-thick $MoSe_2$. *International Journal of Heat and Mass Transfer*, 133 (2019), 1074–1085.

[41] Xiong, H., Nie, X., Zhao, L., Deng, S., Song, X. Twist-Angle-Dependent Phonon Transport of van der Waals $MoSe_2$ Thermoelectric Materials for the Recycling of Waste Heat. *ACS Applied Nano Materials*, 6 (2023), 15685–15696.

[42] Grayfer, E. D., Kozlova, M. N., Fedorov, V. E. Colloidal 2D nanosheets of MoS_2 and other transition metal dichalcogenides through liquid-phase exfoliation. *Advances in Colloid and Interface Science*, 245 (2017), 40–61.

[43] Varrla, E., Backes, C., Paton, K. R., Harvey, A., Gholamvand, Z., McCauley, J., Coleman, J. N. Large-Scale Production of Size-Controlled MoS_2 Nanosheets by Shear Exfoliation. *Chemistry of Materials*, 27 (2015), 1129–1139.

[44] Presolski, S., Wang, L., Loo, A. H., Ambrosi, A., Lazar, P., Ranc, V., Otyepka, M., Zboril, R., Tomanec, O., Ugolotti, J., Sofer, Z., Pumera, M. Functional Nanosheet Synthons by Covalent Modification of Transition-Metal Dichalcogenides. *Chemistry of Materials*, 29 (2017), 2066–2073.

[45] Mitchell, P. C. H., Outteridge, T., Kloska, K., McMahon, S., Epshteyn, Y., Sebenik, R. F., Burkin, A. R., Dorfler, R. R., Laferty, J. M., Leichfried, G., Meyer-Grünow, H., Vukasovich, M. S. Molybdenum and Molybdenum Compounds. *Ullmann's Encyclopedia of Industrial Chemistry*, 1–63 (Wiley, 2020).

[46] Afanasiev, P., Lorentz, C. Oxidation of Nanodispersed MoS_2 in Ambient Air: The Products and the Mechanistic Steps. *Journal of Physical Chemistry C*, 123 (2019), 7486–7494.

[47] Mirabelli, G., McGeough, C., Schmidt, M., McCarty, E. K., Monaghan, S., Povey, I. M., McCarthy, M., Gity, F., Nagle, R., Hughes, G., Cafolla, A., Hurley, P. K., Duffy, R. Air sensitivity of MoS_2, $MoSe_2$, $MoTe_2$, HfS_2, and $HfSe_2$. *Journal of Applied Physics*, 120 (2016), 125102.

[48] Tsai, C., Li, H., Park, S., Park, J., Han, H. S., Nørskov, J. K., Zheng, X. Electrochemical generation of sulfur vacancies in the basal plane of MoS_2 for hydrogen evolution. *Nature Communications,* 8 (2017), 15113.

[49] Chang, Y. S., Chen, C. Y., Ho, C. J., Cheng, C. M., Chen, H. R., Fu, T. Y., Huang, Y. T., Ke, S. W., Du, H. Y., Lee, K. Y., Chao, L. C., Chen, L. C., Chen, K. H., Chu, Y. W., Chen, R. S. Surface electron accumulation and enhanced hydrogen evolution reaction in $MoSe_2$ basal planes. *Nano Energy*, 84 (2021), 105922.

[50] Salazar, N., Rangarajan, S., Rodríguez-Fernández, J., Mavrikakis, M., Lauritsen, J. V. Site-dependent reactivity of MoS_2 nanoparticles in hydrodesulfurization of thiophene. *Nature Communications,* 11 (2020), 4369.

[51] Hu, L., He, X., Yao, J., Li, X., Chen, J., Li, J., Fan, X., Xie, L., Cai, Z., Sun, S., Zheng, D., Ying, B., Wang, Y., Luo, Y., Liu, Q., Farouk, A., Hamdy, M. S., Alfaifi, S., Liao, Y., Kong, Q., Sun, X. Boosting electrocatalytic nitrite reduction to ammonia in neutral media by $MoSe_2$ nanosheet with Se vacancies. *Materials Today Physics*, 36 (2023), 101170.

[52] Fei, H., Guo, T., Xin, Y., Wang, L., Liu, R., Wang, D., Liu, F., Wu, Z. Sulfur vacancy engineering of MoS_2 via phosphorus incorporation for improved electrocatalytic N_2 reduction to NH_3. *Applied Catalysis B: Environmental*, 300 (2022), 120733.

[53] García-Dalí, S., Paredes, J. I., Caridad, B., Villar-Rodil, S., Díaz-González, M., Fernández-Sánchez, C., Adawy, A., Martínez-Alonso, A., Tascón, J. M. D. Activation of two-dimensional MoS_2 nanosheets by wet-chemical sulfur vacancy engineering for the

catalytic reduction of nitroarenes and organic dyes. *Applied Materials Today*, 20 (2020), 100678.

[54] García-Dalí, S., Paredes, J. I., Munuera, J. M., Villar-Rodil, S., Adawy, A., Martínez-Alonso, A., Tascón, J. M. D. Aqueous Cathodic Exfoliation Strategy toward Solution-Processable and Phase-Preserved MoS_2 Nanosheets for Energy Storage and Catalytic Applications. *ACS Applied Materials & Interfaces*, 11 (2019), 36991–37003.

[55] Hasanian, M., Mortazavi, B., Ostadhossein, A., Rabczuk, T., van Duin, A. C. T. Hydrogenation and defect formation control the strength and ductility of MoS2 nanosheets: Reactive molecular dynamics simulation. *Extreme Mechanics Letters*, 22 (2018), 157-165.

[56] Lin, Y. C. Torsi, R., Younas, R., Hinkle, C. L., Rigosi, F. A., Hill, M. H., Zhang, K., Huang, S., Shuck, C. E., Chen, C., Lin, Y. -H., Maldonado-Lopez, D., Mendoza-Cortes, J. L., Ferrier, J., Kar, S., Nayir, N., Rajabpour, S., van Duin, A. C. T., Liu, X., Jariwala, D., Jiang, J., Shi, J., Mortelmans, W., Jaramillo, R., Lopes, J. M. J., Engel-Herbert, R., Trofe, A., Ignatova, T., Lee, S. H., Mao, Z., Damian, L., Wang, Y., Steves, M. A., Knappenberger Jr, K. L., Wang, Z., Law, S., Bepete, G., Zhou, D., Lin, J. -X., Scheurer, M. S., Li, J., Wang, P., Yu, G., Wu, S., Akinwande, D., Redwing, J. M., Terrones, M., Ronbinson, J. A. Recent Advances in 2D Material Theory, Synthesis, Properties, and Applications. *ACS Nano*, 17 (2023), 9694–9747.

[57] Rawat, R. S. Dense Plasma Focus - From Alternative Fusion Source to Versatile High Energy Density Plasma Source for Plasma Nanotechnology. *Journal of Physics: Conference Series*, 591 (2015), 012021.

[58] Ruiz, K. H., Wang, Z., Ciprian, M., Zhu, M., Tu, R., Zhang, L., Luo, W., Fan, Y. Chemical Vapor Deposition Mediated Phase Engineering for 2D Transition Metal Dichalcogenides: Strategies and Applications. *Small Science*, 2 (2022), 2100047.

[59] Tajik, S., Dourandish, Z., Nejad, F. G., Beitollahi, H., Jahani, P. M., di Bartolomeo, A. Transition metal dichalcogenides: Synthesis and use in the development of electrochemical sensors and biosensors. *Biosensors and Bioelectronics*, 216 (2022), 114674.

[60] Eng, A. Y. S., Cheong, J. L., Lee, S. S. Controlled synthesis of transition metal disulfides (MoS_2 and WS_2) on carbon fibers: Effects of phase and morphology toward lithium–sulfur battery performance. *Applied Materials Today*, 16 (2019), 529–537.

[61] Giubileo, F., Grillo, A., Passacantando, M., Urban, F., Iemmo, L., Luongo, G., Pelella, A., Loveridge, M., Lozzi, L., di Bartolomeo, A. Field Emission Characterization of MoS_2 Nanoflowers. *Nanomaterials*, 9 (2019), 717.

[62] Du, W., Jiang, X., Zhu, L. From graphite to graphene: direct liquid-phase exfoliation of graphite to produce single- and few-layered pristine graphene. *Journal of Materials Chemistry A*, 1 (2013), 10592-10606.

[63] Novoselov, K. S., Jiang, D., Schedin, F., Geim, A. K. Two-dimensional atomic crystals. *Proceedings of the National Academy of Sciences*, 102 (2005), 10451–10453.

[64] Tan, C., Cao, X., Wu, X. -J., He, Q., Yang, J., Zhang, X., Chen, J., Zhao, W., Han, S., Nam, G. -H., Sindoro, M., Zhang, H. Recent Advances in Ultrathin Two-Dimensional Nanomaterials. *Chemical Reviews*, 117 (2017), 6225–6331.

[65] Samadi, M., Sarikhani, N., Zirak, M., Zhang, H., Zhang, H. -L., Moshfegh, A. Z. Group 6 transition metal dichalcogenide nanomaterials: synthesis, applications and future perspectives. *Nanoscale Horizons*, 3 (2018), 90–204.

[66] Coleman, J. N., Lotya, M., O'Neill, A., Bergin, S. D., King, P. J., Khan, U., Young, K., Gaucher, A., De, S., Smith, R. J., Shvets, I. V., Arora, S. K., Stanton, G., Kim, H. -Y., Lee, K., Kin, G. T., Duesberg, G. S., Hallam, T., Boland, J. J., Wang, J. J., Donegan, J. F., Grunlan, J. C., Moriarty, G., Shmeliov, A., Nicholls, R. J., Perkins, J. M., Grieveson, E. M., Theuwissen, K., McComb, D. W., Nellist, P. D., Nicolosi, V. Two-Dimensional Nanosheets Produced by Liquid Exfoliation of Layered Materials. *Science*, 331 (2011), 568-571.

[67] Paton, K. R., Varrla, E., Backes, C., Smith, R. J., Kahn, U., O'Neill, A., Boland, C., Lotya, M., Istrate, O. M., King, P., Higgins, T., Barwich, S., May, P., Puczkarski, P., Ahmed, I., Moebius, M., Petterson, H., Long, E., Coelho, J., O'Brien, S. E., McGuire, E. K., Sanchez, B. M., Duesberg, G. S., McEvoy, N., Pennycook, T. J., Downing, C., Crossley, A., Nicolosi, V., Coleman, J. N. Scalable production of large quantities of

defect-free few-layer graphene by shear exfoliation in liquids. *Nature Materials*, 13 (2014), 624–630.

[68] Tyurnina, A. V., Tzanakis, I., Morton, J., Mi, J., Porfyrakis, K., Maciejewska, B. M., Grobert, N., Eskin, D. G. Ultrasonic exfoliation of graphene in water: A key parameter study. *Carbon*, 168 (2020), 737–747.

[69] Hernandez, Y., Nicolosi, V., Lotya, M., Blighe, F. M., Sun, Z., De, S., McGovern, I. T., Holland, B., Byrne, M., Gun'Ko, Y. K., Boland, J. J., Niraj, P., Dueberg, G., Krishnamurthy, S., Goodhue, R., Hutchison, J., Scardaci, V., Ferrari, A. C., Coleman, J. N. High-yield production of graphene by liquid-phase exfoliation of graphite. *Nature Nanotechnology*, 3 (2008), 563–568.

[70] Zhou, K., Mao, N., Wang, H., Peng, Y., Zhang, H. A Mixed-Solvent Strategy for Efficient Exfoliation of Inorganic Graphene Analogues. *Angewandte Chemie International Edition*, 50 (2011), 10839–10842.

[71] Lotya, M., King, P. J., Khan, U., De, S., Coleman, J. N. High-Concentration, Surfactant-Stabilized Graphene Dispersions. *ACS Nano*, 4 (2010), 3155–3162.

[72] Bourlinos, A. B., Georgakilas, V., Zboril, R., Steriotis, T. A., Stubos, A. K., Trapalis, C. Aqueous-phase exfoliation of graphite in the presence of polyvinylpyrrolidone for the production of water-soluble graphenes. *Solid State Communications*, 149 (2009), 2172–2176.

[73] Caridad, B., Paredes, J. I., Pérez-Vidal, O., Villar-Rodil, S., Pagán, A., Cenis, J. L., Martínez-Alonso, A., Tascón, J. M. D. A biosupramolecular approach to graphene: Complementary nucleotide-nucleobase combinations as enhanced stabilizers towards aqueous-phase exfoliation and functional graphene-nucleotide hydrogels. *Carbon*, 129 (2018), 321–334.

[74] Huang, S., You, Z., Jiang, Y., Zhang, F., Liu, K., Liu, Y., Chen, X., Lv, Y. Fabrication of Ultrathin MoS_2 Nanosheets and Application on Adsorption of Organic Pollutants and Heavy Metals. *Processes*, 8 (2020), 504.

[75] Liu, J., Liu, H., Peng, W., Li, Y., Zhang, F., Fan, X. High-yield exfoliation of MoS_2 (WS_2) monolayers towards efficient photocatalytic hydrogen evolution. *Chemical Engineering Journal*, 431 (2022), 133286.

[76] Adilbekova, B., Lin, Y., Yengel, E., Faber, H., Harrison, G., Firdaus, Y., El-Labban, A., Anjum, D. H., Tung, V., Anthopoulos, T. D. Liquid phase exfoliation of MoS_2 and WS_2 in aqueous ammonia and their application in highly efficient organic solar cells. *Journal of Materials Chemistry C*, 8 (2020), 5259–5264.

[77] Bissett, M. A., Kinloch, I. A., Dryfe, R. A. W. Characterization of MoS_2–Graphene Composites for High-Performance Coin Cell Supercapacitors. *ACS Applied Materials & Interfaces*, 7 (2015), 17388–17398.

[78] Dines, M. B. Lithium intercalation via -Butyllithium of the layered transition metal dichalcogenides. *Materials Research Bulletin*, 10 (1975), 287–291.

[79] Voiry, D., Mohite, A., Chhowalla, M. Phase engineering of transition metal dichalcogenides. *Chemical Society Reviews*, 44 (2015), 2702–2712.

[80] Paredes, J. I., Munuera, J. M., Villar-Rodil, S., Guardia, L., Ayán-Varela, M., Pagán, A., Aznar-Cervantes, S. D., Cenis, J. L., Martínez-Alonso, A., Tascón, J. M. D. Impact of Covalent Functionalization on the Aqueous Processability, Catalytic Activity, and Biocompatibility of Chemically Exfoliated MoS_2 Nanosheets. *Applied Materials & Interfaces*, 5 (2016), 27974-27986.

[81] Chou, S. S., De, M., Kim, J., Byun, S., Dykstra, C., Yu, J., Huang, J., Dravid, V. P. Ligand Conjugation of Chemically Exfoliated MoS_2. *Journal of the American Chemical Society*, 135 (2013), 4584–4587.

[82] Acerce, M., Voiry, D., Chhowalla, M. Metallic 1T phase MoS_2 nanosheets as supercapacitor electrode materials. *Nature Nanotechnology*, 10 (2015), 313–318.

[83] Wang, Z., Tu, Q., Zheng, S., Urban, J. J., Li, S., Mi, B. Understanding the Aqueous Stability and Filtration Capability of MoS_2 Membranes. *Nano Letters*, 17 (2017), 7289–7298.

[84] Guardia, L., Paredes, J. I., Munuera, J. M., Villar-Rodil, S., Ayán-Varela, M., Martínez-Alonso, A., Tascón, J. M. D. Chemically Exfoliated MoS_2 Nanosheets as an

Efficient Catalyst for Reduction Reactions in the Aqueous Phase. *ACS Applied Materials & Interfaces*, 6 (2014), 21702–21710.

[85] Lee, J. H., Jang, W. S., Han, S. W., Baik, H. K. Efficient Hydrogen Evolution by Mechanically Strained MoS_2 Nanosheets. *Langmuir*, 30 (2014), 9866–9873.

[86] Haverkamp, R., Sorgenfrei, N. L. A. N., Griangrisostomi, E., Neppl, S., Künh, D., Föhlisch, A. Directional charge delocalization dynamics in semiconducting 2H-MoS_2 and metallic 1T-Li_xMoS_2. *Scientific Reports*, 11 (2021), 6893.

[87] Zeng, Z., Yin, Z., Huang, X., Li, Hai., He, Q., Lu, G., Boey, F., Zhang, H. Single-Layer Semiconducting Nanosheets: High-Yield Preparation and Device Fabrication. *Angewandte Chemie International Edition*, 50 (2011), 11093–11097.

[88] Ambrosi, A., Pumera, M. Exfoliation of layered materials using electrochemistry. *Chemical Society Reviews*, 47 (2018), 7213–7224.

[89] Zhao, M., Casiraghi, C., Parvez, K. Electrochemical exfoliation of 2D materials beyond graphene. *Chemical Society Reviews*, 53 (2024), 3036-3064.

[90] You, X., Liu, N., Lee, C. J., Pak, J. J. An electrochemical route to MoS_2 nanosheets for device applications. *Materials Letters*, 121 (2014), 31–35.

[91] Liu, N., Kim, P., Kim, J. H., Ye, J. H., Kim, S., Lee, C. J. Large-Area Atomically Thin MoS_2 Nanosheets Prepared Using Electrochemical Exfoliation. *ACS Nano*, 8 (2014), 6902–6910.

[92] Alanyalıoğlu, M., Segura, J. J., Oró-Solè, J., Casañ-Pastor, N. The synthesis of graphene sheets with controlled thickness and order using surfactant-assisted electrochemical processes. *Carbon*, 50 (2012), 142–152.

[93] Thirumal, V., Pandurangan, A., Jayavel, R., Venkatesh, K. S., Palani, N. S., Ragavan, R., Ilangovan, R. Single pot electrochemical synthesis of functionalized and phosphorus doped graphene nanosheets for supercapacitor applications. *Journal of Materials Science: Materials in Electronics*, 26 (2015), 6319–6328.

[94] Taheri Najafabadi, A., Gyenge, E. Synergistic production of graphene microsheets by simultaneous anodic and cathodic electro-exfoliation of graphitic electrodes in aprotic ionic liquids. *Carbon*, 84 (2015), 449–459.

[95] Zhang, Y., Hou, W., Chang, R., Yao, X., Xu, Y. Ultrafast alternating-current exfoliation toward large-scale synthesis of graphene and its application for flexible supercapacitors. *Journal of Colloids and Interface Science*, 654 (2024), 246–257.

[96] Zeng, Z., Yin, Z., Huang, X., Li, H., He, Q., Lu, G., Boey, F., Zhang, H. Single-Layer Semiconducting Nanosheets: High-Yield Preparation and Device Fabrication. *Angewandte Chemie International Edition*, 50 (2011), 11093–11097.

[97] Wang, J., Manga, K. K., Bao, Q., Loh, K. P. High-Yield Synthesis of Few-Layer Graphene Flakes through Electrochemical Expansion of Graphite in Propylene Carbonate Electrolyte. *Journal of the American Chemical Society*, 133 (2011), 8888–8891.

[98] Yang, Y., Lu, F., Zhou, Z., Song, W., Chen, Q., Li, X. Electrochemically cathodic exfoliation of graphene sheets in room temperature ionic liquids N-butyl, methylpyrrolidinium bis(trifluoromethylsulfonyl)imide and their electrochemical properties. *Electrochimica Acta*, 113 (2013), 9–16.

[99] García-Dalí, S., Paredes, J. I., Munuera, J. M., Villar-Rodil, S., Martínez-Alonso, A., Tascón, J. M. D. An aqueous cathodic delamination route towards high quality graphene flakes for oil sorption and electrochemical charge storage applications. *Chemical Engineering Journal*, 372 (2019), 1226–1239.

[100] Chang, R., College, W. *Chemistry*, (McGraw-Hill, 2002).

[101] Shi, H., Li, M., Nia, A. S., Wang, M., Park, S., Zhang, Z., Lohe, M, R., Yang, S., Feng, X. Ultrafast Electrochemical Synthesis of Defect-Free In_2Se_3 Flakes for Large-Area Optoelectronics. *Advanced Materials*, 32 (2020), 1907244.

[102] Li, J., Chen, C., Liu, S., Lu, J., Goh, W. P., Fang, H., Qiu, Z., Tian, B., Chen, Z., Yao, C., Liu, W., Yan, H., Yu, Y., Wang, D., Wang, Y., Lin, M., Su, C., Lu, J. Ultrafast Electrochemical Expansion of Black Phosphorus toward High-Yield Synthesis of Few-Layer Phosphorene. *Chemistry of Materials*, 30 (2018), 2742–2749.

[103] Matter, F., Luna, A. L., Niederberger, M. From colloidal dispersions to aerogels: How to master nanoparticle gelation. *Nano Today*, 30 (2020), 100827.

[104] Backes, C., Szydlowska, B. M., Harvey, A., Yuan, S., Vega-Mayoral, V., Davies, B. R., Zhao, P. -L., Hanlon, D., Santos, E. J. G., Katsnelson, M. I., Blau, W. J., Gadermaier,

C., Coleman, J. N. Production of Highly Monolayer Enriched Dispersions of Liquid-Exfoliated Nanosheets by Liquid Cascade Centrifugation. *ACS Nano*, 10 (2016), 1589-1601.

[105] Lowry, G. V., Hill, R, J., Harper, S., Rawle, A. F., Hendren, C. O., Klaessig, F., Nobbman, U., Sayre, P., Rumble, J. Guidance to improve the scientific value of zeta-potential measurements in nanoEHS. *Environmental Science: Nano*, 3 (2016), 953–965.

[106] Cao, H., Bai, Z., Li, Y., Xiao, Z., Zhang, X., Li, G. Solvothermal Synthesis of Defect-Rich Mixed 1T-2H MoS_2 nanoflowers for Enhanced Hydrodesulfurization. *ACS Sustainable Chemistry & Engineering*, 8 (2020), 7343–7352.

[107] Dai, J., Lv, Y., Zhang, J., Zhang, J., Zhang, D., Xie, H., Guo, C., Zhu, A., Xu, Y., Fan, M., Yuan, C., Dai, L. Effect of morphology and phase engineering of MoS_2 on electrochemical properties of carbon nanotube/polyaniline@MoS_2 composites. *Journal of Colloids and Interface Science*, 590 (2021), 591–600.

[108] Leong, S. X., Mayorga-Martínez, C. C., Chia, X., Luxa, J., Sofer, Z., Pumera, M. 2H → 1T Phase Change in Direct Synthesis of WS_2 Nanosheets via Solution-Based Electrochemical Exfoliation and Their Catalytic Properties. *ACS Applied Materials & Interfaces*, 9 (2017), 26350–26356.

[109] Li, W., Shen, Y., Xiao, X., An, C., Wei, G., Wang, Y., Wang, J., Wu, Y., An, C. Simple Te-Thermal Converting 2H to 1T@2H MoS_2 Homojunctions with Enhanced Supercapacitor Performance. *ACS Applied Energy Materials*, 2 (2019), 8337–8344.

[110] Ren, X., Pang, L., Zhang, Y., Ren, X., Fan, H., Liu, S. One-step hydrothermal synthesis of monolayer MoS_2 quantum dots for highly efficient electrocatalytic hydrogen evolution. *Journal of Materials Chemistry A*, 3 (2015), 10693–10697.

[111] Dunne, P. W., Munn, A. S., Starkey, C. L., Lester, E. H. The sequential continuous-flow hydrothermal synthesis of molybdenum disulphide. *Chemical Communications*, 51 (2015), 4048–4050.

[112] Javed, M. S., Dai, S., Wang, M., Guo, D., Chen, L., Wang, X., Hu, C., Xi, Y. High-performance solid state flexible supercapacitor based on molybdenum sulfide hierarchical nanospheres. *Journal of Power Sources*, 285 (2015), 63–69.

[113] Wang, P., Sun, H., Ji, Y., Li, W., Wang, X. Three-Dimensional Assembly of Single-Layered MoS_2. *Advanced Materials*, 26 (2014), 964–969.

[114] Carrasco, D. F., García-Dalí, S., Villar-Rodil, S., Munuera, J. M., Raymundo-Piñeiro, E., Paredes, J. I. $NbSe_2$ Nanosheets/Nanorolls Obtained via Fast and Direct Aqueous Electrochemical Exfoliation for High-Capacity Lithium Storage. *ACS Applied Energy Materials*, 6 (2023), 7180–7193.

[115] Jeffery, A. A., Min, J., Kim, Y., Chougule, S. S., Lee, S., Jeong, J. -R., Jung, N. pH-induced morphological transformation of W_xMoS_2 nanosheets for hydrogen evolution reaction through precursor solution aging. *Journal of Power Sources*, 526 (2022), 231154.

[116] Xue, Y., Bai, X., Xu, Y., Yan, Q., Zhu, M., Zhu, K., Ye, K., Yan, J., Cao, D., Wang, G. Vertically oriented Ni-doped MoS_2 nanosheets supported on hollow carbon microtubes for enhanced hydrogen evolution reaction and water splitting. *Composites Part B: Engineering*, 224 (2021), 109229.

[117] Quirós-Ovies, R., Sulleiro, M. V., Vera-Hidalgo, M., Prieto, J., Gómez, I. J., Sebastian, V., Santamía, J., Pérez, E. M. Controlled Covalent Functionalization of 2H-MoS_2 with Molecular or Polymeric Adlayers. *Chemistry - A European Journal*, 26 (2020), 6629–6634.

[118] Chhowalla, M., Shin, H. S., Eda, G., Li, L. -J., Loh, K. P., Zhang, H. The chemistry of two-dimensional layered transition metal dichalcogenide nanosheets. *Nature Chemistry*, 5 (2013), 263–275.

[119] Guardia, L., Paredes, J. I., Rozada, R., Villar-Rodil, S., Martínez-Alonso, A., Tascón, J. M. D. Production of aqueous dispersions of inorganic graphene analogues by exfoliation and stabilization with non-ionic surfactants. *RSC Advances*, 4 (2014), 14115–14127.

[120] Chen, L., Feng, W., Zhou, X., Qiu, K., Miao, Y., Zhang, Q., Qin, M., Li, L., Zhang, Y., He, C. Facile synthesis of novel albumin-functionalized flower-like MoS_2 nanoparticles for in vitro chemo-photothermal synergistic therapy. *RSC Advances*, 6 (2016), 13040–13049.

[121] Kim, J. W., Kim, S., Kim, T. Effect of Mo Vacancy on the Photoresponse of Bilayer MoS_2 Film. *Applied Science and Convergence Technology*, 31 (2022), 107–109.

[122] Sun, Y., Darling, A. J., Li, Y., Fujisawa, K., Holder, C. F., Liu, H., Janik, M. J., Terrones, M., Schaak, R. E. Defect-mediated selective hydrogenation of nitroarenes on nanostructured WS_2. *Chemical Science*, 10 (2019), 10310–10317.

[123] Budumuru, A. K., Rakesh, B., Sudakar, C. Enhanced high-rate capability of Li intercalation in planar and edge defect-rich MoS_2 nanosheets. *Nanoscale*, 11 (2019), 8882–8897.

[124] Azam, N.¸Boebinger, M. G., Jaiswal, S., Unocic, R. R., Fathi-Hafshejani, P., Mahjouri-Samani, M. Laser-Assisted Synthesis of Monolayer 2D $MoSe_2$ Crystals with Tunable Vacancy Concentrations: Implications for Gas and Biosensing. *ACS Applied Nano Materials*, 5 (2022), 9129–9139.

2 Objetivos

La diversidad de propiedades físicas y químicas y la posibilidad de modularlas selectivamente hace que los materiales 2D sean muy atractivos con vistas a una amplia variedad de aplicaciones en almacenamiento electroquímico de energía, biomedicina, (opto)electrónica, (electro)catálisis o (bio)sensores. A pesar del gran esfuerzo investigador realizado hasta la fecha en este campo, siguen existiendo limitaciones en los métodos de preparación y modificación de materiales 2D en cuanto al control de la calidad estructural y propiedades finales de los productos.

En este contexto, la presente tesis doctoral se ha centrado principalmente en: **(1)** la optimización de metodologías descendentes para la preparación de nanoláminas 2D de TMDs, concretamente MoS_2 y $MoSe_2$; (**2)** la investigación de métodos de funcionalización molecular y de generación de vacantes de calcógeno en TMDs 2D para modular sus propiedades; (**3)** el uso de los TMDs 2D como catalizadores para la degradación de especies contaminantes del agua (reducción de nitroarenos, nitroanilinas y colorantes orgánicos) y como electrodos para almacenamiento electroquímico de energía (almacenamiento de litio).

Los objetivos específicos perseguidos se enumeran a continuación, agrupándolos en las diferentes categorías descritas en el párrafo anterior:

1. *Preparación de dispersiones de nanoláminas 2D de TMDs*
   a. Obtención de dispersiones coloidales de nanoláminas de MoS_2 y $MoSe_2$ mediante LPE asistida por ultrasonidos en medio orgánico y su posterior transferencia a medio acuoso.
   b. Obtención de nanoláminas de MoS_2 mediante EE catódica en medio orgánico y acuoso, con especial énfasis en la optimización de parámetros experimentales como el tiempo de exfoliación, el potencial eléctrico aplicado, así como el electrolito empleado y su concentración.
   c. Caracterización fisicoquímica de las nanoláminas 2D obtenidas mediante distintas técnicas espectroscópicas, microscópicas y otras.

2. *Modificación de nanoláminas 2D de TMDs*
    1. Desarrollo y optimización de una estrategia de funcionalización molecular covalente de MoS_2 por medios electrolíticos; y la investigación de las variables implicadas, tales como el potencial aplicado, el tiempo de tratamiento electrolítico, así como la especie empleada como agente funcionalizante y su concentración en el medio electrolítico.
    2. Desarrollo y optimización de un tratamiento de reducción para generar vacantes superficiales de calcógeno en nanoláminas 2D de MoS_2 y $MoSe_2$ obtenidas por exfoliación directa en fase líquida, estudiando parámetros como el agente reductor empleado, la duración del tratamiento, el disolvente empleado y la temperatura aplicada.

3. *Uso de nanoláminas 2D de TMDs en catálisis y almacenamiento de energía*
    1. Investigación de las prestaciones de nanoláminas 2D de MoS_2 y $MoSe_2$ obtenidas mediante LPE asistida por ultrasonidos, con y sin tratamientos de modificación, como catalizadores para la reducción de nitroarenos.
    2. Investigación de las prestaciones de nanoláminas 2D de MoS_2 obtenidas mediante EE catódica (nanoláminas derivatizadas con ácido iodoacético) para la reacción de reducción de ciertos nitroarenos y colorantes orgánicos.
    3. Investigación de las prestaciones como electrodos para almacenamiento electroquímico de litio (nanoláminas preparadas mediante LPE y exfoliadas en fase orgánica, respectivamente).

3 Materiales y métodos

3.1 Preparación y procesado de dispersiones coloidales de MoS_2 y $MoSe_2$

Exfoliación en fase líquida asistida por ultrasonidos

Se ha llevado a cabo la preparación de dispersiones coloidales de MoS_2 y $MoSe_2$ mediante LPE asistida por ultrasonidos, empleando los correspondientes materiales *bulk* en forma de polvo comercial (*Alfa Aesar*) como precursores. Aunque finalmente se haya escogido DMF (*Sigma Aldrich)* como disolvente, también se estudiaron el isopropanol (*isopropyl alcohol*, IPA) y el ACN (*Sigma Aldrich*) para la elección del disolvente óptimo.

Para llevar a cabo la LPE, se añadió polvo *bulk* a un determinado volumen de DMF, a concentración nominal de dicalcogenuro de 30 $mg \cdot mL^{-1}$. La mezcla se sometió a sonicación en baño de ultrasonidos (*J.P. Selecta Ultrasons System,* 40 kHz) durante 5 h, cambiando el agua del baño cada hora, para evitar el sobrecalentamiento del sistema. La suspensión resultante se centrifugó (*Microcentrifuga Eppendorf 5,430*) a 200 g (*relative centrifugal force*, rcf, habitualmente nombrada como g) durante 25 minutos para sedimentar tanto el material no exfoliado como las partículas exfoliadas de mayor grosor. A continuación, se recogió el 75% del volumen de sobrenadante de la suspensión centrifugada, que constituye la dispersión final de nanoláminas exfoliadas de MoS_2 y $MoSe_2$. La concentración de las dispersiones se determinó mediante espectroscopía UV-vis. El sedimento no exfoliado se almacenó en DMF fresco para su reutilización. El rendimiento de esta exfoliación es aproximadamente del 1%, y las dispersiones finales se ajustaron a una concentración de 0.2 $mg \cdot mL^{-1}$ en DMF para su posterior uso. Se ha usado el convenio anglosajón para la notación de decimales y milésimas (0.2 y 5,430, por ejemplo) para una mayor homogeneidad con los artículos científicos.

Exfoliación electroquímica catódica de MoS_2

Medio acuoso

La exfoliación electroquímica catódica (en adelante EE, ya que no se ha realizado ninguna exfoliación electroquímica anódica en esta tesis) de MoS_2 en medio acuoso se realizó en una celda electroquímica de dos electrodos empleando como cátodo un cristal de MoS_2 (*SPI Supplies*) de aproximadamente $0.4 \times 0.6 \times 0.1$ cm^3 y un contraelectrodo de Pt

(*Good Fellow*) de 25×25×0.025 mm^3, ambos sujetos por pinzas cocodrilo y sumergidos en una disolución de electrolito. Previamente a la realización de cada tratamiento electroquímico, se exfoliaron varias capas superficiales de ambas caras del cristal de MoS_2 con cinta adhesiva para garantizar la exposición de superficie fresca.

Como medio electrolítico, se emplearon 20 mL de diversas disoluciones acuosas de KCl y NaCl, a concentraciones de 0.1, 0.5, 1, 2 y 4 M; LiCl a 4 M; cloruro de tetraetilamonio (TEACl), cloruro de tetrapropilamonio (TPACl) y cloruro de tetrabutilamonio (TBACl) a 0.3 M (*Sigma Aldrich*). Para la realización de las exfoliaciones, se aplicaron voltajes de -10 V y -20 V (*Agilent 6614C DC Power Supply*) al cátodo de MoS_2 en función de las condiciones experimentales deseadas. En todos los experimentos, el tiempo de tratamiento fue de 30 minutos, durante el cual se pudo observar como el cátodo de MoS_2 se expandía, en forma de abanico, desde los bordes del extremo sumergido hasta la región sujetada por la pinza cocodrilo. Finalmente, las condiciones optimizadas de la síntesis fueron KCl4 M y -20 V durante 30 minutos, debido al mayor rendimiento en producto expandido obtenido.

El producto expandido se secó a vacío a temperatura ambiente y, posteriormente, la parte expandida se troceó usando un bisturí. Parte del material triturado se transfirió a una disolución acuosa de adenosín monofosfato (AMP, *Sigma Aldrich*) o guanosín monofosfato (GMP, *Sigma Aldrich*) de concentración 5 mg·mL^{-1}, que se sonicó en baño de ultrasonidos durante 3 h. La concentración inicial de MoS_2 expandido era de 0.3–0.4 mg·mL^{-1}, y como disolventes se emplearon agua Milli-Q (resistividad: 18.2 MΩ cm, *Millipore Corporation*), IPA, NMP y DMF (*Sigma Aldrich*). La dispersión resultante se sometió a dos etapas de lavado consecutivas para eliminar el exceso de AMP o GMP, respectivamente. Cada etapa consistió en la centrifugación (*Microcentrifuga Eppendorf 5,424 y 5,430*) de la dispersión a 20,000 g durante 20 minutos, retirada del sobrenadante y adición del mismo volumen de disolvente fresco. La concentración de las dispersiones se determinó mediante espectroscopía UV-vis.

Medio orgánico

Para la EE de MoS_2 en medio orgánico se empleó un montaje experimental y procedimiento análogo al descrito para la EE en medio acuoso. Las exfoliaciones electroquímicas se realizaron paralelamente en dos fuentes de alimentación (*Equipo*

E3633A, de *Keysight Technologies*; y *Agilent 6614C Power Supply*) para reducir el tiempo de preparación.

Como electrolito se emplearon 20 mL de una disolución de diferentes sales cuaternarias de amonio (Tabla 1) a diferentes concentraciones y voltajes en PC, IPA, ACN y DMF. Todos los reactivos fueron suministrados por *Sigma Aldrich*. Para la etapa de exfoliación en baño de ultrasonidos se usó DMF como disolvente. Tras la aplicación del potencial eléctrico, se observó como el cátodo de MoS_2 comenzaba a expandirse por los bordes, hacia la parte sujeta por la pinza de cocodrilo. Sin embargo, no todas las sales cuaternarias demostraron la misma capacidad de expansión de MoS_2 en los disolventes estudiados. Se encontró que las condiciones óptimas implicaban el uso de HTMABr 0.05 M en PC como electrolito y la aplicación de un potencial de -8 V durante 30 minutos. Las nanoláminas obtenidas en estas condiciones se han denominado ee-MoS_2.

Tabla 1. Electrolitos empleados para la EE en fase orgánica.

Electrolito	Abreviatura
Cloruro de tetrametilamonio	TMACl
Cloruro de tetraetilamonio	TEACl
Cloruro de tetrabutilamonio	TBACl
Cloruro de tetrahexilamonio	THACl
Tetrafluoroborato de tetrahexilamonio	$THABF_4$
Cloruro de hexiltrimetilamonio	HTMACl
Bromuro de hexiltrimetilamonio	HTMABr
Bromuro de octiltrimetilamonio	TMOABr
Bromuro de cetiltrimetilamonio	CTAB

Tras la exfoliación catódica, la parte de la pieza expandida (sumergida en el electrolito) se separó de la no sumergida por medio de un bisturí. La pieza expandida se depositó en un cierto volumen de DMF ajustado para una concentración nominal de MoS_2 de 1 mg·mL^{-1}, y se sonicó en baño de ultrasonidos (*J.P. Selecta Ultrasons System*, 40 kHz) durante 5 h. Posteriormente, el sobrenadante de DMF que contenía las nanoláminas exfoliadas se sometió a cuatro ciclos consecutivos de lavado/resuspensión, que incluían el centrifugado a 10,000 g durante 25 minutos para sedimentar las nanoláminas, el reemplazo del 75% del sobrenadante con DMF fresco y su resuspensión en baño de ultrasonidos (~3 minutos). Tras la etapa de lavado, las dispersiones se dejaron reposar durante aproximadamente 12 h y se recogió el 75% del sobrenadante, descartando el sedimento que contiene material sin exfoliar. La concentración de las dispersiones obtenidas (en el rango de 30-60 µg·L^{-1}) se determinó mediante espectroscopía UV-vis. Las dispersiones de MoS_2 en DMF se conservaron a dicha concentración para su uso posterior.

Lavado de las dispersiones y transferencia a fase acuosa

El lavado de las nanoláminas y/o su transferencia a fase acuosa se realizó aplicando operaciones repetitivas de centrifugación/resuspensión durante varios ciclos consecutivos. Cada ciclo consistía en la sedimentación de las nanoláminas por centrifugación (la velocidad en g se ajustó según la muestra), sustitución del 75% del sobrenadante y la resuspensión mediante ultrasonidos (~3 minutos). En el caso del lavado, se empleó el mismo disolvente que el usado durante la etapa de sonicación. En el caso de la transferencia fase acuosa de dispersiones originalmente en DMF, el sobrenadante se sustituyó por agua Milli-Q (resistividad: 18.2 MΩ cm, *Millipore Corporation*) en cada ciclo de sedimentación.

Concretamente, las dispersiones de MoS_2 y $MoSe_2$ (preparadas mediante LPE) y las dispersiones de ee-MoS_2 (preparadas mediante EE) fueron transferidas desde DMF a agua Milli-Q previamente al estudio de sus aplicaciones. Para ello, se sometieron a cuatro ciclos de centrifugación hasta sedimentación (21,191 g para LPE y 10,000 g para EE, respectivamente, durante 25 minutos), sustitución del 75% del sobrenadante por agua Milli-Q y redispersión asistida por ultrasonidos (~3 minutos).

Determinación de la concentración de las dispersiones coloidales

La concentración de todas las dispersiones coloidales se determinó mediante espectroscopía UV-vis (*Espectrofotómetro Genesys 180, Thermo Fisher Scientific* de doble haz), empleando la siguiente ecuación, análoga a la Ley de Lambert-Beer:

$$Ext(\lambda) = c \cdot \varepsilon_\lambda \cdot l$$

Siendo *Ext* la extinción de la dispersión a una determinada longitud de onda λ; c la concentración de las nanoláminas; ε_λ el coeficiente de extinción molar de las nanoláminas de MoS_2 (34.5 $mg^{-1} \cdot L \cdot cm^{-1}$ a 345 nm) o $MoSe_2$ (24.5 $mg^{-1} \cdot L \cdot cm^{-1}$ a 365 nm); y l el paso óptico de la cubeta de cuarzo utilizada (1 cm). La extinción engloba tanto la absorbancia como la dispersión experimentada por la luz tras incidir sobre las partículas en dispersión cuyo tamaño sea del orden de la longitud de onda de la radiación incidente. Aunque la Ley de Lambert-Beer es estrictamente válida para la absorbancia, se ha demostrado que la forma de los espectros de extinción y absorbancia de dispersiones de nanoláminas es análoga para longitudes de onda por debajo de 700 nm y, por tanto, la información contenida en los espectros de absorbancia puede ser también extraída a partir de los espectros de extinción [1]. Para determinar los coeficientes de extinción molares, se midió la extinción de una dispersión de MoS_2 y $MoSe_2$, respectivamente, y la concentración correspondiente se calculó por pesada directa del material contenido en un volumen determinado de las respectivas dispersiones tras su filtrado y secado a vacío.

3.2 Modificación superficial de nanoláminas de MoS_2 y $MoSe_2$

Funcionalización superficial de nanoláminas de MoS_2

Para la funcionalización de las nanoláminas de MoS_2, se aplicó un tratamiento electroquímico en dos etapas. En la primera etapa, el cátodo de MoS_2 se expandió en KCl en las condiciones seleccionadas como óptimas (KCl 4 M, -20 V, 30 minutos). En la segunda etapa se llevó a cabo la optimización de la funcionalización electroquímica, para lo que se estudiaron diferentes potenciales eléctricos, disolventes (agua Milli-Q, etanol e IPA), varios organoioduros (ácido iodoacético y 4-iodoanilina) y electrolito soporte (Na_2SO_4 y H_2SO_4). Se encontró que las condiciones óptimas para la funcionalización electroquímica implicaban el uso de ácido iodoacético 0.05 M como agente funcionalizante, Na_2SO_4 0.15 M como electrolito soporte y la aplicación de un potencial de -5 V durante 30 minutos.

Generación de vacantes superficiales por tratamiento con hidracina

Previamente al tratamiento de generación de vacantes, las nanoláminas de MoS_2 y $MoSe_2$ fueron transferidas a agua Milli-Q mediante ciclos sucesivos de sedimentación/resuspensión (21,181 g, 25 minutos), sustituyendo en cada etapa el 75% del sobrenadante por agua Milli-Q y redispersando mediante sonicación. La concentración final de las dispersiones se ajustó a 0.1-1.5 $mg\cdot mL^{-1}$. Para la generación de vacantes superficiales de S y Se, se sometieron las respectivas dispersiones de MoS_2 y $MoSe_2$ exfoliadas mediante LPE a un tratamiento reductor con hidracina monohidrato (*Sigma Aldrich*) en proporción de 1 mL hidracina/100 mg dicalcogenuro, durante 1 hora en un baño termostatizado a 70 ºC. Transcurrido este tiempo, las dispersiones se sometieron a tres ciclos de sedimentación/resuspensión (21,181 g, 25 minutos), sustituyendo el 75% del sobrenadante con agua Milli-Q para eliminar los restos de hidracina.

Inmovilización de nanoláminas de dicalcogenuro sobre esponjas para aplicaciones catalíticas

Para facilitar su recuperación y su reutilización, las nanoláminas de MoS_2 funcionalizadas con ácido iodoacético se inmovilizaron sobre una esponja comercial de poliuretano; mientras que las de $MoSe_2$, preparadas por LPE, se adsorbieron sobre una esponja de melamina. Inicialmente, las esponjas se cortaron en cilindros $\sim 1\times 1\times 1$ cm^3, se limpiaron mediante sonicación en etanol durante 20 minutos y se secaron al vacío a temperatura ambiente. Para incrementar la cantidad de nanoláminas adsorbidas, las esponjas de poliuretano y melamina se sometieron a tres ciclos consecutivos de inmersión en una dispersión acuosa de MoS_2 funcionalizado ($\sim$10 $mg\cdot mL^{-1}$), y en una dispersión de $MoSe_2$ en IPA, respectivamente, y se dejaron secar a temperatura ambiente bajo condiciones de vacío. Para los experimentos catalíticos, las esponjas recubiertas de MoS_2 funcionalizado se sumergieron en el medio de reacción que contenía el sustrato y un exceso de agente reductor (borohidruro sódico, $NaBH_4$, *Sigma Aldrich*). Tras la finalización de la reducción, la esponja recubierta se retiró del medio, se aclaró con abundante agua y se secó antes de ser reutilizada. Las esponjas recubiertas de $MoSe_2$ se sumergieron en el medio de reacción que contenía el sustrato y un exceso de $NaBH_4$, bajo condiciones de agitación suave. Tras la finalización de la reacción de reducción, la esponja recubierta se retiró del medio, se aclaró con abundante agua y se escurrió antes de ser reutilizada. En ambos casos, la finalización de la reacción de reducción se comprobó a través de mediciones de espectroscopía UV-vis de pequeñas alícuotas del medio de reacción.

3.3 Aplicaciones

Catálisis

Evaluación de la actividad catalítica

Se estudió la actividad catalítica en fase acuosa de las dispersiones de MoS_2 exfoliado catódicamente con KCl y funcionalizado con ácido iodoacético, y de las nanoláminas de MoS_2 (sin vacantes de S) y de $MoSe_2$ (sin y con vacantes de Se) preparados por LPE para la reacción de reducción de nitroarenos, nitroanilinas y colorantes orgánicos (Tabla 2). Las dispersiones de MoS_2 y $MoSe_2$ preparadas por LPE se transfirieron a fase acuosa previamente a los experimentos de catálisis.

Tabla 2. Sustratos empleados para la reacción de reducción durante los ensayos catalíticos.

Sustrato	Símbolo
2-nitrofenol	2-NP
3-nitrofenol	3-NP
4-nitrofenol	4-NP
2-nitroanilina	2-NA
3-nitroanilina	3-NA
4-nitroanilina	4-NA
Naranja de metilo	MO
Azul de metileno	MB
Hexaferrocianato de potasio	$K_3[Fe(CN)_6]$

En cada ensayo, se mezcló una cantidad fija de catalizador con otra de sustrato, en presencia de un exceso de $NaBH_4$. La evolución de la reacción de reducción se monitorizó mediante espectroscopía UV-vis ya que, en general, los sustratos presentan máximos de absorbancia a longitudes de onda a las que sus correspondientes productos de reducción no tienen una absorbancia significativa, lo que permite relacionar la variación de absorbancia con el consumo de sustrato durante la reacción. Por tanto, la reducción catalítica de cada sustrato se monitorizó midiendo la absorbancia a una longitud de onda característica. Se realizó una estimación de la actividad catalítica de las nanoláminas a partir del número de moles de sustrato convertidos por mol de catalizador por unidad de tiempo. Por tanto, aunque los valores de actividad catalítica no se correspondan directamente con la constante cinética de reacción, sí permiten realizar una comparación sencilla y directa con los resultados descritos en la literatura, siempre que las concentraciones de sustrato empleadas sean similares.

En los experimentos que empleaban como catalizador nanoláminas de MoS_2 y $MoSe_2$ preparadas mediante LPE, se detectó una disminución de su concentración durante la reacción, más acentuada al principio y que tendía a estabilizarse a los pocos minutos. Mediante experimentos de control se constató que la disminución de concentración del catalizador se debía al exceso de sal de $NaBH_4$, ya que un incremento de la fuerza iónica del medio provoca la disminución de la estabilidad de las dispersiones coloidales. Para evitar la sobreestimación de la actividad catalítica, se separaron las contribuciones del catalizador y de los sustratos a la absorbancia total de la reacción de reducción, mediante el seguimiento independiente de cada proceso por espectroscopía UV-vis.

Estudio de la estabilidad al ciclado del catalizador de $MoSe_2$ en fase líquida

Se estudió la estabilidad del catalizador de $MoSe_2$ en fase líquida, sin que las nanoláminas estuvieran adsorbidas sobre un soporte. Para ello, en un volumen total de 50 mL que contenía una dispersión de $MoSe_2$ (~0.3 $mg \cdot mL^{-1}$) y $NaBH_4$ en exceso se añadieron volúmenes sucesivos de 3-NA tras la reducción catalítica del volumen anterior, en condiciones de agitación suave. Esta secuencia se repitió durante diez ciclos. El medio de reacción se sometió a sonicación (~3 minutos) entre ciclos para contrarrestar la posible desestabilización coloidal del catalizador. La reducción completa del sustrato fue verificada por espectroscopía UV-vis de pequeños volúmenes del medio de reacción. Tras diez ciclos de catálisis, las nanoláminas de $MoSe_2$ se sedimentaron por centrifugación y se sometieron a cuatro etapas de lavado para eliminar los restos de $NaBH_4$, 3-NA y su producto de reducción. El catalizador limpio fue posteriormente caracterizado mediante espectroscopías Raman y XPS.

Baterías de ion-Litio

Procesado de material electroactivo

Para la fabricación de los electrodos, se utilizaron las nanoláminas preparadas por sonicación del MoS_2 expandido por EE usando HTMABr 0.05 M en PC a -8 V, denominado ee-MoS_2; y nanoláminas de MoS_2 obtenidas mediante LPE, designado como lpe-MoS_2. La dispersión de ee-MoS_2 se sometió a cuatro ciclos de lavado en DMF (10,000 g, 25 minutos). Posteriormente, las dispersiones de ee-MoS_2 y lpe-MoS_2 se transfirieron a agua (cuatro ciclos a 10,000 y 21,181 g, respectivamente, 25 minutos) y se preconcentraron, para su posterior liofilización (*Telstar Lyoquest-85*) durante cuatro días, obteniéndose así el polvo seco de los correspondientes materiales exfoliados.

Preparación de electrodos

Los electrodos se prepararon mezclando una cierta cantidad de material electroactivo (ee-MoS_2 o lpe-MoS_2) con nanotubos de carbono de pared múltiple (*multi-walled carbon nanotubes*, MWCNTs, *Arkema*), que funcionan tanto como aditivo conductor como refuerzo estructural; negro de carbono (*carbon black*, CB, Super C65 de *Timcal*) que actúa como aditivo conductor; y fluoruro de polivinilideno como aditivo aglomerante (*polyvinylidene fluoride*, PVDF, *Solef*), en una proporción fija de 54:16:20:10 en peso. Previamente al mezclado de los componentes, se preparó una dispersión de PVDF/NMP al 5% en peso para ajustar la cantidad de PVDF añadida. La cantidad de material electroactivo, los MWCNTs y el CB se determinaron por pesada directa del material sólido. Tras la pesada de los componentes, se añadió un cierto volumen de NMP (proporción de ~0.85 gotas/mg MoS_2) y la mezcla se homogeneizó usando un mezclador de cizalla (*Ultra Turrax T-25*) hasta alcanzar una consistencia de *slurry* homogénea (~20 minutos). El *slurry* resultante se extendió homogéneamente por la superficie de un sustrato de cobre modificado, usando una metodología similar a *Doctor Blade* y se dejó secar durante varias horas a 40 ºC y presión atmosférica para evitar el agrietado del recubrimiento. Cuando el recubrimiento alcanzó una textura seca y compacta, las piezas de cobre recubiertas se secaron durante 12 h a 80 ºC en una estufa de vacío para eliminar los restos de NMP. Las piezas de cobre recubiertas con ee-MoS_2 y lpe-MoS_2 se troquelaron en discos de 10 mm de diámetro. La carga de masa de material electroactivo de los electrodos oscilaba entre 1.5 y 2.5 $mg \cdot cm^{-2}$.

Ensamblado de las pilas de botón

Todas las pilas de botón se ensamblaron en atmósfera inerte de argón (niveles de oxígeno y agua inferiores a 0.1 ppm) en el interior de una caja seca (*Jacomex*) usando pilas de botón de tipo CR2032. Previamente a su introducción en la caja seca, todos los electrodos preparados y los separadores de fibra de vidrio utilizados (Whatman, *Sigma Aldrich*) fueron desgasificados en un horno *B-585* de Büchi a 120 ºC durante 12 h. El ensamblado de las pilas de botón se realizó con la disposición que se muestra en la Figura 16:

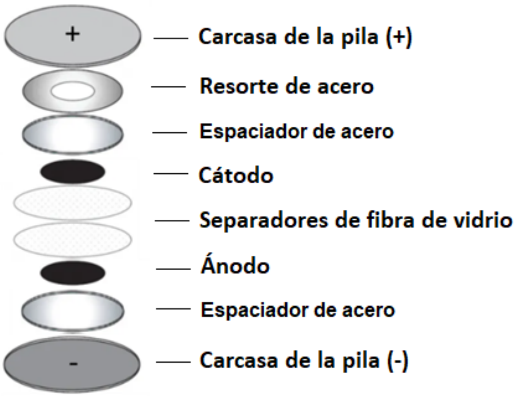

Figura 16. Esquema del montaje de una pila de botón.

Como separador, se usaron dos discos de 12 mm de fibra de vidrio, que se impregnaron con 8 gotas de electrolito LP30 (*Sigma Aldrich*). Como contraelectrodo y electrodo de referencia, se utilizó un disco de 10 mm troquelado de una lámina de Li metálico (*Sigma Aldrich*). Además, cada pila de botón contenía dos espaciadores de acero y un resorte ondulado para asegurar un buen contacto eléctrico.

Evaluación del comportamiento electroquímico

El comportamiento electroquímico de los electrodos de ee-MoS_2 y lpe-MoS_2 se estudió mediante voltametría cíclica (*cyclic voltammetry*, CV), espectroscopía de impedancia electroquímica (*electrochemical impedance spectroscopy*, EIS) y cargas/descargas galvanostáticas (*galvanostatic charge/discharge*, GCD) con limitación de potencial usando un potenciostato *BioLogic-VMP3*. Antes de la realización de cualquier medida electroquímica, cada electrodo se dejó reposar durante 4 h en condiciones de circuito abierto (*open circuit voltaje*, OCV) para asegurar una buena impregnación de electrolito.

Todos los valores de capacidad gravimétrica se han calculado teniendo en cuenta la masa total del electrodo (material electroactivo y aditivos conductores, sin considerar el soporte de Cu). Los valores de capacidad gravimétrica se han calculado aplicando la siguiente fórmula:

$$C\ (mA \cdot h \cdot g^{-1}) = \frac{\left(t_f - t_i\right) \cdot I_{ap}}{m_T}$$

Donde C es la capacidad gravimétrica; t_f y t_i son el tiempo final e inicial, respectivamente, correspondientes al final y al inicio de cada ciclo de carga o descarga; I_{ap} es la intensidad de corriente constante aplicada para cargar y descargar la pila; y m_T es la masa total del electrodo.

Los valores de eficiencia culómbica (EC) para el material anódico de una semicelda se han calculado aplicando la siguiente fórmula [2]:

$$EC\ (\%) = \frac{C_c^n}{C_d^n} \cdot 100$$

Donde EC es la eficiencia coulómbica; C_d y C_c son la capacidad gravimétrica para una descarga y carga, respectivamente; y n el número del ciclo para cada valor de EC.

La diferente contribución de procesos (pseudo)capacitivos y faradaicos al mecanismo de almacenamiento de Li de los electrodos de ee-MoS_2 se evaluó aplicando el método de Dunn (ver sección *Método de Dunn*) [3].

Referencias

[1] Backes, C., Smith, R. J., McEvoy, N., Berner, N. C., McCloskey, D., Nerl, H. C., O'Neil, A., King, P. J., Higgins, T., Hanlon, D., Scheuschner, N., Maultzsch, J., Houben, L., Duesberg, G. S., Donegan, J. F., Nicolosi, V., Coleman, J. N. Edge and confinement effects allow in situ measurement of size and thickness of liquid-exfoliated nanosheets. *Nature Communications*, 5 (2014), 4576.

[2] Li, X., Sun, X., Hu, X., Fan, F., Cai, S., Zheng, C., Stucky, G. D. Review on comprehending and enhancing the initial Coulombic efficiency of anode materials in lithium-ion/sodium-ion batteries. *Nano Energy,* 77 (2020), 105143.

[3] Wang, J., Polleux, J., Lim, J., Dunn, B. Pseudocapacitive contributions to electrochemical energy storage in TiO_2 (anatase) nanoparticles. *Journal of Physical Chemistry C*, 111 (2007), 14925–14931.

4 Técnicas de caracterización

4.1 Espectroscopías

La espectroscopía es la disciplina que estudia la interacción (absorción, emisión, dispersión...) de la radiación electromagnética con la materia. La radiación electromagnética es un tipo de energía radiante que posee naturaleza dual de onda (formada por campo eléctrico y magnético sinusoidales que se transmiten perpendicularmente) y de partícula (fotón). Los fotones de radiación interaccionan con la materia, pudiendo absorberse (o emitirse) radiación en cantidades discretas, ya que los niveles energéticos de sus átomos o moléculas que la forman están cuantizados. La ecuación de Planck-Einstein expresa la mínima cantidad de energía (*cuanto*) que puede absorberse o emitirse en forma de fotón:

$$\Delta E = E_{superior} - E_{inferior} = h \cdot v$$

Siendo $E_{superior}$ la energía del nivel más alto; $E_{inferior}$ la energía del nivel más bajo; h la constante de Planck; y v la frecuencia de la radiación absorbida o emitida. Como se muestra en esta ecuación, los tipo de transiciones entre estados energéticos están determinados por la energía de los fotones de radiación implicada que, a su vez, depende de la frecuencia v. Los espectros de absorción y de emisión se producen cuando una partícula absorbe o emite fotones de energía $h{\cdot}v$, para pasar de un estado de energía inferior a otro superior o viceversa, respectivamente. Por ejemplo, la radiación infrarroja (IR) estimula transiciones entre estados vibracionales, mientras que la UV-vis causa transiciones entre los niveles electrónicos más externos. Sin embargo, no todas las transiciones energéticas están permitidas, y cada modalidad de espectroscopía dispone de unas reglas de selección concretas [1]. Además, todo material posee una serie de niveles energéticos (electrónicos, vibracionales, rotacionales, etc.) característicos y, por tanto, presenta frecuencias de absorción o emisión específicas. Las propiedades espectrales propias de cada material permiten registrar sus espectros de absorción/emisión, facilitando así su identificación y estudio.

Espectroscopía de absorción ultravioleta visible (UV-vis)

La energía total de una molécula puede considerarse como el sumatorio de su energía electrónica, vibracional y rotacional. A su vez, cada estado electrónico tiene asociados un estado vibracional fundamental y varios estados excitados; y, cada estado vibracional, un estado rotatorio fundamental y varios estados excitados. Cuando un haz de radiación en el rango del UV-vis (~160-780 nm) interacciona con la materia, provoca en ella transiciones de los electrones entre niveles electrónicos externos, que a su vez tiene asociados una serie de estados vibracionales y rotacionales próximos en energía. Por esta razón, al ser posible un gran número de transiciones con energías próximas, los espectros UV-vis muestran bandas anchas en lugar de picos estrechos. La interacción de los materiales con el medio (p. ej., con moléculas de disolvente) también puede producir alteraciones en los niveles energéticos y contribuir al ensanchamiento de la señal obtenida. Si bien estas características impiden el uso de la espectroscopía UV-vis para la identificación inequívoca de sustancias, sí es ampliamente utilizada para la detección de ciertos grupos funcionales, complejos organometálicos o nanoestructuras en función de la longitud de onda de las bandas de absorción. Una banda de absorción de un espectro UV-vis se caracteriza por la longitud de onda de la transición, medida en el máximo del pico de absorción; y por su intensidad, que depende de la diferencia de energía entre los estados electrónicos y la probabilidad de ocurrencia de la transición, determinada por sus reglas de selección. Las bandas de absorción en UV-vis están producidas por tres tipos de transiciones: transiciones de electrones π, σ y η; transiciones de electrones d y *f*; y transiciones producidas por transferencia de carga [1,2].

En un espectrofotómetro de doble haz (Figura 17), la fuente de radiación (generalmente una lámpara de tungsteno, para el rango visible, o deuterio, para el rango UV) emite un haz de radiación policromática. A continuación, un monocromador permite filtrar por barrido las longitudes de onda específicas que incidirán sobre la muestra. Un divisor del haz de radiación junto con un sistema de espejos permite irradiar, de manera simultánea, una muestra de referencia (P_0) y una muestra de interés (P), lo que permite calcular la absorbancia (A) a través de la ecuación:

$$A(\lambda) = -Log\left(\frac{P}{P_0}\right)$$

Los espectrofotómetros de doble haz permiten la medición de la absorbancia para radiaciones de longitudes de onda comprendidas entre los 190 y 1000 nm (parte del rango UV, todo el rango visible y parte del IR cercano), aproximadamente, lo que se corresponde con transiciones energéticas entre ~1 y 6 eV, como las de los orbitales moleculares tipo π, pares de electrones no enlazantes y orbitales d [1].

Además, es posible relacionar la *absorbancia* (cantidad de radiación absorbida con relación a la del haz incidente) de un material, a una determinada frecuencia o longitud de onda de la radiación incidente, con su concentración en un medio, según la ley de Lambert-Beer [1]:

$$A(\lambda) = \varepsilon \cdot C \cdot l$$

Siendo A la absorbancia del material a una longitud de onda determinada λ; ε el coeficiente de absorción molar a dicha longitud de onda; C la concentración del material; y l el paso óptico que atraviesa la radiación. Esta relación permite cuantificar la concentración de un material a partir de la medida de su absorbancia, siempre y cuando ésta se encuentre dentro del rango lineal de aplicación (tanto instrumental como teórico) de la ley de Lambert-Beer [2].

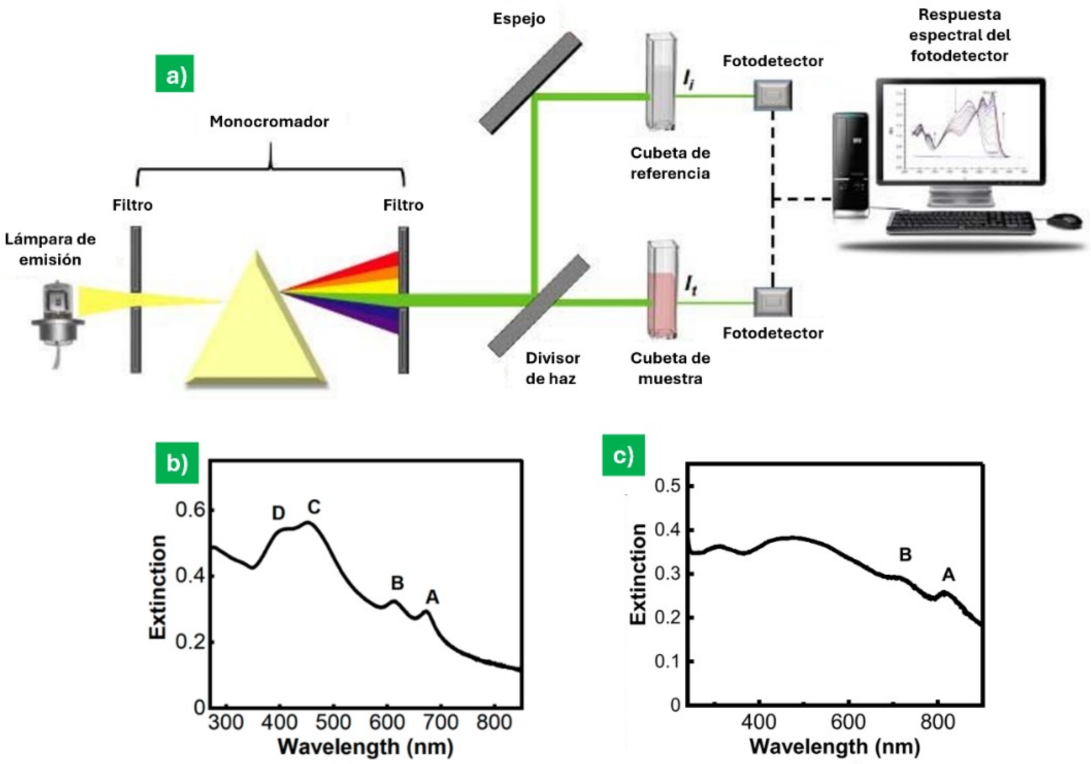

Figura 17. (a) Esquema de funcionamiento de un espectrofotómetro de doble haz. Adaptado de [3]. Espectros UV-vis de una dispersión de nanoláminas de **(b)** ee-MoS_2, preparadas por EE con HTMABr; y **(c)** $MoSe_2$, preparadas por LPE.

En esta tesis, se ha un espectrofotómetro UV-Vis de doble haz Genesys 180 (*Thermo Fisher Scientific*) para:

- Detección de la fase 2H, caracterizada por la presencia de cuatro bandas excitónicas a longitudes de onda características, de las dispersiones de nanoláminas de MoS_2 y $MoSe_2$ preparadas por LPE y EE (Figura 17b y c), y de las nanoláminas modificadas superficialmente con ácido iodoacético y con vacantes de calcógeno.
- Determinación de la concentración de las dispersiones de las nanoláminas a partir de la ecuación de Lambert-Beer y los coeficientes de extinción molar.
- Estimación de los tamaños laterales y grosores de las nanoláminas con las métricas desarrolladas por Coleman *et al* [4].
- Estudio de las cinéticas de reacción en diferentes reacciones de reducción catalítica mediante la monitorización de absorbancia de los reactivos, cuya variación puede relacionarse con la constante de reacción.

Preparación de muestras

Para la medición de espectros UV-vis, se ha utilizado una cubeta de cuarzo con paso óptico de 1 cm. Se han empleado volúmenes de 2-2.5 mL en todos los casos, añadiendo en la cubeta de referencia el mismo disolvente que el presente en la dispersión o disolución analizada. Todas las dispersiones se sometieron a una breve sonicación (~3 minutos) previamente a su análisis mediante espectroscopía UV-vis, para minimizar el grado de agregación de las nanoláminas. Los espectros UV-vis se han tomado en un rango de longitudes de onda de 190-1000 nm.

Espectroscopía infrarroja por transformada de Fourier con reflectancia total atenuada (ATR-FTIR)

La espectroscopía IR estudia la interacción entre la radiación IR y la materia. La radiación infrarroja se puede dividir, a su vez, en el IR cercano (0.75-1-1 μm), IR medio (1.1-15 μm) e IR lejano (15-100 μm). La absorción de un fotón con $h{\cdot}v$ correspondiente al IR produce una transición de la partícula a un estado vibracional de mayor energía (excitado), dentro del mismo estado electrónico en el que se encuentra. Sin embargo, las reglas de selección determinan que, para que un modo normal de vibración (en sustancias moleculares) o fonón (en sólidos extensos) sea activo en IR, debe provocar un cambio en el momento dipolar de la correspondiente estructura. Por ejemplo, aunque los enlaces (dobles y triples, respectivamente) de las moléculas diatómicas de oxígeno y nitrógeno pueden estar en diferentes estados vibracionales, no absorben en el IR, ya que la transición entre ellos no produce un cambio en el momento dipolar neto. La principal característica de la espectroscopía IR es que permite la detección de muchos grupos funcionales ($-CH_2$, -C=O, -OH…) a partir de la observación de bandas con la frecuencia (o número de onda) característica de los modos de vibración de los enlaces implicados [1,2].

En la actualidad, el desarrollo de la espectroscopía infrarroja por transformada de Fourier (*Fourier-transform infrared spectroscopy*, FTIR) ha hecho que los espectrómetros dispersivos de IR tradicionales hayan caído prácticamente en desuso. La FTIR se basa en el empleo del interferómetro de doble haz, que permite generar un patrón de interferencia (interferograma) mediante un sistema de espejos entre los haces de radiación IR que inciden sobre la muestra. El procesado del interferograma generado mediante la transformada de Fourier permite obtener la absorción de la muestra para cada longitud de onda. El empleo de la FTIR permite mejorar la resolución de los espectros y la sensibilidad, ya que aumenta notablemente la relación señal/ruido e incrementa la precisión de la longitud de onda registrada. La modalidad de reflectancia total atenuada (*attenuated total reflectance*, ATR) emplea un accesorio de material transparente al IR y con alto índice de refracción (germanio, diamante…) sobre el que la radiación IR incide con un ángulo inferior a su ángulo crítico. De este modo, la radiación IR sufre una serie de reflexiones internas dentro del material transparente. Si se sitúa una muestra sobre el soporte transparente, ésta absorberá parte de la radiación IR en cada reflexión, atenuando así la radiación (Figura 18) [1,2].

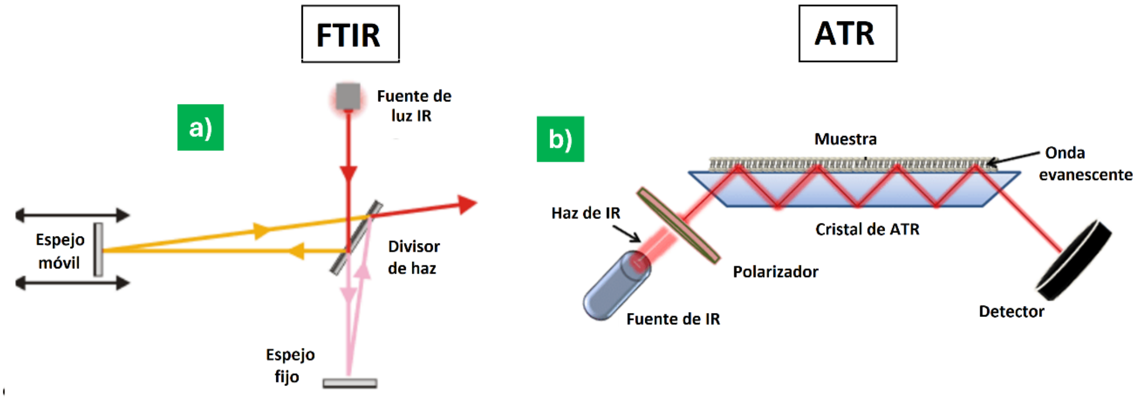

Figura 18. Esquema del funcionamiento de **(a)** un espectrómetro FTIR acoplado a **(b)** un accesorio con modalidad de ATR.

En esta tesis, se ha empleado un espectrómetro Nicolet 8700 (Thermo Scientific) con un cristal de diamante para ATR para la detección de la señal C-S para corroborar la funcionalización por ácido iodoacético en las nanoláminas de MoS_2 preparadas por EE en fase acuosa.

Preparación de muestra

Las muestras de MoS_2 funcionalizado para ATR-FTIR se prepararon en forma de filmes por filtración de las dispersiones acuosas sobre filtros de membrana de plata.

Espectroscopía Raman

Mientras que la espectroscopía IR requiere de un solo fotón (con energía en el rango del IR medio) para producir una transición directa entre dos estados vibracionales, la espectroscopía Raman involucra dos fotones (con energías en el rango del UV, visible o

IR cercano) que no conducen a una transición directa entre estados energéticos. La interacción de un fotón de energía $h\cdot v$ con una partícula produce en ella una transición a niveles de mayor energía (excitación), tras lo cual vuelve a niveles de menor energía (relajación) mediante la emisión de radiación. Si la partícula regresa a su estado inicial mediante la emisión de un fotón de la misma longitud de onda que la incidente, se ha producido una dispersión elástica o *Rayleigh*. Sin embargo, si la relajación se produce mediante la emisión de un fotón con una longitud de onda diferente a la incidente, la partícula vuelve a un estado energético distinto del inicial, en un proceso de dispersión inelástica o *Raman* (Figura 19a).

La espectroscopía Raman estudia los niveles vibracionales de la materia, a través de la diferencia de energía entre el fotón incidente y el fotón dispersado, atribuible a la diferencia energética entre dos estados vibracionales. Si el estado final es más energético que el estado inicial (dispersión *Stokes*), la longitud de onda del fotón emitido es mayor que la del fotón incidente, mientras que si el estado final es menos energético que el inicial (dispersión *anti-Stokes*), la longitud de onda de la radiación emitida es menor (Figura 19b). No todos los modos de vibración (en sustancias moleculares) o fonones (en sólidos extensos) generan una señal Raman, y solamente son activos aquellos que provocan una variación en la polarizabilidad de la estructura de la molécula o de la red, respectivamente [1].

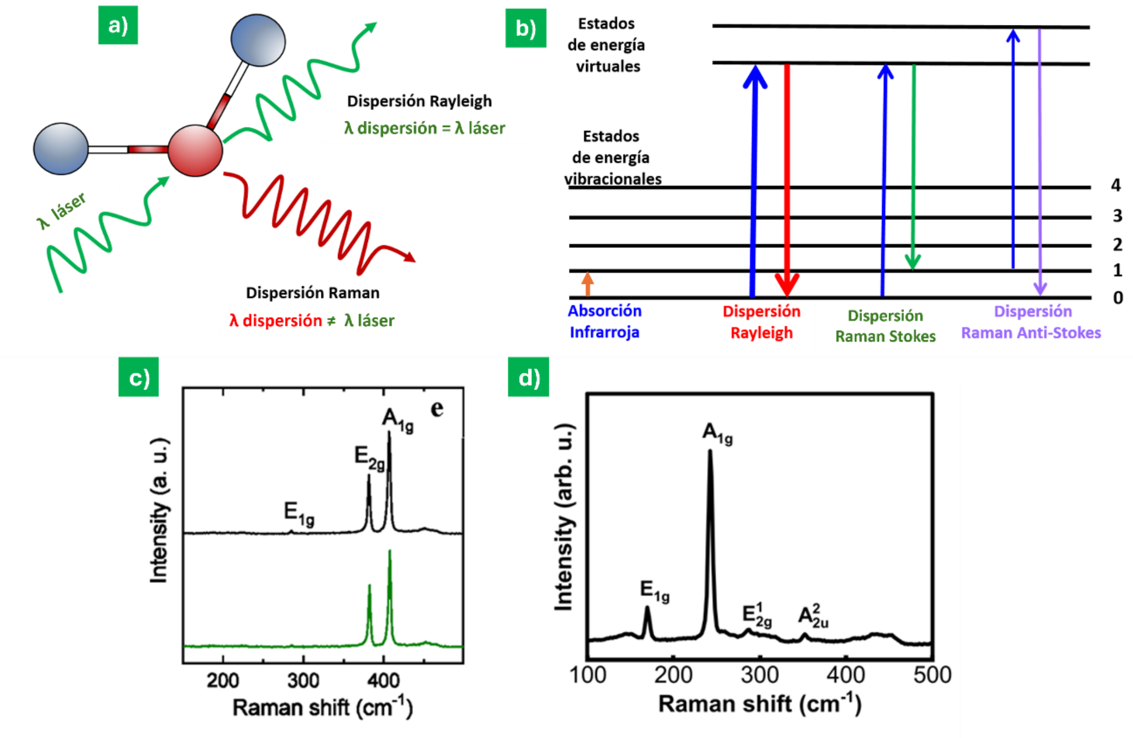

Figura 19. (a) Esquema del mecanismo de dispersión de la energía. **(b)** Diagrama de los mecanismos de excitación/relajación entre estados energéticos que originan la dispersión Rayleigh y Raman. Adaptado de [2]. Espectros Raman de nanoláminas de **(c)** MoS_2 modificadas con ácido iodoacético; y **(d)** nanoláminas de $MoSe_2$ preparadas mediante LPE.

Habitualmente, se emplean láseres como fuentes de radiación, ya que la baja probabilidad de la dispersión Raman requiere el uso de radiación muy intensa y monocromática para incrementar la intensidad de la señal registrada. Como la diferencia entre la frecuencia del haz incidente y dispersado es característica de cada material, los niveles vibracionales de un sólido cristalino pueden relacionarse con su estructura, permitiendo la aplicación de la espectroscopía Raman en caracterización estructural [5,6]. La Figura 20 muestra un esquema del funcionamiento de un espectrofotómetro Raman.

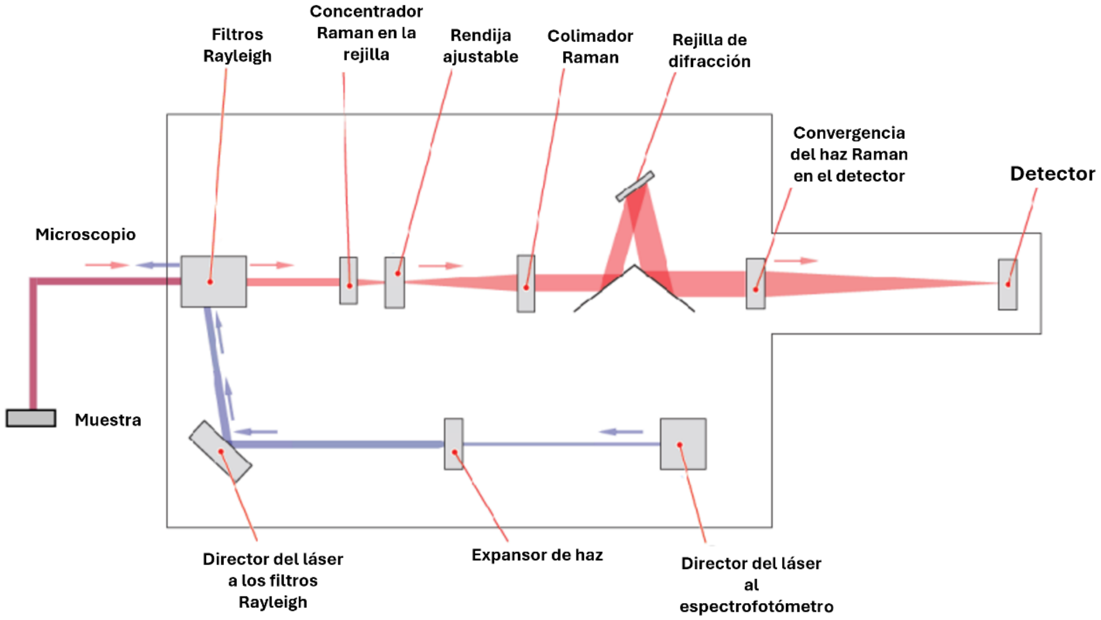

Figura 20. Esquema de los componentes de un espectrofotómetro Raman, con indicación de su funcionamiento. Adaptado de [3].

En esta tesis, se han usado un equipo Horiba Jobin-Yvon LabRam de potencia inferior a 0.2 mW (Artículo II), y un equipo Renishaw inVia Qontor de potencia inferior a 0.5 mW (Artículo I y III), ambos con una fuente de excitación láser de 532 nm (línea verde) para:

- Identificación de las bandas A_{1g}, E_{1g}, E^1_{2g} y A^2_{2u} características de la fase 2H de las nanoláminas de $MoSe_2$ preparadas por LPE y nanoláminas de $MoSe_2$ funcionalizadas con vacantes de Se superficiales (Figura 19d).
- Identificación de las bandas A_{1g}, E_{1g} y E^1_{2g} características de la fase 2H de las nanoláminas de MoS_2 preparadas por LPE, EE y nanoláminas de MoS_2 funcionalizadas con vacantes de S superficiales (Figura 19c).

Preparación de muestras

Las nanoláminas de MoS_2 preparadas por EE en fase acuosa no funcionalizadas y funcionalizadas con ácido iodoacético, respectivamente, se prepararon para su análisis mediante deposición de un cierto volumen de dispersión (en IPA, en el caso del MoS_2 no funcionalizado, y en agua desionizada, en el del funcionalizado) sobre discos de acero previamente pulidos, que se dejaron secar a temperatura ambiente en campana extractora. Se siguió un procedimiento análogo para las nanoláminas de MoS_2 y $MoSe_2$ exfoliadas mediante LPE y para las de ee-MoS_2, respectivamente, usando agua desionizada como disolvente.

Para poder analizar los polvos *bulk* de MoS_2 y $MoSe_2$, se prepararon pastillas mediante prensado hidráulico.

Espectroscopía fotoelectrónica de rayos X (XPS)

Los rayos X son un tipo de radiación electromagnética muy penetrante del espectro no visible, cuya longitud de onda está comprendida entre 10^{-8}-10^{-12} nm (frecuencias del rango 10^{16}-10^{20} Hz). La espectroscopía fotoelectrónica de rayos X (*X-ray photoelectron spectroscopy*, XPS) estudia la emisión de electrones por efecto fotoeléctrico que experimenta un material cuando es irradiado por un haz de fotones de rayos X. La emisión de fotoelectrones (o fotoemisión) se produce cuando los fotones incidentes de rayos X interaccionan con los electrones de los niveles internos de un material y les transfieren su energía. Para que se produzca la emisión de un fotoelectrón, la energía $h{\cdot}\nu$ del fotón incidente tiene que ser superior a la suma de la energía de ligadura (*binding energy*, BE) de los electrones a los átomos y la función de trabajo (energía necesaria para transferir el electrón desde el nivel de Fermi del átomo al vacío), Φ, del equipo. El resto de la energía contenida en el fotón incidente se transfiere como energía cinética (*kinetic energy*, KE) al fotoelectrón emitido (Figura 21a). A través de la ecuación de Planck-Einstein [1]:

$$\Delta E = h \cdot \nu = BE + \Phi + KE$$

se puede determinar la BE de un electrón de una capa interna si se conoce la energía $h{\cdot}\nu$ del haz de rayos X incidente, la función de trabajo del equipo Φ y la KE de los electrones fotoemitidos.

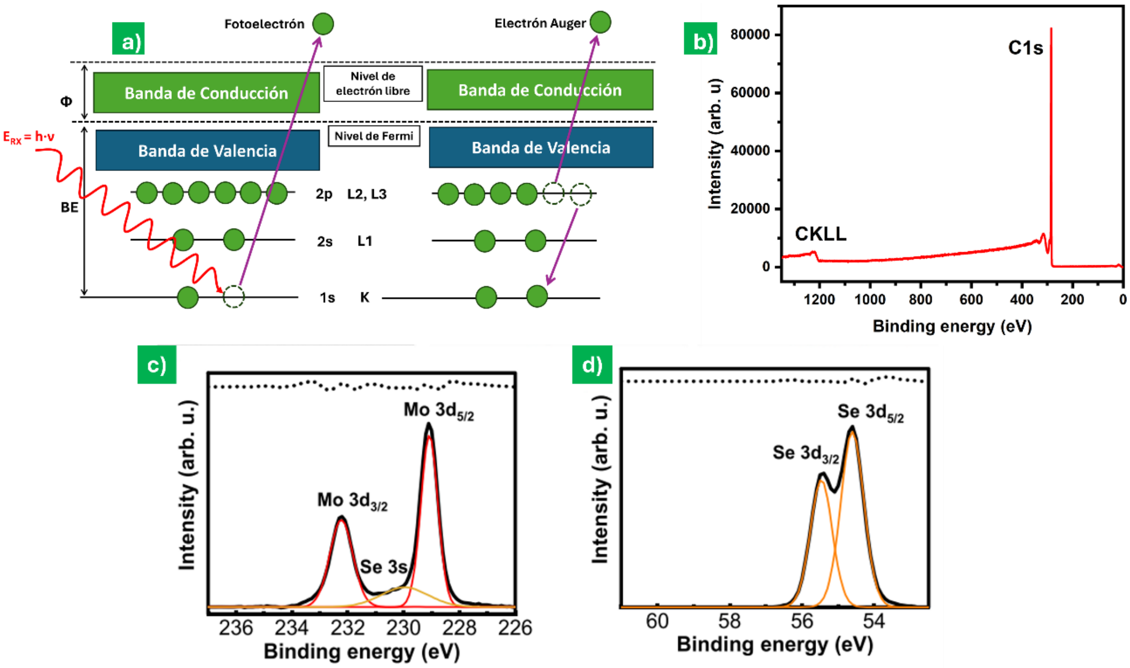

Figura 21. **(a)** Diagrama del mecanismo de emisión de un fotoelectrón y de un electrón Auger en XPS. Adaptado de [2]. Espectros XPS de **(b)** una muestra de HOPG donde se muestra la banda CKLL (electrones Auger) y C1s (fotoelectrones). Espectros XPS de alta resolución y con el fondo sustraído para **(b)** Mo 3d y **(c)** Se 3d de nanoláminas de MoSe$_2$ preparadas por LPE.

Las bandas XPS provienen de los fotoelectrones emitidos por los átomos de las capas más superficiales del material (~10 nm de espesor) que llegan al detector sin pérdida de energía, conservando la información analítica referente a su BE característica (Figura 21b, banda C1s). Por el contrario, los fotoelectrones emitidos desde capas más profundas del material pueden experimentar choques inelásticos con los átomos de su estructura, provocando su reabsorción o su fotoemisión con una energía cinética menor. Estos fotoelectrones de menor energía son detectados como parte del fondo del espectro, contribuyendo a la línea base. Adicionalmente, la irradiación con rayos X también puede estimular la emisión secundaria de electrones Auger, generados como consecuencia de los procesos de relajación electrónicos posteriores a la fotoemisión (Figura 21a y b, banda CKLL) [1]. La Figura 22 representa el esquema de funcionamiento de un espectrofotómetro de XPS, con indicación a sus componentes.

La espectroscopía XPS se emplea en el análisis composicional de una gran variedad de materiales aplicables en campos como la catálisis, polímeros, aleaciones o semiconductores, permitiendo identificar todos los elementos presentes en una muestra, con excepción del H y el He. Además, también aporta información sobre el entorno molecular, la estructura de los compuestos y el estado de oxidación de los átomos, ya que todos estos factores afectan a la energía de ligadura de los electrones [1].

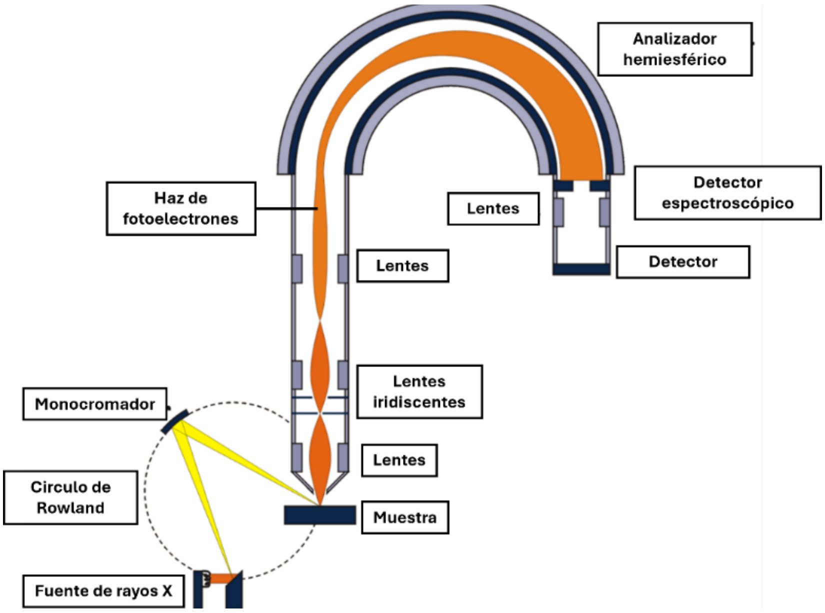

Figura 22. Esquema de los componentes, con indicación de su funcionamiento, de un espectrofotómetro XPS.

En esta tesis se usó un espectrofotómetro XPS SPECS equipado con un analizador electrónico semiesférico Phoibos 100. Los espectros se registraron con un ángulo de despegue de 90º, a presión menor de 10^{-7} Pa y usando una fuente de rayos X de aluminio monocromática a un voltaje de 14.00 kV y una potencia de 175 W. En esta tesis, el XPS se ha empleado para:

- Análisis de la composición de las nanoláminas de MoS_2 y $MoSe_2$ preparadas por LPE con y sin generación de vacantes de S y Se, respectivamente; de las nanoláminas de MoS_2 preparadas por EE en fase acuosa y funcionalizadas con ácido iodoacético; y de las nanoláminas de MoS_2 preparadas por EE en fase orgánica (Figura 21c y d).
- Determinación de la fase 2H o 1T de las respectivas nanoláminas de MoS_2 y $MoSe_2$.
- Cálculo del grado de funcionalización con ácido iodoacético de las nanoláminas de MoS_2.

Preparación de muestras

La preparación de muestras para XPS siguió la misma metodología que en el caso de la Espectroscopia Raman.

Difracción de rayos X (XRD)

El fenómeno de difracción resulta de la dispersión experimentada por la radiación electromagnética al interaccionar con átomos o moléculas en posiciones fijas y ordenadas. La difracción de rayos X (*X-Ray diffraction*, XRD) es una técnica de caracterización estructural de sólidos basada en la difracción que experimentan los rayos X al interaccionar (para distintos ángulos de incidencia) con átomos en posiciones fijas, que actúan como rendijas de difracción y se transforman en fuentes secundarias de reemisión de radiación. Los rayos X difractados generan una serie de patrones de interferencia (constructiva o destructiva) característica de cada material debido a sus distancias interatómicas, y los difractogramas obtenidos contienen información sobre su estructura y la fase cristalina [1].

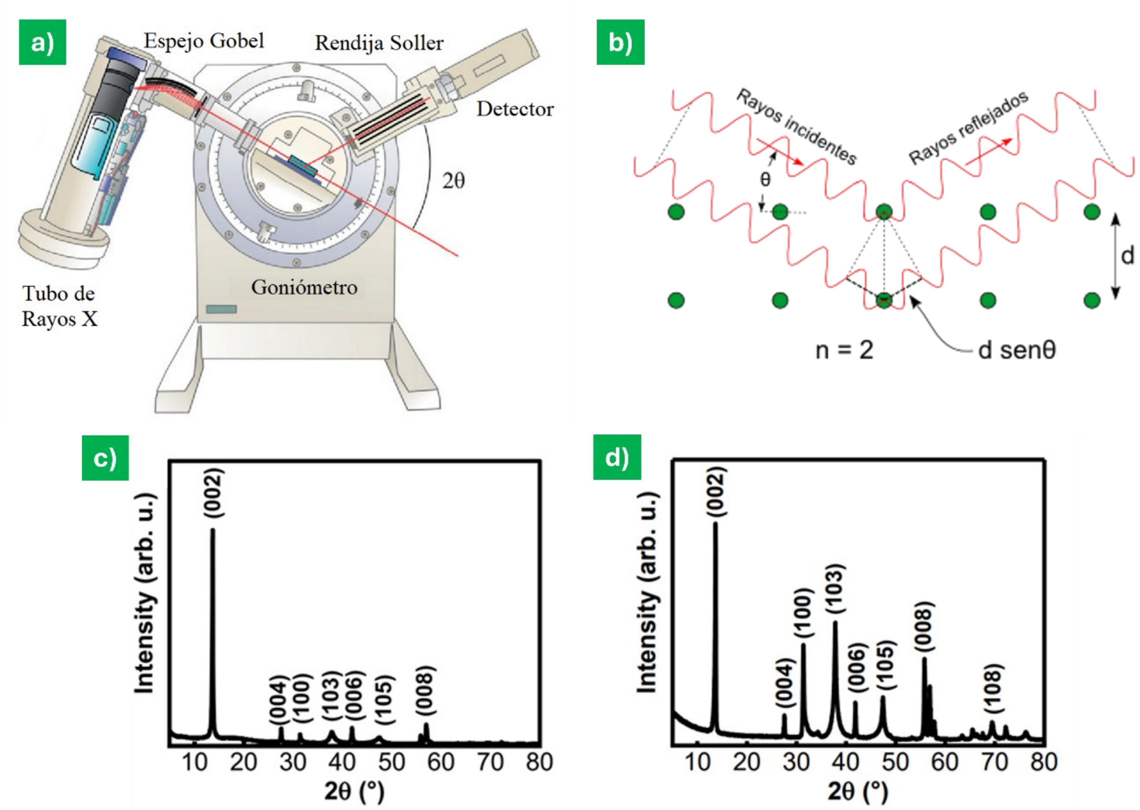

Figura 23. (a) Esquema del funcionamiento de un difractómetro de rayos X. **(b)** Diagrama de aplicación de la Ley de Bragg. Difractogramas de una muestra de nanoláminas de **(c)** $MoSe_2$ y **(d)** MoS_2, preparadas ambas mediante LPE.

El difractómetro es el instrumento empleado para las mediciones de XRD y permite la obtención de difractogramas, que recogen la intensidad de los rayos X difractados en función del ángulo de los rayos X incidentes (Figura 23a).

La aplicación de la Ley de Bragg permite correlacionar un determinado patrón de interferencia constructiva de rayos X, difractados por un material con estructura atómica periódica, con la distancia interplanar de la familia de planos (*hkl*) que la causa (Figura 23b):

$$n \cdot \lambda = 2 \cdot d \cdot \sin\theta$$

Donde n es un número entero (orden de reflexión); λ es la longitud de onda de la radiación incidente; d es la distancia entre dos planos consecutivos de una familia de planos cristalinos (*hkl*); y θ es el ángulo incidente de los rayos X asociado a la difracción [1].

En esta tesis, se ha empleado un difractómetro Bruker D8 Advance equipado con un ánodo de Cu Kα. Los datos se registraron en un rango de 5-80º para 2θ, con toma de puntos cada 0.015º y acumulando la señal durante 6 s en cada punto. La XRD se ha utilizado para la confirmación de la fase 2H de las nanoláminas de MoS_2 y $MoSe_2$ preparadas por LPE, EE y de los materiales *bulk* precursores (Figura 23c y d) y la identificación de las correspondientes familias de planos cristalográficos.

Preparación de muestra

Las muestras de los TMDs *bulk* se han preparado introduciendo una determinada cantidad de material sólido en un portamuestras de vidrio. El material en polvo se molió previamente en un mortero de ágata para disminuir el tamaño del grano. Tras su colocación en el portamuestras, se presionó exhaustivamente con otra pieza de vidrio para garantizar el alisado de la superficie y la uniformidad de la altura de la muestra.

Las muestras de las nanoláminas de MoS_2 y $MoSe_2$ obtenidas vía LPE y EE se prepararon por filtración de las respectivas dispersiones acuosas sobre membranas de policarbonato (50 µm de tamaño de poro, Whatman) para formar filmes. Para garantizar una superficie plana, los filmes se adhirieron a un soporte de vidrio por medio de una grasa amorfa, que no genera señal en XRD.

Espectroscopia de resonancia paramagnética electrónica (EPR)

Un sistema *paramagnético* es aquel que contiene dipolos magnéticos, es decir, electrones desapareados. La espectroscopía de resonancia paramagnética electrónica (*electronic paramagnetic resonance*, EPR), también conocida como resonancia de spin electrónico, se basa en la cuantificación de la absorción de radiación electromagnética de microondas (frecuencia de $3{\cdot}10^8$-10^{11} Hz, longitud de onda entre 1 mm y 1 m) de sustancias que poseen átomos, iones o moléculas con electrones desapareados en presencia de un campo magnético externo. Teniendo en cuenta que el spin electrónico está cuantizado y solo puede adquirir valores de $s = \pm 1/2$, en presencia de un campo magnético se produce el desdoblamiento en dos niveles energéticos. La aplicación de la EPR permite la obtención de información sobre la presencia y tipo de radicales libres y birradicales, iones en estados paramagnéticos, o defectos estructurales en sólidos como las vacantes atómicas, entre otros (Figura 24) [1].

En esta tesis, se ha empleado un espectrómetro X-Band (9.4 GHz) Bruker ELEXSYS E500 usando una modulación de campo magnético con 2 G de amplitud, una modulación de frecuencia de 100 kHz, una constante de tiempo de 20.48 s y una potencia de irradiación de microondas de ~20 mW para:

- Detección de la presencia de átomos de Mo insaturados debido a la existencia de vacantes de S y Se en las nanoláminas de MoS_2 y $MoSe_2$, respectivamente, tratadas con hidracina.
- Detección de vacantes de S en las nanoláminas de MoS_2 funcionalizadas con ácido iodoacético.

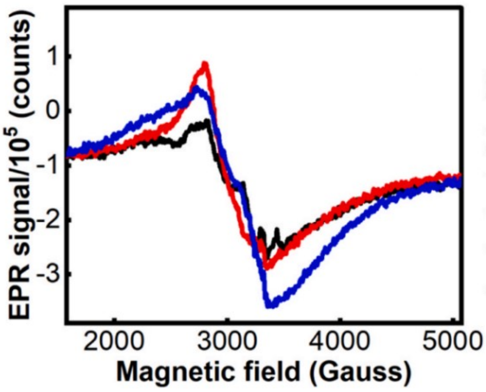

Figura 24. Espectro EPR del polvo *bulk* de $MoSe_2$ (línea negra) y de las nanoláminas de $MoSe_2$ exfoliadas mediante LPE sin vacantes (línea roja) y tras la generación de vacantes (línea azul).

Preparación de muestras

Se introdujo una cierta cantidad de material en polvo en el interior de un capilar muy fino, en los que se realizaron las medidas.

Dispersión de luz dinámica (DLS)

La dispersión dinámica de luz (*dynamic light scattering*, DLS) se basa en la dispersión de la luz por su interacción con partículas en suspensión. Por ello, es habitualmente empleada en la caracterización de la distribución de tamaños y medidas de coeficientes de difusión de partículas y macromoléculas coloidales. Cuando los fotones de un haz de luz visible inciden sobre las partículas de una dispersión coloidal, éstos son dispersados en todas las direcciones con un patrón de intensidad fluctuante debido al movimiento browniano de las partículas. El análisis de la señal fluctuante de la luz dispersada (íntimamente relacionada con el tamaño y difusividad de las partículas en suspensión) se transduce en una función de autocorrelación, que permite calcular el diámetro hidrodinámico de las partículas coloidales (Figura 25a y b). Este parámetro incluye tanto el tamaño de la partícula como el volumen de la esfera de solvatación, formada por moléculas de disolvente adsorbidas sobre su superficie [7].

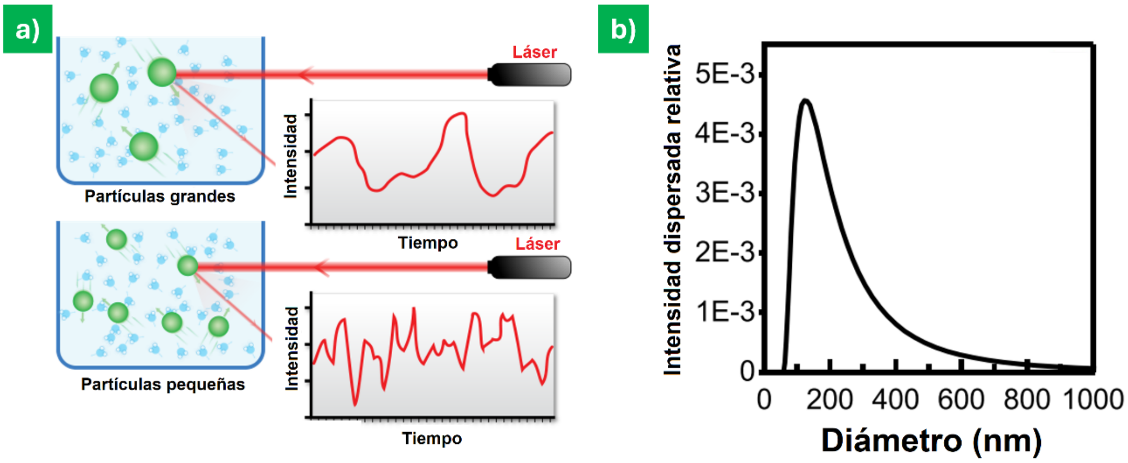

Figura 25. (a) Esquema de la fluctuación de la intensidad de la luz dispersada en función del tamaño de partícula. **(b)** Distribución del tamaño de partícula (obtenida del diámetro hidrodinámico) para una dispersión de nanoláminas de $MoSe_2$.

Determinación del potencial Zeta

Los espectrómetros de DLS actuales suelen permitir la determinación del potencial Zeta de las partículas coloidales, íntimamente relacionado con los fenómenos electrocinéticos que estas experimentan si poseen carga eléctrica. Para su medición, se introduce un cierto volumen de una dispersión coloidal en una cubeta específica equipada con dos electrodos de oro. La aplicación de un campo eléctrico entre ambos electrodos provoca el desplazamiento de las partículas cargadas hacia el electrodo de carga opuesta, con una velocidad de migración proporcional a la magnitud de su potencial Zeta. La movilidad de las partículas en función del potencial se puede determinar midiendo la variación de la fase o la frecuencia de un haz láser (anemometría láser Doppler) que incide sobre la celda. Cuando las partículas cargadas atraviesan el haz láser, la intensidad de la luz dispersada fluctúa con una frecuencia proporcional a la movilidad de las partículas, obteniéndose así su velocidad de migración para diferentes potenciales aplicados. La ecuación de Smoluchowski permite relacionar la movilidad de las partículas y la viscosidad del disolvente para calcular el potencial Zeta [8,9].

En esta tesis, se ha empleado un espectrómetro 3DDLS (LS Instruments), equipado con un láser de He-Ne laser de 632.8 nm (Artículo II); y un espectrómetro Litesizer DLS 500 (Anton Paar), equipado con un láser con longitud de onda de 658 nm (Artículo III), para:

- Medida del potencial zeta de las nanoláminas de MoS_2 funcionalizadas con ácido iodoacético, y de las nanoláminas de MoS_2 y $MoSe_2$ obtenidas mediante LPE.
- Determinación del diámetro hidrodinámico y del tamaño de partícula de las nanoláminas de MoS_2 y $MoSe_2$ obtenidas vía LPE (Figura 25b), y de las nanoláminas de MoS_2 exfoliadas catódicamente en fase orgánica.

Preparación de muestras

Para la medición del potencial Zeta, se introdujeron 600-800 µL de dispersión coloidal de nanoláminas (previamente transferida a agua) en celdas específicas para este análisis, que fueron introducidas en el respectivo instrumento.

4.2 Técnicas cromatográficas

Cromatografía líquida de ultra-alta eficacia de fase reversa acoplada a espectrometría de masas (RP-UHPLC/MS)

La cromatografía es una técnica analítica que persigue la separación física de los componentes (analitos) de una mezcla compleja. La cromatografía líquida de alta eficacia (*high-performance liquid chromatography*, HPLC) es un tipo de cromatografía que emplea una columna constituida por partículas de tamaño micrométrico como fase estacionaria (normalmente polar) y uno, varios disolventes o mezclas de ellos como fase móvil, que se inyecta a la columna bajo alta presión. La fase móvil contiene los diferentes analitos y permite su elución. La fase estacionaria actúa como adsorbente e interacciona con los analitos, que se desplazan por la columna a diferentes velocidades en función de la afinidad específica analito-fase estacionaria. Las diferentes velocidades permiten el análisis separado de cada uno de los analitos. La cromatografía líquida de ultra-alta eficacia (*ultrahigh-performance liquid chromatography*, UHPLC) sigue los mismos principios que la HPLC, pero el menor tamaño de partícula de las columnas y la mayor presión de inyección de la fase móvil conducen a una mejor eficiencia y tiempos reducidos de análisis. La UHPLC de fase reversa (*reverse-phase ultrahigh-performance liquid chromatography*, RP-UHPLC) emplea una fase estacionaria apolar y una fase móvil de polaridad moderada. Con este sistema, los analitos apolares o con fracción apolar muestran una mayor afinidad por la fase estacionaria, de modo que sus tiempos de retención serán mayores. Por el contrario, los analitos polares muestran una menor afinidad por la fase estacionaria y son eluidos antes. Bajo las condiciones apropiadas, los analitos llegan al detector secuencialmente y pueden ser detectados por diferentes medios, resolviéndose en bandas diferenciadas [10]. Cuando el detector es un espectrómetro de masas (*mass spectrometer*, MS), se obtiene la técnica acoplada RP-UHPLC/MS.

La MS es una técnica analítica que permite la separación y cuantificación de iones, en función de su relación masa/carga (m/z). La MS de alta resolución permite calcular la masa de los iones con suficiente exactitud como para determinar, si se detecta el ion molecular, la fórmula molecular del analito correspondiente [11]. La MS implica una primera etapa de vaporización e ionización para transformar los analitos en especies iónicas gaseosas. Dependiendo de la dureza del ionizador empleado, las moléculas analizadas pueden fragmentarse y dar lugar a varios iones, o solamente ionizarse. En una segunda etapa, los iones formados se separan en el analizador de masas en función de sus relaciones m/z específicas. Por último, los iones separados son registrados por un detector adecuado, generándose un espectro de masas (Figura 26). El uso de una fuente de ionización por electrospray (*electrospray ionization*, ESI) permite acoplar la HPLC con la MS. Para ello, se aplica un voltaje elevado (2.5-6 kV) a un capilar muy fino para generar un aerosol (electrospray) a partir de una disolución diluida que contenga los analitos de interés (en este caso, la fase móvil de la UHPLC). La evaporación de las moléculas de disolvente provoca un incremento de la carga de las gotas del electrospray, que eventualmente colapsan y liberan un flujo de iones cargados. Los iones en fase vapor pasan a continuación al analizador, habitualmente un cuadrupolo con tiempo de vuelo (*quadrupole-time of flying*, QTOF). El QTOF está formado por cuatro barras paralelas formando un cuadrupolo, una celda de colisión y una unidad de "tiempo de vuelo", donde los iones son acelerados y se separan en función de su relación m/z [12].

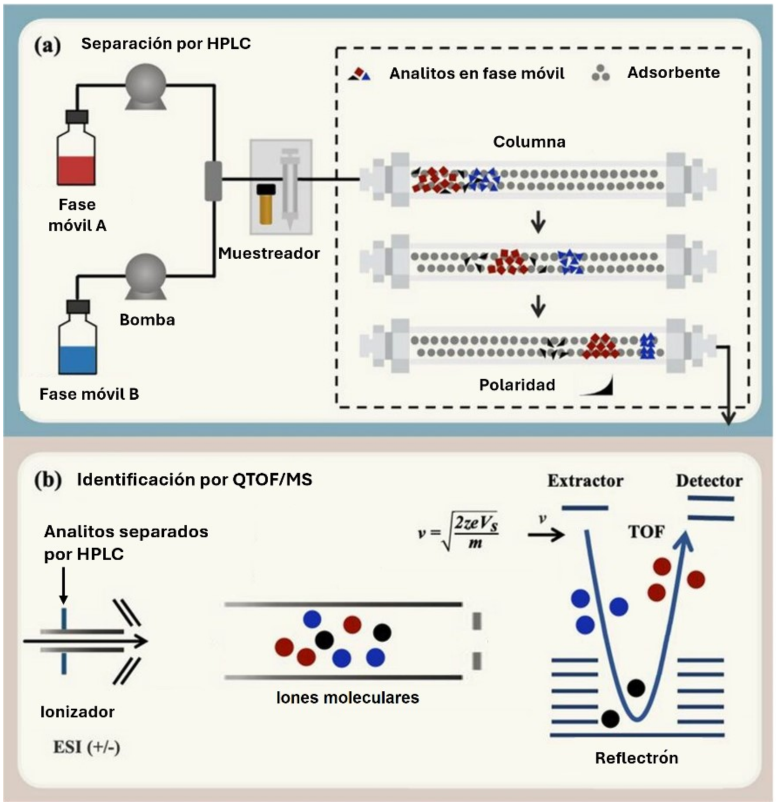

Figura 26. Esquema de la separación y determinación de compuestos mediante HPLC/MS. Adaptado de [13].

En esta tesis, se ha empleado un cromatógrafo de ultra-alta eficiencia de fase reversa (RP-UHPLC, sistema UltiMate™ Dionex 3000 HPLC de Thermo Scientific) acoplado a un espectrómetro de masas de alta resolución (HR-MS, equipo IMPACT II ESI-QTOF de Bruker), para la detección de los intermedios de reacción para la reducción catalítica de 3-NA.

Preparación de muestras

Se preparó el medio de reacción (2.5 mL) que contenía el sustrato, catalizador y $NaBH_4$. Un cierto tiempo después del inicio de la reacción, ésta se detuvo mediante la retirada del catalizador del medio por filtración usando una jeringa de filtración (membrana basada en alúmina, 0.02 µm, Whatman ® Anotop ®) que contenía cartuchos de extracción en fase sólida (HLB Oasis 250 cc, Waters). Los cartuchos fueron acondicionados previamente en agua ultrapura. Tras una etapa de lavado con agua, los analitos se eluyeron del cartucho usando metanol absoluto (6 mL, grado LC-MS, OPTIMA, *Thermo Fisher*) y se recogieron en un vial de vidrio. Inmediatamente después, se transfirieron 300 µL a viales de cromatografía líquida para su inyección en columna. Como fase estacionaria se empleó Luna Omegar Polar, y como fase móvil una mezcla de agua ultrapura y ACN con un 0.1% de ácido fórmico.

4.3 Microscopías

Microscopía electrónica de transmisión (TEM)

La microscopia óptica emplea un sistema de lentes ópticas y luz visible, que limita su resolución a 200 nm (límite de difracción) por la mínima longitud de onda del rango visible (λ=400 nm). Por el contrario, la microscopia electrónica emplea un haz de electrones acelerados con voltajes del orden de kV, que tienen una menor longitud de onda de *De Broglie* y permiten alcanzar una mayor resolución.

Un microscopio electrónico de transmisión (*transmisión electronic microscopy*, TEM) se basa en un sistema de lentes electromagnéticas en el que la muestra se ilumina por su cara anterior con un haz de electrones, formándose una primera imagen invertida en su parte posterior, donde un sistema de lentes proyectoras permite formar la imagen final aumentada (Figura 27a). Los electrones del haz, emitido por un cañón de electrones, son acelerados por la aplicación de un voltaje de 100-400 kV y enfocados sobre la muestra por un sistema de lentes condensadoras. Es necesario que el equipo opere en condiciones de baja presión ($\sim 10^{-4}$ Pa) para evitar fenómenos de dispersión electrónica por colisiones con moléculas de aire, siendo necesaria la incorporación de bombas de vacío en los microscopios TEM para producir una señal registrable. Cuando el haz electrónico incide sobre la muestra, una parte de los electrones la atraviesa sin interaccionar con ella, mientras que otros son absorbidos o dispersados. Tras su paso por la muestra, los electrones dispersados experimentan un fenómeno de difracción, y pueden ser focalizados gracias a la lente objetivo. A continuación, un sistema de lentes intermedias y proyectoras enfocan los electrones para formar una imagen aumentada, que es recogida por un detector digital. Generalmente, las lentes condensadoras, intermedias y proyectoras son electromagnéticas para poder dirigir el haz de electrones. A pesar de la resolución atómica de la microscopía TEM, la imagen formada está afectada por una serie de *aberraciones* o defectos de las lentes que disminuyen su calidad [1,14].

La microscopía electrónica de transmisión de alta resolución (*high-resolution trnasmission electron microscopy,* HR-TEM) es una modalidad especializada de imagen de la microscopía TEM que permite la visualización directa de estructuras atómicas (Figura 27b y c). En este caso, el contraste de la imagen se produce a través de la interferencia de fase de los electrones dispersados por la muestra consigo mismos, y permite alcanzar una mayor resolución en la imagen reconstruida [1,14].

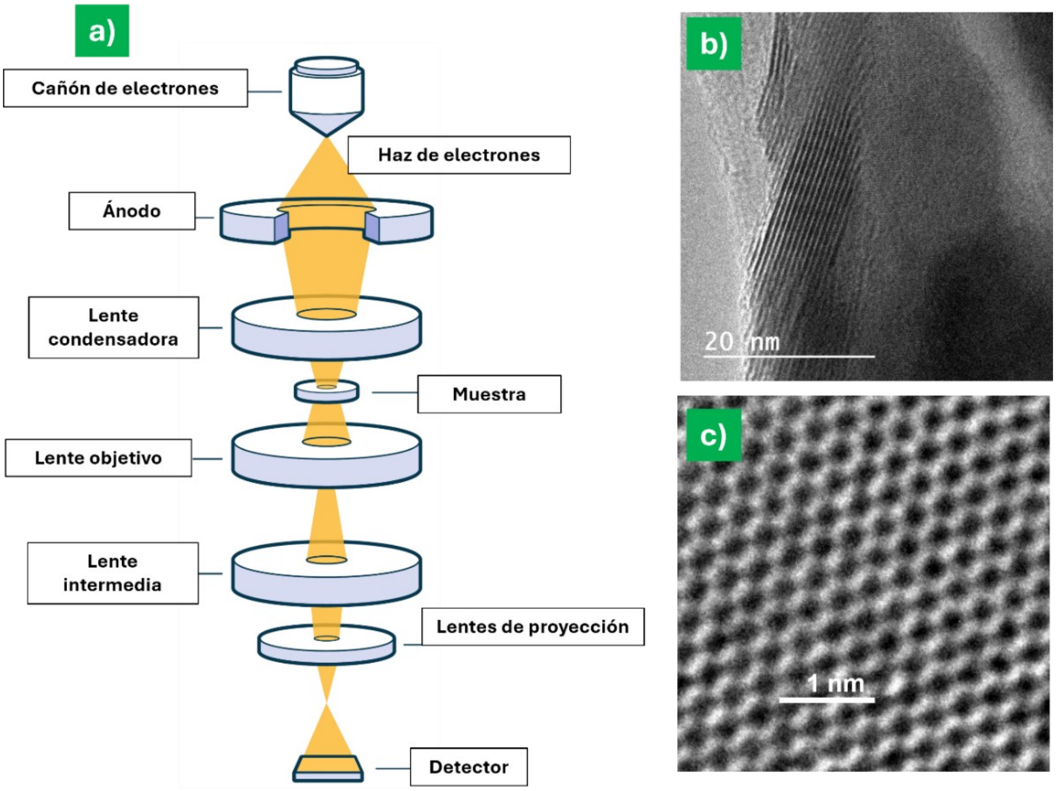

Figura 27. (a) Esquema del funcionamiento de un microscopio de transmisión. Imágenes de HR-TEM, a diferentes aumentos, de **(b)** nanoláminas de $MoSe_2$ preparadas por LPE y **(c)** nanoláminas de ee-MoS_2 preparadas mediante exfoliación catódica en medio orgánico.

Microscopía electrónica de transmisión con barrido (STEM)

Un microscopio electrónico de transmisión de barrido (*scanning transmisión electron microscopy*, STEM) es, en esencia, un microscopio electrónico de transmisión que incorpora un sistema de bobinas deflectoras que permiten realizar un barrido preciso del haz electrónico sobre la superficie de la muestra. En esta modalidad, los electrones no inciden paralelamente entre sí, como ocurre en TEM, sino que el haz electrónico se focaliza en un punto concreto de la muestra, atravesándola y generando una señal que se puede transformar en una imagen digital. Un equipo STEM permite la obtención de tres tipos de imágenes: imágenes de campo claro (*bright field*, BF); imágenes de campo oscuro (*dark field*, DF); o imágenes de campo oscuro anular de alto ángulo (*high angle anular dark field*, HAADF, Figura 28b y c) [1,14].

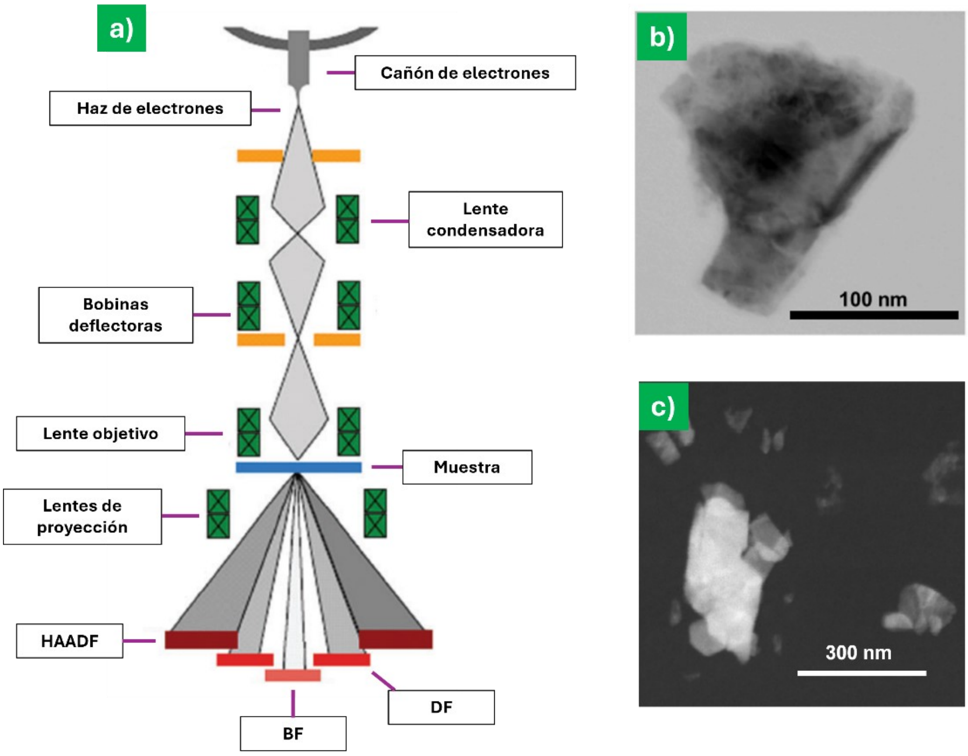

Figura 28. **(a)** Esquema del funcionamiento de un equipo STEM. Adaptado de [15]. Imagen HAADF de **(b)** una nanolámina de $MoSe_2$ y **(c)** una nanolámina de MoS_2, ambas preparadas mediante LPE.

Difracción de electrones de área seleccionada (SAED)

La difracción de electrones de área seleccionada (*selected area electron diffraction*, SAED) es una técnica muy extendida en cristalografía y generalmente realizada usando un TEM. Se basa en la detección del patrón de difracción resultante de la interacción de un haz de electrones acelerados, emitidos por la fuente del TEM, con los átomos de una superficie cristalina que actúan como una rejilla de difracción. Cuando se ilumina una muestra con un haz electrónico acelerado, una parte de los electrones atraviesan la muestra, mientras que otra es difractada en ángulos específicos por la red de átomos. Los electrones que atraviesan la muestra se cruzan justo en el eje óptico (punto brillante central de la Figura 29). Los electrones difractados se cruzan a cierta distancia del eje óptico (correspondiente a la distancia interplanar de los planos que difractan los haces) y bajo cierto ángulo (correspondiente a la orientación de los planos que difractan los haces). Esto permite formar un patrón de puntos brillantes típico de esta técnica que equivale a una proyección en dos dimensiones de la red cristalina en el espacio recíproco. El análisis del patrón de difracción obtenido posibilita la determinación de la orientación de los planos cristalográficos, los parámetros de red y la evaluación de los defectos estructurales de una muestra cristalina. La principal ventaja operativa de la SAED es que permite seleccionar, mediante una apertura controlada, la región específica que se quiere estudiar [14]. En esta tesis, la SAED se ha utilizado para confirmar la estructura cristalina de las nanoláminas de MoS_2 y $MoSe_2$ (Figura 29a y b).

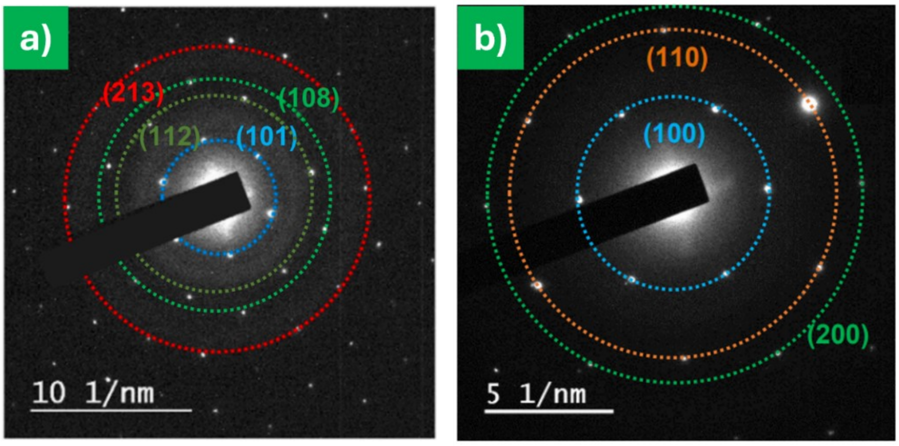

Figura 29. Patrón de SAED de **(a)** nanoláminas de $MoSe_2$ y **(b)** nanoláminas de MoS_2, ambas exfoliadas mediante LPE, incluyendo la familia de planos implicados en las difracciones.

Espectroscopia de dispersión de energía de rayos X (EDX)

En la espectroscopia de dispersión de energía de rayos X (*energy dispersive X-Ray*, EDX), la superficie de un material se irradia con un haz de electrones (si se irradiara con rayos X, la técnica sería fluorescencia de rayos X) lo suficientemente energéticos como para provocar la eyección de un electrón de una capa interna, generando así un hueco, tras lo que se producen una serie de fenómenos de relajación. Una posibilidad es que un electrón de un nivel energético superior ocupe la vacante electrónica generada en un nivel inferior, emitiendo la diferencia de energía entre ambos niveles en forma de un fotón de rayos X, cuya intensidad y energía puede ser medida por un espectrómetro de dispersión de energía. Como la diferencia de energía entre los niveles electrónicos es característica de cada elemento, es posible aplicar la EDX al análisis elemental [16]. En esta tesis, se ha empleado la EDX para el mapeo de los elementos principales de las nanoláminas de MoS_2 exfoliadas con KCl, de nanoláminas de MoS_2 y $MoSe_2$ preparadas por LPE (Figura 30) y de las nanoláminas de MoS_2 exfoliadas con HTMABr.

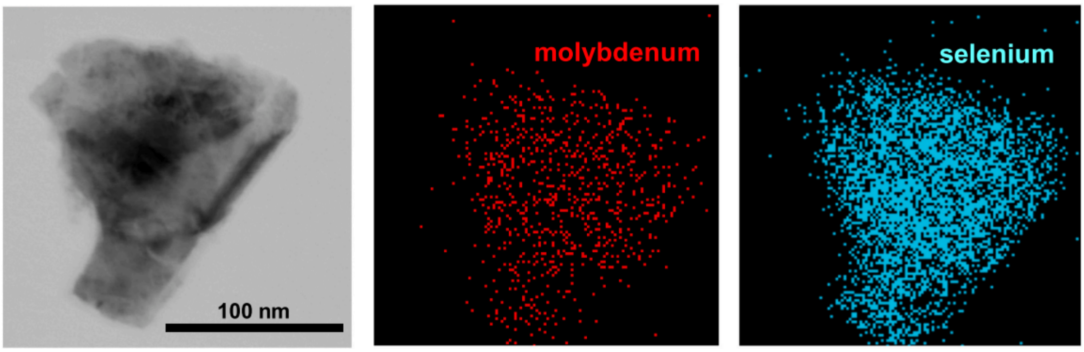

Figura 30. Mapeo EDX **(derecha)** para la determinación elemental de Mo (rojo) y Se (azul) de la correspondiente nanolámina de $MoSe_2$ **(izquierda)** obtenida mediante LPE.

Para la realización de esta tesis, las imágenes de HR-TEM, STEM, SAED y EDX se han tomado con un equipo JEOL JEM-2100 F usando un voltaje de aceleración de 200 kV, equipado con una unidad de control (Gatan) de STEM, un detector de EDX (Oxford Instruments) con un detector de deriva de silicio de 80 mm^2, una cámara CCD (Gatan Orius SC600 de 14 bits) detectores HAADF. En esta tesis, la HR-TEM se ha empleado para:

- Determinación del tipo de simetría de los átomos y de los parámetros de red de las nanoláminas de MoS_2 y $MoSe_2$ preparadas por LPE, y de las nanoláminas de MoS_2 preparadas por EE en fase orgánica.
- Confirmación de la naturaleza multicapa de las nanoláminas.
- Estudio de la morfología, calidad estructural y presencia de defectos superficiales de las nanoláminas.

Preparación de muestras

Para adquirir las imágenes HR-TEM y EDX de las nanoláminas de MoS_2 y $MoSe_2$ preparados por LPE y de ee-MoS_2 preparadas por EE con HTMABr, respectivamente, se depositó un pequeño volumen (~7 µL) de la correspondiente dispersión en agua en una rejilla de cobre (200 *square mesh*) recubierta por un filme de *lacey carbon*. La rejilla se dejó secar a temperatura ambiente tapada por un pequeño embudo.

Para adquirir las imágenes STEM de las nanoláminas de MoS_2 y $MoSe_2$ preparadas por LPE y de ee-MoS_2 preparado por EE, respectivamente, se depositó un pequeño volumen (~7 µL) de dispersión en agua sobre una rejilla de cobre (200 *square mesh*) recubierta por un filme de carbono continuo, y se dejó secar a temperatura ambiente tapado por un pequeño embudo.

Microscopía electrónica de barrido (SEM)

La microscopia electrónica de barrido (*scanning electron microscopy*, SEM) se basa en un sistema de lentes electromagnéticas de reflexión, en el que la muestra se ilumina frontalmente por un haz de electrones, siendo los electrones reflejados los que forman la imagen. El haz electrónico generado por el cañón de electrones es acelerado (20-40 kV) y concentrado gracias a unas lentes electromagnéticas, para ser enfocado y barrido a lo largo de la superficie de la muestra por unas bobinas de barrido. Simultáneamente al barrido, un detector cuantifica el número de electrones secundarios de baja energía que son emitidos por cada punto de la superficie de la muestra, formando así la imagen digital (Figura 31a) [1].

Dependiendo del tipo de interacción entre los electrones emitidos y la superficie de la muestra, pueden ocurrir varios fenómenos [1,16]:

- Emisión de electrones secundarios: son electrones de baja energía emitidos por la muestra a causa de su ionización, producida por las colisiones inelásticas con los electrones del haz incidente. Solamente pueden ser detectados los electrones secundarios generados en las capas más superficiales, puesto que los internos son reabsorbidos por colisiones inelásticas con átomos adyacentes. Por tanto, son los electrones secundarios los que perfilan las características superficiales de la muestra, proporcionando contraste topográfico.
- Emisión de electrones retrodispersados: los electrones retrodispersados son electrones del haz incidente que son dispersados tras colisionar elásticamente con los átomos de la muestra y, por tanto, tienen energías de su mismo orden. Estos electrones provienen de profundidades mayores que los secundarios y, al ser emitidos por un volumen de muestra grande (no sólo por la superficie), el contraste lateral disminuye. Como los átomos más pesados tienen mayor probabilidad de retrodispersar electrones, los electrones retrodispersados proporcionan contraste composicional.

- Emisión de fotones de rayos X: consiste en la emisión de fotones de rayos X con energía y longitud de onda característicos de los átomos emisores, al producirse procesos de relajación tras la expulsión de electrones de capas internas, en un mecanismo idéntico al descrito para EDX.

Cuando en el microscopio SEM se puede acoplar un detector de electrones debajo de la muestra, y la muestra es lo suficientemente delgada para permitir la transmisión de los electrones, es posible registrar imágenes mediante STEM. Otra modificación del SEM consiste en la incorporación de una fuente de emisión de campo como fuente de electrones (*field-emission scanning electron microscopy*, FE-SEM), que proporciona haces de electrones de alta y baja energía muy focalizados. El FE-SEM mejora considerablemente la resolución de la técnica y permite trabajar a bajos potenciales (0.02 – 5 kV).

La microscopia SEM es muy flexible en términos de rango de escala, permitiendo aumentos desde 10× hasta 10^5×. Esto quiere decir que el rango observado puede estar desde en el rango de 1 mm^2 como sólo 1 μm^2, siendo la única microscopía que permite una escala de medida tan flexible. Asimismo, el SEM es la microscopía con mayor profundidad de campo, pudiendo realizarse enfoques simultáneos a diferentes profundidades. Estas características hacen que sea una técnica ampliamente utilizada para el estudio de la morfología de una gran cantidad de materiales [17].

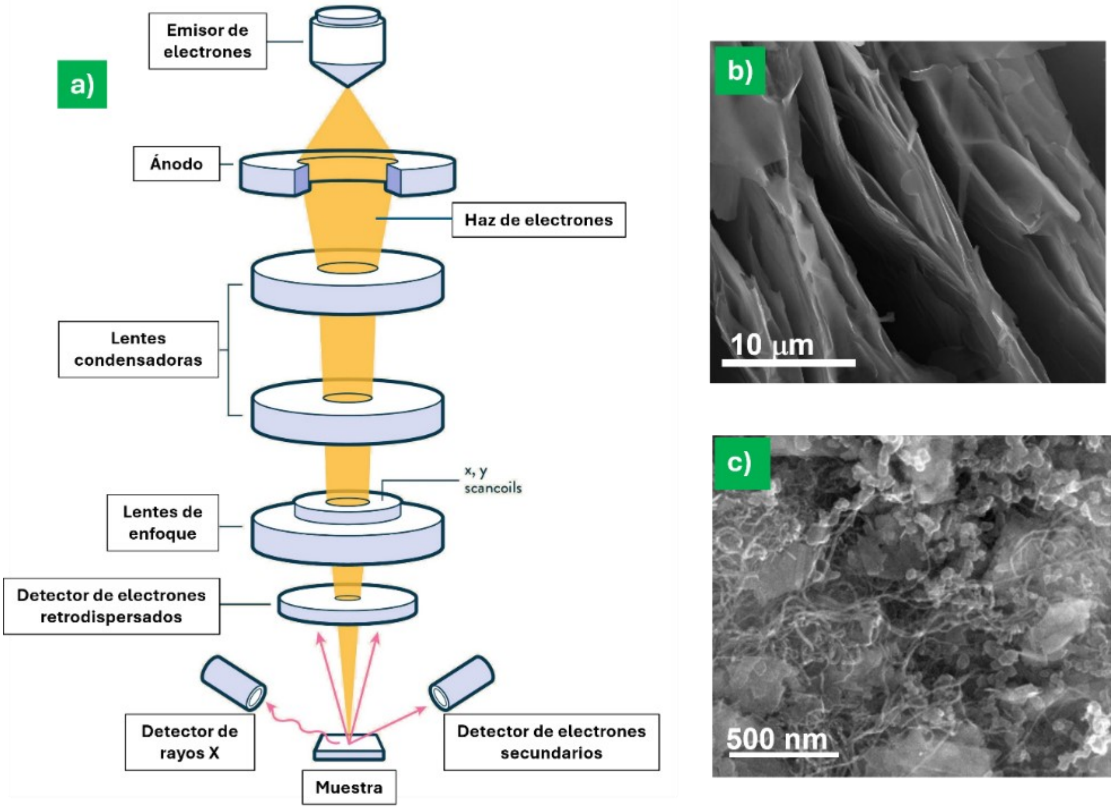

Figura 31. **(a)** Esquema del funcionamiento de un microscopio SEM. **(b)** Imagen SEM de MoS_2 expandido en medio orgánico. **(c)** Imagen FE-SEM de un electrodo inicial de $MoSe_2$.

En esta tesis, las medidas de FE-SEM y STEM se han realizado usando un instrumento Quanta FEG (FEI Company) a un voltaje de trabajo de 20-25 kV, para:

- Estudiar la morfología y dimensiones de las nanoláminas de MoS_2 preparadas por EE en fase orgánica; y de las nanoláminas de MoS_2 y $MoSe_2$ preparadas por LPE.
- Estudio de la morfología y dimensiones del cátodo de MoS_2 expandido tras el tratamiento catódico en fase acuosa y orgánica (Figura 31b y c), respectivamente.
- Estudio de la adsorción de las nanoláminas de MoS_2 funcionalizado con ácido iodoacético y de $MoSe_2$ preparado por LPE sobre esponjas.

Preparación de muestras

Para adquirir las imágenes FE-SEM de las esponjas de melamina y poliuretano con nanoláminas inmovilizadas de $MoSe_2$ y MoS_2 funcionalizado, respectivamente, éstas se adhirieron a los portamuestras (chinchetas) con cinta adhesiva de carbono de doble cara. Las imágenes FE-SEM de los cristales de MoS_2 expandido electroquímicamente se tomaron de la misma forma.

Microscopía de fuerza atómica (AFM)

Se denominan microscopias de proximidad a aquellas técnicas microscópicas que permiten la obtención de imágenes gracias al registro de las interacciones existentes entre la superficie de una muestra y los átomos de una punta (o sonda) que se encuentran a distancias nanométricas. La naturaleza e intensidad de la interacción punta-muestra dependen significativamente de la distancia entre ambas, y la incorporación de un sistema de retroalimentación permite mantener una separación adecuada entre ellas. De esta manera, la punta puede realizar barridos sobre la muestra para obtener un mapa topográfico de su superficie.

La microscopia de fuerza atómica (*atomic force microscopy*, AFM) registra las interacciones (atractivas o repulsivas) que aparecen entre los átomos de la superficie de una muestra y los átomos de una sonda (punta) en función de la distancia que los separa. Para ello, la punta se encuentra situada al final de una micropalanca flexible (cantiléver), situada perpendicularmente a la superficie de la muestra, y que puede deflexionar verticalmente cuando interacciona con los átomos superficiales del material. Sobre el cantiléver se hace incidir un haz láser que se refleja, a su vez, sobre un fotodetector dividido en cuatro secciones (Figura 32a). De esta forma, la punta del cantiléver puede realizar barridos sobre la superficie de la muestra, y las deflexiones del cantiléver por la interacción entre su punta y los átomos superficiales pueden registrarse para obtener mapas topográficos de alta resolución [18].

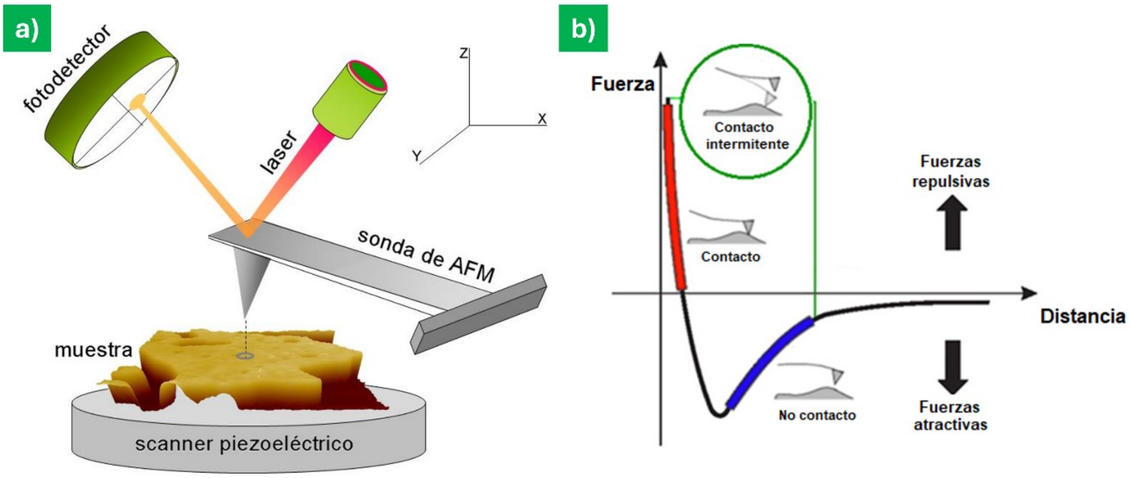

Figura 32. (a) Esquema de operación de un microscopio AFM. **(b)** Perfil típico de la interacción punta-muestra en función de la distancia de separación. Adaptado de [19].

Dependiendo de la distancia que exista entre los átomos de la superficie de la muestra y los átomos de la punta del cantiléver, las interacciones entre ellos pueden ser repulsivas (si la distancia es demasiado pequeña) o atractivas (cuando la distancia es algo mayor) (Figura 32b). Dependiendo del tipo de interacción, el AFM puede trabajar en tres modos [20]:

- Modo de contacto: la punta del cantiléver se mantiene a menos de 2 Å de la superficie de la muestra, y las interacciones entre los átomos son repulsivas. La señal de la interacción se registra por deflexiones verticales del cantiléver según la topografía de la muestra.
- Modo de no contacto: la punta del cantiléver se sitúa a aproximadamente 1 nm de la superficie de la muestra, de tal forma que las interacciones entre los átomos sean atractivas. La señal de la interacción registrada se corresponde con flexiones verticales de la punta por la atracción de los átomos superficiales.
- Contacto intermitente o *tapping*: el cantiléver oscila vertical y periódicamente a ~10 nm sobre la superficie de la muestra, registrándose la variación de la frecuencia de oscilación para generar imágenes en función de la topografía. La amplitud de la oscilación (~100-200 nm) se ajusta aplicando un potencial eléctrico a un material piezoeléctrico situado en el extremo del cantiléver. Cuando la distancia entre la punta y la superficie es inferior a la amplitud de la oscilación del cantiléver, ésta disminuye. Manteniendo constante la frecuencia de la oscilación y registrando sus variaciones durante el barrido de la superficie, es posible realizar mapas topográficos de la superficie de la muestra de manera muy poco invasiva, permitiendo la medida de objetos de escala nanométrica sobre la superficie sin alterarlos.

A diferencia de las microscopías TEM y SEM, la AFM posee una gran resolución (de pocos Å) en la dirección perpendicular a la superficie de muestra, lo que permite determinar el espesor, número de capas, tamaño lateral y morfología de las nanoláminas 2D depositadas sobre superficies atómicamente planas. La gran inespecificidad de las interacciones punta-superficie que producen una deformación medible del cantiléver (y, por tanto, una señal medible en AFM) permite aplicar esta técnica para el análisis de la superficie de casi cualquier material.

En esta tesis se ha utilizado un microscopio Nanoscope IIIa Multimode de VEEo Instruments (Artículo I y III), utilizando cantilévers de silicio de constante de fuerza ~40

N m^{-1} y frecuencia de resonancia ~250–300 kHz (Bruker Corporation); y un microscopio Nanoscope-IIIa multimodo (Veeco Instruments) en modo *tapping* (Artículo II). Las imágenes se han procesado usando el software SPIP (Image Metrology). La microscopía de AFM se ha empleado para la determinación de la morfología, dimensiones laterales y grosores y elaboración de histogramas de: nanoláminas de MoS_2 preparadas por EE en fase acuosa y funcionalizadas con ácido iodoacético (Figura 33a); nanoláminas de MoS_2 preparadas por EE en fase orgánica (Figura 33b); y de las nanoláminas de MoS_2 y $MoSe_2$ preparadas mediante LPE.

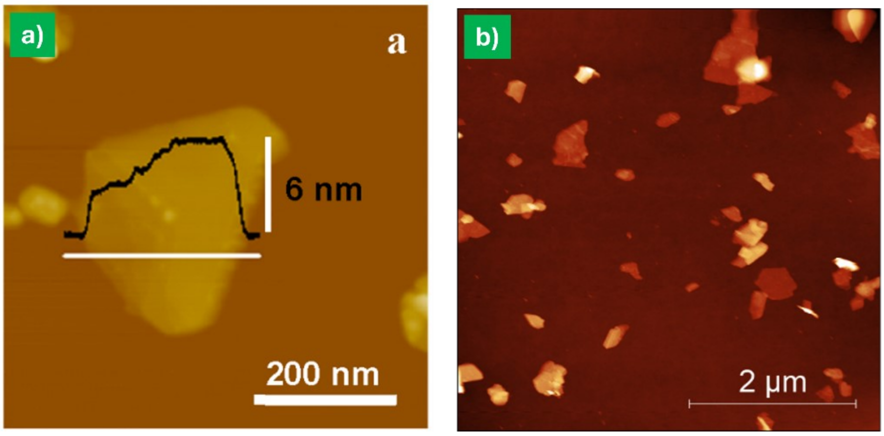

Figura 33. Imágenes de AFM de **(a)** una nanolámina de MoS_2 preparada mediante EE con KCl y **(b)** nanoláminas de ee-MoS_2, preparado mediante EE con HTMABr.

Preparación de muestras

Para la toma de imágenes de AFM de las nanoláminas de MoS_2 exfoliadas con KCl y funcionalizadas con ácido iodoacético, se depositó un pequeño volumen (~10 µL) de una dispersión de MoS_2 en IPA (~0.03 mg·mL^{-1}) sobre HOPG, que se dejó secar a temperatura ambiente y posteriormente en condiciones de vacío.

Para la toma de imágenes de AFM de las nanoláminas de MoS_2 y $MoSe_2$ preparadas por LPE y de las nanoláminas de MoS_2 preparadas por EE con HTMABr, éstas se redispersaron en isopropanol (~0.01 mg·mL^{-1}), se depositó un volumen de 20 µL sobre un soporte de Si/SiO_2 de 2000 nm (cuya superficie había sido lavada previamente por sonicación en acetona/IPA durante 5 minutos) y se dejó durante 16 h en condiciones de vacío a 60 ºC.

4.4 Técnicas electroquímicas

Todas las medidas electroquímicas realizadas en esta tesis se han realizado utilizando un potenciostato *BioLogic-VMP3* multicanal en una habitación termostatizada a 25 ºC.

Potencial de circuito abierto (OCV)

El potencial de circuito abierto (*open circuit voltage*, OCV) es la diferencia de voltaje medible en la celda electroquímica cuando no se le aplica ningún potencial ni intensidad de corriente al WE. Generalmente, esta técnica se utiliza como etapa de preacondicionamiento o para asegurar que la celda electroquímica se encuentre en estado de equilibrio. El valor del OCV depende del material de electrodo, resistencia interna de la celda, del electrolito, temperatura y la polarización de los electrodos.

En esta tesis, se han registrado medidas de OCV durante 4-6 h en todas las pilas de botón preparadas para estimar cualitativamente su estado inicial y asegurar una buena impregnación de electrolito de los separadores de fibra de vidrio.

Voltamperometría cíclica (CV)

La voltametría o voltamperometría es una técnica electroanalítica que constituye la base del análisis electroquímico. Debido a su versatilidad y a la sencilla regulación de sus parámetros experimentales, permite estudiar procesos de oxidación-reducción, de adsorción de especies electroactivas sobre superficies, de intercalación iónica, procesos (electro)catalíticos o cinéticas de reacción, entre otros. Se fundamenta en el registro de la intensidad de corriente (I) generada por la aplicación de un potencial controlado (V), que varía con el tiempo, a un WE en contacto con un electrolito adecuado. La relación entre el potencial aplicado por unidad de tiempo se denomina velocidad de barrido (v), y es un parámetro crucial en el estudio las propiedades de los sistemas electroquímicos. Según el tipo de dependencia del potencial eléctrico aplicado con el tiempo, la voltamperometría puede ser de barrido lineal (*linear sweep voltammetry,* LSV), si el potencial aplicado realiza un barrido creciente o decreciente (Figura 34a); y cíclica (*cyclic voltammetry*, CV), si se realizan ciclos de barridos en ambos sentidos de manera periódica (Figura 34b). La representación de I (eje Y) frente a V (eje X) forma el diagrama conocido como voltamograma o voltamperograma [21].

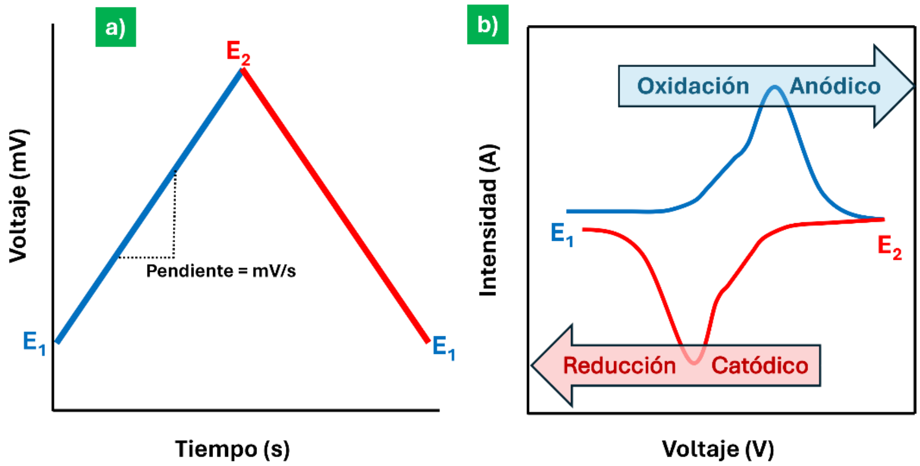

Figura 34. (a) Representación del barrido lineal de potencial frente al tiempo empleado en CV. **(b)** Esquema de un voltamograma típico, indicando las reacciones que ocurren en función del potencial aplicado.

La naturaleza química, estructura interna y la morfología superficial de los materiales determinan el tipo de procesos que ocurren en la interfase electrodo-electrolito. Por tanto, los procesos electroquímicos se pueden clasifican como [22]:

- **Faradaicos**: son procesos que obedecen la primera Ley de Faraday, que indica que la masa depositada o liberada en un electrodo sigue una relación de proporcionalidad directa con la carga suministrada [23], y necesariamente implican una transferencia de carga en la interfase del electrodo. Los procesos faradaicos se clasifican en reacciones de adsorción/desorción de iones, intercalación/desintercalación de iones y reacciones redox reversibles. Los procesos de naturaleza faradaica están limitados por la difusión de las especies electroactivas hasta la superficie del electrodo, son cinéticamente más lentos y suelen incluir reacciones de conversión y de cambio de fase. Es el mecanismo de almacenamiento típico de las baterías.
- **No faradaicos o capacitivos**: son procesos que no obedecen la Ley de Faraday al no implicar una reacción de conversión o transferencia electrónica, y no están limitados por la difusión de la especie electroactiva. La acumulación de iones en una interfase electrificada para formar una doble capa eléctrica (*electric double layer*, EDL) es un ejemplo de un proceso capacitivo altamente reversible. Sustentan el mecanismo de almacenamiento de energía de los condensadores tradicionales y de los condensadores de doble capa eléctrica (*electric double layer capacitor*, EDLC), por ejemplo.

- **Pseudocapacitivos**: muestran un mecanismo mixto entre procesos faradaicos y de doble capa. Son, en esencia, procesos de naturaleza faradaica cuya cinética se ajusta a las ecuaciones descritas para los procesos puramente capacitivos. Así, los materiales pseudocapacitivos muestran una relación (pseudo)lineal entre el potencial aplicado y su estado de carga, una elevada reversibilidad electroquímica y no están limitados por difusión.

La CV es una herramienta muy útil para la obtención de información cualitativa sobre el mecanismo de almacenamiento de energía de un material y de su estructura y morfología interna (Figura 35):

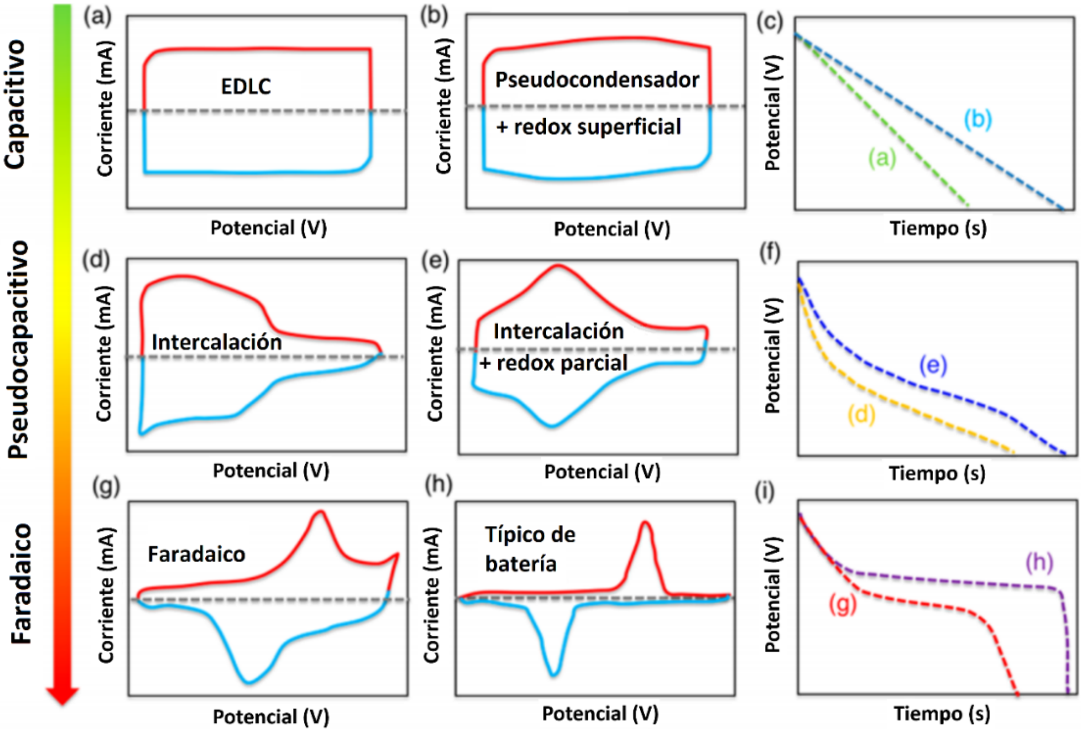

Figura 35. (a, b, d, e, g, h) Voltamogramas cíclicos de materiales con diferentes mecanismos de almacenamiento de energía y **(c, f, i)** dependencia del potencial eléctrico vs tiempo en función del tipo de almacenamiento de energía. Adaptado de [22].

En esta tesis, se ha utilizado la CV para:

- Evaluación del comportamiento electroquímico de los electrodos preparados con nanoláminas de MoS_2 exfoliadas catódicamente con KCl y HTMBr, respectivamente, y con nanoláminas de MoS_2 exfoliado mediante LPE.
- Evaluación del comportamiento cinético de los electrodos de MoS_2 exfoliado con HTMABr, aplicando el método de Dunn.

Método de Dunn

El método de Dunn permite separar la contribución de los procesos faradaicos (controlados por difusión) y capacitivos (no controlados por difusión) de un material, usando la información contenida en voltamperogramas cíclicos obtenidos a diferentes velocidades de barrido (generalmente 0.1-10 mV/s) [24]. Para ello, se asume la carga total almacenada (q_T) de un sistema como la suma de la contribución capacitiva (q_C) y faradaica (q_F):

$$q_T = q_C + q_F$$

Los datos de los CVs se analizan suponiendo que la intensidad de corriente obedece la relación:

$$I = a \cdot v^b$$

Donde *a* y *b* son parámetros experimentales ajustables. Existen dos condiciones bien definidas para los valores de *b*. Cuando b=0.5 el proceso está controlado por difusión [21], mientras que si b=1 el proceso es de naturaleza capacitiva [25]. Para evaluar si un pico redox está controlado por difusión, basta con obtener los valores de *b* de la representación lineal de *log I* vs *log v* de los distintos CVs, al potencial de interés (Figura 36):

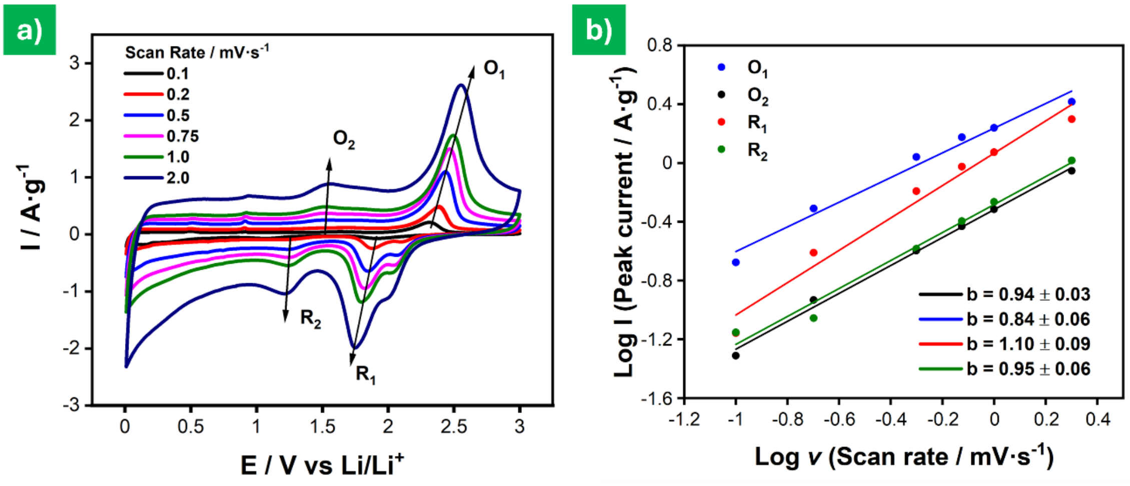

Figura 36. (a) Principales picos redox de un electrodo de MoS_2, registrados por CV a diferentes velocidades de barrido. **(b)** Valores de *b* calculados aplicando el método de Dunn, a partir de los datos de (a).

Análogamente, la intensidad de corriente total medida en la CV en función de la velocidad de barrido (*I(v)*) puede expresarse como la suma de la intensidad de corriente debida a procesos capacitivos (I_C) y faradaicos (I_F):

$$I(v) = I_C + I_F = k_1 \cdot v + k_2 \cdot v^{\frac{1}{2}}$$

Y, reorganizando términos:

$$\frac{I(v)}{v^{1/2}} = k_1 \cdot v^{1/2} + k_2$$

Si se registran CVs a diferentes velocidades de barrido, se correlacionan los diferentes valores de *I(v)* para un potencial fijo y se representa $I(v)/v^{1/2}$ vs $v^{1/2}$, es posible determinar gráficamente los valores de K_1 y K_2. Cuando este procedimiento se repite para todos los valores de potencial, es posible separar las contribuciones de los procesos capacitivos y faradaicos de un CV completo (Figura 37) [24]:

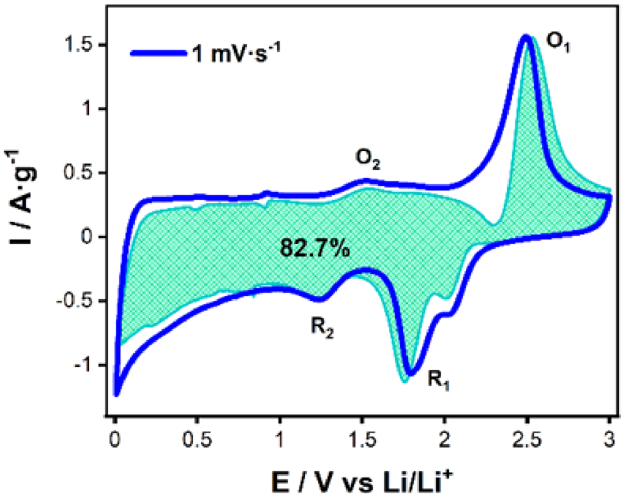

Figura 37. Ejemplos de la proporción de contribución faradaica (no sombreado) y pseudocapacitiva (sombreado) para un electrodo de MoS_2, registradas a 1 mV·s^{-1}.

Espectroscopia de impedancia electroquímica (EIS)

La resistencia eléctrica, definida por la ley de Ohm como la razón del potencial aplicado frente a la corriente medida, se limita a un resistor ideal por el que circula una corriente continua independiente de la frecuencia y sin fase. Sin embargo, en sistemas complejos, se emplea el término de impedancia (Z), que incluye la fase de la señal y permite extender el concepto de resistencia a circuitos de corriente alterna y semiconductores. La espectroscopia de impedancia electroquímica (*electrochemical* *impedance spectroscopy*, EIS) mide la Z mediante la aplicación, a una celda electroquímica, de un potencial que varía sinusoidalmente en un cierto rango de frecuencias (habitualmente 1 mHz-100 kHz) para registrar la corriente alterna producida. Generalmente, se emplean señales de excitación pequeñas para mantener la (pseudo)linealidad del sistema, ya que en estos casos el potencial sinusoidal aplicado y la corriente sinusoidal generada mantienen la misma frecuencia *f*, pero distinta fase *Φ* (Figura 38) [26].

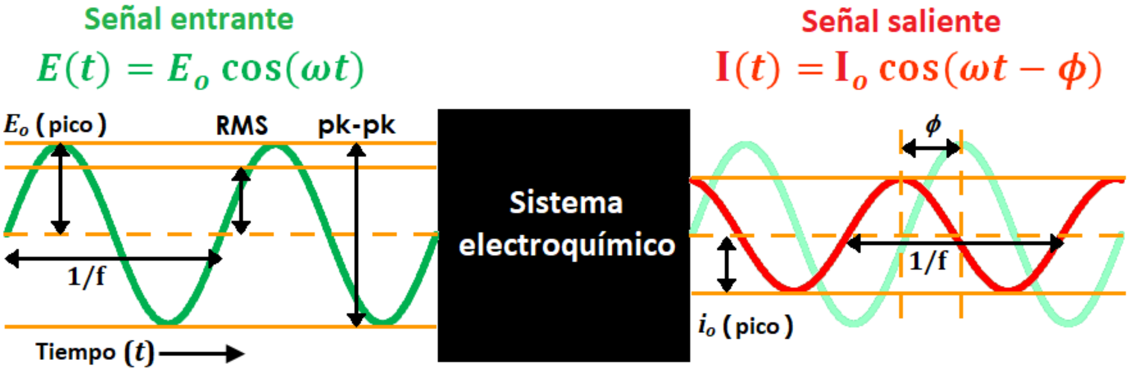

Figura 38. Esquema del mecanismo de perturbación sinusoidal de un sistema electroquímico para la medición de impedancia.

Generalmente, los cambios de impedancia en un sistema electroquímico pueden deberse a procesos de transferencia de carga en la superficie de un electrodo, cambios en su morfología, difusión iónica o adsorción de especies cargadas, y dependen del valor de frecuencia al que se aplica el potencial sinusoidal. Las formas más habituales de presentar los resultados de impedancia son los diagramas de Nyquist y de Bode. Los diagramas de Nyquist son los más comunes y representan la parte real de la impedancia (Z' o Z_{re}) en el eje X frente a la parte imaginaria cambiada de signo (-Z" o $-Z_{im}$) en el eje Y. De ellos se puede obtener información cualitativa de los procesos implicados (Figura 39a y b) [27].

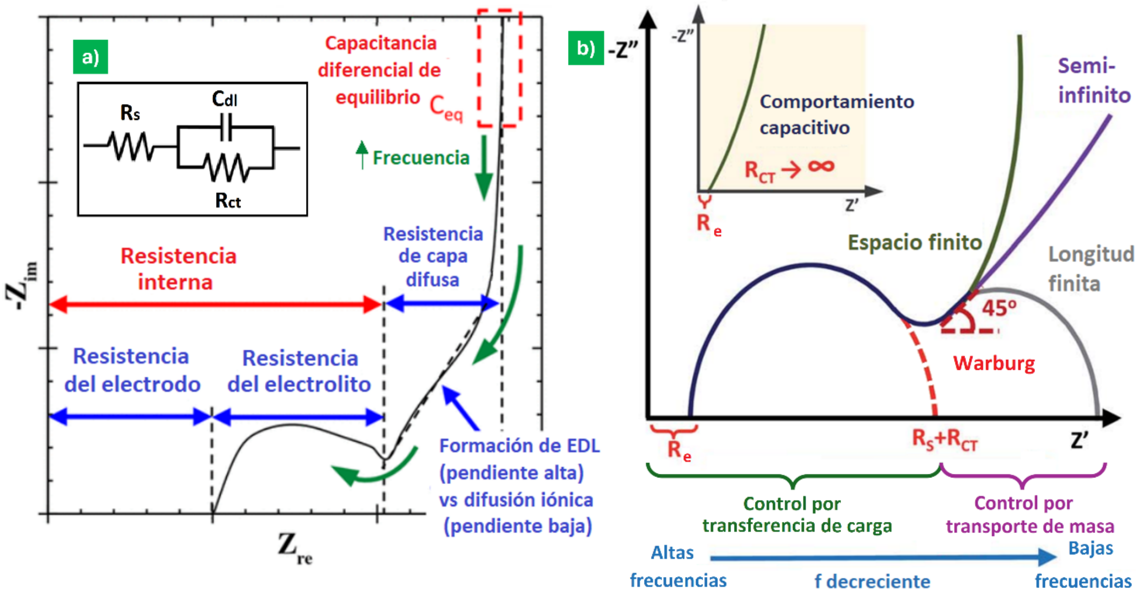

Figura 39. Diagrama de Nyquist que muestra **(a)** la correlación entre la Z medida y los fenómenos físicos de los que depende, y un ejemplo de circuito equivalente (*inset*). **(b)** Relación entre la Z de un sistema y el tipo de mecanismo de almacenamiento de carga.

Semicuantitativamente y de manera simplificada, se puede obtener la siguiente información de un diagrama de Nyquist [27]:

- **Resistencia del electrodo (R_e)**: se corresponde con el primer valor de impedancia real (Z_{re}) del diagrama de Nyquist.
- **Resistencia del electrolito (R_s)**: se corresponde con el diámetro del primer semicírculo del diagrama de Nyquist. Incluye la resistencia a la transferencia de carga (*resistance to charge transfer*, R_{CT}, procesos de interfase electrodo-disolución) y de masa (difusión de iones), y la capacitancia de la EDL. La existencia de varios semicírculos implica contribuciones independientes a la impedancia.
- **Elemento Warburg**: caracterizado por una línea oblicua de aproximadamente 45º. Representa el inicio de la región controlada por difusión. El Warburg de espacio finito, paralelo al eje Z”, se interpreta como capacitancia pura. Por el contrario, el Warburg de longitud finita indica resistividad pura. El Warburg seminfinito, por tanto, representa un comportamiento controlado por transferencia de masa con contribuciones de la transferencia de carga.

Adicionalmente, los procesos electroquímicos implicados en la generación de impedancia pueden ser representados por los elementos característicos de los circuitos de corriente alterna. Esta representación se conoce como circuito equivalente, y permite esquematizar la estructura general de los procesos electroquímicos en circuitos simplificados (Figura 39a, *inset*) [27].

En esta tesis, se ha empleado la EIS para la caracterización de los electrodos preparados a partir de nanoláminas de MoS_2 exfoliadas catódicamente con HTMABr, en distintos momentos del ciclado, y para la representación de circuitos equivalentes.

Carga-descarga galvanostática (GCD) con limitación de potencial

Una curva de carga/descarga galvanostática (*galvanostatic charge/discharge*, GCD) representa la variación de potencial de una celda electroquímica como consecuencia de la aplicación de una intensidad de corriente constante (normalmente entre 0.1 y 20 $A \cdot g^{-1}$) al WE. La limitación externa de potencial (impuesta y controlada desde el potenciostato) asegura que el rango de potencial sea el óptimo para el funcionamiento del dispositivo electroquímico, evitando así la descomposición del electrolito, reacciones secundarias innecesarias o pérdidas por polarización óhmica, entre otras. Generalmente, la reacción de descarga implica una disminución del potencial de celda registrado, mientras que la carga conlleva un incremento de este. Dependiendo del mecanismo de almacenamiento de energía del material (capacitivo, pseudocapacitivo o faradaico) las curvas de carga/descarga de los materiales presentan diferentes perfiles (Figura 40).

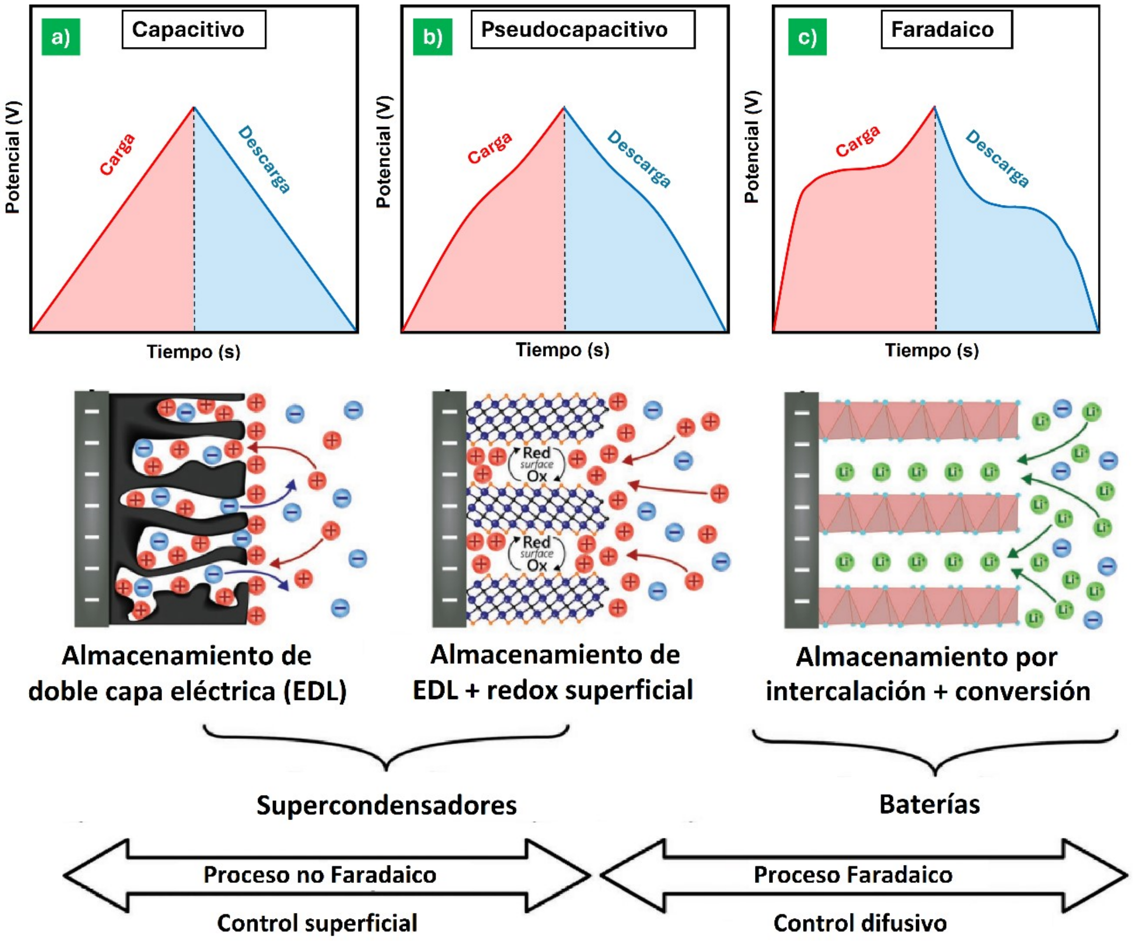

Figura 40. Diferentes perfiles de curvas GCD según el mecanismo de almacenamiento de energía (indicado debajo). Adaptado de [28].

La cantidad de energía eléctrica que puede almacenar o liberar un material en cada ciclo de carga/descarga se denomina *capacidad* (Q, expresada en mA·h), si el material es principalmente faradaico o pseudocapacitivo; o *capacitancia* (C, expresada en F), si el material es principalmente capacitivo. Es habitual emplear C indistintamente para capacidad y capacitancia, y sus valores se suelen expresar normalizados respecto de la masa del electrodo de trabajo (en semipilas) o del promedio de la masa de ambos electrodos (en pilas completas).

$$Q\ (mA \cdot h \cdot g^{-1}) = \frac{1}{m_T} \int_{t_i}^{t_f} I \cdot dt = \frac{\left(t_f - t_i\right) \cdot I_{aplicada}}{m_T}$$

$$C\ (F \cdot g^{-1}) = \frac{I}{m_T} \int_{t_i}^{t_f} \frac{I \cdot dt}{V(t)} = \frac{\left(t_f - t_i\right) \cdot I_{aplicada}}{\left(|V_f - V_i|\right) \cdot m_T}$$

Donde m_T es la masa total de material electroactivo; t_f y t_i son los tiempos de finales e iniciales de cada carga/descarga, respectivamente; $I_{aplicada}$ es la intensidad de corriente constante que se suministra a la celda en cada ciclo; y $|V_f - V_i|$ es la ventana de potencial en la que se almacena la carga [28]. La eficiencia coulómbica (EC) es un parámetro ampliamente utilizado para estimar la reversibilidad y la ciclabilidad de los sistemas electroquímicos. En una semipila, la EC se expresa como el porcentaje del cociente entre la capacidad o capacitancia de cada ciclo de carga/descarga, respectivamente [29]:

$$EC\ (\%) = \frac{C_c^n}{C_d^n} \cdot 100$$

Donde EC es la eficiencia coulómbica; C_d y C_c representan la capacidad gravimétrica para un ciclo de descarga y carga, respectivamente, y n el número del ciclo.

En esta tesis, se ha empleado la GCD con limitación de potencial para evaluar la capacidad de carga y descarga gravimétrica y la EC de los electrodos de ee-MoS_2 y lpe-MoS_2, respectivamente (Figura 41).

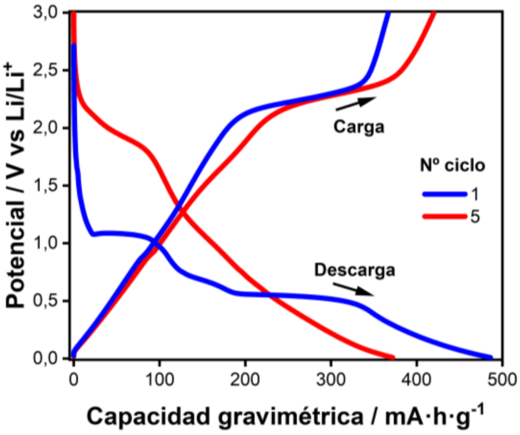

Figura 41. Curva de polarización donde se representa la variación del potencial en función de la capacidad gravimétrica de carga y descarga para un electrodo de ee-MoS_2, a 0.2 $A \cdot g^{-1}$.

4.5 Métodos computacionales

Teoría del Funcional de la Densidad (DFT)

La Teoría del Funcional de la Densidad (*Density Functional Theory*, DFT) es uno de los métodos de cálculo cuántico más utilizados. Se trata de un procedimiento alternativo a la resolución de la ecuación de Schrödinger en la que el funcional de la energía electrónica se minimiza respecto de la densidad electrónica. Un *funcional* es una función matemática de otras funciones, que en este caso describe la energía de interacción de los electrones en un sistema polielectrónico. Esta aproximación se sustenta en la idea de que la densidad electrónica de un sistema puede determinar muchas de sus propiedades (estructuras, frecuencias de vibración, energías de ionización…), y permite entonces predecir las y simular el transcurso de muchas reacciones químicas [30].

El funcional de Perdew-Burke-Ernzerhof (PBE) es uno de los funcionales de intercambio y correlación más utilizados dentro de la DFT. Este funcional considera el gradiente de densidad electrónica, y permite una mejor simulación de los enlaces químicos, propiedades electrónicas y reactividad de las moléculas y materiales en estado sólido [30].

En esta tesis, los cálculos computacionales se realizaron aplicando la DFT usando el paquete software Ab-Initio Vienna. Para el termino de correlación-intercambio de energía, se usó el funcional de PBE. Los modelos estructurales se construyeron usando Powder Cell y VESTA. Los gráficos de estructura se realizaron con VESTA. Para los cálculos computacionales del mecanismo de la reducción catalítica de nitroarenos, la celda unidad simulada consistía en una monocapa de 2H-$MoSe_2$ 4×4. Partiendo de esta simulación, se trabajó con modelos que incluían una y cuatro vacantes de átomos de Se (en el mismo lado de la lámina) por cada supercelda modelizada. Para los estados adsorbidos, se situó una molécula de nitroareno en las vacantes de Se. Se asumió que los intermedios moleculares de los nitroarenos estaban cargados negativamente y con un contraión de Na^+ (procedente del $NaBH_4$) que mantenía la electroneutralidad del conjunto.

Referencias

[1] Faraldos, M., Goberna, C. *Técnicas de Análisis y Caracterización de Materiales*. (CSIC, 2011).

[2] Banwell, C. N., McCash, E. M. *Fundamentals of Molecular Spectroscopy*, (McGraw-Hill, 1994).

[3] Braga, M. S., Gomes, O. F., Villamil-Jaimes, R. F. V., Braga, E. R., Borysow, W., Salcedo, W. J. Multispectral colorimetric portable system for detecting metal ions in liquid media, in *2019 4th International Symposium on Instrumentation Systems, Circuits and Transducers (INSCIT)*.

[4] Backes, C., Smith, R. J., McEvoy, N., Berner, N. C., McCloskey, D., Nerl, H. C., O'Neil, A., King, P. J., Higgins, T., Hanlon, D., Scheuschner, N., Maultzsch, J., Houben, L., Duesberg, G. S., Donegan, J. F., Nicolosi, V., Coleman, J. N. Edge and confinement effects allow in situ measurement of size and thickness of liquid-exfoliated nanosheets. *Nature Communications*, 5 (2014), 4576.

[5] Ferrari, A. C., D. M. Basko. Raman spectroscopy as a versatile tool for studying the properties of graphene. *Nature Nanotechnology*, 8 (2013), 235-246.

[6] Wu, H., Lin, M. -L., Zhou, Y., Zhang, X., Tan, P. -H. Analyzing Fundamental Properties of Two-Dimensional Materials by Raman Spectroscopy from Microscale to Nanoscale. *Analytical Chemistry*, 95 (2023), 10821-10838.

[7] J. Berne, B. & Pecora, R. *Dynamic Light Scattering: With Applications to Chemistry, Biology and Physics* (Dover Publications, 2000).

[8] Selvamani, V. Chapter 15: Stability Studies on Nanomaterials Used in Drugs. *Nanoscience and Nanotechnology in Drug Delivery* (2019), 425-444.

[9] Delgado, A. V., González-Caballero, F., Hunter, R. J., Koopal, L. K., Lyklema, J. Measurement and Interpretation of Electrokinetic Phenomena. *Pure and Applied Chemistry*, 77 (2005), 1753-1805.

[10] Skoog, D. A., Holler, F. J., Crouch, S. R. *Principles of Instrumental Analysis*, (Brooks/Cole, 2007).

[11] Allen, D., McWhinney, B. Quadrupole Time-of-Flight Mass Spectrometry: A Paradigm Shift in Toxicology Screening Applications. *Clinical Biochemist Reviews*, 40 (2019), 135–146.

[12] Kebarle, P., Verkerk, U. H. Electrospray: From ions in solution to ions in the gas phase, what we know now. *Mass Spectrometry Reviews*, 28 (2009), 898–917.

[13] Yang, M., Li, J., Zhao, C., Xiao, H., Fang, X., Zheng, J. LC-Q-TOF-MS/MS detection of food flavonoids: principle, methodology, and applications. *Critical Reviews in Food Science and Nutrition*, 63 (2023), 3750–3770.

[14] Fultz, B., Howe, J. M. *Transmission Electron Microscopy and Diffractometry of Materials* (Springer, 2002).

[15] Stroppa, D. G., Zagonel, L. F., Montoro, L. A., Leite, E. R., Ramirez, A. J. High-Resolution Scanning Transmission Electron Microscopy (HRSTEM) Techniques: High-Resolution Imaging and Spectroscopy Side by Side, *ChemPhysChem*, 13 (2012), 437–443.

[16] Goldstein, J. *Scanning Electron Microscopy and X-Ray Microanalysis* (Springer, 2003).

[17] Egerton, R. F. *Physical Principles of Electron Microscopy* (Springer, 2008).

[18] Giessibl, F. J. Advances in atomic force microscopy. *Reviews of Modern Physics*, 75 (2003), 949–983.

[19] Tararam, R., Garcia, P. S., Deda, D. K., Varela, J. A., de Lima Leite, F. Atomic Force Microscopy: A Powerful Tool for Electrical Characterization. *Nanocharacterization Techniques*, 1 (2017), 37–64.

[20] Haugstad, G. *Atomic Force Microscopy: Understanding Basic Modes and Advanced Applications* (Wiley, 2012).

[21] Bard, A. J., Faulkner, L. R. *Electrochemical Methods. Fundamentals and Applications* (John Wiley & Sons, 2001).

[22] Fleischmann, S., Mitchell, J. B., Wang, R., Zhan, C., Jiang, D., Presser, V., Augustyn, V. Pseudocapacitance: From Fundamental Understanding to High Power Energy Storage Materials. *Chemical Reviews*, 120 (2020), 6738–6782.

[23] Faraday, M. On Electrical Decomposition. *Philosophical Transactions of the Royal Society*, 124 (1834), 77-122.

[24] Wang, J., Polleux, J., Lim, J., Dunn, B. Pseudocapacitive contributions to electrochemical energy storage in TiO_2 (anatase) nanoparticles. *Journal of Physical Chemistry C*, 111, 40, (2007), 14925–14931.

[25] Lindström, H., Södergren, S., Solbrand, A., Rensmo, H., Hjelm, J., Hagfeldt, A., Lindquist, S. -E. Li^+ Ion Insertion in TiO_2 (Anatase). Voltammetry on Nanoporous Films. *The Journal of Physical Chemistry B*, 101 (1997), 7717–7722.

[26] Mei, B. A., Lau, J., Lin, T., Tolbert, S. H., Dunn, B. S., Pilon, L. Physical Interpretations of Electrochemical Impedance Spectroscopy of Redox Active Electrodes for Electrical Energy Storage. *Journal of Physical Chemistry C*, 122 (2018), 24499–24511.

[27] Laschuk, N. O., Easton, E. B., Zenkina, O. V. Reducing the resistance for the use of electrochemical impedance spectroscopy analysis in materials chemistry. *RSC Advances*, 11 (2021), 27925–27936.

[28] Mathis, T. S., Kurra, N., Wang, X., Pinto, D., Simon, P., Gogotsi, Y. Energy Storage Data Reporting in Perspective—Guidelines for Interpreting the Performance of Electrochemical Energy Storage Systems. *Advanced Energy Materials*, 9 (2019), 1902007.

[29] Li, X., Sun, X., Hu, X., Fan, F., Cai, S., Zheng, C., Stucky, G. Review on comprehending and enhancing the initial Coulombic efficiency of anode materials in lithium-ion/sodium-ion batteries. *Nano Energy,* 77 (2020), 105143.

[30] del Campo, J. M., Gázquez, J. L., Trickey, S. B., Vela, A. Non-empirical improvement of PBE and its hybrid PBE0 for general description of molecular properties. *The Journal of Chemical Physics*, 136 (2012), 104108.

5 Resúmenes y artículos

5.1 Exfoliación electroquímica catódica

Resumen de Artículo I

Two-dimensional MoS_2 nanosheets derived from cathodic exfoliation for lithium storage applications. *Nanomaterials*, 14 (2024), 932.

A. Martínez-Jódar, S. Villar-Rodil, J. M. Munuera, A. Castro-Muñiz, J. N. Coleman, E. Raymundo-Piñero, J. I. Paredes.

La exfoliación electroquímica de sólidos laminares se ha convertido en una de las alternativas más prometedoras para la obtención de materiales 2D debido a su bajo coste, escalabilidad, simplicidad, rapidez, bajo impacto medioambiental y a la posibilidad de producción de nanoláminas de pocas capas de espesor. En particular, la exfoliación electroquímica catódica permite la obtención de nanoláminas de buena calidad estructural, ya que las condiciones reductoras aplicadas previenen su oxidación y la consiguiente modificación de su estructura química. En el **artículo I** se ha desarrollado un método de exfoliación electroquímica catódica en medio orgánico para la obtención de nanoláminas de MoS_2, con vistas a su aplicación como material electroactivo para ánodos en dispositivos de almacenamiento de litio. Mediante la elección de electrolitos apropiados, se optimizó el proceso de intercalación, obteniéndose un mayor grado de exfoliación; y se evitó la transición de fase 2H a 1T de las nanoláminas, que ocurre con cationes lo suficientemente pequeños como para intercalarse en grandes cantidades y desencadenar la inyección de un elevado número de electrones. En concreto, se probaron cationes de trimetilalquilamonio como electrolitos, superando a sus homólogos de tetraalquilamonio, de mayor volumen (en los que se han centrado estudios anteriores), respecto del grado de exfoliación obtenido.

Se estudió la aplicación de las nanoláminas de MoS_2 obtenidas electroquímicamente (ee-MoS_2) como ánodo para almacenamiento de energía en dispositivos de ion-litio, y su funcionamiento se comparó con el de las nanoláminas de MoS_2 obtenidas mediante LPE

(lpe-MoS_2). El menor grosor de las nanoláminas de ee-MoS_2 (que disminuye su resistencia eléctrica y acorta los canales de difusión de Li) y su mayor flexibilidad dio lugar a un mejor funcionamiento electroquímico como ánodo para almacenamiento de Li en comparación con el lpe-MoS_2, en términos de capacidad gravimétrica obtenida de retención de capacidad con el aumento de la densidad de corriente (*rate capability*) y de ciclabilidad.

ARTÍCULO I

Two-Dimensional MoS_2 Nanosheets Derived from Cathodic Exfoliation for Lithium Storage Applications

Alberto Martínez-Jódar [1,2], Silvia Villar-Rodil [1,*], José M. Munuera [3,4], Alberto Castro-Muñiz [1], Jonathan N. Coleman [4], Encarnación Raymundo-Piñero [2] and Juan I. Paredes [1,*]

[1] Instituto de Ciencia y Tecnología del Carbono, INCAR-CSIC, Francisco Pintado Fe 26, 33011 Oviedo, Spain; alberto.mj@incar.csic.es (A.M.-J.); alberto@incar.csic.es (A.C.-M.).

[2] CEMHTI UPR3079, University of Orléans, CNRS, 1D avenue de la Recherche Scientifique, 45071, Orléans, France; encarnacion.raymundo@cnrs-orleans.fr.

[3] Department of Physics, Faculty of Sciences, University of Oviedo, C/ Leopoldo Calvo Sotelo, 18, 33007 Oviedo, Spain; munuerajose@uniovi.es (J.M.M.).

[4] School of Physics, CRANN and AMBER Research Centre, Trinity College Dublin, D02 E8C0 Dublin, Ireland; colemaj@tcd.ie (J.N.C.).

[*] Correspondence: silvia@incar.csic.es (S.V.-R.), paredes@incar.csic.es (J.I.P.).

Abstract

The preparation of 2H-phase MoS_2 thin nanosheets by electrochemical delamination remains a challenge, despite numerous efforts in this direction. In this work, by choosing appropriate intercalating cations for cathodic delamination, the insertion process was facilitated, leading to a higher degree of exfoliation while maintaining the original 2H-phase of the starting bulk MoS_2 material. Specifically, trimethylalkylammonium cations were tested as electrolytes, outperforming their bulkier tetraalkylammonium counterparts, which have been the focus of past studies. The performance of novel electrochemically derived 2H-phase MoS_2 nanosheets as electrode material for electrochemical energy storage in lithium-ion batteries was investigated. The lower thickness and thus higher flexibility of cathodically exfoliated MoS_2 promoted better electrochemical performance compared to liquid-phase and ultrasonically assisted exfoliated MoS_2, both in terms of capacity (447 vs. 371 $mA{\cdot}h{\cdot}g^{-1}$ at 0.2 $A{\cdot}g^{-1}$) and rate capability (30% vs. 8% capacity retained when the current density was increased from 0.2 $A{\cdot}g^{-1}$ to 5 $A{\cdot}g^{-1}$), as well as cycle life (44% vs. 17% capacity retention at 0.2 $A{\cdot}g^{-1}$ after 580 cycles). Overall, the present work provides a convenient route for obtaining MoS_2 thin nanosheets for their advantageous use as anode material for lithium storage.

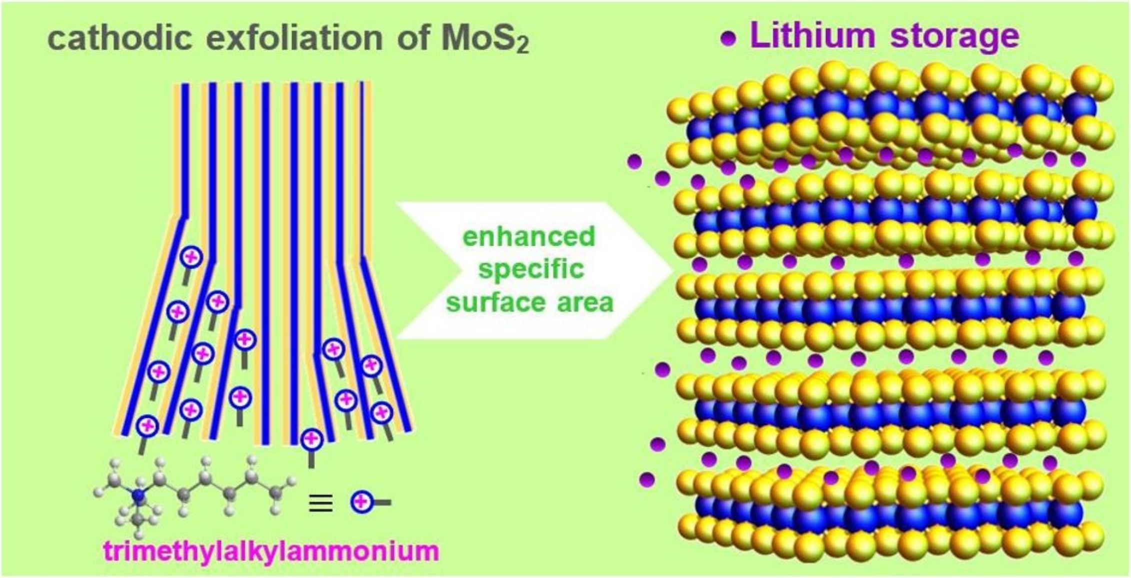

Keywords: transition metal dichalcogenide (TMD); MoS_2; electrochemical exfoliation; energy storage; lithium-ion batteries.

1. Introduction

In the last few decades, lithium-ion batteries (LIBs) have become a widespread energy storage solution for different purposes, mainly mobile applications that demand devices with high energy densities (e.g., portable electronic gadgets or electric vehicles [1]), but also stationary applications where cost considerations are probably a top priority over energy density (e.g., energy storage systems for the power grid [2]). To this day, graphite has been by far the anode material of choice for most commercial LIBs due to its appropriate features, such as laminar structure (allowing reversible accommodation of Li^+ ions in substantial amounts), reduced volume expansion (~10%) and high electrical conductivity, as well as relatively low cost and wide availability [3]. However, a major drawback of graphite arises from its limited energy density, determined by its somewhat low gravimetric and volumetric theoretical capacity (372 $mA{\cdot}h{\cdot}g^{-1}$ and 850 $mA{\cdot}h{\cdot}cm^{-3}$, respectively) [3,4]. In concern of this drawback, several alternative materials have been studied with the aim of replacing graphite as a LIB anode [5]. Specifically, some members of the transition metal dichalcogenide (TMD) family of compounds are being considered promising candidates due to their layered structure, thus allowing the intercalation of ions in their lattice and opening the prospect for their implementation as LIB anodes [5,6]. More to the point, the wider availability and lower cost of MoS_2 with respect to other TMDs, together with its outstanding gravimetric and volumetric theoretical capacity (670 $mA{\cdot}h{\cdot}g^{-1}$ and 3390 $mA{\cdot}h{\cdot}cm^{-3}$, respectively), justify the attraction of this TMD as a potential anode for LIBs [7]. In addition, given their layered nature, TMDs can be readily prepared as, or processed in-to, two-dimensional (2D) nanostructures, i.e., in the form of single-layer to several-layer nanosheets (NSs), which commonly demonstrate distinct properties when compared to their 3D, bulk counterparts [8,9]. Such a downsizing generally lends the resulting 2D materials a special interest for their use in energy storage systems, as it facilitates more extensive interactions with electrolyte and active redox species while shortening the pathway for the solid-state diffusion of charge carriers in the electrode [10]. In fact, previous reports in the literature suggest that 2D MoS_2 could show a number of advantages as an anode for LIBs over other emerging materials (e.g., Si and Ge), including better cycling stability, higher rate performance and less influence of volumetric expansion [9]. In fact, recent re-ports where MoS_2 was combined with materials with higher electrical conductivity high-light its potential as an electrode for lithium storage in LIBs [11-14], and in other types of lithium batteries, such as lithium–sulfur batteries [15].

As is normally the case when pursuing the practical implementation of any novel material, the real-life applications of 2D MoS_2 NSs rely on the availability of the material in large amounts, preferentially obtained by cost-effective means. Currently, there are several bottom-up and top-down approaches to preparing MoS_2 NSs. Among the bottom-up strategies, chemical vapor deposition and epitaxial growth are based on the reaction of sulfur and molybdenum precursors on an appropriate substrate, generally allowing precise control of the thickness, morphology and chemical doping of the resulting 2D crystals. How-ever, these strategies are usually limited in their scalability beyond thin supported films, i.e., they cannot be used to access the large number of stand-alone NSs that would be desirable for their application as electrodes in LIBs and other electrochemical energy storage devices [16,17]. Likewise, solvothermal synthesis is a straightforward, scalable bottom-up approach to obtain 2D MoS_2 at moderate temperatures, but the resulting NSs are in many cases obtained in an agglomerated form (e.g., nanoflowers), rather than as stand-alone objects, which may complicate their processing towards different applications [18]. On the other hand, top-down methods relying on the exfoliation of bulk MoS_2 crystals appear to be particularly convenient for accessing stand-alone, processable 2D MoS_2 flakes in substantial amounts [19,20]. For example, direct liquid-phase exfoliation of MoS_2 in proper organic solvents [21] or water/surfactant solutions [22,23], prompted by ultrasound or shear forces, is a common strategy to attain stable colloidal dispersions of MoS_2 NSs in considerable quantities. Nonetheless, this method typically suffers from low exfoliation yields and degrees (NSs comprising several layers rather than single/few layers), thus limiting their practical application potential.

Alternatively, the exfoliation of bulk MoS_2 based on chemical or electrochemical intercalation with proper ionic species has also been a matter of considerable research interest over the last few years [24-29]. For instance, exfoliation by chemical and electrochemical intercalation of lithium is relatively widely employed to obtain substantial quantities of monolayer/few-layer MoS_2 NSs, but the stringent conditions needed for their production (use of oxygen/water-free environments, long reaction times for chemical intercalation) de-crease their practical attraction [27,30]. Moreover, (electro)chemical lithium intercalation generally induces a structural transition in the resulting exfoliated NSs, from the semi-conducting 2H-phase to the metastable semimetallic 1T-phase, which is triggered by the massive injection of electrons in the host lattice associated with ion insertion [31,32]. Thus, achieving delamination into monolayer/few-layer NSs with no phase transition would strengthen the scope of applications where 2D MoS_2 can display a prominent performance [20,33]. In this regard, the issue of phase transition upon ion intercalation has been circumvented by replacing the small Li^+ cations with larger molecular species like tetraalkylammonium cations [34,35]. The larger size of the latter compared to Li^+ limits the number of cations that can be packed into the interlayer spaces of MoS_2, and consequently the number of electrons that are injected into the TMD lattice, thus preventing the 2H- to 1T-phase transition associated with excess electrons [25]. However, the use of large cations does not generally lead to full exfoliation of the material, i.e., single-layer or even few-layer NSs are not usually the majority objects resulting from this ex-foliation process [34]. Such an outcome has been rationalized by Lin et al. as resulting from a “self-retarding effect” associated with the insertion of large species [36]: as the intercalation of large cations proceeds in a given interlayer space, the mechanical strain induced in the TMD lattice progressively hinders subsequent intercalation into neighboring layers, preventing a complete exfoliation of MoS_2 into single/few layers [36]. Exfoliation of bulk MoS_2 can be also conducted by (electrochemical) intercalation of anions rather than cations [33]. Nonetheless, the intrinsically oxidizing conditions associated with the anodic process commonly imply a substantial transformation of the MoS_2 lattice into MoO_x species, and thus a deterioration of many of the attractive features of 2D MoS_2 [33].

Although substantial efforts have been devoted to this issue [33-37], attaining thinner 2H-phase MoS_2 NSs by electrochemical delamination is still a challenge. To address this question, we hypothesize that choosing appropriate intercalating cations can ease the insertion process and lead to enhanced exfoliation degrees while retaining the original 2H-phase of the starting bulk MoS_2 material. Specifically, while past work has focused on the use of tetraalkylammonium cations with alkyl substituents of identical length to drive MoS_2 exfoliation [34-37], here, we propose their replacement by cations with alkyl substituents of dissimilar lengths, such as trimethylalkylammonium. The rationale behind this proposal is the following: an alkylammonium cation combining a (relatively) long alkyl chain with three very short chains would (1) still be large enough to prevent phase transformation in the resulting exfoliated MoS_2 NSs and (2) have a small cross-sectional size in the direction of the long alkyl chain to promote a smoother intercalation compared to the case of larger, tetraalkylammonium cations with tetrahedral symmetry. Therefore, to probe this hypothesis, in this work, we have explored the use of a range of alkylammonium cations for the exfoliation of bulk MoS_2 into thinner, 2H-phase NSs. The results indicate that trimethylalkylammonium ions with substituents of different lengths outperform their tetraalkylammonium counterparts for accessing few-layer MoS_2 NSs. A discussion on the nature of this intercalation is addressed to account for such results. Additionally, the potential use of these new electrochemically derived 2H-phase MoS_2 NSs as an electrode material for lithium storage is also investigated, delivering competitive results.

2. Experimental section

2.1 Materials and reagents

MoS_2 natural crystals were purchased from SPI Supplies (West Chester, PA, USA), whereas MoS2 powder was provided by Alfa Aesar (Ward Hill, MA, USA). Platinum foil ($25 \times 25 \times 0.025$ mm^3) was purchased from Goodfellow (Delson, QC, Canada). The following ammonium salts were supplied by Sigma-Aldrich (Saint Louis, MO, USA): tetramethylammonium chloride (TMACl); tetraethylammonium chloride (TEACl); tetrabutylammonium chloride (TBACl); tetrahexylammonium chloride (THACl); tetrahexylammonium tetrafluoroborate ($THABF_4$); hexyltrimethylammonium chloride (HTMACl)/bromide (HTMABr); trimethyloctylammonium bromide (TMOABr); and hexadecyltrimethylammonium bromide, commonly referred to as cetrimonium bromide or cetyltrimethylbromide (CTAB). As for the solvents, propylene carbonate (PC), N,N-dimethylformamide (DMF) and N-methylpirrolidone (NMP) were obtained from Sigma-Aldrich, whereas acetone was purchased from VWR (Radnor, PA, USA). Multiwall carbon nanotubes and carbon black Super C65 were purchased from Arkema (Colombes, France) and Timcal (Bodio, Switzerland), respectively. Polyvinylidene difluoride (PVDF, Solef) and glass fiber paper (thickness 670 µm) were acquired from Solvay (Brussels, Belgium) and Whatman® (Little Chalfont, UK), respectively. Li foil was purchased from Sigma-Aldrich. A 1 M lithium hexafluorophosphate solution in ethylene carbonate/dimethyl carbonate (1/1 weight ratio) (LP30) was supplied by Solvionic (Toulouse, France). Coin cells CR2032 were provided by S4R (Anaheim, CA, USA). Milli-Q deionized water (Milli-pore Corporation, Billerica, MA, USA; resistivity: 18.2 MΩ cm) was used for all the experiments.

2.2 Cathodic exfoliation of MoS_2 Crystals

First of all, a ~4×6×1 mm^3 piece of MoS_2 was cut from the as-received crystal and cleaved on both sides to expose a fresh surface by removing the top layers. The electrochemical exfoliation was carried out in a two-electrode setup under cathodic conditions, using the piece of MoS_2 crystal and platinum foil as the working and counter electrodes, respectively, and an organic solution of a given quaternary ammonium salt as the electrolytic medium (15 mL). Both electrodes were connected to a DC power supply (E3633A apparatus, from Keysight Technologies, Santa Monica, CA, USA and Agilent 6614C power supply from Agilent, Santa Clara, CA, USA were indistinctly used) with crocodile clips and kept at a distance of ~2 cm from each other in the electrolytic solution. In this configuration, about two-thirds of the MoS_2 electrode was immersed in the electrolyte. A negative voltage (−8 V) was then applied to the MoS_2 electrode for 30 min, during which it was generally seen to swell and fan out starting from its free (non-clipped) end. Also, some of the outer layers of the crystal eventually detached from the electrode surface. After the cathodic treatment, the MoS_2 electrode was extracted from the solution and the lower part of the crystal was separated from the part which had not been submerged with a scalpel. The portions detached from the electrode during the cathodic treatment were also gathered with a spatula from the bottom of the electrolytic medium vessel and stored in DMF with the rest of the electrochemically treated MoS_2 for further use. It was preferred not to dry the product to prevent its expansion from reversing by deintercalation.

To obtain individualized MoS_2 NSs from the electrochemically treated material, the latter was transferred to DMF at a nominal concentration of 1 mg mL^{-1} and bath-sonicated

(Ultrasons systems from J.P. Selecta, Cerdanyola del Vallès, Spain, 40 kHz) during 5 h (changing from one bath to another to avoid the overheating of water). The obtained suspensions were washed to eliminate any remnants of the electrolytic medium through four consecutive sedimentation/re-suspension cycles. In each cycle, the dispersions were first subjected to centrifugation (Eppendorf 5430 microcentrifuge from Eppendorf, Hamburg, Germany) at 10,000 g for 25 min to sediment all the material, followed by replacement of 75% of the supernatant by an equal volume of DMF, and finally redispersion by bath sonication (~3 min) before the next washing sequence. After the four washing cycles, the dispersions were left to rest undisturbed overnight to allow for the sedimentation of non- and poorly exfoliated fractions. A ~75% of the supernatant volume, expected to contain the well electrochemically exfoliated MoS_2 NSs, hereinafter referred to as ee-MoS_2, was collected for further use.

For comparison purposes, liquid-phase exfoliated MoS_2 (lpe-MoS_2) was also prepared from bulk MoS_2 powder as previously reported [38]. Briefly, the protocol was the same as described above for the extraction of ee-MoS_2 NSs but omitting the washing step and starting from a nominal concentration of 30 mg mL^{-1} of bulk MoS_2 powder.

2.3. Characterization techniques

The materials were characterized by UV-Vis absorption spectroscopy, field-emission scanning electron microscopy (FE-SEM), high-resolution transmission electron microscopy (HR-TEM), energy dispersive X-ray spectroscopy (EDX), selected area diffraction (SAED), X-ray diffraction (XRD), atomic force microscopy (AFM), X-ray photoelectron spectroscopy (XPS), Raman spectroscopy, krypton physisorption, as well as dynamic light scattering (DLS). UV-Vis absorption spectra were recorded on a double-beam Genesys 180 spectrophotometer (Thermo Fischer Scientific, Waltham, MA, USA) with a wave-length step of 0.5 nm. FE-SEM imaging was performed on a Quanta FEG instrument (FEI Company, Hillsboro, OR, USA) that worked at a bias voltage of 20–25 kV. HR-TEM and SAED were carried out with a JEOL JEM-2100F instrument (JEOL, Tokyo, Japan) operated at an accelerating voltage of 200 kV and equipped with a 14-bit Gatan Orius SC600 CCD camera (Gatan, CA, USA), and bright-field and high-angle annular dark field detectors (JEOL). To prepare graphene specimens for HR-TEM, a few microliters of their aqueous suspensions were dropped onto copper grids (200 square mesh) covered with a lacey carbon film (Micro to Nano Innovative Microscopy Supplies, Haarlem, Netherlands) and then allowed to dry under ambient conditions. XRD diffractograms were ac-quired on a Bruker D8 Advance diffractometer (Bruker, Karlsruhe, Germany) equipped with a Cu Kα anode. The data were recorded in a 2θ range of 5°–80° with a step size of 0.015° and time per step of 6 s for XRD measurements, the starting TMD powders were used as received, while the exfoliated materials were prepared in the form of films by filtering from dispersion through polycarbonate membranes with a pore size of 50 µm (Nucleopore™, Whatman®). AFM images were recorded with a Veeco Nanoscope-IIIa (Digital Instruments, Tonawanda, NY, USA) working in the tapping mode of operation. For AFM imaging, a few microliters of polyvinylpyrrolidone-assisted MoS_2 dispersion were drop-cast onto atomically flat Si/SiO_2 (2000 nm SiO_2) substrates. XPS was measured on a spectrometer equipped with a monochromatic Al K_α X-ray source (14.00 KV, 175 W) and a Phoibos 100 hemispherical electron energy analyzer (SPECS Surface Nano Analysis, Berlin, Germany) and working at a pressure below 10−7 Pa. The XPS spectra were recorded at a take-off angle of 90°, analyzing the photoexcited electrons in the constant pass energy mode at a pass energy of 50 and 10 eV for survey and high-resolution core-level spectra, respectively. Raman spectra were registered with a Renishaw in Via Qontor apparatus (Renishaw, London, UK), working at a laser excitation wavelength of 532 nm (green line) and using an incident laser power sufficiently low (<0.5 mW) so as to minimize sample damage. Graphene samples for XPS and Raman spectroscopy were prepared by first pre-concentrating their dispersions in DMF, then transferring to a small volume of water and finally sequentially drop-casting small volumes of dispersion onto circular stainless steel discs (12 mm in diameter) and allowing them to dry at ambient conditions until a continuous film was seen to uniformly cover the whole disc. Due to the low values of the specific surface area expected for the parent MoS_2 materials, mostly in the case of the MoS_2 crystals, krypton rather than more common nitrogen physisorption was used for its determination, given that the former is more suitable for determining surface areas below 5 $m^2 \cdot g^{-1}$ [39]. Krypton physisorption at 77 K was measured in an ASAP 2420 surface area and porosity analyzer (Micromeritics, Norcross, GA, USA). Prior to the adsorption experiments, the samples were degassed under a vacuum at 120 °C for 12 h. The specific surface areas were obtained from the adsorption branch of the Kr isotherms by the standard Brunauer–Emmett–Teller (BET) method in the relative pressure range from 0.04 to 0.24. DLS measurements of MoS_2 dispersions in DMF were carried out on a Litesizer DLS 500 instrument (Anton Paar, Graz, Austria), equipped with a 658 nm wavelength laser. Ten replicates of each sample were made at a backscatter (angle of 175°).

2.4. Electrochemical Measurements and Post-Mortem Characterization of the electrodes

Both ee-MoS_2 and lpe-MoS_2 were tested as active materials for electrodes for Li storage in coin cells in a half-cell configuration, performing as an anode for LIB. The exfoliated MoS_2 materials were subjected to lyophilization prior to their use. First, lpe-MoS_2 or ee-MoS_2 NSs colloidal dispersions in DMF were subjected to high-speed centrifugation until complete sedimentation of the corresponding material was achieved. Then, 75% of the supernatant was discarded and the sedimented MoS_2 powders were redispersed in the remaining volume in order to increase the concentration of the resulting dispersions. After several concentration steps, the sedimented powders were subjected to three washing cycles (as previously described in Section 2.3), and then freeze-dried (Telstar Lyoquest-85 from Telstar, Terrassa, Spain) for 4 days. The working electrode consisted of a mixture of the electroactive MoS_2 material with multi-wall carbon nanotubes and carbon black as the conductive additives, and PVDF as the binder in a weight ratio of 54:16:20:10. To prepare such a mixture, appropriate masses of the first three components were added to the corresponding weighted volume of 5% PVDF/NMP. In order to produce a slurry, some pure NMP was added to the mixture which was then subjected to high-shear mixing (Ultra-Turrax T25 from IKA, Staufen im Breisgau, Germany) for 20 min. The resulting homogeneous slurry was cast onto chemically modified Cu foil and evenly distributed on its surface using a Doctor Blade. The wet covered substrate was subjected to slow drying for several hours at low temperature (~40–50 °C) on a heating plate, followed by a second drying step in a vacuum oven at 80 °C for 12 h. The coated Cu foil was cut into 10 mm diameter discs with a total mass loading between 1.4 and 2.5 $mg\cdot cm^{-2}$. A piece of Li foil was used as both the counter and reference electrode in a half-cell configuration. The coin cells were assembled in a glove box (Jacomex, Dagenux, France) under an argon atmosphere, with LP30 as the electrolyte and two stacked glass fiber filters as the separator. Prior to that, the different components (electrodes, separator, etc.) had been dried in an oven (B-545 from Büchi, Flawil, Switzerland) at 120 °C for 12 h.

The electrochemical response of the materials was monitored with a VMP3 potentiostat (Biologic, Grenoble, France), recording open circuit voltage (OCV), cyclic voltammograms (CVs) at different scan rates, electrochemical impedance spectroscopy (EIS) and galvanostatic charge–discharge (GCD) profiles with potential limitation at different current densities. Prior to any electrochemical measurement, the coin cells were left unbiased under OCV for 4 h to ensure wetting with the electrolyte.

Post-mortem microscopic studies of the electrodes after long-term cycling were conducted by FE-SEM. The used coin cells were disassembled using a hydraulic crimping machine. The electrodes were washed six times through several hours-long immersions in dimethyl carbonate, which was the same solvent of the electrolyte used in the electrochemical measurements (LP30). After that, most of the solvent was removed with the help of a pipette, and the electrode was dried first under ambient conditions and then overnight under a vacuum at room temperature. If present, the dry remains of the glass fiber separator were removed with tweezers, taking care not to scratch the surface of the electrode.

3. Results and Discussion

3.1. Optimization of the Cathodic Exfoliation Protocol

In the search for an electrochemical exfoliation protocol for the preparation of thin MoS_2 NSs, cations with alkyl substituents of dissimilar lengths, specifically, alkyltrimethylammonium salts, have been tested as electrolytes, in contrast with previous studies, where tetraalkylammonium cations with alkyl substituents of equal length were explored for such use [34-37]. To test our hypothesis that alkyltrimethylammonium cations (with trigonal pyramidal symmetry) could be more effective as electrolytes than tetraalkyllammonium cations (tetrahedral symmetry) in accessing thinner exfoliated MoS_2 flakes through cathodic delamination, the performance of both types of compounds was compared on an equal footing. In a typical experiment, cathodic exfoliation was carried out in a two-electrode configuration, using MoS_2 pieces (~4×6×1 mm^3 in size,

Figure 1a) as the working electrode, platinum foil as the counter electrode, and a solution of a certain ammonium salt in polycarbonate (PC) as the electrolytic medium (Figure 1b, see the Section 2 for further details). In an optimized procedure (−8 V, 0.05 M HTMABr in PC), upon application of the negative bias voltage to the MoS_2 cathode (Figure 1c), an accordion-like swelling of the former became visible to the naked eye (Figure 1f, Supplementary Movie S1). After completion of the cathodic expansion step, the electrochemically treated part of the MoS_2 crystal was separated from the non-treated portion (see the Section 2 for details) and characterized. The overall field-emission scanning electron microscopy (FE-SEM) image of the expanded portion of the cathode (Figure 1g), consisting of separated lamellae, contrasted sharply with the compact nature observed for the starting crystal at the same magnification (Figure 1d). A more detailed inspection confirmed that the lamellae were made up of thin, wrinkled layers separated by micrometer or sub-micrometer-sized voids (Figure 1h), again in contrast with the morphology of the starting, untreated MoS_2 piece, which was dominated by non-expanded and closed-packed layers (Figure 1e). Simultaneous to the expansion, gas bubble evolution in the cathode and the generation of a yellow substance in the counter electrode were observed when HTMABr was used as the electrolyte (see Supplementary Movie S1). The nature and production mechanism of the released substances will be discussed below. Nevertheless, all the ammonium salts tested as electrolytes but the smallest, TMACl, led to some expansion of the MoS_2 crystal whether there was gas evolution and/or yellow substance generation or not.

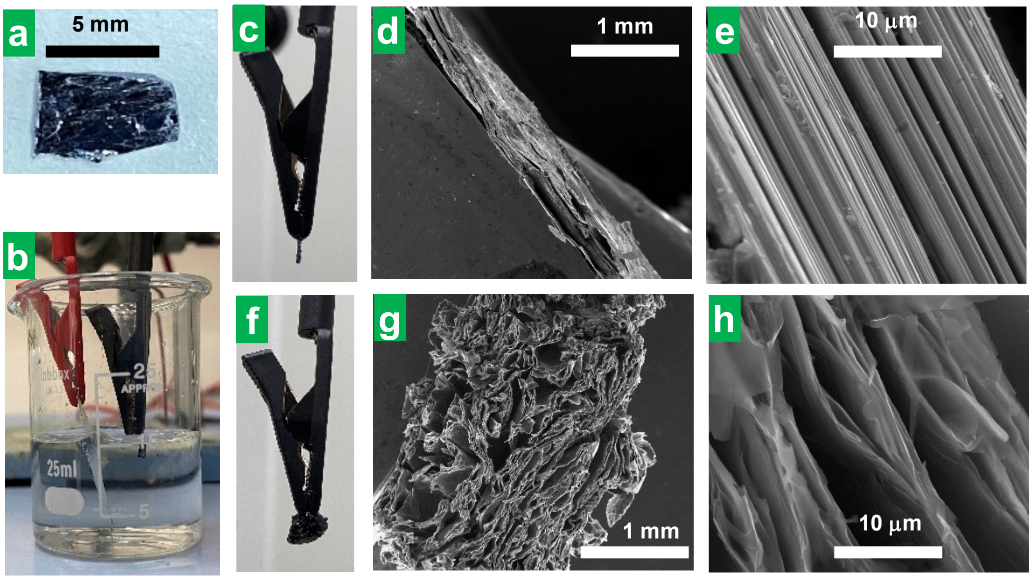

Figure 1. Cathodic expansion of bulk MoS_2 crystals. Digital photographs of (**a**) a typical bulk MoS_2 crystal used as a cathode for electrochemical exfoliation and (**b**) the experimental set-up for the cathodic exfoliation of MoS_2 using quaternary ammonium salt solutions in polycarbonate as the electrolyte. (**c**) Digital photograph and (**d**,**e**) FE-SEM micrographs at different magnifications of the edge of the MoS_2 cathode before electrochemical expansion. (**f**) Digital photograph and (**g**,**h**) SEM micrographs of the MoS_2 cathode after electrochemical expansion at −8 V for 30 min using 0.05 M HTMABr in PC as the electrolytic medium.

To extract individual, stand-alone MoS_2 NSs from the cathodically expanded materials, they were transferred to DMF at a nominal concentration of 1 mg mL^{-1}, and subjected first to sonication for 5 h and then to 4 washing cycles to remove any remaining electrolytic medium from the cathodic step (see Section 2 for details). The dispersions obtained after discarding the non- and poorly exfoliated fractions (see Section 2 for details) exhibited the Tyndall effect, which is indicative of the presence of a colloid (Figure 2a, right). They also displayed the characteristic green tone of nanostructured MoS_2 in the thermodynamically stable 2H-phase (Figure 2a, left) [8,40]. Indeed, their UV-Vis extinction spectrum (Figure 2b) featured the excitonic bands (A, B, C and D) characteristic of semiconducting 2H-phase MoS_2 [8]. Although the data shown in Figure 2 correspond to the dispersions obtained with HTMABr as an electrolyte, all the electrolytes that allowed MoS_2 crystal expansion (i.e., all the ammonium salts tested here except TMACl) yielded greenish MoS_2 dispersions which showed UV-Vis spectra typical of 2H-phase MoS_2. This provided confirmation that the phase transformation from the stable 2H phase of the starting natural crystal to the metastable 1T-phase in the resulting exfoliated MoS_2 NSs was prevented for every electrolyte. This means that all the electrolytes were large enough to limit the number of molecules that can fit into the interlayer species of the host crystal and thus the number of electrons injected per MoS_2 formula unit to values below the phase-transition threshold [41]. The preservation of the 2H-phase of the starting bulk MoS_2 material in the final exfoliated material obtained upon ammonium cations intercalation had already been shown in previous reports for the case of some of the larger cross-section, tetraalkylammonium cations with alkyl substituents of identical length tested here [34-37]. However, it was yet to be confirmed for the alkyltrimethylammonium cations with a smaller cross-sectional size, which were the subject of the current study.

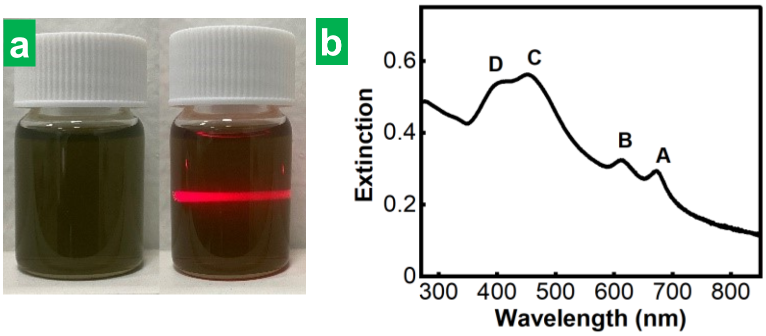

Figure 2. Electrochemically exfoliated MoS_2 colloidal dispersions. (**a**) Digital photographs of MoS_2 colloidal dispersions in DMF obtained after ultrasound-assisted exfoliation (**left**) showing the Tyndall effect (**right**). (**b**) UV-Vis extinction spectrum of the dispersion in (**a**). The excitonic peaks A–D, characteristic of the 2H-MoS_2 phase are labeled for clarity.

To test our second hypothesis that alkyltrimethylammonium cations, with a smaller cross-section in the direction of the long alkyl chain, could yield thinner MoS_2 flakes compared to the case of tetraalkylammonium cations, the thickness of MoS_2 NSs obtained with the different electrolytes were estimated and compared. Based on the metrics previously developed by Backes et al. for 2H-MoS_2 NSs, where the wavelength of the maximum of the A excitonic band of dispersion was shown to correlate with the thickness of the flakes therein [8], the position of A excitonic band was taken as a proxy of the thickness of the MoS_2 NSs. When the electrolytes were compared under equal conditions (bias voltage of −8 V, electrolyte concentration of 0.05 M in PC) for the cathodic expansion of MoS_2, HTMABr led to the lowest wavelength for the A band of the corresponding MoS_2 dispersion amongst all the tested electrolytes, as can be seen from the data gathered in Table 1. Therefore, HTMABr was selected as the optimal electrolyte because it allowed dispersions with the thinnest flakes.

Table 1. A-band position for MoS_2 dispersions obtained by cathodic exfoliation using different ammonium salts as electrolytes. Wavelength for the maximum of the A exciton band of the MoS_2 dispersions obtained by electrochemical exfoliation with different electrolytes at a concentration of 0.05 M in PC using a bias voltage of −8 V.

Electrolyte	**λ_A (nm)**
TMACl	-
TEACl	673.5
TBACl	673.5
$THABF_4$	678.0
HTMABr	672.0
TMOABr	676.5
CTAB	676.0

3.2. Physicochemical Characterization of the Cathodically Exfoliated Products

Microscopic and spectroscopic characterization of the solvent-extracted material derived from the cathodically expanded MoS_2 using HTMABr as the electrolyte confirmed that it consisted of individual, stand-alone, multilayer 2H-phase MoS_2 NSs of high structural quality. Indeed, the atomic force microscopy (AFM) images of the product depicted NSs of irregular polygonal shapes (Figure 3a) with lateral sizes typically in the range of several hundreds of nanometers. Assuming a thickness of MoS_2 monolayer of ~1.9 nm and a height offset of ~1 nm [8], we concluded that the exfoliated NSs were typically between 2 and 6 monolayers thick (Figure 3b). The electrochemically exfoliated

MoS_2 material obtained in this work compared favorably in terms of flake thinness with a typical liquid-phase exfoliated MoS_2 material, lpe-MoS_2 (see the Section 2 for details on its preparation), which displayed thickness between ~7 and 30 monolayers (see Figure S1b in Section S1 of the Supplementary Materials). As previously indicated by the A-band position for MoS_2 dispersions (Table 1), ee-MoS_2 nanosheets obtained using HTMABr as electrolyte were also found to be thinner on average than those obtained different ammonium salts as electrolytes by AFM (see representative images and the corresponding histograms in Figure S2, Section S1 of the Supplementary Materials, for the case MoS_2 obtained with $THABF_4$ and TMOABr). Dynamic light scattering (DLS) measurements yielded hydrodynamic diameters for the colloidally dispersed ee-MoS_2 NSs roughly between 80 and 460 nm (Figure 3c). Using the quantitative relationship between hydrodynamic diameter and NS lateral size previously developed for graphene and other 2D materials [42], the actual lateral size of the MoS_2 NSs was estimated to stretch between 50 and 700 nm, which was in reasonable agreement with the microscopy results (see Figure 3a). Figure S2 HR-TEM images of the MoS_2 revealed their high structural quality (Figure 3d). Atomic resolution images of the basal planes and the corresponding SAED patterns (Figure 3e and Figure 3f, respectively) disclosed their hexagonal symmetry and unit cell parameters.

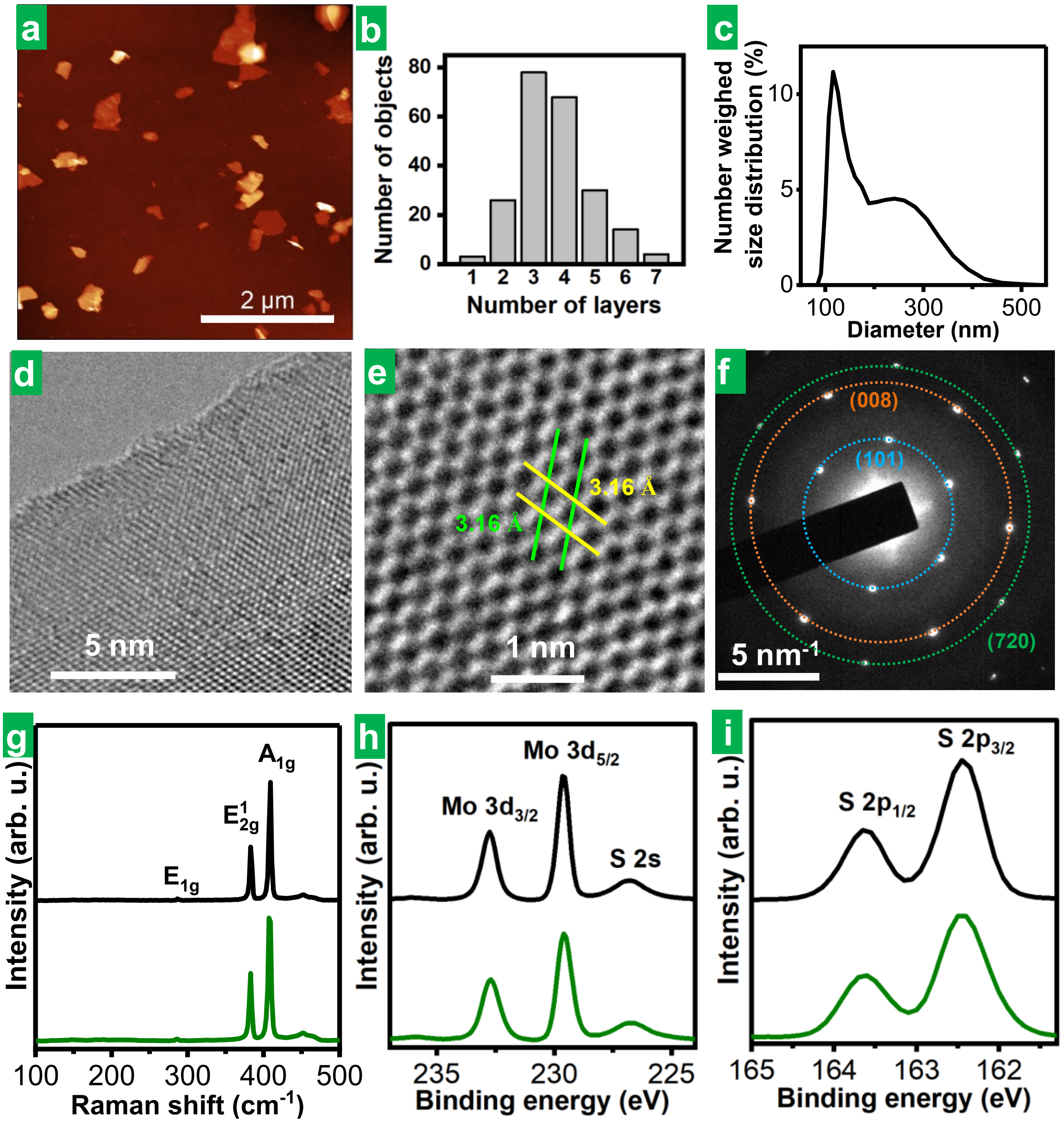

Figure 3. Microscopic and spectroscopic characterization of electrochemically exfoliated MoS_2 colloidal dispersions. (**a**) Representative AFM image of the MoS_2 nanosheets deposited onto a Si/SiO_2 substrate from dispersion. (**b**) Histogram of the apparent thickness of MoS_2 nanosheets derived from a pool of over 200 nanosheets measured from the AFM images. (**c**) DLS-derived number-weighed hydrodynamic diameter distribution for MoS_2 dispersion in DMF. (**d**,**e**) Representative HR-TEM images of the MoS_2 basal planes at different magnifications. The parallel lines in (**e**) assist in visualizing *a* and *b* cell parameters in the hexagonal cell of the MoS_2 lattice. (**f**) SAED pattern of the MoS_2 lattice with an indication of the families of planes involved in the observed diffractions.

(**g**) Typical Raman spectra of the starting bulk MoS_2 bulk crystal (black trace) and cathodically exfoliated MoS_2 (green trace). (**h**,**i**) Typical XPS spectra of (**h**) Mo 3d and (**i**) S 2p core levels for bulk MoS_2 crystal (black trace) and cathodically exfoliated (green trace) MoS_2 NSs. The main bands have been labeled for clarity.

Raman spectroscopy further confirmed that the thermodynamically stable 2H-phase of the starting bulk MoS_2 natural crystal (Figure 3g, black trace) was preserved in the exfoliated NSs (Figure 3g, green trace), as both materials showed equivalent spectra featuring the phonon bands expected for such structure [43]. This was only to be expected from the fact that the parent dispersion of the film drop-cast for Raman analysis yielded UV-Vis spectra typical of 2H-phase MoS_2 (see Figure 2b). XRD analysis provided diffractograms typical of 2H-MoS_2 (Figure S3a,c in Section S1 of the Supplementary Materials) as well. XPS spectroscopy showed that the chemical nature of the material was not altered either to any significant extent during its exfoliation and subsequent processing. Indeed, the core-level spectra of the main elements, molybdenum and sulfur, of the exfoliated material (Figure 3h and Figure 3i, respectively, green trace) were essentially identical to those of the starting bulk MoS_2 crystal (Figure 3h,i, black trace). Certainly, the high resolution, core-level Mo 3d, S 2s and S2p spectra (Figure 3h,i) exhibited the binding energies (BE) expected for such elements in 2H-phase MoS_2, namely, ~229.6 eV for Mo $3d_{5/2}$ and 232.8 eV for Mo $3d_{3/2}$ for Mo^{4+} with trigonal prismatic coordination to six sulfide ions, and ~226.8 eV for S 2s, ~162.4 eV for S $2p_{3/2}$ and ~163.6 eV for S $2p_{1/2}$ for S^{2-} with pyramidal coordination to three Mo^{4+} [44]. Apart from that, no oxidized Mo or S species could be found at the level of detection of XPS (i.e., above a few tenths of at%), either in the starting material or in its exfoliated counterpart.

By way of comparison, Figures S1 and S3d in Section S1 of the Supplementary Materials show the results of the characterization, carried out in a completely analogous way to that of ee-MoS_2, with MoS_2 obtained by liquid-phase ultrasound-assisted exfoliation of bulk MoS_2 powder. As in the case of the electrochemically delaminated material obtained from bulk MoS_2 crystals, XRD results as well as microscopic and spectroscopic characterization confirmed that the 2H-phase and the chemical nature of the starting bulk MoS_2 powder were preserved in the material derived from it by liquid-phase exfoliation (lpe-MoS_2). As for the dimensions of the exfoliated NSs, their lateral size, shown by AFM and estimated from DLS hydrodynamic diameters (Figure S1a,c in the Supplementary Materials) ranged between 40 and 425 nm, below that of ee-MoS_2. However, as said above, the ee-MoS_2 flakes were much thinner than their lpe-MoS_2 counterparts (compare Figures 3b and S1b), which is expected to lead to increased surface area. As will be explained later, thinner ee-MoS_2 NSs were found to perform better than thicker lpe-MoS_2 in their application to electrochemical energy storage, where high accessibility of the electrolyte to the surface is crucial. However, the specific surface areas of the ee-MoS_2 and lpe-MoS_2 materials measured by gas physisorption were found to be similar to each other, both being in the range of several tens of $m^2 \cdot g^{-1}$, which is in the order of the values reported in the literature for nanostructured MoS_2 materials [7,13]. Although the specific surface areas of the exfoliated materials were not significantly different from each other, they were notably higher, as expected, than those of the parent bulk materials, which showed values in the units of $m^2 \cdot g^{-1}$ range for the powder and in the hundredths of $m^2 \cdot g^{-1}$ range in the case of the crystal (just the geometrical surface). Nevertheless, these surface areas, measured by gas adsorption on dry powders, need not be representative of the area exposed to the electrolyte in their application to electrochemical energy storage. In fact, the dry powder, even if obtained by freeze-drying, must consist of re-stacked 2D films. Although it is not known how exactly this re-stacking occurs or how it depends on the thickness of the sheets, the fact that thicker sheets tend to be stiffer makes it reasonable to think that they will re-stack worse than the thinner ones and, therefore, tend to lose less area with respect to the case without re-stacking. Indeed, there are previous instances in the literature where a thinner, electrochemically exfoliated 2D material (e.g., graphene) is shown to lead to more compact, less porous re-stacked films than its thicker, liquid-phase exfoliated counterpart [45].

3.3. Rationalization of the Cathodic Exfoliation Process

Having established that the alkyltrimethylammonium cations, with a smaller cross-section in the direction of the long alkyl chain, yield thinner MoS_2 flakes compared to the case of larger tetraalkylammonium cations, it is pertinent to discuss the factors that lead to such different performance. Let us first analyze the nature of the intercalation process. Driven by the negative electrochemical potential, a certain number x of ammonium cations ($R_3R'N^+$, where R and R' are alkyl radicals; R = R' for tetraalkylammonium; R = $CH_3 \neq R'$ for trimethylalkylammonium) intercalates between the MoS_2 cathode layers in the electrochemical cell, generating an intercalation compound [Equation (1)]:

$$MoS_2 + xR_3R'N^+ + xe^- \rightarrow (R_3R'N^+)_xMoS_2^{x-} \qquad (1)$$

According to previous theoretical studies, the phase transition from the semiconductor 2H-phase to the semimetal 1T-phase in TMDs occurs only when the electron injection is above a certain threshold, which in the case of MoS_2 acquires the relatively high value of 0.29–0.35 electrons per formula unit [41]. The absence of phase transition in our MoS_2 exfoliated materials revealed by their characterization (see previous section) demonstrates that this threshold was not exceeded by intercalation with the tested substituted ammonium species. Subsequently, the decomposition of the cations [Equation (2)] can contribute to enlarging the inter-layer distance of MoS_2, favoring further intercalation and weakening the van der Waals interactions, eventually pushing the layers apart. In fact, tetraalkylammonium can accept an electron and reduce to trialkylamine and an alkyl radical, which can react with another alkyl radical to yield an alkene [46].

$$(R_3R'N^+)_xMoS_2^{x-} \rightarrow MoS_2 + \text{trialkylamines} + \text{alkenes} \qquad (2)$$

In this respect, cathodic gas generation was clearly observed for every tested electrolyte (see, for example, Supplementary Movies S1 and S2 for HTMABr and TEACl, respectively) but for TBACl and THACl (see Supplementary Movie S3 for THACl). The generation of cathodic gas depends on whether or not the given alkyl-substituted ammonium has the potential to give rise to low-molecular-weight alkenes by electrochemical reduction. In the case of TBA^+ and THA^+, the alkyl substituents are too long to generate gaseous alkenes by reduction, producing liquids instead.

Obviously, the size of the cations (or rather their effective intercalation cross-section) is a crucial factor in the intercalation process. Indeed, as explained above, for sufficiently large cations, the intercalation promoted a volume expansion of the MoS_2 crystal that facilitated its subsequent ultrasound-assisted exfoliation (see Table 1). Indeed, for tetraalkylammonium electrolytes with identical substituents, the intensity of the electrochemical expansion phenomenon was observed to increase with the length of the alkyl chain, i.e., with the size of the intercalated cation. In fact, the smallest cation, TMA^+, led to no expansion at all of the MoS_2 cathode, and thus the subsequent extraction of MoS_2 NSs by sonication was not possible (see Table 1). The ineffectiveness of this intercalant to expand the host crystal can be traced back to its diameter (0.56 nm) [46] being smaller than the interlayer distance of the crystal (0.61 nm) [34]. The next tetraalkylammonium cation in size, TEA^+ (0.67 nm) [46], did give rise to some expansion (see Supplementary Movie S2), but the subsequent ultrasound-assisted exfoliation of the portion subjected to electrochemical treatment led to very slightly green-colored, diluted dispersions, which was indicative of incomplete, scarce exfoliation. For the larger, butyl- and hexyl-substituted tetraalkylammonium cations, the increase in the volume of the MoS_2 crystals upon electrochemical treatment was much more pronounced (see Supplementary Movie S3 for the electrochemical expansion using THA^+) and led to significant exfoliation during the subsequent ultrasonication step. Thus, the extent of the electrochemical expansion was seen to determine the amount of exfoliated material extracted in the subsequent bath sonication step, which was non-existent for the smallest TMA^+, negligible for TEA^+, but increasingly significant for the larger cations TBA^+ and THA^+. Although, in principle, the more vigorous electrochemical expansion process observed for TBA^+ and THA^+ seemed advantageous, such intercalants were still not optimal. In fact, they led to an early saturation of the intercalation process, which did not allow for the expansion of the whole MoS_2 piece to take place over the 30 min electrochemical treatment. Indeed, the cathode swelling was very fast for the first 10 min, but it became arrested afterward (see Supplementary Movie S3), consistently leaving a preserved, internal portion of the MoS_2 piece with no appreciable expansion to the naked eye. As mentioned before, this type of phenomenon—the incomplete intercalation of bulk TMD crystals by large tetraalkylammonium cations—has been previously reported and explained by Lin at al. on the basis of a so-called "self-retarding effect" [36]. According to this explanation, during the first stages of the electrochemical treatment, the intercalation takes place mainly within the interlayer gaps near the TMD crystal surface, promoting a great initial expansion in its vicinity [36]. Then, the presence of the already intercalated bulky ammonium cations hinders the advance of the process in the neighboring layers due to the appearance of steric and electrostatic repulsions. The presence of accumulated mechanical strain at the interface between expanded and pristine areas in the host crystal prevents its complete, uniform intercalation, yielding thicker, multilayer NSs (Figure 4a). The trend of increasing thickness observed in this work for the series of exfoliated materials obtained with increasingly larger tetraalkylammonium cations (see Table 1) agrees with this explanation.

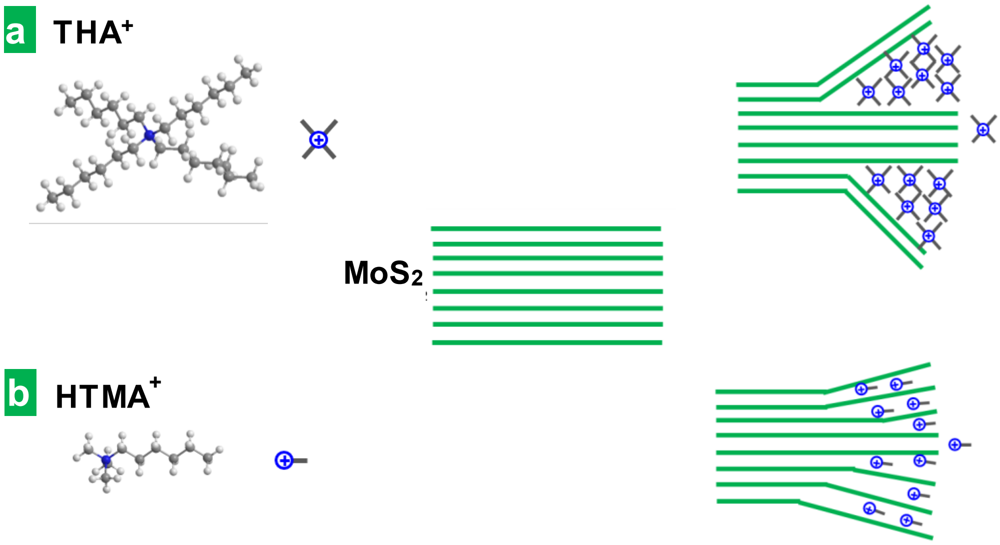

Figure 4. Schematic of the intercalation and exfoliation of layered MoS_2 by tetraalkylammonium and alkyltrimethylammonium cations. Intercalation and exfoliation of MoS_2 with (**a**) larger cross-section tetraalkylammonium cations, and (**b**) alkyltrimethylammonium cations, with a smaller cross-section in the direction of the long alkyl chain.

However, when alkyltrimethylammonium cations, with a smaller cross-section in the direction of the long alkyl chain, were used as electrolytes, the intercalation they promoted was found to be smoother. As the long alkyl chains of the three tested alkyltrimethylammonium cations are in fact equal ($HTMA^+$ vs THA^+) or longer ($TMOA^+$, CTA^+) than the substituents in the four tetraalkylammonium, the smoother intercalation of the former suggests that their long chains are oriented in parallel instead of in perpendicular to the atomic layers. This is supported by a previous study on an electrochemical molecular intercalation approach to obtain 2D superlattices where the intercalation of trimethylalkylammonium cations with alkyl substituents of dissimilar lengths was found to produce MoS_2 superlattices with very similar interlayer expansion [47], indicating that the species preferentially intercalate through their smaller, common trimethylammonium "head". Indeed, using $HTMA^+$, unlike the case of its fully hexyl-substituted counterpart THA^+, the expansion of the electrode was seen to proceed at a steadier pace along the whole electrochemical treatment (compare Supplementary Movies S1 and S3) leaving no unexpanded internal regions behind. Furthermore, the thickness of the MoS_2 flakes obtained with $HTMA^+$ was smaller, as indicated by the lower position of the A exciton of the corresponding dispersions (see Table 1). All these facts suggested that the self-retarding effect was alleviated in these conditions. As seen in Supplementary Movie S1, the smaller size and cross-section of $HTMA^+$ decreased the rate and extent of the initial volume expansion of the MoS_2 piece, which must have lowered the steric repulsion and the mechanical strain therein and facilitated further delamination (see Figure 4b). As previously found in the case of the tetraalkylammonium series, the thickness of the resulting MoS_2 NSs increased with the size of the electrolyte. Indeed, as the length of the dissimilar alkyl chain grew along the series of homologous alkyltrimethylammonium cations, the wavelength of the A exciton increased (see Table 1). This must come from the increase in the steric repulsion and mechanical strain induced by the intercalation of bulkier species. HTMABr was thus selected as the best among the tested electrolytes and its concentration was varied in the range from 0.01 M to 0.1 M in search of an optimum. A concentration of 0.05 M was found to be optimal: while lower concentrations led to less vigorous expansion of the MoS_2 piece, higher concentrations promoted an early arrest of the swelling. The latter was presumably due to the saturation of the intercalation process by the presence of an excessive amount of intercalated electrolyte in near-surface interlayer spaces of the crystal.

On the other hand, the corresponding anions of the electrolytic salts oxidize in the anode. For instance, the intense yellow substance released from the anode when bromide salts (HTMABr, TMOABr and CTAB) were used (see Supplementary Movie S1 for the case of HTMABr) was molecular bromine, which was generated by the oxidation of the bromide counterions. This was verified by substitution of the bromide counterion by chlorine, using HTMACl. In the latter case, the pale greenish-yellow color of molecular chlorine was observed instead of the intense yellow color of bromine.

3.4. Lithium, storage Performance of the Cathodically Delaminated MoS_2 Material

The lower thickness of cathodically delaminated MoS_2 NSs is expected to be beneficial for its use in electrochemical charge storage applications. In order to verify this assumption, the Li storage performance of both the thinner cathodically delaminated MoS_2 (ee-MoS_2) and the thicker liquid-phase exfoliated material (lpe-MoS_2) was evaluated under the same conditions for comparison. The tests were carried out in a half-cell configuration, using delaminated MoS_2 as the working electrode in combination with conductive additives (a mixture of carbon nanotubes and carbon black) and a binder. In the case of carbon nanotubes, their role was to improve not only the electrical conductivity of the electrode but also the mechanical properties, dampening the volumetric changes during charge/discharge cycles [48]. A weight ratio of 54:16:20:10 was used for exfoliated MoS_2/carbon nanotubes/carbon black/binder. The low relative content in active material ensures the absence of kinetic restrictions. The latter is desirable to assess the potential of the material for Li storage, although the formulation would have to be optimized for its actual implementation. However, we note that the mass loading of the active materials was ~0.7–1.3 g cm^{-2}, which is within the usual range used for tests in half-cell configuration. The morphology of the electrodes was revealed by FE-SEM (Figure S5 in Section S3 of the Supplementary Materials), showing a homogeneous appearance on a micrometer scale (Figure S5a,b) and the expected features from the individual nanostructured components of the mixture at the nanometer scale (Figure S5c,d). Specifically, nanosheets with dimensions in agreement with those found from AFM and DLS analyses (Figure 3a–c) corresponding to 2D MoS_2, nanometer-sized globules from carbon black as well as nanotubes were found. Li metal foil was used as both the counter and reference electrode, and 1 M $LiPF_6$ solution in an ethylene carbonate/diethylene carbonate solvent mixture (1/1 weight ratio) as the electrolyte (see the Section 2 for details). Figure 5a and Figure 5b show the first four CVs of the ee-MoS_2 and lpe-MoS_2 samples, respectively, at a potential scan rate of 0.2 mV s^{-1}. All the voltages are referenced to Li/Li^+, i.e., given as V vs. Li/Li^+, but will be henceforth given just as V for simplicity. The electrodes were biased from the OCV to 3.00 V (average OCV of 2.60–3.00 V after coin cell assembling) and then towards cathodic potentials. An initial comparison between lpe-MoS_2 and ee-MoS_2 revealed a strong qualitative resemblance, although the observed peaks tended to be more intense for ee-MoS$_2$, suggesting a higher extension of the Li storage processes for the latter.

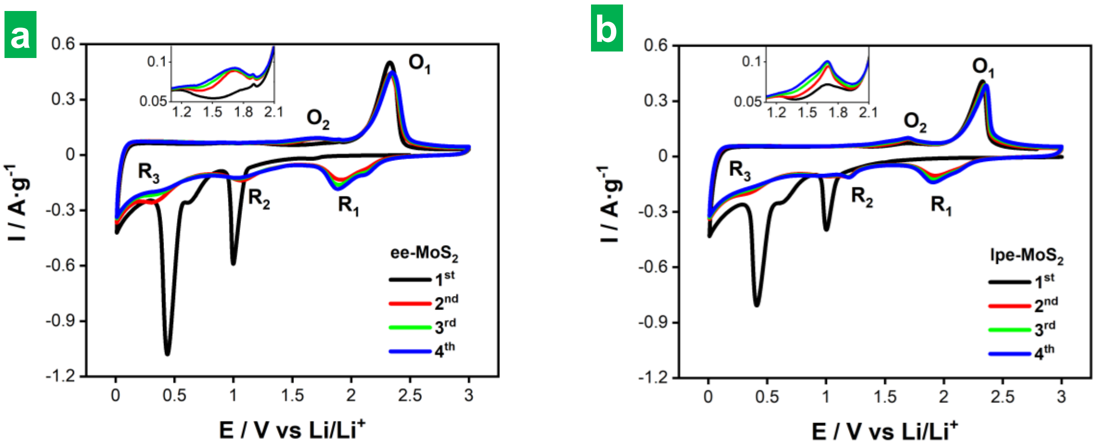

Figure 5. First four cyclic voltammograms (CVs) of electrodes based on exfoliated MoS$_2$ materials. CVs of the first four cycles at 0.2 mV s^{-1} of (**a**) ee-MoS$_2$ and (**b**) lpe-MoS$_2$ electrodes. The insets show a magnification in the voltage range of 0.8–1.9 V.

The lithium storage mechanism in MoS$_2$-based electrodes is thought to involve both intercalation and conversion processes during discharge, whereas the opposite processes take place during charge [9]. During the first discharge (black trace in Figure 5a,b), two prominent peaks emerged at 0.99 and 0.44 V for ee-MoS$_2$, and 1.00 and 0.41 V for lpe-MoS$_2$, with a soft split at ~0.60 V in both cases. The peak at ~1.00 V is ascribed to Li$^+$ intercalation into the MoS$_2$ lattice according to Equation (3) [9,49]:

$$\mathrm{MoS_2 + x\,Li^+ + xe^- \rightarrow Li_xMoS_2\ (0 \leq x \leq 1),} \qquad (3)$$

which results in a phase transition from semiconducting 2H to semimetallic 1T MoS$_2$ for x > 0.29–0.35 [41]. The peaks located at 0.41–0.44 V with a soft split at ~0.60 V are consistent with the irreversible conversion of 1T Li$_x$MoS$_2$ to metallic Mo nanoparticles and Li$_2$S [9,49]:

$$\mathrm{1T\ Li_xMoS_2 + (4 - x)\ Li^+ + (4 - x)\ e^- \rightarrow Mo + 2\ Li_2S,} \qquad (4)$$

where the split at ~0.60 V suggested a two-step conversion mechanism. In addition, the formation of the solid-electrolyte interphase (SEI) is thought to occur during the first cathodic scan at potentials that overlap with those of the Li_xMoS_2 conversion reaction at 0.40–0.60 V [50,51]. During charge, both MoS_2 materials exhibited a weak peak at ~1.70 V (O_2 peak) that was slightly more intense for lpe-MoS_2 (see insets to Figure 5a,b). Such a peak has been attributed to the formation of soluble lithium polysulfides (Li-PSs; Li_2S_n, $4 \leq n \leq 8$) from the oxidation of Li_2S [52-54], although other reports suggest two-step oxidation of Mo nanoclusters to give Mo^{4+} (~1.47 V) and Mo^{6+} (~1.70 V) [55,56], as well as partial delithiation of unreacted 1T Li_xMoS_2 [7,58]. However, the most prominent peak of the anodic scan appeared at ~2.30 V (O_1 peak), ascribed to the oxidation of Mo nanoparticles back to (amorphous) 2H-MoS_2 [Equation (5)] [7,56,57] and Li_2S oxidation to elemental S [S_8, Equation (6)] and Li-PSs [9,18,54,58].

$$Mo + 2\ Li_2S \rightarrow 2H\text{-}MoS_2 + x\ Li^+ + x\ e^- \tag{5}$$

$$8\ Li_2S \rightarrow S_8 + 16\ Li^+ + 16\ e^- \tag{6}$$

In the second discharge, the peaks associated with Li^+ intercalation and Li_xMoS_2 conversion noticed in the first discharge tended to vanish and to shift slightly (peaks denoted as R_2 and R_3; see Figure 5a,b, red traces). Further, a new peak (R_1) appeared at 1.91–1.93 V with a shoulder at ~2.10 V, which shifted to 1.88 V after four cycles. Peaks R_1 and R_2 were ascribed to the reduction of elemental S back to Li_2S [reverse of Equation (6)] and Li-PSs [9,54,59], respectively, although R_2 could also arise from some lithiation of restored 2H MoS_2 [7,55,56]. In line with the latter, the weak R_3 feature would correspond to the conversion of some remaining Li_xMoS_2 material [9,58]. In the second charge cycle, both MoS_2 electrodes exhibited a weak feature at ~1.70 V (O_2 peak; reactions involving Li-PSs) together with an intense peak at 2.32–2.34 V (O_1 peak). All these features then appeared recurrently with little changes in the subsequent CV scans (green and blue traces in Figure 5a,b). We, therefore, conclude that lithium storage in both the ee-MoS_2 and lpe-MoS_2 electrodes relies on intercalation and conversion reactions, with Li_2S/S_8 conversion processes very likely playing a main role. Here, the presence of Mo nanoclusters/nanoparticles is thought to be beneficial, as this metal is known to be efficient at immobilizing Li-PSs as well as catalyzing their conversion reactions, thus contributing to alleviating the shuttle issues associated with the Li_2S/S_8 conversion processes [53,54,60].

Figure 6a and Figure 6b show representative GCD profiles for ee-MoS_2 and lpe-MoS_2 electrodes, respectively, measured at different currents. Specifically, each profile is the fifth of five cycles recorded at the same current. They were recorded after the CVs shown in Figure 5 and that is why the capacity associated with SEI formation is absent from them. The corresponding gravimetric capacities for the five GCD cycles (relative to the total mass of the electrode) are plotted in Figure 6c, together with their coulombic efficiency values. As expected, the profiles displayed clear potential plateaus at low currents (e.g., 0.1 and 0.2 A g^{-1}) reflecting the Li_2S/S_8 conversion processes at ~2.1–2.3 V vs. Li/Li^+, although such plateaus were only retained in part at higher currents. Indeed, the shape of the profiles tended to become straight at the highest currents (up to 5 A g^{-1}), such constant variation of potential vs. time indicating increasing contributions of (pseudo)capacitive processes [54,61]. The straight, steep nature of the profiles at increasing currents was also indicative of ohmic polarization, which resulted in capacity losses and was more pronounced for lpe-MoS_2 [54]. Ohmic polarization was also reflected in the GCD profiles by a sudden decrease in potential when the sign of the intensity was inverted. When the current density was returned to its starting low value (0.1 A g^{-1}; cyan traces in Figure 6a,b), only a partial recovery of the potential plateaus was observed, implying some irreversibility of the corresponding storage processes. Nonetheless, the total capacity was very similar to that of the first 0.1 A g^{-1} routine (compare cyan and black GCD profiles). In any case, the shape of the GCD profiles (Figure 6a,b) and the capacity values (Figure 6c) were better preserved at higher currents with the ee-MoS_2 electrode, implying a better overall electrochemical performance of this material compared to its lpe-MoS_2 counterpart. In particular, the ee-MoS_2 electrode boasted larger gravimetric capacities at all currents between 0.1 and 5 A g^{-1} as well as a higher rate capability than those of lpe-MoS_2 (30% vs. 8% capacity retained when the current density was increased from 0.2 $A \cdot g^{-1}$ to 5 $A \cdot g^{-1}$). The values of the coulombic efficiency were in general quite similar for both electrodes. The gravimetric capacity of both exfoliated MoS_2 materials compared favorably with the theoretical capacity of graphite (372 $mA \cdot h \cdot g^{-1}$), the commercial anode material par excellence for LIBs, showing values of 47 and 371 $mA \cdot h \cdot g^{-1}$ at 0.2 $A \cdot g^{-1}$ for ee-MoS_2 and lpe-MoS_2, respectively (Figure 6c). As mentioned above, these gravimetric capacity values were calculated relative to the total mass of the electrode but, if they were calculated relative to the mass of active material, the comparison would be even more favorable, reaching values close to or even higher than the theoretical capacity of MoS_2. The latter has been explained in the literature as coming from the contribution of capacitive processes derived from the nanostructuring of MoS_2 [7,9]. These capacity values show the potential of the exfoliated materials, especially that of ee-MoS_2. Although its rate capability (and cyclability, as will be seen below) is limited, we expect that these parameters could be improved by optimization of the electrode formulation or, as recent reports suggest, through combination with materials with high electrical conductivity [7,9].

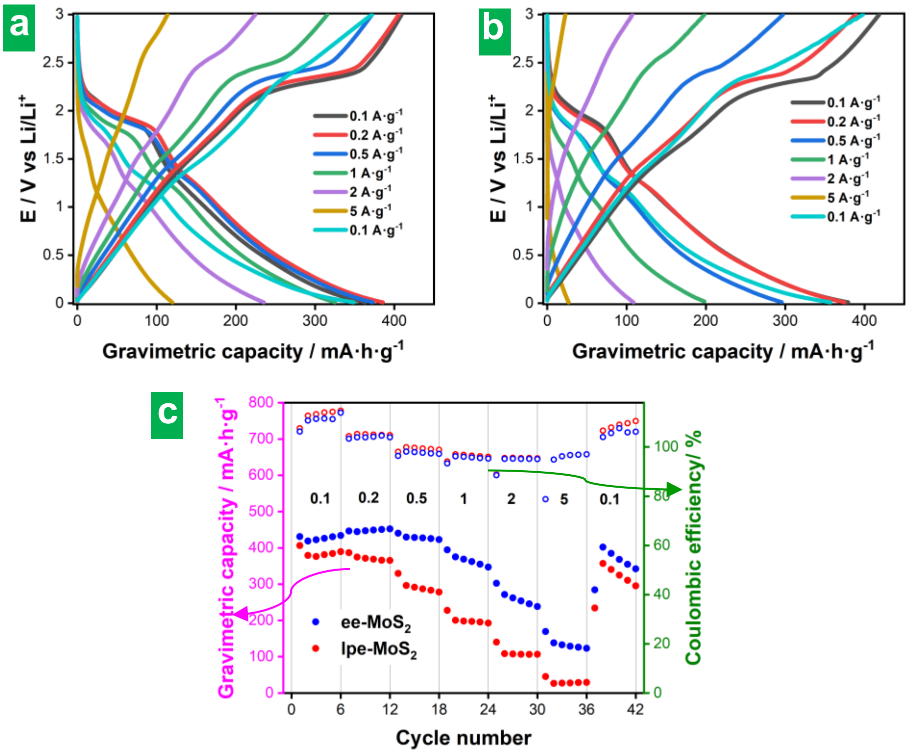

Figure 6. Galvanostatic charge–discharge (GCD) of the exfoliated MoS_2 electrodes. Charge/discharge profiles at several gravimetric currents for (**a**) ee-MoS_2 and (**b**) lpe-MoS_2 electrodes. (**c**) Gravimetric discharge capacities (full circles) and Coulombic efficiency values (hollow circles) for ee-MoS_2 (blue) and lpe-MoS_2 (red) at different gravimetric currents (in A/g units). The gravimetric capacities are calculated relative to the total mass of the electrode.

The behavior of the MoS_2-based electrodes was also investigated by EIS. Figure 7a,b show Nyquist plots of the ee-MoS_2 and lpe-MoS_2 electrodes after 4 h of resting at the open circuit voltage (OCV) before any electrochemical measurement (solid traces) and after recording 5 full CVs (hollow traces). A magnification of the high-frequency region of the plots is provided in Figure 7b. EIS was modeled using different electrical equivalent circuits for the electrodes. Before cycling, a model $R_{el}(R_{CT}WM)(CPE_{int})$ was used [7], where R_{el} is the sum of the resistance of the electrolyte, separator and internal resistance of the cell. A parallel circuit $(R_{CT}WM)(CPE_{int})$ simulated the charge storage activity at the electrode–electrolyte interface, where R_{CT} is the charge transfer resistance and CPE_{int} is the capacitance at the interface. The latter is represented by a constant phase element (CPE) to account for its frequency-dispersed behavior. W and M are both open circuit termini accounting for diffusion processes, with W as the Warburg element, modeling semi-infinite linear unrestricted diffusion to a large planar electrode, while M accounts for finite length restricted diffusion. To model the EIS of the electrodes after 5 cycles, a parallel circuit $(R_{SEI})(CPE_{SEI})$ was added to account for the contribution of the SEI, where R_{SEI} and CPE_{SEI} are the SEI resistance and capacitance (also a CPE), respectively [7]. The initial electrode resistance (R_{el}), related to the intercept of the plot with the Z' axis at the highest frequency, was seen to be lower for ee-MoS_2 (6.8 Ω) than it was for lpe-MoS_2 (11.4 Ω). Such a difference can in principle be put down to the thinner nature of the ee-MoS_2 NSs: thinner 2D objects are expected to be more flexible than thicker ones, and hence contacts between neighboring NSs in the electrode should be more conformal, leading to a lower inter-nanosheet resistance [62]. The charge transfer resistance (R_{CT}), associated with the diameter of the semicircle in the Nyquist plots, was also smaller with ee-MoS_2 (45 vs. 139 Ω). The better charge transfer kinetics of this material can be related again to its thinner nanosheets, as it implies a larger active material–electrolyte contact area [63,64]. After recording the CVs, the Nyquist plots revealed a small increase in R_{el} (<1 Ω for both electrodes), ascribed to SEI formation. On the other hand, the R_{CT} became smaller in both cases (35 and 47 Ω for ee-MoS_2 and lpe-MoS_2, respectively), which could be attributed to morphological changes taking place in the active material upon cycling, as will be discussed below, e.g., to the development of nanoporosity on the MoS_2 surface [7]. Likewise, the almost vertical straight-line characteristic of the low-frequency region of the initial Nyquist plot for both electrodes was largely retained after recording the CVs with ee-MoS$_2$, but not with lpe-MoS$_2$, which became slanted. The latter was indicative of more diffusion-controlled behavior that at least in part accounted for the poorer electrochemical performance of this electrode.

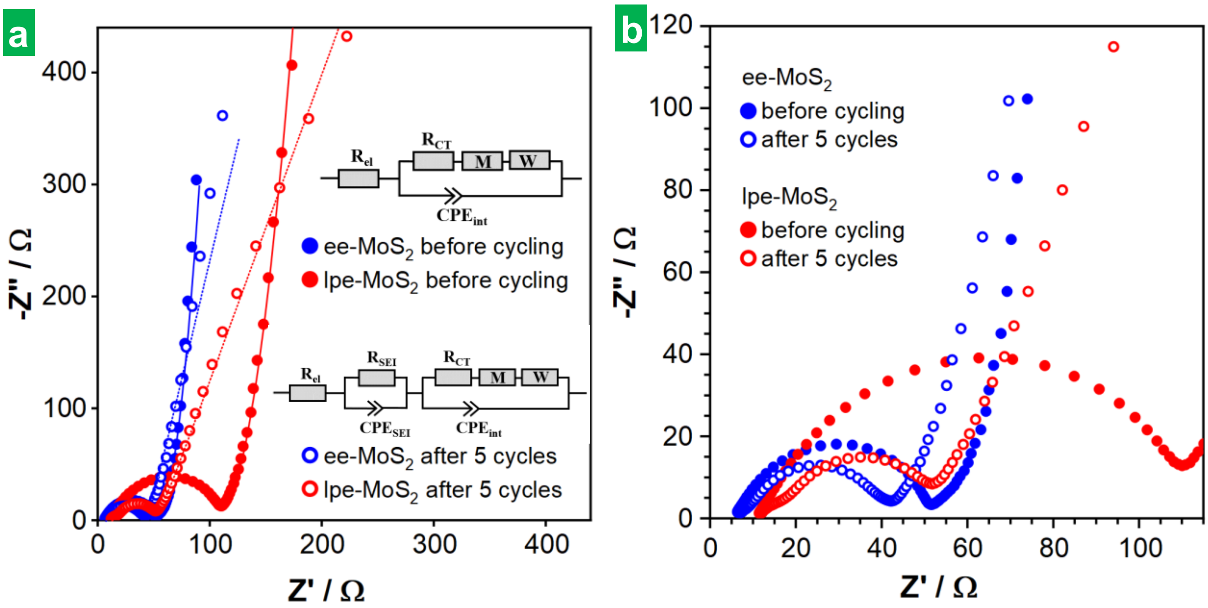

Figure 7. Electrochemical impedance spectroscopy (EIS) of the exfoliated MoS$_2$ materials. (**a**) Nyquist plot after 4 h at the OCV (full circles) and after five charge/discharges cycles (hollow circles) for ee-MoS$_2$ (blue) and lpe-MoS$_2$ materials (red). Their fitting to the indicated equivalent circuits are graphed with solid and dotted lines, respectively. (**b**) Magnification of the high-frequency region of the Nyquist plots in (**a**).

Figure 8a shows results on the long-term GCD cycling at 0.2 and 0.5 A g^{-1} for ee-MoS$_2$ and 0.2 A g^{-1} for lpe-MoS$_2$, with profiles at selected cycles shown in Figure 8b–d. SEI formation and other processes that took place mainly during the first cycle, as discussed above for the CVs (see Figure 5 and accompanying text), showed up in the first cycle in the form of marked plateaus. However, as the number of GCD cycles progressed into a few or several tens, a clear fading of the voltage plateaus, even those corresponding to Li$_2$S/S$_8$ conversion processes at 2.1–2.3 V, was observed. Indeed, the CVs after long-term cycling (see Figure S4a,b in Section S2 of the Supplementary Materials) suggested that the conversion reactions taking place in the bulk of the active material were no longer the major contributors to electrode capacitance and that surface-controlled processes became dominant instead. Such a decline in conversion reactions could stem from structural changes affecting the active material during cycling or the irreversible exhaustion of 2H-MoS_2 [7,61,65]. As shown in Figure 8a, the capacity increased somewhat during the first 10–20 GCD cycles for all the tested electrodes and then decreased rapidly over a few (ee-MoS_2) or several (lpe-MoS_2) tens of additional cycles. We note that the first cycle, where SEI formation took place, afforded an initial high capacity that is not considered in this discussion. Afterward, a stable cycling behavior was observed, during which the measured capacity tended to remain constant (lpe-MoS_2; ~45 mAh g^{-1}) or to increase somewhat (ee-MoS_2, especially at 0.5 A g^{-1}; in the 100–200 mAh g^{-1} range). The capacity values in the stable cycling region were much larger with the ee-MoS_2 electrode than they were with their lpe-MoS_2 counterpart. Thus, the thinner nature of the former has been shown to be beneficial to its global electrochemical performance, both to its capacity and rate capability (Figure 6c) and to its cycle life (Figure 8). The Coulombic efficiency fell below 100% during the first cycles due to the SEI formation and then increased to values higher than 100% for all the electrodes, the effect being more pronounced for the ee-MoS_2-based electrode than for the lpe-MoS_2-based one. The origin of Coulombic efficiencies larger than 100% is not clear at the moment. However, their occurrence has been previously reported in the literature [7,11,66] and attributed to surface-based oxidation processes developed upon cycling [7]. Modeling of the EIS after long-term cycling (Figure S4c in Section S2 of the Supplementary Materials) showed that the SEI became best simulated by a parallel circuit (R_{SEI}) (C_{SEI}) where R_{SEI} and C_{SEI} are the SEI resistance and capacity, respectively [7].

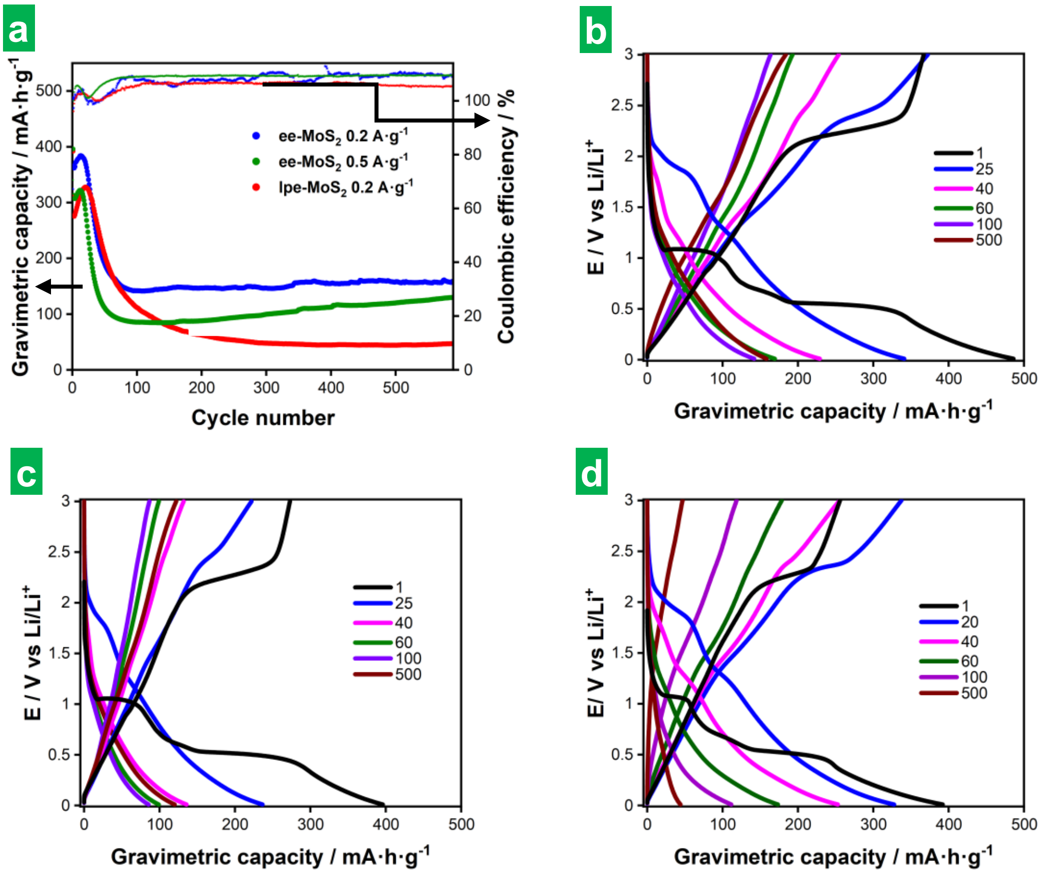

Figure 8. Long-term cyclability of ee-MoS2 and lpe-MoS2 electrodes on the basis of GCD measurements. (**a**) Gravimetric capacity (larger circles) and Coulombic efficiency (smaller circles) vs. cycle number for ee-MoS2 at 0.2 (blue color) and 0.5 A g^{-1} (green), and for lpe-MoS2 at 0.2 A g^{-1} (red). (**b**–**d**) GCD profiles recorded at different cycle numbers (indicated in the legends) for ee-MoS2 at (**b**) 0.2 A g^{-1} and (**c**) 0.5 A g^{-1} as well as for lpe-MoS2 at (**d**) 0.2 A g^{-1}. The gravimetric capacities are calculated relative to the total mass of the electrode.

The type of cycling behavior observed here with the MoS2-based electrodes has been previously described [10]. It was demonstrated that the different cycling regimes (i.e., capacity increase, decrease, stabilization) result from morphological changes occurring at the electrode. These changes involve alterations in the exposed surface area, electrolyte permeability or electrical conductivity, which affect the storage capacity [7,65]. For example, the increase in capacity during the first few tens of cycles was explained by the development of a nanopore-rich surface morphology upon cycling [7]. Such an opening of nanoporosity promoted electrolyte penetration and contact with the active material, thus improving lithiation, and leading to an activation process of the electrode [67]. The fact that fewer cycles were required to reach the top capacity in this first regime with the ee-MoS_2 electrode, relative to the case of lpe-MoS_2, suggested a more efficient evolution of the surface morphology in the former material. In turn, this was probably due to a larger exposed surface area of the ee-MoS_2 NSs arising from their thinner nature [10,67]. Concerning the capacity decrease regime, it is known that MoS_2-based electrodes shift from a battery-type storage mechanism to extrinsic pseudocapacitive behavior with an increasing nanostructuring of the material [68,69]. Thereby, it could be argued that the capacity decay during this regime was rooted in the variable contributions from decreasing battery-like reactions and emerging pseudocapacitive processes that stemmed from the morphological changes experienced by the active material. Such a trend towards less battery-like and more pseudocapacitive behaviors was clearly observed in the GCD profiles of Figure 8b–d. The third regime (capacity stabilization) would then be reached when charge storage becomes completely dominated by pseudocapacitive processes and any purely battery-type behavior is rendered largely residual. Here, the much larger capacity values afforded by the ee-MoS_2 electrode could again well be the result of the thinner nature of its corresponding NSs. Specifically, when morphological and compositional changes are triggered in the MoS_2 material by the cycling routine, we would expect the resulting primary active particles to be smaller if they originate from thinner NSs. In turn, smaller active particles should favor the surface-driven, pseudocapacitive processes that dominate the third regime and thus lead to larger capacities. This reasoning would also explain the larger number of cycles required for the lpe-MoS_2 electrode to reach the third regime, as thicker MoS_2 NSs would take longer to fully convert to the final active products. Post-mortem microscopic studies of the cycled electrodes confirmed these expectations and showed their thorough morphological transformation after long-term cycling. Indeed, the original morphology (see Figure S5 in Section S3 of the Supplementary Materials) changed completely, displaying microlamellae (Figure S6a,b for ee-MoS_2, Figure S8a,d for lpe-MoS_2), microspheres (Figures S6c and S7c,d for ee-MoS_2, Figure S8c for lpe-MoS_2), as well as combinations of both (Figure S6d), and other morphologies (Figure S8b,e,f). For the electrodes cycled at 0.2 A g^{-1}, the microspheres were smaller and more abundant for the electrodes based on ee-MoS_2 than for those based on lpe-MoS_2 (Figure 6c,d vs. Figure 8c), which implies a higher surface area. As for the microlamellae, their surface showed more rugosity in the case of ee-MoS_2 than in that of lpe-MoS_2 (Figure S6e,f,h,i vs. Figure S8d). The more developed surface in ee-MoS_2-based electrodes would explain their higher gravimetric capacity after cycling (Figure 8a), given that the lithium storage is dominated by surface-driven, pseudocapacitive processes in this regime. In the case of lpe-MoS_2 electrodes, a minoritarian nanoflower-like morphology, similar to that developed by solvothermal MoS_2 [18], which could contribute to some extent to the surface area, was also detected (Figure S8b,e,f). The ee-MoS_2-based electrode cycled at 0.5 A g^{-1} also displayed microlamellae and microspheres (Figure S7), but the most frequent morphology showed the development of porosity (Figure S7a,b), which is indicative of an activation process. The shortening of the ion transport paths could explain the increasing trend of the capacity of this electrode upon cycling (Figure 8a, green circles).

Finally, an analysis of the kinetic behavior of the ee-MoS_2 electrode was carried out to probe the nature of its charge storage mechanism. To this end, CVs were recorded at different potential scan rates between 0.1 and 2 mV s^{-1} (Figure 9a). The main redox peaks (i.e., O_1, R_1, O_2, R_2, as previously defined in Figure 5) were then fitted to the following exponential equation to determine the values of the exponent (b)

$$i = av^b, \tag{7}$$

where i is the measured peak current at a given scan rate, v, and a and b are adjustable parameters. A b value of 1 denotes purely (pseudo)capacitive charge storage processes that are not limited by diffusion, while a value of 0.5 indicates purely diffusion-controlled processes. b values in between these two extremes imply the occurrence of mixed (pseudo)capacitive and diffusion-controlled processes in different proportions [70]. The results of peak fitting are presented in Figure 9b. For the O_1/R_1 redox pair, the b parameters were calculated as 0.84 (O_1) and 1.10 (R_1). The latter was obviously artifactual and very likely stemmed from contributions of the shoulder peak observed in Figure 9a at the positive potential side of the R_1 peak (i.e., in the 2.0–2.1 V region). The separation between the R_1 and shoulder peaks tended to decrease with increasing v, implying an increasingly large contribution of the shoulder peak to the R_1 current and thus enhancing its *b* value. For the O_2/R_2 pair, the *b* values were 0.94 (O_2) and 0.95 (R_2). All these figures indicated charge storage in the ee-MoS_2 electrode to comprise both (pseudo)capacitive and diffusion-limited processes, but with a very clear dominance of the former. Such a conclusion was reasonable, considering that these redox peaks were associated with Li_2S/S_8 and Li-PS conversion reactions, which are thought to be mainly surface processes and are consequently not or little affected by diffusion [53,54,71].

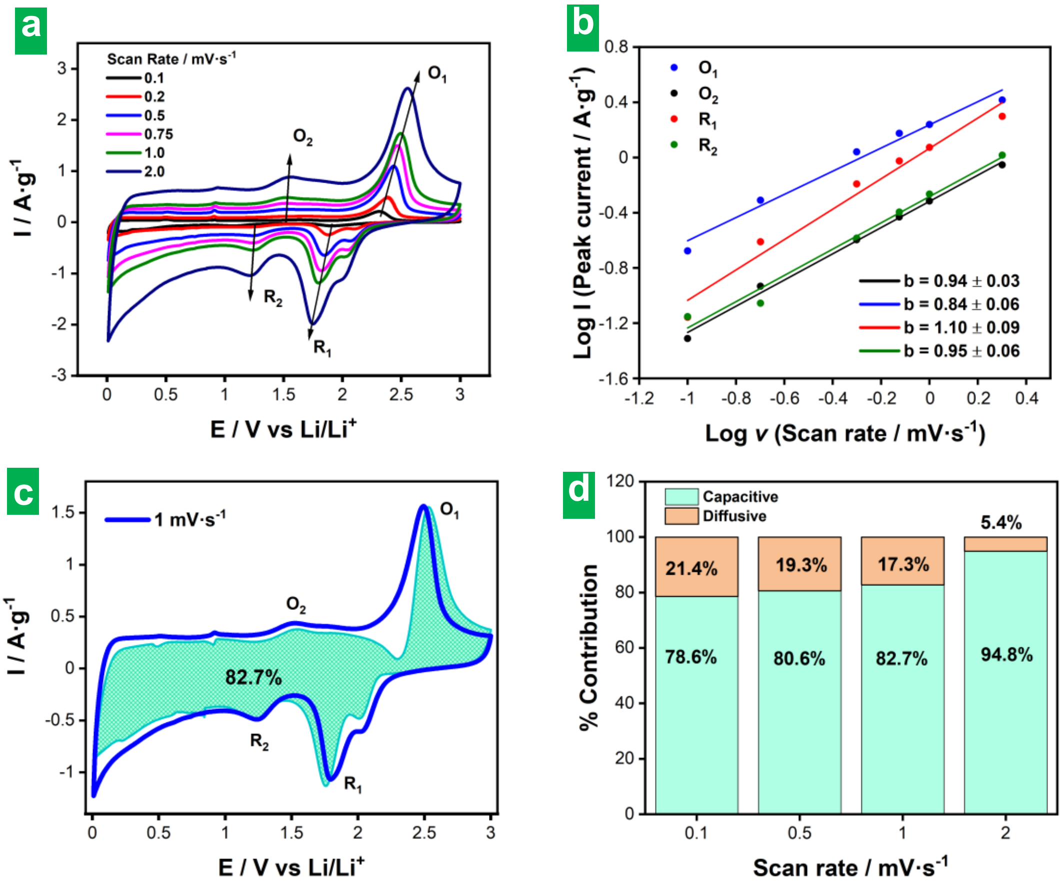

Figure 9. Kinetic analysis of the ee-MoS_2 electrode. (**a**) CVs recorded at several scan rates between 0.1 and 2 mV s^{-1}. (**b**) Determination of *b* values for the main redox peaks shown in (**a**). (**c**) Representation of (pseudo)capacitive contribution (green-shaded plot) to the CV recorded at 1 mV s^{-1} (blue plot). (**d**) Contributions from (pseudo)capacitive and diffusion-controlled processes to the total capacity of the electrode measured at different potential scan rates.

To further discriminate the (pseudo)capacitive and diffusion-controlled contributions to the measured current in the CVs, the following equation was employed for fitting routines

$$i = k_1 v + k_2 v^{1/2}, \qquad (8)$$

where the first (second) term on the right-hand side of the equation represents the (pseudo)capacitive (diffusion-controlled) contribution to the total measured current, and k_1 and k_2 are adjustable parameters [70,72]. Figure 9c shows the actual CV recorded at 1 mV s^{-1} together with its (pseudo)capacitive contribution as derived from Equation (8). In agreement with the results of the fitting of b parameters, (pseudo)capacitive processes totally dominated the charge storage behavior (82.7% of the total capacity). Figure 9d displays the contributions from (pseudo)capacitive and diffusion-controlled processes to the total capacity of the electrode measured at different potential scan rates. As expected for any material and previously found for this particular one from the results in Figure 6a, the contribution of (pseudo)capacitive processes to the total capacity increased with increasing potential scan rate. However, for the present ee-MoS_2 material, this contribution was already quite high at low rates (e.g., 78.6% at 0.1 mV s^{-1}). The latter was in contrast with typical results from MoS_2-based electrodes, which tend to exhibit lower contributions at low scan rates [71,73-75]. Again, this particular behavior of ee-MoS_2 could be ascribed to the smaller thickness and hence higher exposed area associated with the ee-MoS_2 NSs.

4. Conclusions

We have demonstrated a simple and straightforward method for the preparation of phase-preserved 2H-MoS_2 thin nanosheets through cathodic delamination of bulk MoS_2 crystals with suitable electrolytes. Specifically, trimethylalkylmamonium cations were shown to outperform bulkier tetraalkylammonium with substituents of equal length, which were the subject of previous studies, in accessing thinner nanosheets. On the one hand, the trimethylalkylammonium intercalants were large enough to prevent the intercalation of such a high number of cations that the corresponding electron injection would exceed the 2H to 1T transformation threshold for MoS_2. On the other hand, their smaller cross-section compared to tetraalkylammonium cations led to lower steric repulsion between the intercalated areas, promoting a more homogeneous and smoother intercalation that allowed obtaining thinner nanosheets after sonication of the expanded crystals. The higher flexibility and smaller thickness of MoS_2 nanosheets enabled electrode materials with lower electrical resistance and shorter pathways for solid-state diffusion, resulting in higher capacity, rate capability and cycle life as anodes for lithium storage.

Supplementary Materials: The following supporting information can be downloaded at: www.mdpi.com/xxx/s1. Figure S1: microscopic and spectroscopic characterization of ultrasound-assisted liquid-phase exfoliated MoS_2 colloidal dispersions. Figure S2: AFM characterization of cathodically exfoliated MoS_2 materials obtained using ammonium salts other than HTMABr as electrolyte. Figure S3: X-ray diffraction patterns of bulk and exfoliated MoS_2 materials. Figure S4: cyclic voltammograms and electrochemical impedance spectroscopy (EIS) of the exfoliated MoS_2 materials after long-term cycling. Figure S5: microscopic characterization of the ee-MoS_2 electrodes. Figure S6: post-mortem microscopic characterization of the ee-MoS_2 electrodes cycled at 0.2 A g^{-1}. Figure S7: post-mortem microscopic characterization of the ee-MoS_2 electrodes cycled at 0.5 A g^{-1}. Figure S8: post-mortem microscopic characterization of the lpe-MoS_2 electrodes cycled at 0.2 A g^{-1}. Supplementary Movies S1–S3: electrochemical expansion of MoS_2 over 30 min using HTMABr, TEACl and THACl as electrolytes, respectively.

Author Contributions: Conceptualization, A.M.-J., S.V.-R., E.R.-P. and J.I.P.; Data Curation: A.M.-J. and S.V.-R.; Formal Analysis, A.M.-J., S.V.-R., A.C.-M. and J.M.M.; Investigation, A.M.-J., S.V.-R. and J.M.M.; Methodology, J.I.P., S.V.-R., E.R.-P. and A.M.-J.; Validation: S.V.-R.; Software: A.C.-M. Project Administration, J.I.P.; Resources, J.N.C., E.R.-P. and J.I.P.; Supervision, S.V.-R., E.R.-P. and J.I.P.; Visualization, A.M.-J., J.M.M. and S.V.-R.; Writing—Original Draft, A.M.-J., S.V.-R. and J.I.P.; Writing—

Review and Editing, S.V.-R., J.M.M., E.R.-P. and J.I.P. All authors have read and agreed to the published version of the manuscript.

Funding: A.M.-J., S.V.-R. and J.I.P. gratefully acknowledge funding by the Spanish Ministerio de Ciencia e Innovación and Agencia Estatal de Investigación (MCIN/AEI/10.13039/501100011033), as well as the European Regional Development Fund (ERDF, A Way of Making Europe) through grant PID2021-125246OB-I00 and by Plan de Ciencia, Tecnología e Innovación (PCTI) 2018-2022 del Principado de Asturias and the ERDF through grant IDI/2021/000037. A.M.-J. is grateful to the Spanish MCIN for his pre-doctoral contract (PRE2019-087583). J.M.M. acknowledges funding from a Margarita Salas Fellowship from the Spanish Ministry of Universities (ref. MU-21-UP2021-03071726050).

Data Availability Statement: The raw data supporting the conclusions of this article will be made available by the authors upon request.

Acknowledgments: We are very grateful to Alaa Adawy from the Laboratory of High-resolution Transmission Electron Microscopy (Scientific and Technical Services, University of Oviedo) for her expert assistance with the HR-TEM and SAED measurements.

Conflicts of Interest: The authors declare no conflicts of interest. The funders had no role in the design of the study; in the collection, analyses, or interpretation of data; in the writing of the manuscript; or in the decision to publish the results.

References

1. Durmus, Y.E.; Zhang, H.; Baakes, F.; Desmaizieres, G.; Hayun, H.; Yang, L.; Kolek, M.; Küpers, V.; Janek, J.; Mandler, D.; et al. Side by side battery technologies with lithium-ion based batteries. *Adv Energy Mater.* **2020**, *10*, 2000089.

2. Armand, M.; Tarascon, J.-M. Building better batteries. *Nature* **2008**, *451*, 652–657.

3. Liu, Y.; Artyukhov, V.I.; Liu, M.; Harutyunyan, A.R.; Yakobson, B.I. Feasibility of lithium storage on graphene and its derivatives. *J. Phys. Chem. Lett.* **2013**, *4*, 1737–1742.

4. Du, C.; Zhao, Z.; Liu, H.; Song, F.; Chen, L.; Cheng, Y.; Guo, Z. The status of representative anode materials for lithium-ion batteries. *Chem. Rec.* **2023**, *23*. e2023000.

5. Goriparti, S.; Miele, E.; De Angelis, F.; Di Fabrizio, E.; Zaccaria, R.P.; Capiglia, C. Review on recent progress of nanostructured anode materials for Li-ion batteries. *J. Power Sources* **2014**, *257*, 421–443.

6. Bello, I.T.; Oladipo, A.O.; Adedokun, O.; Dhlamini, S.M. Recent advances on the preparation and electrochemical analysis of MoS_2-based materials for supercapacitor applications: A mini-review. *Mater Today Commun.* **2020**, *25*, 101664.

7. Liu, T.; Melinte, G.; Dolotko, O.; Knapp, M.; Mendoza-Sánchez, B. Activation of 2D MoS_2 electrodes induced by high-rate lithiation processes. *J. Energ. Chem.* **2023**, *78*, 56–70.

8. Backes, C.; Smith, R.J.; McEvoy, N.; Berner, N.C.; McCloskey, D.; Nerl, H.C.; O'Neill, A.; King, P.J.; Higgins, T.; Hanlon, D.; et al. Edge and confinement effects allow in situ measurement of size and thickness of liquid-exfoliated nanosheets. *Nat. Commun.* 2014, 5, 4576.

9. Stephenson, T.; Li, Z.; Olsen, B.; Mitlin, D. Lithium ion battery applications of molybdenum disulfide (MoS_2) nanocomposites. *Energ. Environ. Sci.* **2014**, *7*, 209–231.

10. Yuan, D.; Dou, Y.; Wu, Z.; Tian, Y.; Ye, K.H.; Lin, Z.; Dou, S.X.; Zhang, S. Atomically thin materials for next-generation rechargeable batteries. *Chem Rev.* **2022**, *122*, 957–999.

11. Wang, L.; Zhang, X.; Xu, Y.N.; Li, C.; Liu, W.J.; Yi, S.; Wang, K.; Sun, X.Z.; Wu, Z.-S.; Ma, Y.W. Tetrabutylammonium-intercalated 1T-MoS_2 nanosheets with expanded interlayer spacing vertically coupled on 2D delaminated MXene for high-performance lithium-ion capacitors. *Adv. Funct. Mater.* **2021**, *31*, 2104286.

12. Baheri, Y.T.; Hedayati, M.A.; Maleki, M.; Karimian, H. A vapor-liquid-solid mechanism for in-situ deposition of ultra-small hollow MoS_2 nanoparticles in N-doped carbon foam as an anode of lithium-ion batteries. *J. Energy Storage* **2023**, *68*, 107682.

13. Liu, S.; Jia, K.; Yang, J.; He, S.; Liu, Z.; Wang, X.; Qiu, J. Encapsulating flower-like MoS_2 nanosheets into interlayer of nitrogen-doped graphene for high-performance lithium-ion storage. *Chem. Eng. J.* **2023**, *475*, 146181.

14. Dang, L.; Yuan, Y.; Wang, Z.; Li, H.; Yang, R.; Fu, A.; Liu, X.; Li, H. Carbon nanofibers decorated by MoS_2 nanosheets with tunable quantity as self-supporting anode for high-performance lithium ion batteries. *Nanomaterials* **2023**, *13*, 2689.

15. Zuo, J.H.; Zhai, P.B.; He, Q.Q.; Wang, L.; Chen, Q.; Gu, X.K.; Yang, Z.L.; Gong, Y.J. In-situ constructed three-dimensional MoS_2–MoN heterostructure as the cathode of lithium–sulfur battery. *Rare Met.* **2022**, *41*, 1743–1752.

16. Zhang, Y.; Yao, Y.; Sendeku, M.G.; Yin, L.; Zhan, X.; Wang, F.; Wang, Z.; He, J. Recent progress in CVD growth of 2D transition metal dichalcogenides and related heterostructures. *Adv. Mater.* **2019**, *31*, 190169.

17. Xu, M.; Liang, T.; Shi, M.; Chen, H. Graphene-like two-dimensional materials. *Chem. Rev.* **2013**, *113*, 3766–3798.

18. Samadi, M.; Sarikhani, N.; Zirak, M.; Zhang, H.; Zhang, H.L.; Moshfegh, A.Z. Group 6 transition metal dichalcogenide nanomaterials: Synthesis, applications and future perspectives. *Nanoscale Horiz.* **2018**, *3*, 90–204.

19. Bertolazzi, S.; Brivio, J.; Kis, A. Stretching and breaking of ultrathin MoS_2. *ACS Nano* **2011**, *5*, 9703–9709.

20. Cai, X.; Luo, Y.; Liu, B.; Cheng, H.M. Preparation of 2D material dispersions and their applications. *Chem Soc Rev.* **2018**, *47*, 6224–6266.

21. Nicolosi, V.; Chhowalla, M.; Kanatzidis, M.G.; Strano, M.S.; Coleman, J.N. Liquid exfoliation of layered materials. *Science* **2013**, *340*, 1420.

22. Backes, C.; Szydłowska, B.M.; Harvey, A.; Yuan, S.; Vega-Mayoral, V.; Davies, B.R.; Zhao, P.L.; Hanlon, D.; Santos, E.J.G.; Katsnelson, M.I.; et al. Production of highly monolayer enriched dispersions of liquid-exfoliated nanosheets by liquid cascade centrifugation. *ACS Nano* **2016**, *10*, 1589–1601.

23. Schiettecatte, P.; Singh, S.; Zhou, P.; Hens, Z. The dynamic interaction of surfactants with colloidal molybdenum disulfide nanosheets calls for thermodynamic stabilization by solvents. *Langmuir* **2023**, *39*, 6568–6579.

24. Ambrosi, A.; Pumera, M. Exfoliation of layered materials using electrochemistry, *Chem. Soc. Rev.* **2018**, *47*, 7213–7224.

25. Li, F.; Xue, M.; Zhang, X.; Chen, L.; Knowles, G.P.; MacFarlane, D.R.; Zhang, J. Advanced composite 2D energy materials by simultaneous anodic and cathodic exfoliation. *Adv. Energy Mater.* **2018**, *8*, 1702794.

26. Yang, Y.; Hou, H.; Zou, G.; Shi, W.; Shuai, H.; Li, J.; Ji, X. Electrochemical exfoliation of graphene-like two-dimensional nanomaterials. *Nanoscale* **2019**, *11*, 16–33.

27. Eng, A.Y.S.; Ambrosi, A.; Sofer, Z.; Šimek, P.; Pumera, M. Electrochemistry of transition metal dichalcogenides: Strong dependence on the metal-to-chalcogen composition and exfoliation method. *ACS Nano* **2014**, *8*, 12185–12198.

28. Kim, T.I.; Kim, J.; Park, I.-J.; Cho, K.-O.; Choi, S.-Y. Chemically exfoliated 1T-phase transition metal dichalcogenide nanosheets for transparent antibacterial applications. *2D Mater* **2019**, *6*, 025025.

29. Peng, J.; Liu, Y.; Luo, X.; Wu, J.; Lin, Y.; Guo, Y.; Zhao, J.; Wu, X.; Wu, C.; Xie, Y. High phase purity of large-sized 1T′-MoS_2 monolayers with 2D superconductivity. *Adv. Mater.* **2019**, *31*, 1900568.

30. Ejigu, A.; Kinloch, I.A.; Prestat, E.; Dryfe, R.A.W. A simple electrochemical route to metallic phase trilayer MoS_2: Evaluation as electrocatalysts and supercapacitors. *J. Mater Chem. A* **2017**, *5*, 11316–11330.

31. Gan, X.; Lee, L.Y.S.; Wong, K.Y.; Lo, T.W.; Ho, K.H.; Lei, D.Y.; Zhao, H. 2H/1T Phase transition of multilayer MoS_2 by electrochemical incorporation of S vacancies. *ACS Appl. Energy Mater.* **2018**, *1*, 4754–4765.

32. Lei, Z.; Zhan, J.; Tang, L.; Zhang, Y.; Wang, Y. Recent development of metallic (1T) phase of molybdenum disulfide for energy conversion and storage. *Adv. Energy Mater.* **2018**, *8*, 1703482.

33. Li, J.; Song, P.; Zhao, J.; Vaklinova, K.; Zhao, X.; Li, Z.; Qiu, Z.; Wang, Z.; Lin, L.; Zhao, M.; et al. Printable two-dimensional superconducting monolayers. *Nat. Mater.* **2021**, *20*, 181–187

34. Lin, Z.; Liu, Y.; Halim, U.; Ding, M.; Liu, Y.; Wang, Y.; Jia, C.; Chen, P.; Duan, X.; Wang, C.; et al. Solution-processable 2D semiconductors for high-performance large-area electronics. *Nature* **2018**, *562*, 254–258.

35. Kong, L.; Li, G.; Su, Q.; Zhang, X.; Liu, Z.; Liao, G.; Sun, B.; Shi, T. Inkjet-printed, large-area, flexible photodetector array based on electrochemical exfoliated MoS_2 film for photoimaging. *Adv. Eng. Mater.* **2023**, *25*, 2200946.

36. Lin, Z.; Wan, Z.; Song, F.; Huang, B.; Jia, C.; Qian, Q.; Kang, J.S.; Wu, Y.; Yan, X.; Peng, L.; et al. High-yield exfoliation of 2D semiconductor monolayers and reassembly of organic/inorganic artificial superlattices. *Chem* **2021**, *7*, 1887–1902.

37. Wells, R.A.; Zhang, M.; Chen, T.H.; Boureau, V.; Caretti, M.; Liu, Y.; Yum, J.H.; Johnson, H.; Kinge, S.; Radenovic, A.; et al. High performance semiconducting nanosheets via a scalable powder-based electrochemical exfoliation technique. *ACS Nano* **2022**, *16*, 5719–5730.

38. Martínez-Jódar, A.; Villar-Rodil, S.; Salvadó, M.A.; Carrasco, D.F.; Pertierra, P.; Recio, J.M.; Paredes, J.I. Two-dimensional transition metal dichalcogenides beyond

MoS_2 for the catalytic reduction of nitroarenes: $MoSe_2$ exhibits enhanced performance. *Appl. Catal. B* **2023**, *339*, 123174.

39. Youssef, A.M.; Bishay, A.F.; Hammad, F.H. Determination of small surface areas by krypton adsorption. *Surf. Technol.* **1979**, *9*, 365–37.

40. García-Dalí, S.; Paredes, J.I.; Munuera, J.M.; Villar-Rodil, S.; Adawy, A.; Martínez-Alonso, A.; Tascón, J.M.D. Aqueous cathodic exfoliation strategy toward solution-processable and phase-preserved MoS_2 nanosheets for energy storage and catalytic applications. *ACS Appl. Mater. Interfaces* **2019**, *11*, 36991–37003.

41. Li, Y.; Duerloo, K.-A.N.; Wauson, K.; Reed, E.J. Structural semiconductor-to-semimetal phase transition in two-dimensional materials induced by electrostatic gating. *Nat. Commun.* **2016**, *7*, 10671.

42. Lotya, M.; Rakovich, A.; Donegan, J.F.; Coleman, J.N. Measuring the lateral size of liquid-exfoliated nanosheets with dynamic light scattering. *Nanotechnol.* **2013**, 24, 265703.

43. Zhang, X.; Qiao, X.-F.; Shi, W.; Wu, J.-B.; Jiang, D.-S.; Tan, P.-H. Phonon and Raman scattering of two-dimensional transition metal dichalcogenides from monolayer, multilayer to bulk Material. *Chem. Soc. Rev.* **2015**, 44, 2757–2785.

44. Eda, G.; Yamaguchi, H.; Voiry, D.; Fujita, T.; Chen, M.; Chhowalla, M. Photoluminescence from chemically exfoliated MoS_2. *Nano Lett.* **2011**, 11, 5111–5116.

45. Gabbett, C.; Doolan, L.; Synnatschke, K.; Gambini, L.; Coleman, E.; Kelly, A.G.; Liu, S.; Caffrey, E.; Munuera, J.; Catriona, M.; et al. Quantitative analysis of printed nanostructured networks using high-resolution 3D FIB-SEM nanotomography. *Nat. Commun.* **2024**, 15, 278.

46. Shi, H.; Li, M.; Nia, A.S.; Wang, M.; Park, S.; Zhang, Z.; Lohe, M.R.; Yang, S.; Feng, X. Ultrafast electrochemical synthesis of defect-free In_2Se_3 flakes for large-area optoelectronics. *Adv. Mater.* **2020**, 32, 1907244.

47. Wang, C.; He, Q.; Halim, U.; Liu, Y.; Zhu, E.; Lin, Z.; Xiao, H.; Duan, X.; Feng, Z.; Cheng, R.; et al. Monolayer atomic crystal molecular superlattices. *Nature* **2018**, 555, 231–236.

48. Ma, Y. Past, present and future of carbon nanotubes and graphene based electrode materials for energy storage batteries. *Int. J. Electrochem. Sci.* **2000**, 15, 10315–10329.

49. Cheng, Y.; Nie, A.; Zhang, Q.; Gan, L.Y.; Shahbazian-Yassar, R.; Schwingenschlogl, U. Origin of the phase transition in lithiated molybdenum disulfide. *ACS Nano* **2014**, 8, 11447–11453.

50. An, S.J.; Li, J.; Daniel, C.; Mohanty, D.; Nagpure, S.; Wood, D.L. The state of understanding of the lithium-ion-battery graphite solid electrolyte interphase (SEI) and its relationship to formation cycling. *Carbon* **2016**, 105, 52–76.

51. Zhao, T.; Shu, H.; Shen, Z.; Hu, H.; Wang, J.; Chen, X. Electrochemical lithiation mechanism of two-dimensional transition-metal dichalcogenide anode materials: Intercalation versus conversion reactions. *J. Phys. Chem. C* **2019**, 123, 2139–2146.

52. Zhang, L.; Sun, D.; Feng, J.; Cairns, E.J.; Guo, J. Revealing the electrochemical charging mechanism of nanosized Li_2S by in situ and operando X-ray absorption spectroscopy. *Nano Lett.* **2017**, 17, 5084–5091.

53. Lin, H.; Yang, L.; Jiang, X.; Li, G.; Zhang, T.; Yao, Q.; Zheng, G.W.; Lee, J.Y. Electrocatalysis of polysulfide conversion by sulfur-deficient MoS_2 nanoflakes for lithium-sulfur batteries. *Energy Environ. Sci.* **2017**, 10, 1476–1486.

54. Budumuru, A.K.; Rakesh, B.; Sudakar, C. Enhanced high rate capability of Li intercalation in planar and edge defect-rich MoS_2 nanosheets. *Nanoscale* **2019**, 11, 8882–8897.

55. Zhu, Z.; Xi, S.; Miao, L.; Tang, Y.; Zeng, Y.; Xia, H.; Lv, Z.; Zhang, W.; Ge, X.; Zhang, H.; et al. Unraveling the formation of amorphous MoS_2 nanograins during the electrochemical delithiation process. *Adv. Funct. Mater.* **2019**, 29, 1904843.

56. He, Q.; Lin, Z.; Ding, M.; Yin, A.; Halim, U.; Wang, C.; Liu, Y.; Cheng, H.C.; Huang, Y.; Duan, X. In situ probing molecular intercalation in two-dimensional layered semiconductors. *Nano Lett.* 2019, 19, 6819–6826.

57. Wei, C.Y.; Lee, P.C.; Tsao, C.W.; Lee, L.H.; Wang, D.Y.; Wen, C.Y. In situ scanning electron microscopy observation of MoS_2 nanosheets during lithiation in lithium ion batteries. *ACS Appl. Energy Mater.* **2020**, 3, 7066–7072.

58. Zhang, L.; Sun, D.; Kang, J.; Feng, J.; Bechtel, H.A.; Wang, L.W.; Cairns, E.J.; Guo, J. Electrochemical reaction mechanism of the MoS_2 electrode in a lithium-ion cell revealed by in situ and operando x-ray absorption spectroscopy. *Nano Lett.* **2018**, 18, 1466–1475.

59. Choi, W.; Choi, Y.S.; Kim, H.; Yoon, J.; Kwon, Y.; Kim, T.; Ryu, J.H.; Lee, J.H.; Lee, W.; Huh, J.; et al. Evidence for the coexistence of polysulfide and conversion reactions in the lithium storage mechanism of MoS_2 anode material. *Chem. Mater.* **2021**, 33, 1935–1945.

60. Zhang, T.; Zhang, L.; Zhao, L.; Huang, X.; Hou, Y. Catalytic effects in the cathode of Li-S batteries: Accelerating polysulfides redox conversion. *EnergyChem* **2020**, 2, 100036.

61. Fleischmann, S.; Mitchell, J.B.; Wang, R.; Zhan, C.; Jiang, D.E.; Presser, V.; Augustyn, V. Pseudocapacitance: From fundamental understanding to high power energy storage materials. *Chem. Rev.* **2020**, 120, 6738–6782.

62. Kelly, A.G.; O'Suilleabhain, D.; Gabbett, C.; Coleman, J.N. The electrical conductivity of solution-processed nanosheet networks. *Nat. Rev. Mater.* **2021**, 7, 217–234.

63. Du, G.; Guo, Z.; Wang, S.; Zeng, R.; Chen, Z.; Liu, H. Superior stability and high capacity of restacked molybdenum disulfide as anode material for lithium ion batteries. *Chem. Commun.* **2010**, 46, 1106–1108.

64. Laschuk, N.O.; Easton, E.B.; Zenkina, O.V. Reducing the resistance for the use of electrochemical impedance spectroscopy analysis in materials chemistry. *RSC Adv*. **2021**, 11, 27925–27936.

65. Subramanian, Y.; Veerasubramani, G.K.; Park, M.-S.; Kim, D.-W. Investigation of layer structured $NbSe_2$ as an intercalation anode material for sodium-ion hybrid capacitors. *J. Electrochem. Soc*. **2019**, 166, A598–A604.

66. Zhou, F.; Xin, S.; Liang, H.W.; Song, L.T.; Yu, S.H. Carbon nanofibers decorated with molybdenum disulfide nanosheets: Synergistic lithium storage and enhanced electrochemical performance. *Angew. Chem.-Int. Edit*. **2014**, 53, 11552–11556.

67. Mendoza-Sánchez, B.; Gogotsi, Y. Synthesis of two-dimensional materials for capacitive energy storage. *Adv. Mater*. **2016**, 28, 6104–6135.

68. Augustyn, V.; Simon, P.; Dunn, B. Pseudocapacitive oxide materials for high-rate electrochemical energy storage. *Energy Environ. Sci*. **2014**, 7, 1597–1614.

69. Choi, C.; Ashby, D.S.; Butts, D.M.; DeBlock, R.H.; Wei, Q.; Lau, J.; Dunn, B. Achieving high energy density and high power density with pseudocapacitive materials. *Nat. Rev. Mater*. **2019**, 5, 5–19.

70. Wang, J.; Polleux, J.; Lim, J.; Dunn, B. Pseudocapacitive contributions to electrochemical energy storage in TiO_2 (anatase) nanoparticles. *J. Phys. Chem. C* **2007**, 111, 14925–14931.

71. Li, Z.; Ottmann, A.; Sun, Q.; Kast, A.K.; Wang, K.; Zhang, T.; Meyer, H.P.; Backes, C.; Kübel, C.; Schröder, R.R.; et al. Hierarchical MoS_2 -carbon porous nanorods towards atomic interfacial engineering for high-performance lithium storage. *J. Mater. Chem. A* **2019**, 7, 7553–7564.

72. Augustyn, V.; Come, J.; Lowe, M.A.; Kim, J.W.; Taberna, P.-L.; Tolbert, S.H.; Abruña, H.D.; Simon, P.; Dunn, B. High-rate electrochemical energy storage through Li^+ intercalation pseudocapacitance. *Nat. Mater*. **2013**, 12, 518–522.

73. Cao, M.; Feng, Y.; Zhang, P.; Yang, L.; Gu, X.; Yao, J. Synthesis of MoS_2 nanotube using a sacrificial template method as advanced anode material for lithium-ion batteries. *J. Alloys Compd*. **2022**, 907, 164499.

74. Liu, X.; Zhang, X.; Ma, S.; Tong, S.; Han, X.; Wang, H. Flexible amorphous MoS_2 nanoflakes/N-doped carbon microtubes/reduced graphite oxide composite paper as binder free anode for full cell lithium ion batteries. *Electrochim. Acta* **2020**, 333, 135568.

75. Zhang, R.; Tang, Z.; Wang, H.; Sun, D.; Tang, Y.; Xie, Z. The fabrication of hierarchical MoO_2@MoS_2/rGO composite as high reversible anode material for lithium ion batteries. *Electrochim. Acta* **2020**, 364, 136996.

Supplementary Material

Two-Dimensional MoS_2 Nanosheets Derived from Cathodic Exfoliation for Lithium Storage Applications

Alberto Martínez-Jódar [1,2], Silvia Villar-Rodil [1,], José M. Munuera [3,4], Alberto Castro-Muñiz [1], Jonathan N. Coleman [4], Encarnación Raymundo-Piñero [2] and Juan I. Paredes [1,*]*

[1] *Instituto de Ciencia y Tecnología del Carbono, INCAR-CSIC, Francisco Pintado Fe 26, 33011 Oviedo, Spain; alberto.mj@incar.csic.es (A.M.-J.); alberto@incar.csic.es (A.C.-M.).*

[2] *CEMHTI UPR3079, University of Orléans, CNRS, 1D avenue de la Recherche Scientifique, 45071, Orléans, France; encarnacion.raymundo@cnrs-orleans.fr.*

[3] *Department of Physics, Faculty of Sciences, University of Oviedo, C/ Leopoldo Calvo Sotelo, 18, 33007 Oviedo, Spain; munuerajose@uniovi.es (J.M.M.).*

[4] *School of Physics, CRANN and AMBER Research Centre, Trinity College Dublin, D02 E8C0 Dublin, Ireland; colemaj@tcd.ie (J.N.C.).*

[*] Correspondence: silvia@incar.csic.es (S.V.-R.), paredes@incar.csic.es (J.I.P.).

S1. Additional characterization of the exfoliated MoS_2 materials

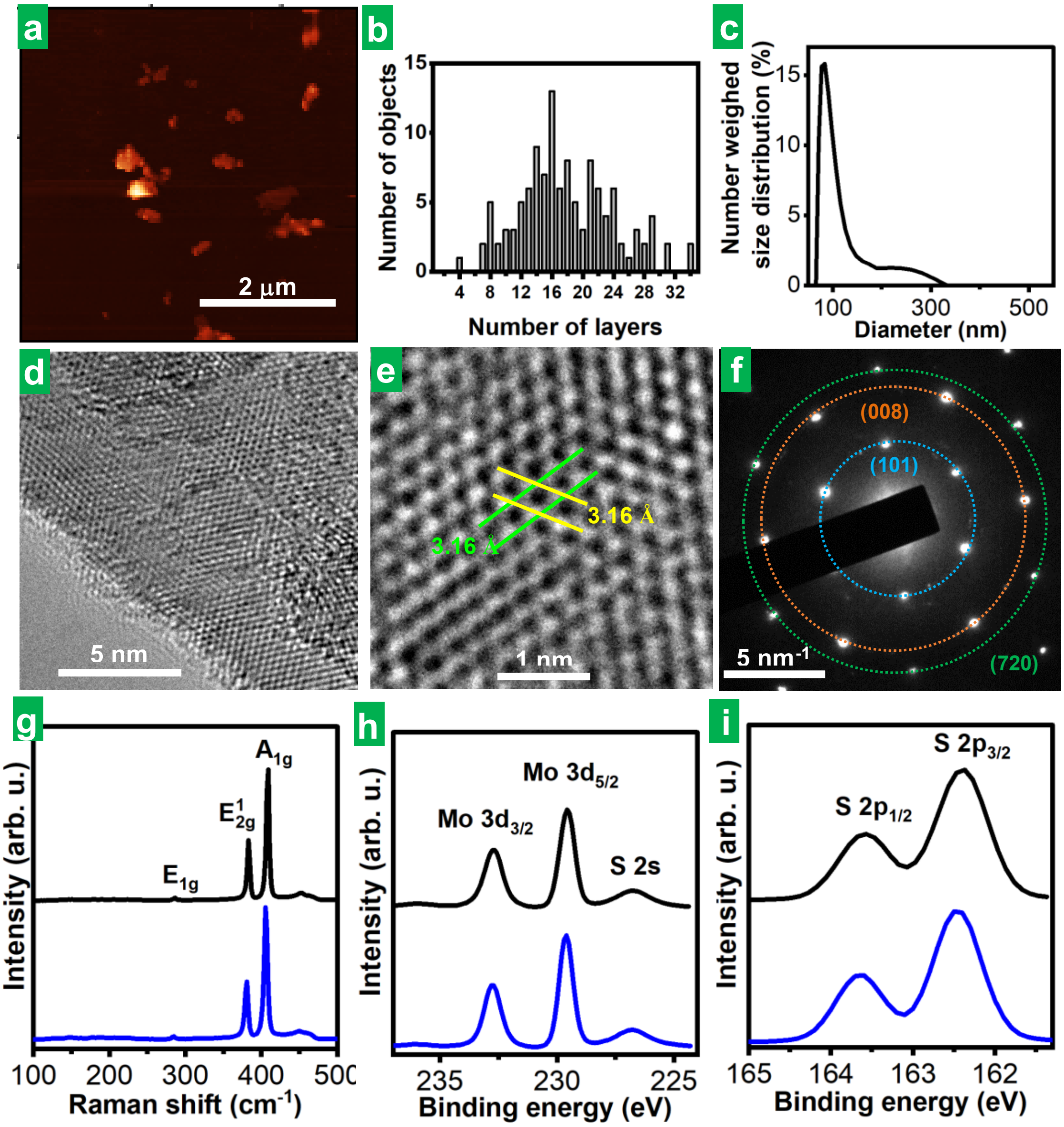

Figure S1. Microscopic and spectroscopic characterization of ultrasound-assisted liquid-phase exfoliated MoS_2 colloidal dispersions. (a) Representative AFM image of the MoS_2 nanosheets deposited onto a Si/SiO_2 substrate from dispersion. **(b)** Histograms of apparent thickness of MoS_2 nanosheets derived from a pool of over 100 nanosheets measured from AFM images. **(c)** DLS-derived number-weighed hydrodynamic diameter distribution for MoS_2 dispersion in DMF. **(d,e)** Representative HR-TEM images of the MoS_2 basal planes at different magnifications. The parallel lines in (e) assist in visualizing *a* and *b* cell parameters in the hexagonal cell of MoS_2 lattice. **(f)** SAED pattern of the MoS_2 lattice with indication of the families of planes involved in the observed diffractions. **(g)** Typical Raman spectra of the starting MoS_2 bulk powder (black trace) and liquid-phase exfoliated MoS_2 (blue trace). **(h, i)** Typical XPS spectra of (h) Mo 3d and (i) S 2p core levels for bulk MoS_2 powder (black trace) and liquid-phase exfoliated (blue trace) MoS_2 NSs. The main bands have been labeled for clarity.

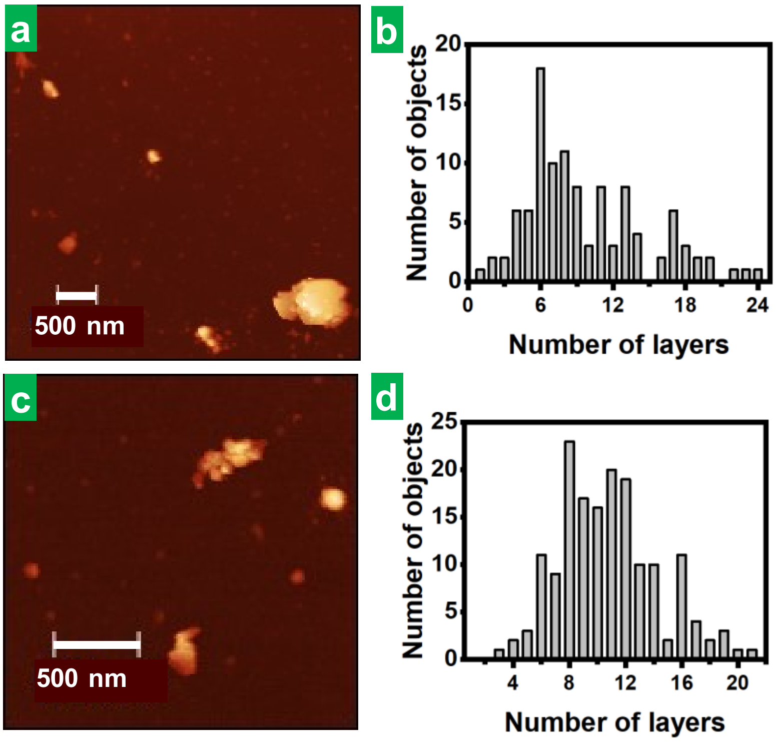

Figure S2. AFM characterization of cathodically exfoliated MoS_2 materials obtained using ammonium salts other than HTMABr as electrolyte. Representative AFM images of the MoS_2 nanosheets deposited onto a Si/SiO_2 substrate from dispersions prepared using **(a)** $HTHABF_4$ and **(c)** TMOABr as electrolytes. Histograms of apparent thickness of MoS_2 nanosheets derived from a pool of over 100 nanosheets measured from AFM images for materials obtained using **(b)** $HTHABF_4$ and **(d)** TMOABr as electrolytes.

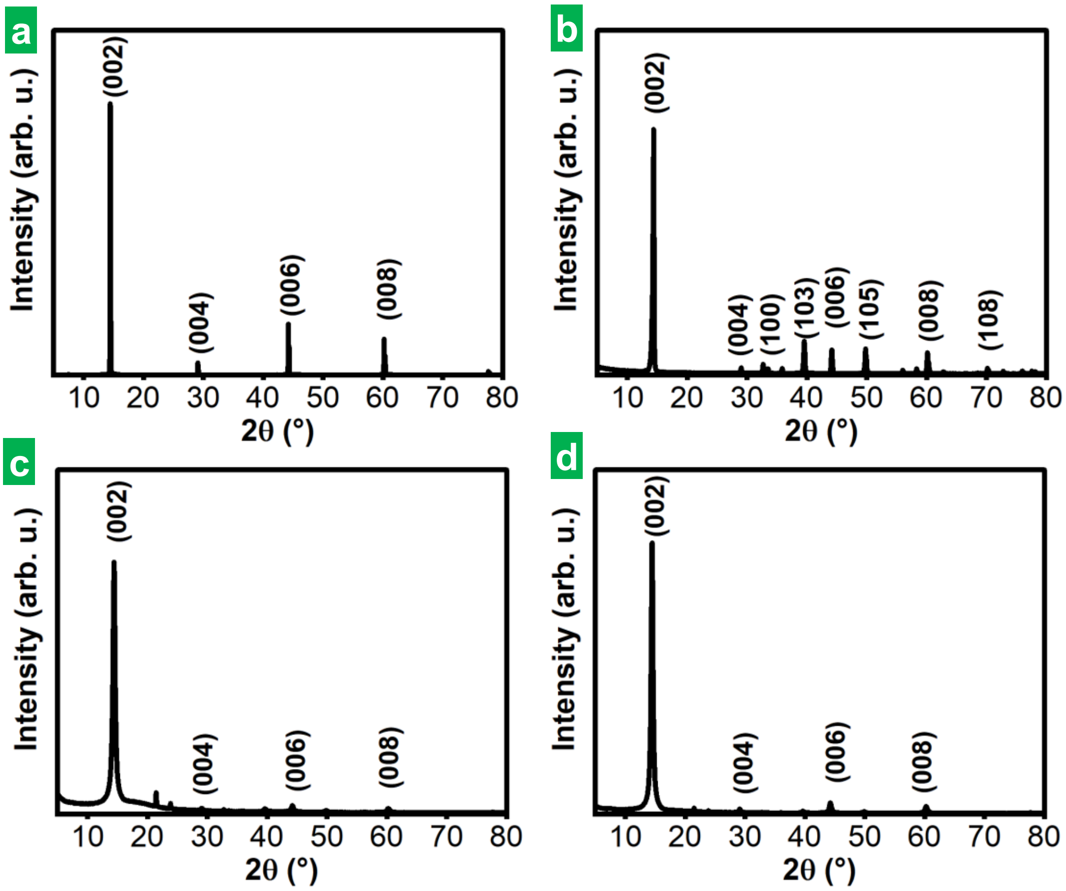

Figure S3. X-ray diffraction (XRD) patterns of bulk and exfoliated MoS_2 materials. X-ray diffraction patterns of both MoS_2 parent materials, namely, **(a)** bulk crystal and **(b)** bulk powder, as well as of films prepared from dispersions of exfoliated materials derived from them: **(c)** electrochemically exfoliated and **(d)** liquid-phase exfoliated MoS_2 nanosheets, respectively. The XRD peaks have been labelled according to JCPDS card 37-1492.

S2. Additional electrochemical characterization of the electrodes based on exfoliated MoS_2

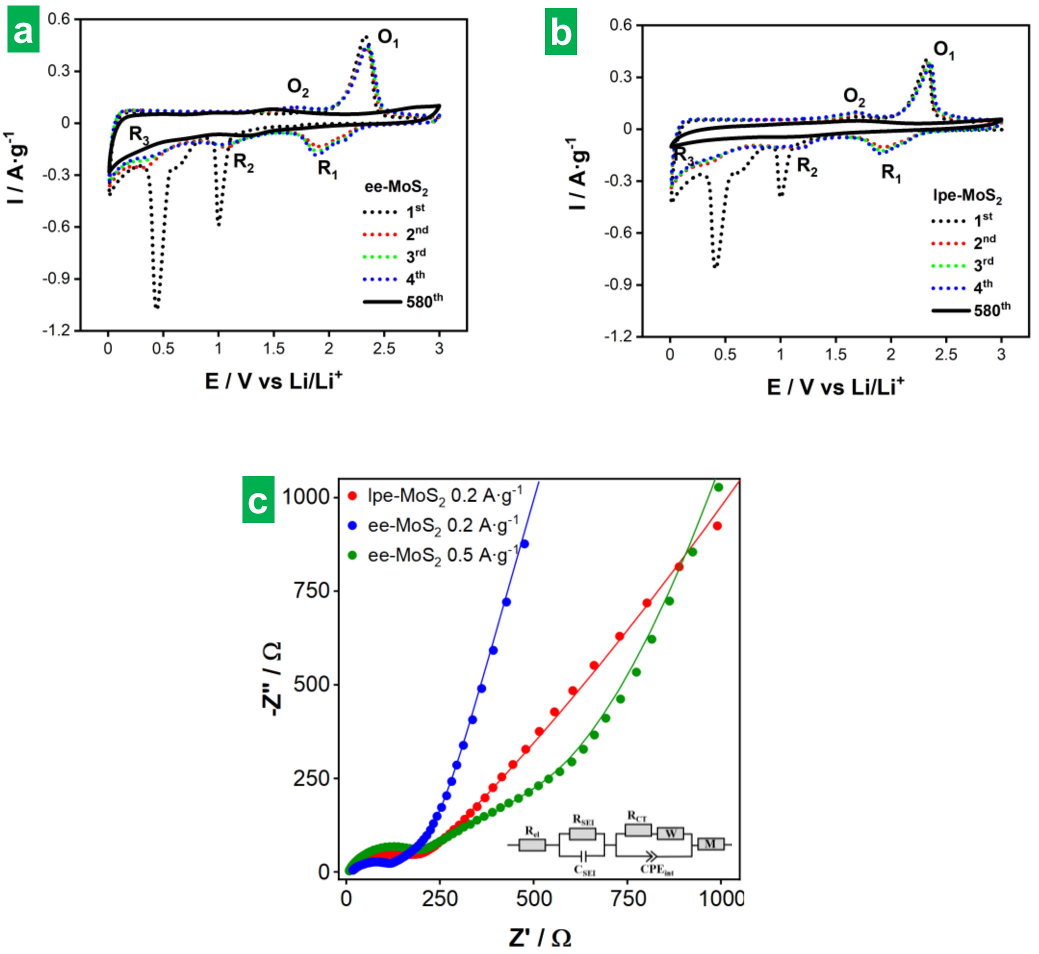

Figure S4. Cyclic voltammograms (CVs) and Electrochemical impedance spectroscopy (EIS) of the exfoliated MoS_2 materials after long-term cycling. CVs of the first four (dotted trace) and after long-term cycling (solid trace) of **(a)** ee-MoS_2 and **(b)** lpe-MoS_2 electrodes. Scan rate: 0.2 mV s^{-1}. **(c)** EIS Nyquist plots after the long-term cycling for ee-MoS_2 electrode at 0.2 A g^{-1} (blue circles) and 0.5 A g^{-1} (green circles), and for lpe-MoS_2 electrode at 0.2 A g^{-1} (red circles). The fitting of the experimental data to the indicated electrical equivalent circuit used for data modelling is shown in solid traces of the same color as the corresponding experimental data.

S3. Post-mortem studies of the electrodes based on exfoliated MoS_2

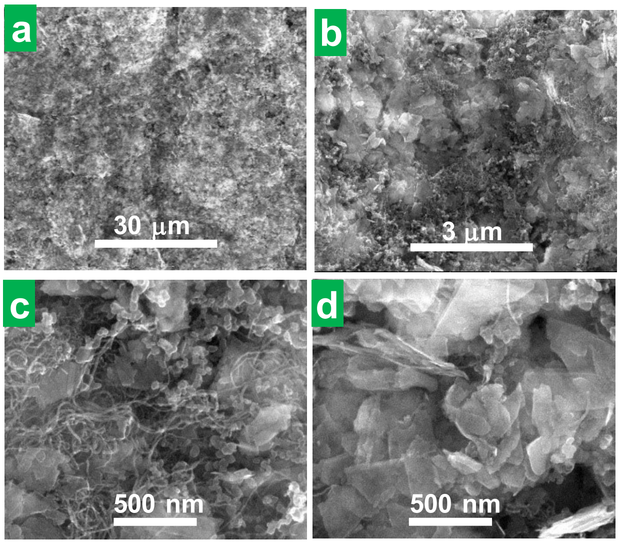

Figure S5. Microscopic characterization of the ee-MoS_2 electrodes. FE-SEM images of the starting ee-MoS_2 electrode at different magnifications.

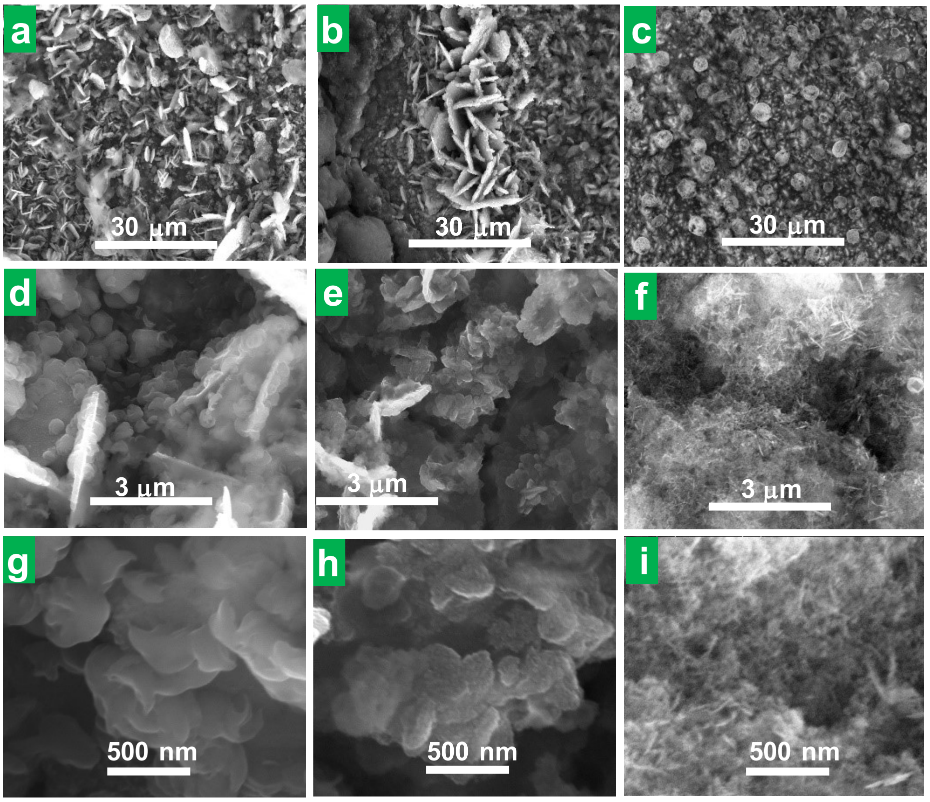

Figure S6. Post-mortem microscopic characterization of the ee-MoS_2 electrodes cycled at 0.2 A g^{-1}. FE-SEM images of the ee-MoS_2 electrodes after long-term cycling at 0.2 A g^{-1} showing varied morphologies at different magnifications.

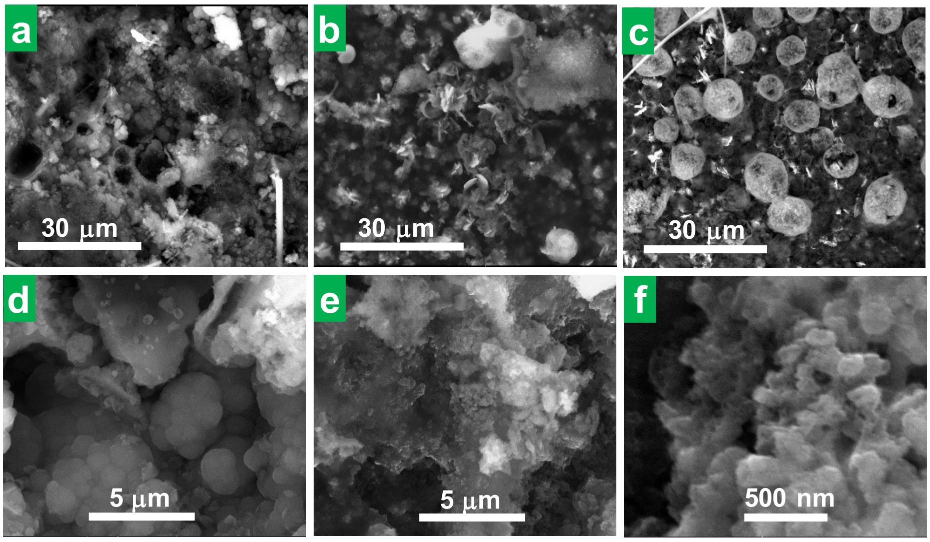

Figure S7. Post-mortem microscopic characterization of the ee-MoS$_2$ electrodes cycled at 0.5 A g^{-1}. FE-SEM images of the ee-MoS$_2$ electrodes after long-term cycling at 0.5 A g^{-1} showing varied morphologies at different magnifications.

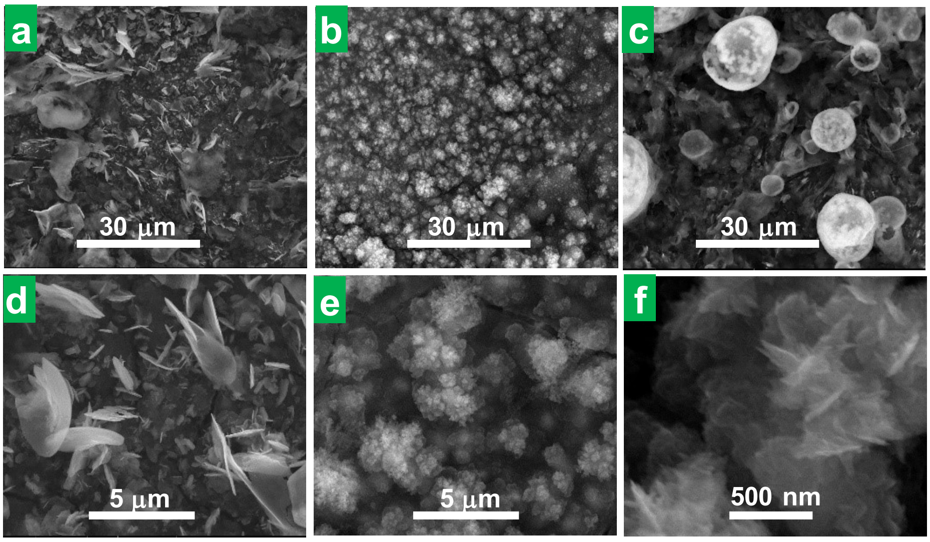

Figure S8. Post-mortem microscopic characterization of the lpe-MoS$_2$ electrodes cycled at 0.2 A g^{-1}. FE-SEM images of the lpe-MoS$_2$ electrodes after long-term cycling at 0.2 A g^{-1}, showing varied morphologies at different magnifications, namely: **(a,d)** microlamellae, **(c)** microspheres and **(b,e,f)** nanoflower-like microstructure

Resumen de Artículo II

Molecular Functionalization of 2H-Phase MoS_2 Nanosheets via an Electrolytic Route for Enhanced Catalytic Performance. *ACS Applied Materials Interfaces*, 13 (2021), 33157-33171.

S. García-Dalí, J.I. Paredes, S. Villar-Rodil, **A. Martínez-Jódar**, A. Martínez-Alonso, and J. M. D. Tascón.

El MoS_2 2D también encuentra aplicaciones relevantes en el campo de la catálisis (reducción de nitroarenos) y la electrocatálisis (HER y reducción de O_2, CO_2 y N_2). La principal motivación del uso de TMDs como (electro)catalizadores alternativos a los basados en metales nobles (típicamente utilizados en estos procesos) radica en la mayor abundancia y asequibilidad de los primeros. La aplicación de los catalizadores de MoS_2 2D en dispersión coloidal en procesos en fase acuosa está condicionada por su estabilidad coloidal en dicho medio. Por ello, en el **artículo II**, se ha desarrollado un método sencillo de funcionalización electroquímica de nanoláminas de MoS_2 orientado a la mejora de la estabilidad coloidal de MoS_2 en medio acuoso para su uso como catalizador de la reducción de nitroarenos y colorantes orgánicos, relevante tanto en la descontaminación de agua como en la síntesis de ciertos fármacos. Concretamente, las nanoláminas se funcionalizaron con grupos acético y anilina mediante reacción con los correspondientes organoioduros, obteniéndose nanoláminas de MoS_2 con estabilidad coloidal mejorada en agua.

El estudio detallado del mecanismo de funcionalización reveló que ocurría gracias al suministro externo de electrones, provenientes del potencial catódico aplicado (aunque también podían ser suministrados por un agente reductor adecuado); así como a la presencia de defectos intrínsecos (vacantes de S) en el plano basal de las nanoláminas de MoS_2, donde pueden anclarse los grupos funcionales. Las nanoláminas de MoS_2 funcionalizadas con ácido acético se estudiaron como catalizadores de la reducción de varios nitroarenos y colorantes orgánicos, demostrando una actividad catalítica significativamente mayor que otros catalizadores basados en MoS_2 (fase 1T o 2H) previamente descritos. También se pudo correlacionar el orden de la reacción de reducción con la carga eléctrica neta de las moléculas de sustrato, que influye en la capacidad de difusión de las estas hasta la superficie del catalizador. Con vistas a la aplicación práctica de las nanoláminas de MoS_2 como catalizadores, se comprobó que las nanoláminas funcionalizadas mantenían una buena eficiencia catalítica a concentraciones realistas de nitroarenos (del orden de las encontradas en aguas residuales) y en mezclas binarias y ternarias de tales reactivos. Además, para facilitar su manipulación y reutilización, las nanoláminas pudieron ser inmovilizadas en un soporte polimérico.

ARTÍCULO II

Molecular functionalization of 2H-phase MoS_2 nanosheets via an electrolytic route for enhanced catalytic performance

S. García-Dalí, J.I. Paredes*, S. Villar-Rodil*, A. Martínez-Jódar, A. Martínez-Alonso, J.M.D. Tascón

Instituto de Ciencia y Tecnología del Carbono, INCAR-CSIC, Francisco Pintado Fe 26, 33011 Oviedo, Spain

* Corresponding author: paredes@incar.csic.es (J. I. Paredes),

* Corresponding author: silvia@incar.csic.es (S. Villar-Rodil)

Abstract

The molecular functionalization of two-dimensional MoS_2 is of practical relevance with a view to, e.g., facilitating its liquid-phase processing or enhancing its performance in target applications. While derivatization of metallic 1T-phase MoS_2 nanosheets has been relatively well studied, progress involving their thermodynamically stable, 2H-phase counterpart has been more limited due to the lower chemical reactivity of the latter. Here, we report a simple electrolytic strategy to functionalize 2H-phase MoS_2 nanosheets with molecular groups derived from organoiodides. Upon cathodic treatment of a pre-expanded MoS_2 crystal in an electrolyte containing the organoiodide, water-dispersible nanosheets derivatized with acetic acid or aniline moieties (~0.10 molecular groups inserted per surface sulfur atom) were obtained. Analysis of the functionalization process indicated it to be enabled by the external supply of electrons from the cathodic potential, although they could also be sourced from a proper reducing agent, as well as by the presence of intrinsic defects in the 2H-phase MoS_2 lattice (e.g., sulfur vacancies), where the molecular groups can bind. The acetic acid-functionalized nanosheets were tested as a non-noble metal-based catalyst for nitroarene and organic dye reduction, which is of practical utility in environmental remediation and chemical synthesis, and exhibited a markedly enhanced activity, surpassing that of other (1T- or 2H-phase) MoS_2 materials and most non-noble metal catalysts previously reported for this application. The reduction kinetics (reaction order) was seen to correlate with the net electric charge of the nitroarene/dye molecules, which was ascribed to the distinct abilities of the latter to diffuse to the catalyst surface. The functionalized MoS_2 catalyst also worked efficiently at realistic (i.e., high) reactant concentrations as well as with binary and ternary mixtures of the reactants, and could be immobilized on a polymeric scaffold to expedite its manipulation and re-use.

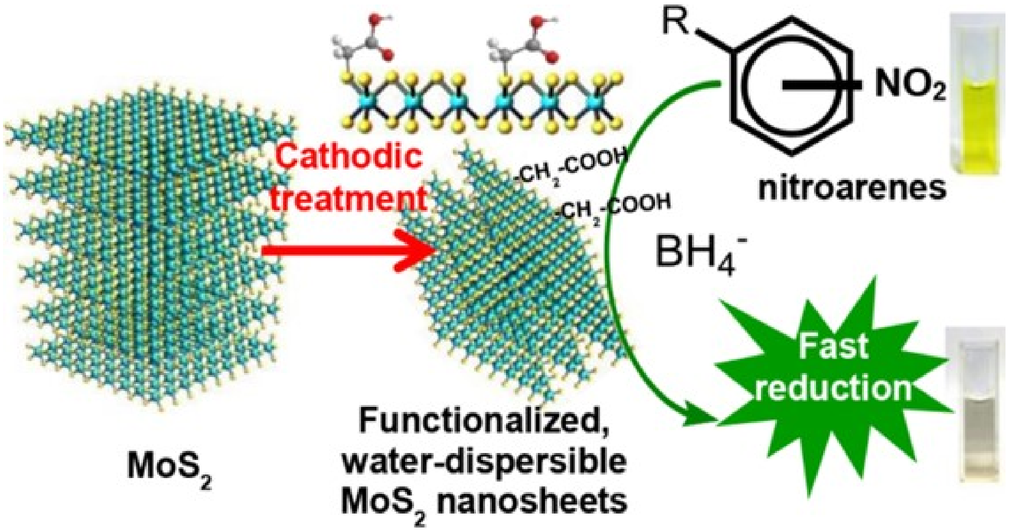

Keywords: Two-dimensional (2D) material; transition metal dichalcogenides (TMDs); MoS_2; electrochemical exfoliation; colloidal dispersion; functionalization; catalytic reduction.

1. Introduction

Over the last decade, layered transition metal dichalcogenides (TMDs) in the form of nanosheets (NSs) have become one of the most intensively investigated members from the family of two-dimensional (2D) materials. Such a strong interest in 2D TMDs is rooted in their unique and wide-ranging physical properties as well as in their considerable promise for impactful applications in many key technological areas, including (opto)electronics, (photo/electro)catalysis, electrochemical energy storage, chemical sensing and biomedicine.[1] While these 2D compounds can be useful for many practical purposes already in their pristine, unmodified configuration, it is generally accepted that reaching their full potential will require resorting to chemically modified variants, which can be accessed through heteroatom doping[2] or molecular functionalization.[3,4] For instance, substitutional doping of TMD NSs with selected heteroatoms (mainly other transition metal and chalcogen atoms, but also phosphorus, nitrogen or chlorine) allows fine-tuning their electronic structure and, as a result, can lead to enhanced performance when they are used as components of electronic devices or as electrocatalysts for industrially relevant reactions (e.g., hydrogen evolution).[2] Likewise, functionalization with proper molecular groups is an effective means to engineer the interaction of 2D TMDs with their surrounding environment, which facilitates their colloidal dispersion and processing in the liquid phase, their detection of analytes with high sensitivity and selectivity in sensing applications or their uptake by cells when used as a carrier for drug delivery, to name a few examples.[4]

The molecular functionalization of 2D TMD NSs can be carried out by either physisorption (non-covalent) or chemisorption (covalent) strategies.[4,5] The former are particularly widespread as a tool to improve their dispersibility in solvents or to modulate their charge carrier density, and rely on van der Waals and/or charge transfer interactions to incorporate surfactants, polymers and other (bio)molecules on the TMD surface. Chemisorption approaches, on the other hand, are comparatively much less prevalent. At least for the most commonly explored 2D TMDs, i.e., mainly MoS_2 but also WS_2 or $MoSe_2$, this fact can be attributed to the general lack of dangling bonds on their pristine basal surface and to the semiconducting nature of their thermodynamically stable 2H phase. Such features imply that these 2H-phase TMDs are rather chemically inert and thus not especially prone to take part in bond-forming processes.[3] To circumvent this limitation, researchers have turned to the 1T(or 1T′)-phase counterparts of 2D MoS_2, WS_2 or $MoSe_2$. The latter are metallic in nature (i.e., more electron-rich) and tend to possess substantial amounts of structural defects and imperfections (chalcogen vacancies, cracks, pinholes) as a result of their preparation mode (typically, lithium intercalation/exfoliation routes), making them considerably more reactive than their 2H-phase equivalents.[4,6,7] As a matter of fact, these metallic 1T-phase TMDs have been successfully functionalized via reaction with organothiols,[6] organoiodides[8,9] and aryl diazonium salts.[10]

Although metallic 1T-phase TMD NSs and their chemically functionalized derivatives are relevant materials on their own merit,[11,12] they suffer from a number of drawbacks when compared to their 2H-phase versions. These include structural instability (the 1T phase is metastable), higher propensity to environmental oxidation and degradation, or more stringent preparation conditions (e.g., need to work under inert atmosphere during the lithium intercalation step).[11] By heat treatment at moderate temperatures (~150–300 ºC), the functionalized 1T-phase NSs can in some cases be converted back to the 2H phase while retaining at the same time many of their grafted molecular groups.[8,9] Still, the multi-step nature of the overall process makes it unattractive with a view to its practical implementation. Hence, several research efforts have been made in recent years to explore the direct covalent functionalization of semiconducting 2H-phase TMDs, especially MoS_2. As a result, the derivatization of 2H-phase MoS_2 NSs using organothiols or dithiolanes,[13,14] aryl diazonium salts,[15] metal complexes[16] and maleimides[17] has been shown to be feasible, mainly by drawing on common organic chemistry protocols carried out in non-aqueous solvents (alcohols, acetonitrile). It is noteworthy, however, that despite their potential intrinsic advantages, except for a very recent report,[18] electrochemical or electrolytic methods for the functionalization of 2D TMDs (either 2H- or 1T-phase) have not yet been documented. Electrochemical strategies for molecular functionalization, and more generally for organic synthesis, are often more attractive than their classical, reagent-based counterparts in terms of, e.g., atom economy and environmental friendliness (chemical redox agents being replaced by electrons) or industrial scalability, particularly if carried out in water.[19] Thus, the availability of electrolytic routes towards chemically derivatized 2D TMDs could ease the deployment of such materials in practical uses.

Here, we address this gap and report the electrolytic functionalization of 2H-phase MoS_2 NSs based on their reaction with organoiodides. While metallic 1T-phase MoS_2 has been previously derivatized with this type of reagents via direct reaction, the latter was thought to be made possible by the presence of excess electrons in the NSs derived from the lithium intercalation step as well as by the relatively high chemical reactivity associated to the metallic phase.[7–9] None of these features can be found a priori in semiconducting 2H-phase MoS_2. However, we show that with an external supply of electrons (typically in the form of an electrical current, although proper reducing agents can also be used), the functionalization of semiconducting MoS_2 NSs with organoiodides is possible. Importantly, we also demonstrate this derivatization route to be highly beneficial for the 2H-phase MoS_2 NSs application-wise. Specifically, the functionalized NSs exhibited a much enhanced performance when used as a catalyst for the reduction of nitroarenes and organic dyes, with catalytic activity values that surpassed not only those of most previously reported MoS_2-based catalysts, but also those of most non-noble metal-based catalysts in general. Thus, the present work illustrates both the feasibility of functionalizing 2H-phase TMD NSs by electrochemical means and the advantages associated to such functionalization in terms of practical utility.

2. Results and discussion

2.1. General aspects of the cathodic functionalization of 2H-phase MoS_2 with organoiodides

Due to their simplicity and versatility, electrolytic methods constitute a very attractive tool for the exfoliation and functionalization of 2D materials,[20,21] but such methods have so far remained underexplored, especially in the case of TMDs. Fig. 1a shows a schematic representation of the protocol developed here to obtain functionalized 2H-phase MoS_2 NSs, which consisted of two consecutive electrolytic steps, namely, (1) delamination of a bulk MoS_2 electrode and (2) functionalization proper of the delaminated MoS_2. Both steps were carried out in a two-electrode configuration using a piece of MoS_2

as the working electrode and platinum foil as the counter electrode. The detailed experimental procedure is described in the Supporting Information (SI), but its main features are outlined in the following. First, based on an electrochemical exfoliation method that preserves the original 2H phase of the starting material and was recently reported elsewhere,[22] a piece of natural MoS_2 crystal was cathodically delaminated in aqueous KCl electrolyte (Fig. 1a, step 1). Such an electrolytic treatment triggered expansion of the MoS_2 crystal in an accordion-like fashion (Fig. 1b and c). As a result, micrometer- and submicrometer-sized voids were generated between the delaminated MoS_2 layers within the crystal [see field emission scanning electron microscopy (FE-SEM) images in Fig. 1d and e], but at the same time electrical contact of the delaminated layers with the electrode was preserved. Because access of both electrical current and electrolyte to the expanded layers should be guaranteed under such conditions, this initial cathodic treatment was expected to set a favorable stage for any subsequent electrochemical modification of the MoS_2 material.[23]

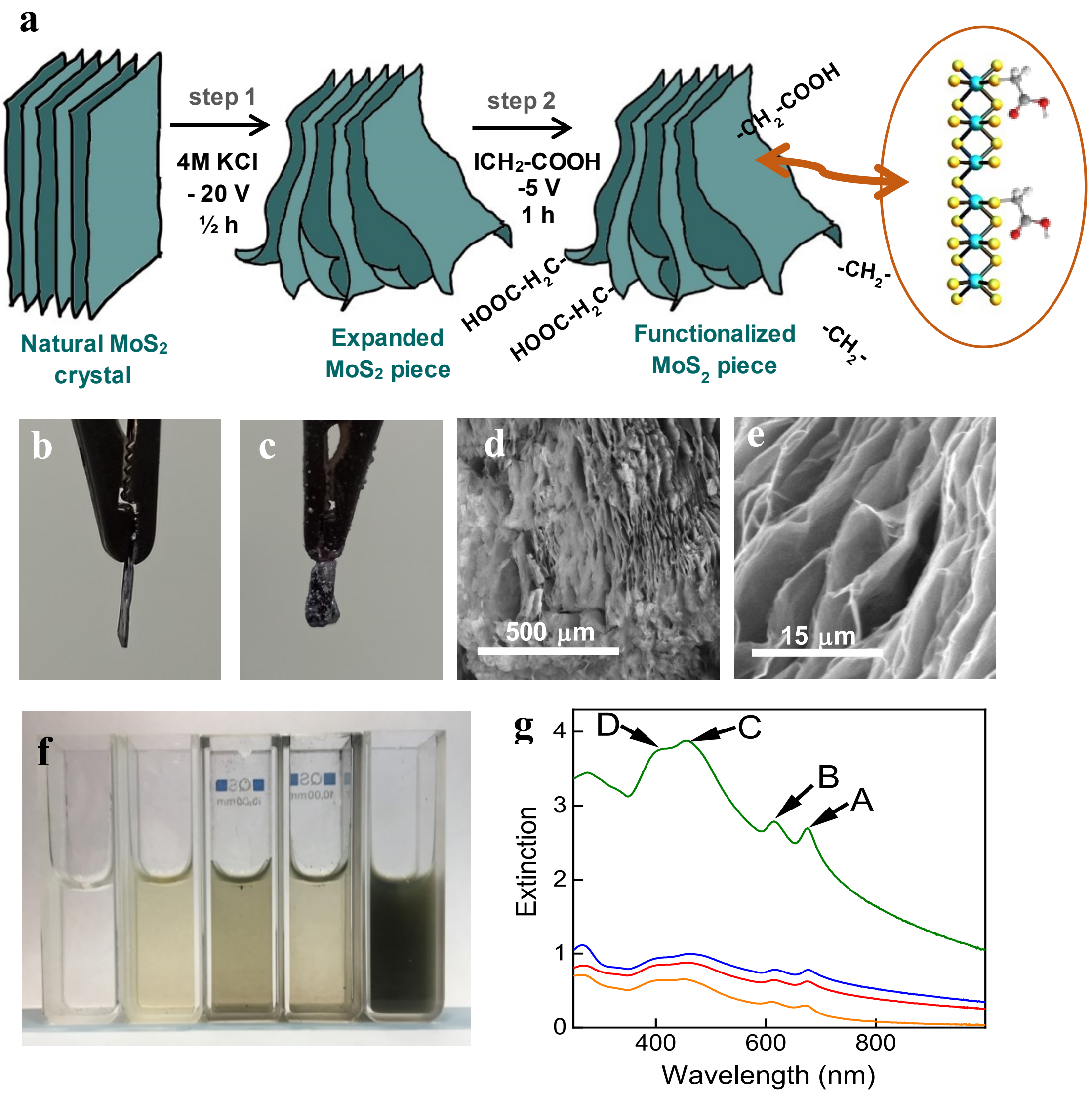

Figure 1. (a) Schematic of the electrochemical functionalization of 2H-MoS_2, which consisted of two consecutive cathodic treatments: a natural MoS_2 crystal was first expanded in aqueous KCl electrolyte (step 1) and then treated with iodoacetic acid (step 2). The inset illustrates the bonding of the acetic functionalities to sulfur atoms in areas of local metallic character of the 2H lattice, i. e., close to sulfur vacancies and edges, as will be explained in section 2.3 below. **(b,c)** Digital photographs of the cross-section of a MoS_2 crystal (b) before and (c) after cathodic expansion in KCl. **(d,e)** Typical FE-SEM images of the cathodically expanded MoS_2 material at different scales. **(f)** Digital photograph of the dispersions obtained by sonication in water of cathodically expanded MoS_2 (i) without any subsequent treatment with iodoacetic acid or followed by a

electrochemical treatment at -5 V with (ii) 0.25 M iodoacetic in water; (iii) 0.25 M iodoacetic in ethanol; (iv) 0.25 M iodoacetic in isopropanol; (v) 0.05 M iodoacetic and 0.15 M Na_2SO_4 in water. **(g)** UV-Vis extinction spectra of the aqueous dispersions displayed in (f): (i) black (null absorbance), (ii) orange, (iii) red, (iv) blue and (v) green trace. The excitonic bands A, B, C and D, which are characteristic of 2H-phase MoS_2, have been labeled for clarity.

We note that anodic exfoliation approaches documented in the literature for MoS_2 tend to give expanded/delaminated products that easily detach from their parent electrode material,[24–26] making them less amenable to serial electrolytic treatments. In contrast, other cathodic exfoliation processes generally afford expanded TMD materials that remain attached to the electrode as a single entity (i.e., very much like what is observed here in Fig. 1c-e), but rely on the use of organic cations and non-innocuous organic solvents as the electrolytic medium.[27,28] Here, expansion of the MoS_2 electrode was accomplished in water with a widely available and inexpensive salt (KCl), and was therefore more attractive from a practical perspective.

Following electrolytic expansion, the MoS_2 crystal was subjected to a second cathodic treatment in a solvent containing an organoiodide for the purpose of functionalization (Fig. 1a, step 2). The main rationale behind this second step was that the iodine-carbon bond in the organoiodide should be readily cleaved under cathodic conditions, as it is well known from prior organic electrosynthesis studies carried out mainly in polar aprotic solvents but also in water.[29,30] Such a cathodic reaction could in principle give the iodide anion, I^-, and the corresponding organic radical, ·R, as described in Eq. 1:

$$\text{I-R} + e^- \rightarrow I^- + \cdot R \qquad (1)$$

In turn, the generated organic radical could be expected to react with the 2H-phase MoS_2 surface to afford a derivatized product. As a matter of fact, the grafting of organic (aryl and alkyl) moieties onto metal and carbon surfaces based on the cathodic reduction of their corresponding organoiodides has been previously shown to be feasible.[31,32] We note that the organic radical can be further reduced to yield a carbanion, R^-, as in Eq. 2:

$$\cdot R + e^- \rightarrow R^- \qquad (2)$$

, but it is known that this does not preclude the grafting of the organic moiety on the metal or carbon surface.[31,32] In our case, iodoacetic acid was selected as the main benchmark reagent with a two-fold purpose. Specifically, if the proposed strategy was to succeed in functionalizing the 2H-phase MoS_2 NSs with acetic acid groups, we would expect the NSs to become hydrophilic and thus (i) to be readily dispersible in water, so that their aqueous dispersibility could be taken as a straightforward proxy for successful derivatization, and (ii) to exhibit enhanced performance in certain target applications, as will be discussed below.

Preliminary functionalization tests were accomplished by cathodic treatment of the expanded MoS_2 electrode at –5 V for 60 min with 0.25 M iodoacetic acid in three different solvents: water, ethanol and isopropanol. To probe the effect of the treatments on the aqueous dispersibility of the MoS_2 NSs, the treated electrode was rinsed with water, dried under a vacuum, and then a weighed amount of it was transferred to neat water and bath-sonicated for 1 h to extract individual NSs. After allowing the sonicated product to stand undisturbed for 24 h or subjecting it to low-speed centrifugation, the resulting supernatant volume was collected and kept for subsequent analysis. It is well known that non-functionalized 2H-phase MoS_2 NSs, including those obtained by cathodic exfoliation, are not generally dispersible in aqueous medium by themselves.[22,33] In fact, sonication of the as-expanded MoS_2 crystal (i.e, the crystal that was just cathodically delaminated but not subjected to any subsequent treatment with iodoacetic acid) failed to give MoS_2 dispersed in water in any detectable quantity. This was readily apparent from the fully transparent and colorless solution shown in Fig. 1f(i) but was also confirmed by UV-Vis absorption spectroscopy, which revealed virtually null absorbance in the whole wavelength range between 300 and 1000 nm (see black trace in Fig. 1g).

On the other hand, the efficacy of a given cathodic treatment in derivatizing the MoS_2 electrode with acetic acid groups should be reflected on the amount of MoS_2 NSs that are retained in the aqueous supernatant after sonication, larger dispersed amounts denoting higher derivatization abilities. Indeed, treatment of the expanded MoS_2 electrode at -5 V with 0.25 M iodoacetic acid in the abovementioned solvents led to solutions (after sonication in water) that exhibited a faint, although clearly visible, green tone, as noticed in Fig. 1f(ii), (iii) and (iv) for the cathodic treatment in water, ethanol and isopropanol, respectively. This result was consistent with the presence of 2H-phase MoS_2 NSs dispersed in the aqueous medium,[12,22] which in turn suggested that some functionalization of the expanded electrode was attained. Indeed, the features observed in the UV-Vis extinction spectra of these aqueous solutions (orange, red and blue traces in Fig. 1g) completely agreed with those expected for 2H-phase MoS_2, in particular the A, B, C, and D exciton peaks located at ~675, 615, 456 and 411 nm, respectively.[34] By contrast, cathodic treatment of the expanded electrode in the neat solvents (i.e., in the absence of iodoacetic acid) yielded colorless solutions after sonication that had null absorbance (spectra not shown), thus highlighting the central role played by the organoiodide in attaining water-dispersible MoS_2. Furthermore, based on previously developed metrics,[35] the UV-Vis extinction spectra were used to estimate the concentration of MoS_2 in their corresponding aqueous dispersions. Table 1 collects the concentrations determined for a set of functionalization trials, where it can be seen that cathodic treatment with 0.25 M iodoacetic acid in the three tested solvents afforded values around 10 mg L^{-1}, being slightly lower for water. However, because working with the latter is preferable to using organic solvents on environmental and practical grounds, all further functionalization efforts were carried out in aqueous medium. Likewise, replacing iodoacetic acid by its non-halogenated counterpart (i.e., acetic acid) led to cathodically treated MoS_2 that could not be dispersed in water. This was consistent with the idea that stabilization of the MoS_2 NSs relied mainly on the implantation of acetic acid radicals generated via reductive cleavage of the iodine-carbon bond of iodoacetic acid.

Table 1. Concentrations of MoS_2 aqueous dispersions for a set of functionalization trials. Concentrations of MoS_2 aqueous dispersions, [MoS_2 (aq)], obtained by sonication of a MoS_2 electrode in water (nominal concentration: 2 mg mL^{-1}) after cathodic expansion at -20 V in 4 M KCl aqueous solution followed by subsequent functionalization treatments in the specified conditions.

Reagent	Solvent	Supporting electrolyte	Voltage (V)	[MoS_2 (aq)] (mg L^{-1})
0.25 M ICH_2-COOH	water	-	-5	8
0.25 M ICH_2-COOH	ethanol	-	-5	10
0.25 M ICH_2-COOH	isopropanol	-	-5	12
0.25 M CH_3-COOH	water	-	-5	0
0.25 M ICH_2-COOH	water	0.15 M Na_2SO_4	-5	16
0.05 M ICH_2-COOH	water	0.15 M Na_2SO_4	-5	45
0.01 M ICH_2-COOH	water	0.15 M Na_2SO_4	-5	11
0.05 M ICH_2-COOH	water	0.15 M Na_2SO_4	-2.5	26
0.05 M ICH_2-COOH	water	0.15 M H_2SO_4	-5	20
0.25 M ICH_2-COOH	water	-	-10	0
0.5 M ICH_2-COOH	water	-	-10	11

The above results suggested that cathodic treatment in the presence of only iodoacetic acid is associated to somewhat poor derivatization efficiencies, which were embodied in rather low dispersed MoS_2 concentrations in water. To facilitate the functionalization reaction and attain larger amounts of derivatized NSs dispersed in water, a supporting electrolyte (Na_2SO_4) was added to the aqueous iodoacetic acid solution. Specifically, in the presence of 0.15 M Na_2SO_4, a higher dispersed concentration (about twice as large) could be achieved with 0.25 M iodoacetic acid. However, even higher MoS_2 concentrations (~45 mg L^{-1}) were obtained by decreasing the amount of iodoacetic acid in the electrolytic solution to 0.05 M [see Table 1, Fig. 1f(v) and green trace in Fig. 1g]. The latter appeared to be the optimum organoiodide concentration, since further reducing it to 0.01 M led to a substantial decrease in the final MoS_2 concentration in water (see Table 1). Such an outcome implied that a limit in the extent of derivatization of the expanded MoS_2 electrode was reached for iodoacetic acid concentrations around 0.05 M. The concentration of dispersed MoS_2 also decreased noticeably when using smaller cathodic potentials (e.g., -2.5 V). From the results gathered in Table 1, the following cathodic treatment conditions were selected as the most efficient in terms of the amount of derivatized product that could be obtained: 0.05 M iodoacetic acid at -5 V with 0.15 M Na_2SO_4 as supporting electrolyte.

2.2. Physicochemical characterization of the cathodically funcitonalized 2H-phase MoS_2 nanosheets

Analysis of the aqueous dispersed, cathodically treated MoS_2 material by atomic force microscopy (AFM; Fig. 2a and b) revealed it to be comprised of NSs with typical lateral dimensions between one and several hundred nanometers as well as thickness in the 2–11 nm range, the latter amounting to flakes that incorporated ~1–16 monolayers. Histograms providing the distribution of NS lateral size and layer number from the AFM images are shown in Fig. 2c and d, respectively. These data were in agreement with the average lateral size (~300 nm) and layer number (~10) of the dispersed MoS_2 NSs as estimated from their UV-Vis absorption/extinction spectral features.[35] Significantly, such results were very similar to those obtained for NSs extracted by sonication from the as-expanded MoS_2 electrode and dispersed in water and organic solvents with the aid of colloidal stabilizers or surfactants,[22] indicating that the present cathodic functionalization treatment did not have any substantial impact on the morphology of the derivatized products. We note that 2H-phase MoS_2 NSs can be made water-dispersible by themselves (i.e., without the need to use any colloidal stabilizers) when they are aggressively broken down into nanodots having lateral sizes of a few tens of nanometers or below,[36] but such a scenario did not appear to be in place here. Furthermore, Raman spectroscopy (Fig. 2e) indicated that the microscopic structure of the NSs was not significantly altered by the functionalization treatment, as evidenced by the virtually identical spectral features (A_{1g} and E^1_{2g} bands characteristic of 2H-phase MoS_2)[37] noticed for NSs directly extracted from the as-expanded MoS_2 electrode (black trace) and for NSs extracted from the cathodically derivatized electrode (green trace). We therefore concluded that the dispersibility of the latter in aqueous medium had to be related to changes in their surface chemistry (i.e., introduction of acetic acid groups on the NS surface) rather than to morphological and/or structural changes.

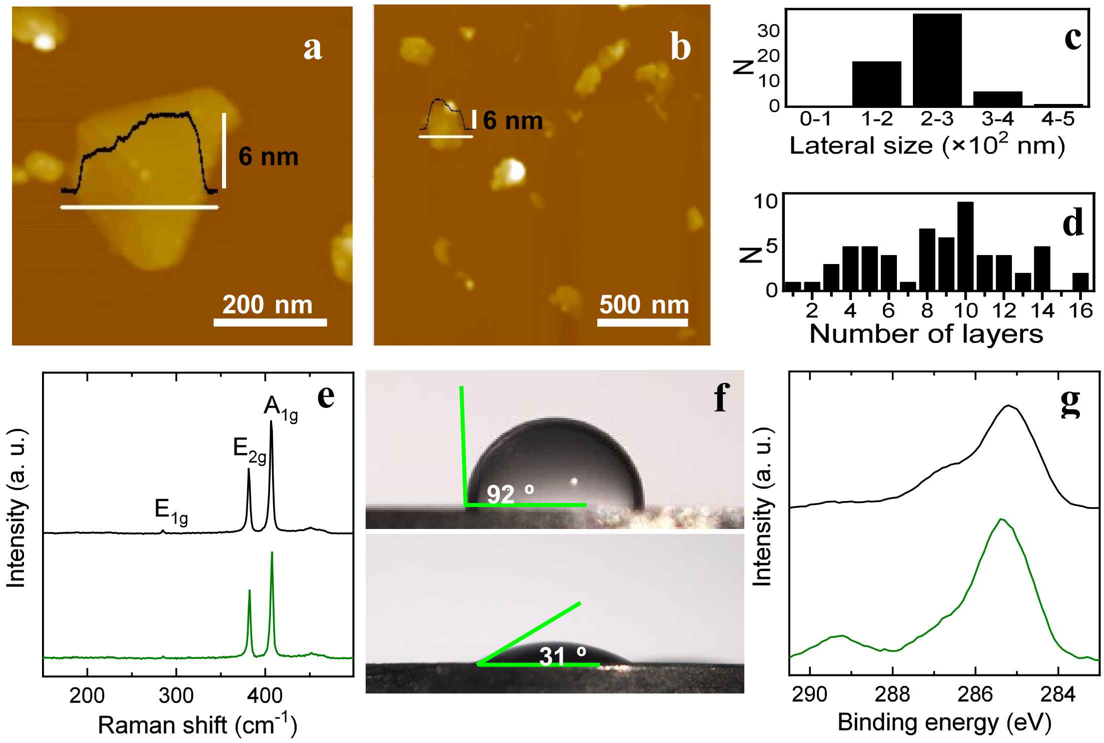

Figure 2. Characterization of aqueous dispersed, cathodically modified MoS_2 flakes. **(a,b)** Representative AFM images of a MoS_2 flakes deposited from their dispersion. A representative line profiles (black lines) taken along the marked white lines are shown overlaid on the images. Histograms of **(c)** nanosheet lateral size and **(d)** layer number measured from the AFM images. **(e)** Raman spectrum of nanosheets extracted from as-expanded, non-functionalized MoS_2 (black trace) and from functionalized MoS_2 (green trace). The main bands are labeled for clarity. **(f)** Digital pictures of droplets of water on thin films of (top) non-functionalized and (bottom) functionalized MoS_2 nanosheets, with indication of the contact angle. **(g)** High resolution C 1s core level XPS spectra of non-functionalized (black trace) and functionalized (green trace) MoS_2 nanosheets.

According to zeta potential measurements, the cathodically functionalized NSs were colloidally stabilized in water by the presence of negative electrical charges. Specifically, the zeta potential was determined to be about -41 and -25 mV at a pH of ~10 and 4, respectively. These values were sufficient to endow the dispersed MoS_2 NSs with some degree of colloidal stability based on electrostatic repulsions (even good stability at pH 10).[38] Indeed, the corresponding dispersions were seen to remain stable (i.e., they remained visually homogeneous) at least for days or weeks. Under more acidic conditions (e.g., pH ~2), the MoS_2 dispersions were highly unstable, with the NSs sedimenting very rapidly, which made the zeta potential measurement unreliable. These results agreed with the negative charges in the NSs being mainly furnished by deprotonation of the carboxylic acid in the acetic acid groups. We assumed that the pK_a of the acetic acid groups grafted onto MoS_2 was around 4, which was reasonable considering that the corresponding values for iodoacetic, acetic and mercaptoacetic acids are ~3.2, 4.8 and 3.6, respectively.[39] The latter molecule was taken as a realistic approximation of the scenario found in the functionalized MoS_2 NSs, as the acetic acid groups are believed to be bound to the NSs through their sulfur atoms (see below). Based on these considerations, we would expect the acetic acid groups in MoS_2 to be (i) fully deprotonated at pH values well above 4, thus providing the NSs with their largest possible net negative charge and zeta potential (in absolute value), (ii) ~50% deprotonated at pH 4, yielding NSs with zeta potential about half the magnitude of that measured at higher pH, and (iii) essentially non-deprotonated at pH below 4, so that the net charge and zeta potential of the dispersed NSs should approach zero, yielding highly unstable dispersions.[38] Indeed, this expected trend was in agreement with the actual results from the zeta potential measurements and colloidal stability at the different pH values. Decoration of the MoS_2 NSs with acetic acid groups should also be associated to them being more hydrophilic relative to their non-functionalized counterparts. While the ability to disperse the former in water was a clear indication of increased hydrophilicity, a more quantitative estimate was obtained from the measurement of water contact angles. The contact angles determined for thin films of non-functionalized and cathodically functionalized MoS_2 NSs were, respectively, ~92 and 31º (Fig. 2f), which confirmed the improved hydrophilicity of the latter.

The presence of carboxylic acids on the cathodically derivatized NSs was corroborated by X-ray photoelectron spectroscopy (XPS). First, we note that upon cathodic treatment with iodoacetic acid, no sign of iodine could be detected in the survey spectrum of the MoS_2 NSs (see Fig. S1 in the SI). By contrast, while the high resolution C 1s core level spectrum of the non-functionalized material only exhibited the well-known adventitious carbon-related band located at ~285 eV (Fig. 2g, black trace),[40] that of the cathodically functionalized material included an additional component at ~289 eV (green trace), which is typical of carbon atoms from carboxylic acids.[41] Hence, the appearance of a carboxylic acid signal together with the lack of iodine bands in the spectra was strong indication of the successful functionalization of the MoS_2 NSs with acetic acid groups. Additional evidence on functionalization obtained by ATR-IR is given in the SI of the manuscript (Fig. S8). In addition, the high resolution Mo 3d and S 2p core level spectra of the non-functionalized and functionalized NSs (Fig. S2a of the SI) provided evidence that the original 2H phase of the material was preserved upon the cathodic derivatization step. Specifically, the two peaks of the Mo 3d doublet band ($3d_{3/2}$ and $3d_{5/2}$ peaks) appeared at virtually the same location in both the non-functionalized and functionalized NSs, namely ~233 ($3d_{3/2}$) and ~229.8 ($3d_{5/2}$) eV, and such a position is known to be characteristic of the 2H polymorph of MoS_2 (the peaks of the 1T phase would appear downshifted by ~0.8 eV).[12,28,42] Similarly, the position of the S 2p doublet band, i.e., ~163.9 ($2p_{1/2}$) and ~162.7 ($2p_{3/2}$) eV, remained unchanged after functionalization (Fig. S2b) and was also consistent with 2H-phase MoS_2.[42]

To estimate the extent of surface functionalization achieved by the present cathodic approach, XPS data were used to calculate the number of carbon atoms from carboxylic acids, which amount to the number of acetic acid groups, relative to the number of sulfur atoms located in the outermost atomic layer of the MoS_2 NSs (we assume that acetic acid groups are only grafted on the very surface of the NSs, which is made up of a monolayer of sulfur atoms). The measurements were carried out on a piece of as-received, non-exfoliated MoS_2 crystal that was just cathodically derivatized with iodoacetic acid, rather than on a thin film formed by the re-stacking of exfoliated and functionalized NSs. The reason behind such a modus operandi was the following. Because the MoS_2 NSs produced by the present methodology were multilayered objects that exhibited a broad layer number distribution (see Fig. 2d), it was not possible to accurately determine the fraction of surface sulfur atoms in the NSs out of the total number of sulfur atoms probed by the XPS technique for a thin film of restacked NSs. On the other hand, such a fraction could be reasonably assessed for a non-exfoliated, bulk MoS_2 crystal, where cathodic derivatization was expected to take place only on its very surface. Here, the corresponding fraction of surface sulfur atoms out of the total sulfur probed by XPS could be readily gauged from the photoelectron emission cross-section of MoS_2 for 2p electrons from S2p core level as a function of emission depth, (see SI for details). Specifically, the outermost sulfur atomic layer of the MoS_2 crystal contributed ~14 % of the total sulfur signal (details of the calculation can be found in the SI). From this data and the calculated amount of carbon atoms from carboxylic acids derived from the C 1s spectrum of the functionalized crystal (Fig. S3 of the SI), the degree of functionalization was estimated to be ~0.10 acetic acid groups per surface sulfur atom. This figure can be compared with values in the range of ~0.15–0.35 molecular groups per surface sulfur atom previously reported for (mainly monolayer) 1T-phase MoS_2 NSs derivatized with different organoiodides.[8,9,43] In general terms, the somewhat lower extent of derivatization observed here for the 2H-phase NSs was not surprising, considering that their semiconducting nature should make them less chemically reactive than their metallic 1T-phase counterparts.[7] It is worth noting that cathodic functionalization could also be attained with other potentially useful organoiodides, which is exemplified here for the case of 4-iodoaniline. The derivatized NSs became dispersible in water as well (Fig. S4a of the SI) and again their analysis by XPS confirmed the incorporation of the key chemical group (amino group in this case; Fig. S4b), together with the lack of any iodine (Fig. S4c).

2.3. Rationalizing the derivatization of 2H-phase MoS_2 nanosheets with organoiodides

While the results presented above indicated that 2H-phase MoS_2 NSs can be functionalized with organoiodides by way of cathodic treatment, there still remains the question of how such a derivatization was actually made possible. In the case of 1T-phase MoS_2 dispersed in water, the functionalization reaction is known to be spontaneous due to the presence of excess electrons in the NSs that can be readily transferred to the organoiodide, as in Eq. 1.[8,9] These excess electrons are directly inherited from the preparation of the metallic 1T polymorph, which is generally based on chemical/electrochemical lithium intercalation processes,[44,45] and thus are not to be found in the semiconducting 2H-phase counterpart, suggesting that reaction of the latter with organoiodides is not spontaneous. Such a hypothesis was corroborated from control experiments whereby a cathodically expanded MoS_2 crystal was exposed to an aqueous 0.25 M iodoacetic acid solution, either under still conditions or under continuous sonication, in the absence of any applied voltage. In both instances, attempts to disperse the treated MoS_2 material in water were unsuccessful, i.e., the concentration of MoS_2 in the final supernatant after sonication of the treated material in neat water was virtually zero. These results demonstrated that derivatization of the 2H-phase NSs with organoiodides needs to be triggered by an external supply of electrons, which in the present case took the form of a cathodic potential.

The external electrons required to prompt functionalization could also be sourced from a chemical species, e.g., by resorting to a proper reducing agent. To illustrate this possibility, we selected sodium borohydride as the reductant, which is known to be able to cleave the iodine-carbon bond in organoiodides but cannot reduce carboxylic acids to aldehydes or alcohols.46,[47] Thus, treatment of an expanded MoS_2 crystal by sonication in an aqueous solution containing 0.25 M iodoacetic acid and 0.25 M sodium borohydride yielded a product that, after being rinsed, dried and sonicated in neat water, afforded a non-negligible amount of dispersed MoS_2 (~15 mg L^{-1}), as noticed from the corresponding photograph and UV-Vis extinction spectrum (Fig. S5 of the SI). By contrast, no dispersed MoS_2 could be obtained at all when replacing iodoacetic acid by acetic acid in this experiment, which stressed the idea that NS functionalization relied on the generation of acetic acid radicals. Furthermore, we note that selected reducing agents (metallocenes) have been very recently used to boost the functionalization of 1T-phase MoS_2 NSs with alkyl iodides (as well as other alkyl halides).[43] thus constituting a similar strategy to that developed here for 2H-phase NSs with sodium borohydride. However, a key difference between both cases was that whereas a reductant was just employed to increase the extent of functionalization of the 1T-phase NSs with alkyl iodides (e.g., from ~0.20 to 0.35 alkyl groups per sulfur atom), the reductant was strictly necessary to enable derivatization of the 2H-phase NSs. In summary, functionalization of both 1T- and 2H-phase MoS_2 NSs with organoiodides requires an amount of extra electrons to be available.

While the derivatization reaction is spontaneous for 1T-phase MoS_2, it is not for 2H-phase MoS_2, which is less reduced, and thus needs an external electrochemical (or chemical) supply of extra electrons for the functionalization reaction to progress.

Another key issue to consider in the functionalization of 2H-phase MoS_2 NSs with organoiodides concerns the type of interaction that is established between the NSs and the implanted moieties. It was apparent that the latter were not simply physisorbed on the MoS_2 surface, since we noticed that both iodoacetic acid and acetic acid failed to act as aqueous colloidal stabilizers for 2H-phase NSs, either obtained by electrochemical exfoliation of MoS_2 crystals or by direct exfoliation of MoS_2 powder via sonication. Furthermore, the NSs that were cathodically derivatized with iodoacetic acid and then dispersed in water could be sedimented by centrifugation and easily re-dispersed in neat water as many times as desired, which constituted a strong indication that the acetic acid moieties were tightly bound to the NS surface (if the acetic acid groups were just weakly adsorbed, this procedure would have led to their progressive removal from the NS surface and thus to a loss of colloidal stability). Taking again the 1T-phase MoS_2 NSs as a reference system, we note that the grafting of organic radicals from organoiodides has been previously shown to proceed in that case through formation of covalent bonds with the NS sulfur atoms (i.e., carbon-sulfur bonds).[8,9] However, such a scenario is not immediately applicable to the case of 2H-phase NSs. The metallic character of the 1T polymorph implies that it possesses a non-negligible amount of (both occupied and empty) electronic states close to the Fermi level, which are absent from its semiconducting 2H counterpart.[7] Such electronic states are expected to endow the former with increased chemical reactivity compared with 2H-phase MoS_2. Indeed, theoretical work has demonstrated that attachment of alkyl and other radicals on the (pristine) MoS_2 surface is energetically very favorable in the 1T polymorph but not in the 2H one.[7]

Nonetheless, the presence of certain defects in the 2H-phase MoS_2 lattice is known to locally change its electronic structure from semiconducting to metallic (increased density of electronic states around the Fermi level). This is particularly the case not only of edge defects,[48] which are relatively abundant in submicrometer-sized NSs, but also of sulfur vacancies.[49] The latter are quite prevalent in bulk and 2D MoS_2 of both natural and synthetic origin,50,[51] given that S vacancies with one or two absent atoms possess the lowest energies of formation among all defects.[51] Such low formation energies render the introduction of S vacancies easy during synthesis and processing of MoS_2 materials. Furthermore, as the removal of a sulfur atom from the MoS_2 lattice (yielding MoS_{2-x}) is formally a reduction process, sulfur vacancies can be created by reaction with a sufficiently strong reducing agent[52] or by electrochemical reduction.[53] Thus, their generation can be expected to be favored under the intrinsically reductive conditions of the present cathodic treatments. The local metallic character of the 2H lattice around sulfur vacancies and edges in MoS_2 should thus provide a number of sites with increased reactivity where organic radicals and other species can covalently attach to sulfur atoms, as recently shown for the grafting of aryl radicals from diazonium salts[15] and for the interfacial bonding with non-layered chalcogenides.[54] Both possibilities, i. e., acetic groups bonding to sulfur atoms on the edges of the layers and near sulfur vacancies, are illustrated in the inset to Fig. 1a. We note that functionalization does not deactivate the sulfur vacancies, as it does not take place in the vacancy itself (the undercoordinated molybdenum) but in its surroundings (sulfur atoms nearby). Thus, molybdenum atoms which lack sulfur remain unsaturated after functionalization. This is demonstrated by the detection of a well-defined, significant signal associated to the presence of Mo-S dangling bonds in the electron paramagnetic resonance (EPR) spectrum of the functionalized MoS_2 material (see Fig. S9 in the SI). A typical vacancy passivation method would involve reaction with alkanethiol molecules,55 which would provide extra sulfur atoms to fill the vacancy. The grafting of the acetic groups to sulfur atoms in MoS_2 layers is indeed suggested by the weak IR absorption observed ~630 cm^{-1} in the ATR-IR spectrum of functionalized MoS_2, which is ascribable to C-S stretching[8] (see Fig. S8 of the SI).The formation of carbon-sulfur bonds in the cathodically functionalized NSs could in principle be disclosed by XPS as well through the emergence of a doublet component (S-C component) in the S 2p spectrum at ~164 eV ($2p_{1/2}$) and 163 eV ($2p_{3/2}$).[8,9] However, in the present case such a component could not be clearly detected for two main reasons: (1) The multi-layered nature of the MoS_2 NSs implies that the percentage of (surface) sulfur atoms that are covalently bonded to carbon must be very small. From the degree of derivatization with iodoacetic acid determined above, the relative weight of the S-C component in the S 2p spectrum was estimated to be just a very few percent, compared to ~20 percent for functionalized 1T-phase MoS_2 monolayers.[9] (2) The S-C component overlaps significantly with the component associated to the pristine 2H phase, although less so with that of the 1T phase. In fact, even for monolayer MoS_2, functionalization has been very recently reported to introduce only subtle changes in the XPS S 2p core level spectrum.[18] Both factors contributed to making the S-C component in the functionalized 2H-phase NSs virtually unnoticeable (Fig. S2b). (As a side note, a signal at a binding energy very close to that of the S-C component was occasionally seen in the spectra; this signal arose from the presence of bismuth, which is a common impurity in natural MoS_2 crystals; see Fig. S6 of the SI). On the other hand, carbon-sulfur bonds can also be detected in the C 1s spectrum through a C-S component that would be located at about 285.5 eV.[56] Although this component overlaps with the signal arising from adventitious carbon, its presence could be readily brought to light by subtracting the normalized C 1s spectrum of the non-functionalized NSs from that of their functionalized counterpart, the result of which is shown in Fig. S7 of the SI. In addition to the expected component at about 289 eV associated to carboxylic acids, a new component at ~285.5 eV emerged in the differential spectrum, which could be ascribed to carbon-sulfur bonding. This result was thus consistent with the acetic acid groups derived from iodoacetic acid being covalently bonded to sulfur atoms from the MoS_2 NSs.

Finally, we note that during the cathodic treatment of MoS_2 with organoiodides, other types of reaction can be expected to compete with the functionalization reaction proper. Because the derivatization process was carried out in water, this should be the case of the hydrogen evolution reaction (HER), which is known to be catalyzed by MoS_2, especially under acidic conditions.[57] Indeed, when Na_2SO_4 was replaced by H_2SO_4 as the supporting electrolyte in the cathodic treatment with iodoacetic acid, a substantial decrease in the amount of MoS_2 dispersed in water was observed (Table 1). Moreover, in the absence of a supporting electrolyte, the application of larger cathodic potentials (e.g., -10 V), which should trigger a more vigorous HER, failed to give any dispersed MoS_2, although this outcome could be reversed if the concentration of iodoacetic acid was also increased (e.g., from 0.25 to 0.50 M). Such results can be rationalized bearing in mind that edges and sulfur vacancies are the main catalytic active sites for HER on the surface of 2H-phase MoS_2,[53,57–59] i.e., the very same sites that are thought to be reactive towards organoiodide functionalization. Consequently, a competition for these sites should be at work between the derivatization reaction and the HER, and so any change in the cathodic treatment conditions that favors the latter should negatively impact the former. It can also be argued that hydrogen atoms adsorbed on MoS_2 vacancies/edges, as an intermediate species of the HER, will react with the cathodically reduced organoiodide to give the corresponding organic molecule (e.g., acetic acid in the case of iodo acetic acid), thus preventing the derivatization of the MoS_2 surface. While this reaction might be taking place to some extent, we believe that it will be significantly inhibited by the generation of molecular hydrogen from the hydrogen adatoms via the Tafel and/or Heyrovsky steps of HER, which is favored at the catalytic sites of MoS_2.[57] The promoted generation of molecular hydrogen should then give the organic radicals derived from the organoiodide the opportunity to react with the MoS_2 surface.

2.4. Application of cathodically derivatized 2H-phase MoS_2 nanosheets in the catalytic reduction of nitroarenes and organic dyes

The reduction of nitroarenes and organic dyes is of practical interest in the areas of environmental remediation and chemical synthesis. For example, a number of nitroarenes, such as 4-nitrophenol (4-NP) and 2-nitroaniline (2-NA), as well as organic dyes, including methyl orange (MO) and methylene blue (MB), are found in the wastewater effluents of the pesticide, herbicide or pigment industries. These compounds frequently possess a highly toxic and recalcitrant character. Hence, they must be degraded before the effluents are released into the aquatic environment, with their reduction into more benign forms being a viable technological solution (e.g., anilines derived by nitroarene reduction are biodegradable and exhibit a lower toxicological profile).[60,61] Also, the reduction of certain nitroarenes into their corresponding anilines constitutes one of the main steps in the synthesis of relevant pharmaceutical drugs (e.g., paracetamol) and polymers, such as Kevlar.[60,61] While nitroarene/dye reduction has traditionally relied on precious metals (Pt, Pd, Ag, etc.) to catalyze the reaction, the need to deploy more earth-abundant and affordable catalysts has driven recent efforts on the use of non-noble metal-based systems.[60] In this context, 2D MoS_2 has demonstrated catalytic activity towards reduction reactions in water with sodium borohydride as the reductant, with the 1T-phase NSs being quite efficient in this role (probably due to their intrinsically metallic nature).[62,63] Still, issues related to the structural instability/degradation of 1T-phase MoS_2

mentioned above are an obstacle to its practical implementation. 2H-phase MoS_2 NSs can also be used as reduction catalysts, but so far their activity has considerably lagged behind that of their 1T-phase counterparts.[52,64] Thus, strategies that boost the performance of the 2H-phase NSs would be highly desirable. We show in the following that the cathodic functionalization approach developed here is one such effective strategy.

The catalytic tests were carried out in aqueous medium at room temperature with the nitroarenes 4-NP, 2-nitrophenol (2-NP), 4-nitroaniline (4-NA), 2-NA and nitrobenzene (NB), and with the organic dyes MO and MB, using the acetic acid-functionalized 2H-phase MoS_2 NSs as the catalyst. To allow direct comparisons with other catalysts reported in the literature, as well as to facilitate kinetic analyses of the reactions, typical substrate concentrations were chosen to be in the 0.06-0.12 mM range and the sodium borohydride reductant was used in a large excess relative to the substrate (see Experimental section for details). In all cases, the reaction progress was followed with UV-Vis absorption spectroscopy, by monitoring the intensity of an absorption peak that was characteristic of the substrate molecule (in the presence of the reducing agent) but was absent from its reduced counterpart (see Fig. S10 of the SI for the corresponding spectra). Thus, according to the Beer-Lambert law, a change in the concentration of the substrate molecule as a result of its reduction should induce a directly proportional variation in the intensity of its absorption peak, which provided the basis for recording kinetic profiles for these reactions from the absorbance data. More specifically, kinetic profiles of the reactions were obtained by plotting the evolution of absorbance measured at 400, 416, 382, 410, 270, 461 and 675 nm for 4-NP, 2-NP, 4-NA, 2-NA, NB, MO and MB, respectively. Fig. 3 (solid lines) shows typical kinetic profiles recorded for the nitroarenes (a) and the organic dyes (b). Profiles corresponding to blank experiments, which monitored aqueous solutions that contained a given substrate and the reductant but lacked any catalyst, are also given in Fig. 3 (dotted lines). As expected, the latter revealed time-invariant absorbance for all the tested nitroarenes and dyes, indicating that the molecules could not be reduced in the absence of a proper catalyst.

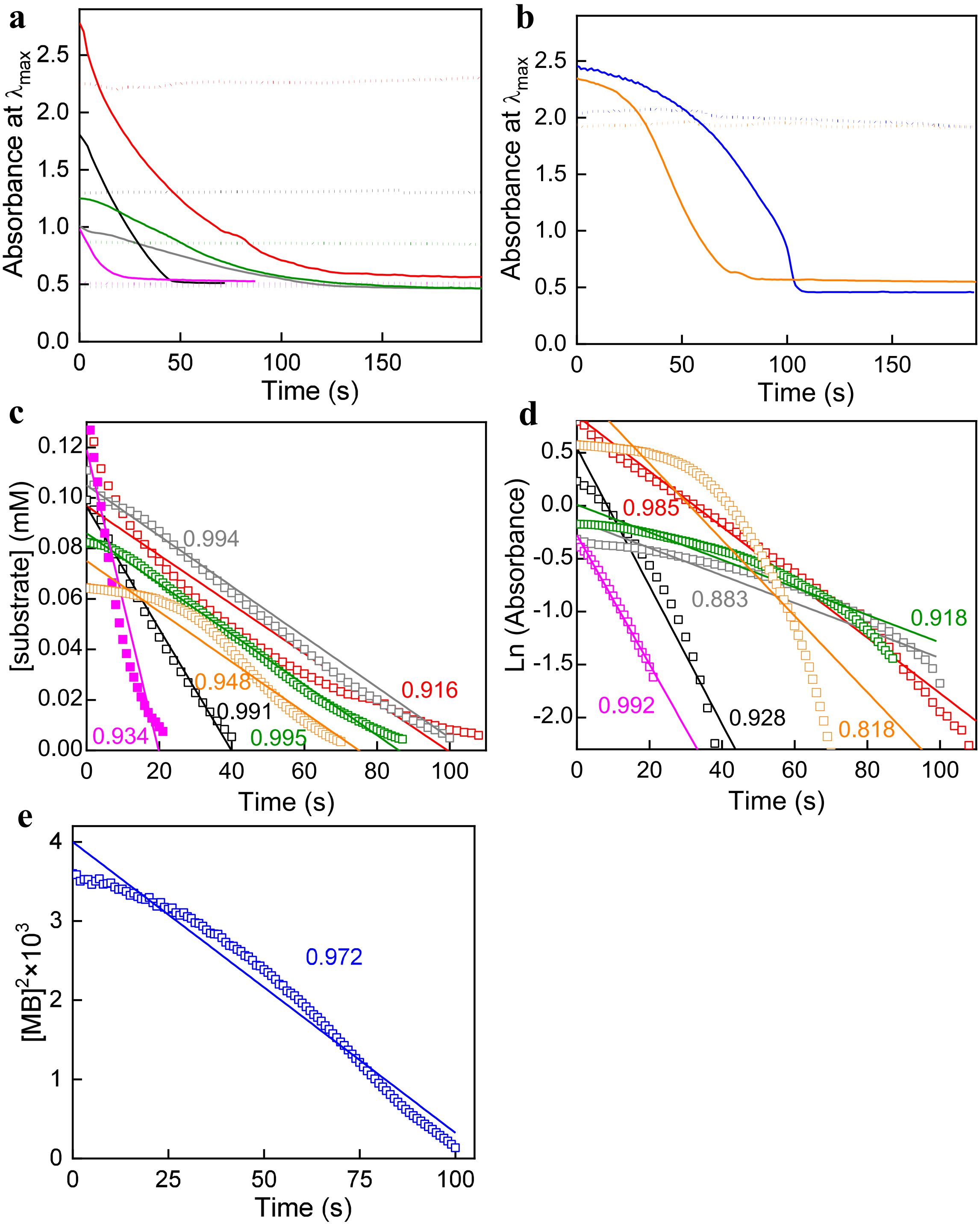

Figure 3. (a,b) Typical kinetic profiles (solid lines) measured for the reduction of different substrates with of $NaBH_4$ using functionalized MoS_2 nanosheets as catalyst. The kinetic profiles were obtained by monitoring the absorbance at the wavelength of an absorption maximum of the substrate molecule (λ_{max}). **(a)** Nitroarenes: 4-NP (red trace,

λ_{max}=400 nm), 2-NP (magenta, 416 nm), 4-NA (black trace, 380 nm), 2-NA (gray trace, 410 nm), nitrobenzene (green trace, 270 nm). **(b)** Organic dyes: MO (orange trace, 461 nm) and MB (blue trace, 675 nm). The corresponding blank experiments (dotted lines), i. e., experiments where no catalyst was added, are included for comparison. **(c-e)** Fitting (solid line) of the experimental kinetic profile data (empty squares) to different orders of reaction with respect to the substrate: **(c)** first order, i. e., exponential decay dependence of reaction rate with time, **(d)** zero order, i. e., linear dependence, and **(e)** minus one order. For clarity, the corresponding regression coefficients R^2 for the fittings are indicated using the same color code.

On the other hand, efficient substrate conversion was observed for all the nitroarenes and dyes in the presence of the acetic acid-functionalized 2H-phase NSs, as noticed by the sharp decrease of absorbance in their corresponding kinetic profiles. A plateau having non-zero absorbance was seen to develop upon reaction completion in the kinetic profiles (Fig. 3). Rather than arising from unreacted substrate molecules, the finite absorbance associated to the plateaus was mostly due to the MoS_2 catalyst itself. Indeed, the absorbance values measured for the latter at the concentration used in the reaction medium (~7 mg L^{-1}) were very similar to those recorded for the plateaus (e.g., ~0.6 at 400 nm in the case of 4-NP; see Fig. S11 of the SI for the absorption spectrum of the catalyst at 7 mg L^{-1}). This observation indicated that essentially full conversion of the substrate molecules was attained in their reduction with the acetic acid-functionalized MoS_2 catalyst.

To provide a quantitative measure of catalytic performance, the kinetic profiles were used to calculate the number of moles of substrate converted per unit time per mole of MoS_2 in the reaction medium, which was taken as a direct proxy of catalytic activity. The resulting values for the different nitroarenes and dyes are collected in Table 2 and compared in Tables S1 and S2 of the SI with those reported in the literature for other MoS_2- and non-noble metal-based catalysts. For example, a catalytic activity value of 63 h^{-1} was determined for the reduction of 4-NP, which could be directly weighed against a large pool of data available for this reaction (see Table S1; 4-NP reduction is a model reaction for the testing of catalytic systems in aqueous medium).[65]

Good colloidal stability in the aqueous catalysis medium must be an important asset of the current functionalized MoS_2 material, as it ensures that the NSs will not aggregate and thus the active catalytic sites on their surface will remain accessible for catalysis. Anyway, comparing with other previously reported colloidally stabilized MoS_2 NSs, the catalytic activity was ~3 times larger than that obtained with (non-functionalized) 2H-phase NSs produced by the present cathodic exfoliation method and dispersed in water with the aid of a biomolecular stabilizer [guanosine monophosphate (GMP)],[22] and of the order of 10 times larger than that of NSs prepared by direct exfoliation of MoS_2 via sonication in aqueous GMP solution.[66] We believe the much improved performance of the acetic acid-funtionalized NSs to be due to three main factors: (1) the intrinsically reductive conditions of the cathodic exfoliation/derivatization processes should favor the generation of sulfur vacancies on the NSs,[53] as was indeed the case (see Fig. S9 in the SI) which are known to be highly active catalytic sites towards nitroarene/dye reduction (see the proposed reaction mechanism in subsection 3.4 and Fig. S12 in the SI);[65] (2) compared with GMP, the relatively small size of the acetic acid moieties present on the MoS_2 NSs is expected to be associated to lower steric barriers for reagent access to the catalytic active sites, and (3) while GMP adsorbs preferentially at sulfur vacancy sites on the MoS_2 surface due to specific interactions of acid-base type between its nucleobase moiety and the vacancy,[66] the current functionalization takes place through sulfur atoms near the unsaturated molybdenum in edges and sulfur vacancies, but not on the vacancy itself (see inset to Fig. 1a), and thus leaves the active sites unaffected and available for catalysis (see additional details in subsection 3.4 of the SI). The latter factor implies that, while colloidal stabilization with GMP as dispersant takes place at the expense of catalytic activity, the present functionalization strategy does not present such drawback. Other strategies to boost the catalytic activity of 2H-phase MoS_2 NSs, including inserting them within the galleries of montmorillonite,[64] have met with considerable success, but the present approach clearly outperformed all of them (see Table S1). The acetic acid-functionalized 2H-phase NSs also outperformed 1T-phase MoS_2 (obtained either by the lithium intercalation/exfoliation route or by hydrothermal synthesis), as well as most reported catalysts based on non-noble metals (e.g., Cu, Co or Ni). Likewise, the cathodically derivatized NSs compared very favorably with other documented catalysts in the reduction of the other nitroarenes and the organic dyes (see Table S2). It was therefore concluded that the present functionalization strategy affords enhanced and highly competitive MoS_2 catalysts.

Table 2. Catalytic activity of the acetic acid-functionalized 2H-phase MoS_2 nanosheets. Catalytic activity calculated as the number of moles of substrate converted per unit time per mole of MoS_2 catalyst in the reaction medium.

Substrate	**Catalytic activity (h^{-1})**
4-nitrophenol	63
2-nitrophenol	340
4-nitroaniline	180
2-nitroaniline	90
nitrobenzene	78
methyl orange	71
methylene blue	44

The experimental kinetic profiles recorded for nitroarene and dye reduction with different catalysts usually obey either first- or zero-order behavior with respect to the substrate,[52,65] i.e., they obey one of the two following equations

Reaction order of 1: $$d[S]/dt = -k_1[S] \tag{3}$$

Reaction order of 0: $$d[S]/dt = -k_0 \tag{4}$$

, where [S] is the substrate concentration, and k_1 and k_0 are the apparent reaction rate constants. Because the reductant was used in a large excess relative to the substrate, its concentration was assumed to remain roughly constant throughout the reaction, and so its contribution to the rate equations was not explicitly included as it was implicitly incorporated in the k_1 and k_0 rate constants. Even though the catalytic reduction of nitroarenes/dyes is extensively investigated, the specific factors that govern its kinetic behavior and the corresponding reaction order are not usually known. As a first step to rationalize the kinetics, we note that in the presence of a large excess of reducing agent, the reaction rate should be mainly limited by the rate of diffusion of the substrate molecules to the catalyst surface.[67] Within this framework, we hypothesized that the reaction kinetics for the present acetic acid-functionalized MoS_2 catalyst was largely determined by the net electric charge of the substrate molecule. Such a hypothesis was based on the following reasoning. In the basic medium of the reduction reaction (pH ~11 generated by the presence of sodium borohydride), the functionalized NSs are negatively charged, as discussed above. If the substrate molecule is negatively charged as well, its access to the catalyst will be hampered by an electrostatic repulsion barrier. Under such a scenario, the reaction rate can be expected to positively correlate with the substrate concentration, i.e., the higher the substrate concentration, the higher the probability that a substrate molecule will be able to reach a catalytic active site, and thus the higher the reaction rate. This behavior would be better described by Eq. 3 (reaction order of 1). In our case, this situation would be in place for 4-NP, 2-NP and MO, which are negatively charged in the reaction medium (the pK_a of both 4-NP and 2-NP is around 7, and that of MO is around 3.5).[39]

On the other hand, electrostatically unimpeded access to the catalyst is to be expected in the case of electrically neutral substrate molecules. As a result, the catalytic active sites should be more likely to become saturated with the substrate, so that the reaction rate will be much less sensitive to its concentration and hence will more probably obey Eq. 4 (reaction order of 0). 4-NA, 2-NA and NB are electrically neutral in the basic reaction medium (the pK_a of the conjugate acid of 4-NA and 2-NA is around 1 and 0, respectively).[39] Finally, a special situation may arise when the substrate molecule is positively charged (MB in our case). Here, a diffuse layer of substrate molecules should form on the surface of the MoS_2 NSs by electrostatic attraction,[68] which can be expected to hinder transport of the reactants and reaction products between the bulk of the solution and the catalytic active sites. Accordingly, the reaction rate should negatively correlate with the substrate concentration: as the latter is decreased, less compact diffuse layers should develop, which in turn should make reactant/product transport easier and lead to higher reaction rates. Hence, the corresponding kinetic behavior could be well described by a reaction order of -1 as reflected in the following equation

Reaction order of -1: $d[S]/dt = -k_{-1}/[S]$ (5)

If the above reasoning is correct, Eq. 3, 4 and 5 predict that the kinetic profiles of the reactions must adhere to exponential, linear and square-root decay functions for negatively charged, neutral and positively charged substrate molecules, respectively. To probe this, the experimental kinetic profiles (Fig. 3a and b) were fitted to such types of decay function and the quality of the fits was assessed from their regression coefficients (R^2). Fig. 3c and d shows the results of the linear and exponential fits, respectively, for 4-NP, 2-NP, 4-NA, 2-NA, NB and MO, with the corresponding R^2 values also indicated in the plots. MB was not included because it was obvious (Fig. 3b) that its kinetic profile could not be described by either a linear or exponential decay function. The quality of the fits was good (R^2 ~0.99) in the linear case with 4-NA, 2-NA and NB, and in the exponential case with 4-NP and 2-NP, but it was poor ($R^2 < 0.94$) in the linear case with 4-NP and 2-NP, and in the exponential case with 4-NA, 2-NA and NB. Moreover, for MB a reasonable fit to a square-root decay function (R^2 ~0.97) was attained (Fig. 3e). In the specific case of MO the fit was not good either in the linear case or in the exponential case. Given that MO reduction yields two distinct aniline derivatives as the reaction products (see Fig. S10 in the SI),[69] one neutral and the other negatively charged, their presence in the reaction medium is expected to result in a mixture of zero and first order kinetics, which explains why the profiles do not fit to either linear or exponential decay. Thus, overall, the results of the fittings of the experimental kinetic profiles agreed with the above prediction of the kinetic behavior with the present MoS_2 catalyst being largely determined by the substrate charge. We note, however, that while the latter can be used as a proxy to understand the kinetics of the catalytic reduction, careful consideration of the specific characteristics of the catalyst should always be taken. For instance, the formation of a diffuse layer of positively charged substrate molecules on a catalyst that is negatively charged by weakly adsorbed (physisorbed) anionic surfactant molecules will probably be compromised by molecular exchange of the latter for the substrate molecules. Hence, the corresponding reduction kinetics will likely not be described by a reaction order of -1, as recently observed for MB reduction with MoS_2 NSs stabilized by an anionic dispersant.[52] In the present case, a robust diffuse layer is expected to form because the anionic acetic acid groups are strongly bound to the MoS_2 NSs.

Finally, with a view to the practical implementation of the functionalized MoS_2 catalyst, a number of further issues were considered. First, although the substrate concentrations used here (in the range of 0.1 mM) are quite convenient for the testing and comparison of catalyst performance, actual wastewater effluents usually contain much higher concentrations of the pollutants (~10 mM).[70] To test the ability of the functionalized NSs to work in more concentrated reaction media, the reduction of 4-NP was carried out at concentrations ten and a hundred times higher (i.e., 1.2 and 12 mM). The resulting kinetic profiles are presented in Fig. 4a. An exponential decay function (reaction order of 1, Eq. 3) was still observed for both concentrations, which means that the substrate concentrations are not still sufficiently high to saturate the active sites of the catalyst. In fact, the time required to reaction completion with a concentration ten times higher than that originally tested (1.2 mM 4-NP) is more or less the same, and thus the catalytic activity is ten times higher (660 h^{-1} at 1.2 mM vs. 63 h^{-1} at 0.12 mM 4-NP). With a difference of another factor of ten (12 mM 4-NP), the time required to reaction completion was ~10 times higher so that the catalytic activity remained similar (~600 h^{-1}), which indicated that the catalytic performance of the NSs was not impaired by the presence of a large amount of substrate. Second, the catalyst was also efficient in the reduction of nitroarene mixtures, which can be present in industrial wastewaters, as shown in Fig. 4b for the kinetic profiles of a binary (4-NA, 2-NA) and a ternary (4-NA, 2-NA, 4-NP) mixture. The measured catalytic activities (~370 and 75 h^{-1} for the binary and ternary mixture, respectively) were in the range of those determined for the corresponding single substrates (see Table 2). Third, immobilization of the catalyst on a proper substrate can be a convenient way to facilitate its handling and re-use. The functionalized MoS_2 NSs could be immobilized on a polyurethane foam scaffold by dipping the latter into an aqueous NS solution that was then allowed to dry. Fig. 4c-e shows FE-SEM images and digital pictures of the foam before (c and d) and after (e) NS coating. The cellular, macroporous structure of the polyurethane foam is clearly appreciated in the lower resolution image (Fig. 4c). Testing of the immobilized catalyst toward 4-NP reduction indicated that it could be used for 9 consecutive cycles without experiencing a large decline in activity (Fig. 4f).

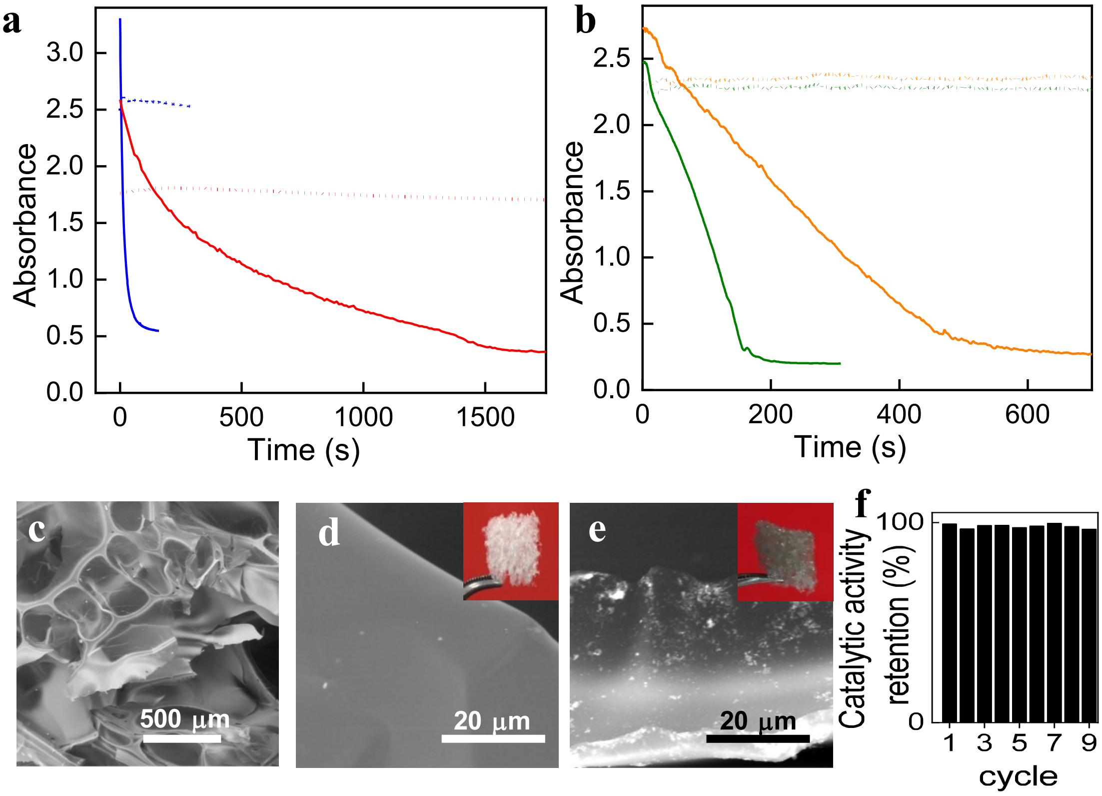

Figure 4. (a) Kinetic profiles for the reduction of 4-NP catalyzed by functionalized MoS_2 nanosheets (catalyst concentration: 7 mg L^{-1}) carried out in concentrated reaction media, namely: 1.2 mM 4-NP (λ=455 nm, blue trace) and 12 mM 4-NP (λ=479 nm, red trace). Blank experiments for each profile are also shown as dotted lines. **(b)** Kinetic profiles for the reduction of mixtures of nitroarenes catalyzed by functionalized MoS_2 nanosheets (catalyst concentration: 3.5 mg L^{-1}), namely: binary mixture of 4-NA (0.12 mM) and 2-NA (0.24 mM) (orange trace), and a ternary mixture of 4-NP (0.06 mM), 4-NA (0.06 mM) and 2-NA (0.12 mM) (gray trace). Blank experiments for each profile are also shown as dotted lines. **(c-e)** FE-SEM micrographs of polyurethane foam before (c,d) and after (e) coating with MoS_2 nanosheets. Insets to d and e: digital photographs of cylinders ~1 cm in diameter and ~1 cm in height of the foam before and after coating, respectively. **(f)**

Reusability experiments of polyurethane foam-supported MoS_2 nanosheets in the catalytic reduction of 4-NP with $NaBH_4$ ([4-NP] = 0.12 mM).

3. Conclusions

We have demonstrated that 2H-phase MoS_2 NSs can be functionalized with molecular groups derived from organoiodides by a straightforward and expeditious electrolytic method. Such a method relies on the cathodic treatment of a previously expanded MoS_2 crystal in an electrolyte that contains the organoiodide (iodoacetic acid or 4-iodoaniline), yielding a derivatized material that, contrary to its non-functionalized counterpart, can be colloidally dispersed in aqueous medium. Changes detected in the surface chemistry, water contact angle and zeta potential of the MoS_2 NSs confirmed their successful molecular functionalization. The derivatization reaction was not spontaneous and required an external supply of electrons to proceed, which in the present case originated from the application of a cathodic potential, but could be obtained from a reducing agent as well. Grafting of the molecular groups on the 2H-phase MoS_2 NSs was also thought to be made possible by the locally enhanced chemical reactivity associated to intrinsic lattice defects, especially sulfur vacancies. The acetic acid-functionalized NSs exhibited a high catalytic activity in the reduction of nitroarenes and organic dyes, which is of practical relevance for the treatment of industrial wastewater effluents, outperforming most (if not all) 1T- and 2H-phase MoS_2 and other non-noble metal-based catalysts previously investigated for this purpose. The functionalized MoS_2 catalyst retained most of its activity even at the high reactant concentrations typical of actual wastewater effluents, also performed efficiently in the reduction of binary and ternary mixtures of the reactants, and could be immobilized onto a polymer scaffold to facilitate its manipulation and re-use. Further, a correlation between the kinetic behavior of the reduction reaction (i.e., reaction order) and the net electric charge of the reactant molecule was established and rationalized on the basis of the relative ability of the latter to diffuse to the active sites of the catalyst. Finally, we note that the molecular derivatization strategy developed here should be beneficial for the application of 2H-phase MoS_2 NSs in areas beyond catalysis. For instance, biomolecules, polymers and other nanostructures could be covalently attached to the functionalized NSs through their carboxylic acid or amino groups, yielding hybrid materials that could find practical use in, e.g., biomedicine or energy conversion and storage.

Supporting Information. The Supporting Information is available free of charge on the ACS Publications website at DOI: 10.1021/acsami.1c08850.

Experimental section, additional characterization of the functionalized MoS_2 materials, additional information on the performance of functionalized MoS_2 NSs as catalysts.

Acknowledgements. Funding by the Spanish Ministerio de Ciencia, Innovación y Universidades (MICINN), Agencia Estatal de Investigación (AEI) and the European Regional Development Fund (ERDF) through project RTI2018-100832-B-I00, as well as Plan de Ciencia, Tecnología e Innovación (PCTI) 2013-2017 del Principado de Asturias and the ERDF (project IDI/2018/000233) is gratefully acknowledged. S.G.-D. is grateful to the Spanish MINECO for his pre-doctoral contract (BES/2016 077830).

References

[1] Tan, C.; Cao, X.; Wu, X.-J.; He, Q.; Yang, J.; Zhang, X.; Chen, J.; Zhao, W.; Han, S.; Nam, G.-H.; Sindoro, M.; Zhang, H. Recent Advances in Ultrathin Two-Dimensional Nanomaterials, *Chem. Rev.* **2017**, *117*, 6225–6331.

[2] Luo, P.; Zhuge, F.; Zhang, Q.; Chen, Y.; Lv, L.; Huang, Y.; Li, H.; Zhai, T. Doping Engineering and Functionalization of Two-Dimensional Metal Chalcogenides, *Nanoscale Horiz.* **2019**, *4*, 26–51.

[3] Chen, X.; McDonald, A.R. Functionalization of Two-Dimensional Transition-Metal Dichalcogenides, *Adv. Mater.* **2016**, *28*, 5738–5746.

[4] Bertolazzi, S.; Gobbi, M.; Zhao, Y.; Backes, C.; Samorì, P. Molecular Chemistry Approaches for Tuning the Properties of Two-Dimensional Transition Metal Dichalcogenides, *Chem. Soc. Rev.* **2018**, *47*, 6845–6888.

[5] Ippolito, S.; Ciesielski, A.; Samorì, P. Tailoring the Physicochemical Properties of Solution-Processed Transition Metal Dichalcogenides via Molecular Approaches, *Chem. Commun.* **2019**, *55*, 8900–8914.

[6] Chou, S.C.; De, M.; Kim, J.; Byun, S.; Dykstra, C.; Yu, J.; Huang, J.; Dravid, V.P. Ligand Conjugation of Chemically Exfoliated MoS_2, *J. Am. Chem. Soc.* **2013**, *135*, 4584–4587.

[7] Tang, Q.; Jiang, D.; Stabilization and Band-Gap Tuning of the 1T-MoS_2 Monolayer by Covalent Functionalization, *Chem. Mater.* **2015**, *27*, 3743–3748.

[8] Voiry, D.; Goswami, A.; Kappera, R.; Silva, C.C.C.; Kaplan, D.; Fujita, T.; Chen, M.; Asefa, T.; Chhowalla, M. Covalent Functionalization of Monolayered Transition Metal Dichalcogenides by Phase Engineering, *Nat. Chem.* **2015**, *7*, 45–49.

[9] Paredes, J.I.; Munuera, J.M.; Villar-Rodil, S.; Guardia, L.; Ayán-Varela, M.; Pagán, A.; Aznar-Cervantes, S.D.; Cenis, J.L.; Martínez-Alonso, A.; Tascón, J.M.D. Impact of Covalent Functionalization on the Aqueous Processability, Catalytic Activity, and

Biocompatibility of Chemically Exfoliated MoS_2 Nanosheets, *ACS Appl. Mater. Interfaces*, **2016**, *8*, 27974–27986.

[10] Knirsch, K.C.; Berner, N.C.; Nerl, H.C.; Cucinotta, C.S.; Gholamvand, Z.; McEvoy, N.; Wang, Z.; Abramovic, I.; Vecera, P.; Halik, M.; Sanvito, S.; Duesberg, G.S.; Nicolosi, V.; Hauke, F.; Hirsch, A.; Coleman, J.N.; Backes, C. Basal-Plane Functionalization of Chemically Exfoliated Molybdenum Disulfide by Diazonium Salts, *ACS Nano* 2015, 9, 6018–6030.

[11] Lei, Z.; Zhan, J.; Tang, L.; Zhang, Y.; Wang, Y. Recent Development of Metallic (1T) Phase of Molybdenum Disulfide for Energy Conversion and Storage, *Adv. Energy Mater.* **2018**, *8*, 1703482 (1–29).

[12] Shi, S.; Sun, Z.; Hu, Y.H. Synthesis, Stabilization and Applications of 2-Dimensional 1T Metallic MoS_2, *J. Mater.Chem. A* **2018**, *6*, 23932–23977.

[13] Ding, Q.; Czech, K.J.; Zhao, Y.; Zhai, J.; Hamers, R.J.; Wright, J.C.; Jin, S. Basal-Plane Ligand Functionalization on Semiconducting 2H-MoS_2 Monolayers, *ACS Appl. Mater. Interfaces* **2017**, *9*, 12734–12742.

[14] Canton-Vitoria, R.; Sayed-Ahmad-Baraza, Y.; Pelaez-Fernandez, M.; Arenal, R.; Bittencourt, C.; Ewels, C.P.; Tagmatarchis, N. Functionalization of MoS_2 with 1,2-Dithiolanes: toward Donor-Acceptor Nanohybrids for Energy Conversion, *npj 2D Mater. Appl.* **2017**, *1*, 13 (1–9).

[15] Chu, X.S.; Yousaf, A.; Li, D.O.; Tang, A.A.; Debnath, A.; Ma, D.; Green, A.A.; Santos, E.J.G.; Wang, Q.H. Direct Covalent Chemical Functionalization of Unmodified Two-Dimensional Molybdenum Disulfide, *Chem. Mater.* **2018**, *30*, 2112–2128.

[16] Backes, C.; Berner, N.C.; Chen, X.: Lafargue, P.; LaPlace, P.; Freeley, M.; Duesberg, G.S.; Coleman, J.N.; McDonald, A.R. Functionalization of Liquid-Exfoliated Two-Dimensional 2H-MoS_2, *Angew. Chem. Int. Ed.* **2015**, *54*, 2638–2642.

[17] Vera-Hidalgo, M.; Giovanelli, E.; Navío, C.; Pérez, E.M.; Mild Covalent Functionalization of Transition Metal Dichalcogenides with Maleimides: a "Click" Reaction for 2H-MoS_2 and WS_2, *J. Am. Chem. Soc.* **2019**, *141*, 3767–3771.

[18] Park, Y.; Shin, S.; An, Y.; Ahn, J.-G.; Shin, G.; Ahn, C.; Bang, J.; Baik, J.; Kim, Y.; Jung, J.; Lim, H. Tunable Optical Transition in 2H-MoS_2 via Direct Electrochemical Engineering of Vacancy Defects and Surface S–C Bonds, *ACS Appl. Mater. Interfaces* **2020**, *12*, 40870–40878.

[19] Horn, E.J.; Rosen, B.R.; Baran, P.S. Synthetic Organic Electrochemistry: an Enabling and Innately Sustainable Method, *ACS Cent. Sci.* **2016**, *2*, 302–308.

[20] Paredes, J.I.; Munuera, J.M. Recent Advances and Energy-Related Applications of High Quality/Chemically Doped Graphenes Obtained by Electrochemical Exfoliation Methods, *J. Mater. Chem. A* **2017**, *5*, 7228–7242.

[21] Yang, S.; Zhang, P.; Nia, A.S.; Feng, X. Emerging 2D Materials Produced via Electrochemistry, *Adv. Mater.* **2020**, *32*, 1907857 (1–19).

[22] García-Dalí, S.; Paredes, J.I.; Munuera, J.M.; Villar-Rodil, S.; Adawy, A.; Martínez-Alonso, A.; Tascón, J.M.D. Aqueous Cathodic Exfoliation Strategy toward Solution-Processable and Phase-Preserved MoS_2 Nanosheets for Energy Storage and Catalytic Applications, *ACS Appl. Mater. Interfaces* **2019**, *11*, 36991–37003.

[23] Xue, Y.; Zhang, Q.; Wang, W.; Cao, H.; Yang, Q.; Fu, L. Opening Two-Dimensional Materials for Energy Conversion and Storage: a Concept, *Adv. Energy Mater.* **2017**, *7*, 1602684 (1–23).

[24] X. You, N. Liu, C.J. Lee, J.J. Pak, An Electrochemical Route to MoS_2 Nanosheets for Device Applications, *Mater. Lett.* **2014**, *121*, 31–35.

[25] Liu, N.; Kim, P.; Kim, J.H.; Ye, J.H.; Kim, S.; Lee, C.J. Large-Area Atomically Thin MoS_2 Nanosheets Prepared Using Electrochemical Exfoliation, *ACSNano* **2014**, *8*, 6902–6910.

[26] Ambrosi, A.; Pumera, M. Electrochemical Exfoliation of MoS_2 Crystal for Hydrogen Electrogeneration, *Chem. Eur. J.* **2018**, *24*, 18551–18555.

[27] Garah, M.E.; Bertolazzi, S.; Ippolito, S.; Eredia, M.; Janica, I.; Melinte, G.; Ersen, O.; Marletta, G.; Ciesielski, A.; Samorì, P. MoS_2 Nanosheets via Electrochemical Lithium-Ion Intercalation under Ambient Conditions, *FlatChem* **2018**, *9*, 33–39.

[28] Lin, Z.; Liu, Y.; Halim, U.; Ding, M.; Liu, Y.; Wang, Y.; Jia, C.; Chen, P.; Duan, X.; Wang, C.; Song, F.; Li, M.; Wan, C.; Huang, Y.; Duan, X. Solution-processable 2D Semiconductors for High-Performance Large-Area Electronics, *Nature* **2018**, *562*, 254–258.

[29] Fry, A.J. *Synthetic Organic Electrochemistry,* 2nd ed; John Wiley & Sons: New York, 1989; Chapter 5, pp. 136–155.

[30] Fedurco, M.; Sartoretti, C.J.; Augustynski, J. Reductive Cleavage of the Carbon-Halogen Bond in Simple Methyl and Methylene Halides. Reactions of the Methyl Radical and Carbine at the Polarized Electrode/Aqueous Solution Interface, *Langmuir* **2001**, *17*, 2380–2387.

[31] Chehimi, M.M.; Hallais, G.; Matrab, T.; Pinson, J.; Podvorica, F.I. Electro- and Photografting of Carbon or Metal Surfaces by Alkyl Groups, J. Phys. Chem. C 2008, 112, 18559–18565.

[32] Koefoed, L.; Pedersen, S.U.; Daasbjerg, K. Covalent Modification of Glassy Carbon Surfaces by Electrochemical Grafting of Aryl Iodides, *Langmuir* **2017**, *33*, 3217–3222.

[33] Smith, R.J.; King, P.J.; Lotya, M.; Wirtz, C.; Khan, U.; De, S.; O´Neill, A.; Duesberg, G.S.; Grunlan, J.C.; Moriarty, G.; Chen, J.; Wang, J.; Minett, A.I.; Nicolosi, V.; Coleman, J.N. Large-Scale Exfoliation of Inorganic Layered Compounds in Aqueous Surfactant Solutions, *Adv. Mater.* **2011**, *23*, 3944–3948.

[34] Li, B.L.; Zou, H.L.; Lu, L.; Yang, Y.; Lei, J.L.; Luo, H.Q.; Li, N.B. Size-Dependent Optical Absorption of Layered MoS_2 and DNA Oligonucleotides Induced Dispersion

Behavior for Label-Free Detection of Single-Nucleotide Polymorphism, *Adv. Funct. Mater.* **2015**, *25*, 3541–3550.

[35] Backes, C.; Smith, R.J.; McEvoy, N.; Berner, N.C.; McCloskey, D.; Nerl, H.C.; O´Neill, A.; King, P.J.; Higgins, T.; Hanlon, D.; Scheuschner, N.; Maultzsch, J.; Houben, L.; Duesberg, G.S.; Donegan, J.F.; Nicolosi, V.; Coleman, J.N. Edge and Confinement Effects Allow in Situ Measurement of Size and Thickness of Liquid-Exfoliated Nanosheets, *Nat. Commun.* **2014**, *5*, 4576 (1–10).

[36] Zhang, J.; Wang, Y.; Cui, J.; Wu, J.; Li, Y.; Zhu, T. Kang, H.; Yang, J.; Sun, J.; Qin, Y.; Zhang, Y.; Ajayan, P.M.; Wu, Y. Water-Soluble Defect-Rich MoS_2 Ultrathin Nanosheets for Enhanced Hydrogen Evolution, *J. Phys. Chem. Lett.* **2019**, *10*, 3282–3289.

[37] Zhang, X.; Qiao, X.-F.; Shi, W.; Wu, J.-B.; Jiang, D.-S.; Tan, P.-H. Phonon and Raman Scattering of Two-Dimensional Transition Metal Dichalcogenides from Monolayer, Multilayer to Bulk material, *Chem. Soc. Rev.* **2015**, *44*, 2757–2785.

[38] Everet, D.H. *Basic Principles of Colloid Science*; Royal Society of Chemistry: London, 1988; Chapter 9, p. 130.

[39] Dean, J.A. *Lange´s Handbook of Chemistry*, 15th ed; McGraw-Hill: New York, 1999; Section 8, pp. 8.24–8.72.

[40] Greczynski, G.; Hultman, L. X-Ray Photoelectron Spectroscopy: towards Reliable Binding Energy Referencing, *Prog. Mater. Sci.* **2020**, *107*, 100591 (1–46).

[41] Povstugar, V. I.; Mikhailova, S. S.; Shakov, A. A. Chemical Derivatization Techniques in the Determination of Functional Groups by X-Ray Photoelectron Spectroscopy, *J. Anal. Chem.* **2000**, *55*, 405–416.

[42] Eda, G.; Yamaguchi, H.; Voiry, D.; Fujita, T.; Chen, M.; Chhowalla, M. Photoluminescence from Chemically Exfoliated MoS_2, *Nano Lett.* **2011**, *11*, 5111–5116.

[43] Yan, E.X.; Cabán-Acevedo, M.; Papadantonakis, K.M.; Brunschwig, B.S.; Lewis, N.S. Reductant-Activated, High-Coverage, Covalent Functionalization of 1T′-MoS_2, *ACS Materials Lett.* **2020**, *2*, 133–139.

[44] Heising, J.; Kanatzidis, M.G. Exfoliated and Restacked MoS_2 and WS_2: Ionic or Neutral Species? Encapsulation and Ordering of Hard Electropositive Cations, *J. Am. Chem. Soc.* **1999**, *121*, 11720–11732.

[45] Chhowalla, M.; Shin, H.S.; Eda, G.; Li, L.-J.; Loh, K.P.; Zhang, H. The Chemistry of Two-Dimensional Layered Transition Metal Dichalcogenide Nanosheets, *Nat. Chem.* **2013**, *5*, 263–275.

[46] Krishnamurthy, S.; Brown, H.C. Selective reductions. 27. Reaction of Alkyl Halides with Representative Complex Metal Hydrides and Metal Hydrides. Comparison of Various Hydride Reducing Agents, *J. Org. Chem.* **1980**, *45*, 849–856.

[47] Seyden-Penne, J. *Reductions by the Alumino- and Borohydrides in Organic Synthesis*; Wiley-VCH: New York, 1997; Chapters 1 and 2, pp. 1–35.

[48] Bollinger, M.V.; Lauritsen, J.V.; Jacobsen, K.W.; Nørskov, J.K.; Helveg, S.; Besenbacher, F. One-Dimensional Metallic Edge States in MoS_2, *Phys. Rev. Lett.* **2001**, *87*, 196803 (1–4).

[49] Gali, S.M.; Pershin, A.; Lherbier, A.; Charlier, J.-C.; Beljonne, D. Electronic and Transport Properties in Defective MoS_2: Impact of Sulfur Vacancies, *J. Phys. Chem. C* **2020**, *124*, 15076–15084.

[50] Addou, R.; Colombo, L.; Wallace, R.M. Surface Defects on Natural MoS_2, *ACS Appl. Mater. Interfaces* **2015**, *7*, 11921–11929.

[51] Hong, J.; Hu, Z.; Probert, M.; Li, K.; Lv, D.; Yang, X.; Gu, L.; Mao, N.; Feng, Q.; Xie, L.; Zhang, J.; Wu, D.; Zhang, Z.; Jin, C.; Ji, W.; Zhang, X.; Yuan, J.; Zhang, Z. Exploring Atomic Defects in Molybdenum Disulphide Monolayers, *Nat. Commun.* **2015**, *6*, 6293 (1–8).

[52] García-Dalí, S.; Paredes, J.I.; Caridad, B.; Villar-Rodil, S.; Díaz-González, M.; Fernández-Sánchez, C.; Adawy, A.; Martínez-Alonso, A.; Tascón, J.M.D. Activation of Two-Dimensional MoS_2 Nanosheets by Wet-Chemical Sulfur Vacancy Engineering for the Catalytic Reduction of Nitroarenes and Organic Dyes, *Appl. Mater. Today* **2020**, *20*, 100678 (1–13).

[53] Tsai, C.; Li, H.; Park, S.; Han, H.S.; Nørskov, J.K.; Zheng, X.; Abild-Pedersen, F. Electrochemical Generation of Sulfur Vacancies in the Basal Plane of MoS_2 for Hydrogen Evolution, *Nat. Commun.* **2017**, *8*, 15113 (1–8).

[54] Wen, Y.; He, P.; Yao, Y.; Zhang, Y.; Cheng, R.; Yin, L.; Li, N.; Li, J.; Wang, J.; Wang, Z.; Liu, C.; Fang, X.; Jiang, C.; Wei, Z.; He, J. Bridging the Van der Waals Interface for Advanced Optoelectronic Devices, *Adv. Mater.* **2020**, *32*, 1906874 (1–7).

[55] Cho, K.; Min, M.; Kim, T.-Y.; Jeong, H.; Pak, J.; Kim, J.-K.; Jang, J.; Yun, S.J.; Lee, Y.H.; Hong, W.-K.; Lee, T. Electrical and Optical Characterization of MoS_2 with Sulfur Vacancy Passivation by Treatment with Alkanethiol Molecules, *ACS Nano* **2015**, *9*, 8044–8053.

[56] Ye, J.; He, F.; Nie, J.; Cao, Y.; Yang, H.; Ai, X. Sulfur/Carbon Nanocomposite-Filled Polyacrylonitrile Nanofibers as a Long Life and High Capacity Cathode for Lithium–Sulfur Batteries. *J. Mater. Chem. A* **2015**, *3*, 7406–7412.

[57] Jayabal, S.; Saranya, G.; Wu, J.; Liu, Y.; Geng, D.; Meng, X. Understanding the High-Electrocatalytic Performance of Two-Dimensional MoS_2 Nanosheets and their Composite Materials, *J. Mater. Chem. A* **2017**, *5*, 24540–24563.

[58] Yin, Y.; Han, J.; Zhang, Y.; Zhang, X.; Xu, P.; Yuan, Q.; Samad, L.; Wang, X.; Wang, Y.; Zhang, Z.; Zhang, P.; Cao, X.; Song, B.; Jin. S. Contributions of Phase, Sulfur Vacancies, and Edges to the Hydrogen Evolution Reaction Catalytic Activity of Porous Molybdenum Disulfide Nanosheets. *J. Am. Chem. Soc.* **2016**, *138*, 7965–7972.

[59] Ding, Q.; Song, B.; Xu, P.; Jin. S. Efficient Electrocatalytic and Photoelectrochemical Hydrogen Generation Using MoS_2 and Related Compounds, *Chem* **2016**, *1*, 699–726.

[60] Hu, H.; Xin, J.H.; Hu, H.; Wang, X.; Miao, D.; Liu, Y. Synthesis and Stabilization of Metal Nanocatalysts for Reduction Reactions – a Review, *J. Mater. Chem. A* **2015**, *3*, 11157–11182.

[61] Naseem, K.; Begum, R.; Farooqi, Z.H. Catalytic Reduction of 2-Nitroaniline: a Review, *Environ. Sci. Pollut. Res.* **2017**, *24*, 6446-6460.

[62] Guardia, L.; Paredes, J.I.; Munuera, J.M.; Villar-Rodil, S.; Ayán-Varela, M.; Martínez-Alonso, A.; Tascón, J.M.D. Chemically Exfoliated MoS_2 Nanosheets as an Efficient Catalyst for Reduction Reactions in the Aqueous Phase, *ACS Appl. Mater. Interfaces* **2014**, *6*, 21702–21710.

[63] Jeffery, A.A.; Rao, S.R.; Rajamathi, M. Preparation of MoS_2-Reduced Graphene Oxide (rGO) Hybrid Paper for Catalytic Applications by Simple Exfoliation-Costacking, *Carbon* **2017**, *112*, 8–16.

[64] Peng, K.; Fu, L.; Yang, H.; Ouyang, J.; Tang, A. Hierarchical MoS_2 Intercalated Clay Hybrid Nanosheets with Enhanced Catalytic Activity, *Nano Res.* **2017**, *10*, 570–583.

[65] Aditya, T.; Pal, A.; Pal, T. Nitroarene Reduction: a Trusted Model Reaction to Test Nanoparticle Catalysts, *Chem. Commun.* **2015**, *51*, 9410–9431.

[66] Ayán-Varela, M.; Pérez-Vidal, Ó.; Paredes, J.I.; Munuera, J.M.; Villar-Rodil, S.; Díaz-González, M.; Fernández-Sánchez, C.; Silva, V.S.; Cicuéndez, M.; Vila, M.; Martínez-Alonso, A.; Tascón, J.M.D. Aqueous Exfoliation of Transition Metal Dichalcogenides Assisted by DNA/RNA Nucleotides: Catalytically Active and Biocompatible Nanosheets Stabilized by Acid-Base Interactions, *ACS Appl. Mater. Interfaces* **2017**, *9*, 2835–2845.

[67] Hervés, P.; Pérez-Lorenzo, M.; Liz-Marzán, L.M.; Dzubiella, J.; Lu, Y.; Ballauff, M. Catalysis by Metallic Nanoparticles in Aqueous Solution: Model Reactions, *Chem. Soc. Rev.* **2012**, *41*, 5577–5587.

[68] Butt, H.-J.; Graf, K.; Kappl, M. *Physics and Chemistry of Interfaces*; Wiley-VCH: Weinheim, 2003; Chapter 4, pp. 42–56.

[69] Zheng, L.-Q.; Yu, X.-D.; Xu, J.-J.; Chen, H.-Y. Reversible Catalysis for the Reaction between Methyl Orange and $NaBH_4$ by Silver Nanoparticles, *Chem. Commun.* **2015**, *51*, 1050–1053.

[**70**] Liu, T.; Sun, Y.; Jiang, B.; Guo, W.; Qin, W.; Xie, Y.; Zhao, B.; Zhao, L.; Liang, Z.; Jiang, L. Pd Nanoparticle-Decorated 3D-Printed Hierarchically Porous TiO2 Scaffolds for the Efficient Reduction of a Highly Concentrated 4-Nitrophenol Solution, *ACS Appl. Mater. Interfaces*. **2020**, 12, 28100–28109.

Supporting Information

Molecular functionalization of 2H-phase MoS_2 nanosheets via an electrolytic route for enhanced catalytic performance

S. García-Dalí, J.I. Paredes, S. Villar-Rodil*, A. Martínez-Jódar, A. Martínez-Alonso, J.M.D. Tascón*

Instituto de Ciencia y Tecnología del Carbono, INCAR-CSIC, Francisco Pintado Fe 26, 33011 Oviedo, Spain

* Corresponding author: paredes@incar.csic.es (J. I. Paredes),

* Corresponding author: silvia@incar.csic.es (S. Villar-Rodil)

1. Experimental section

1.1. Materials and reagents

Pieces of MoS_2 natural crystals (approximate dimensions: ~10×10×0.5 mm^3) were obtained from SPI Supplies. Platinum foil (25×25×0.025 mm^3) was purchased from Good Fellow. Ethanol was obtained from VWR. H_2SO_4 25 %, KCl (>0.005% Br), isopropanol, iodoacetic acid (purity ≥98.0%), $NaBH_4$, 4-iodoaniline (≥98.0%), 4-nitrophenol (4-NP), 2-nitrophenol (2-NP), 4-nitroaniline (4-NA), 2-nitronailine (2-NA), nitrobenzene (NB), methylene blue (MB), and methyl orange (MO) were obtained from Sigma-Aldrich and used as received. Milli-Q deionized water (Millipore Corporation; resistivity: 18.2 MΩ•cm) was employed in all the experiments.

1.2. Electrochemical functionalization

The functionalization of MoS_2 was carried out in two consecutive electrochemical steps, both performed in cathodic conditions and in a two-electrode set-up. A ~5×5×0.5 mm^3 piece of MoS_2 was first cut from the as-received crystal, then cleaved by mechanical exfoliation with scotch tape, which removed the top-most layers of MoS_2, leaving a freshly exposed crystal surface. The latter was used as the working electrode and platinum foil as counter electrode, both of them being connected to a DC power supply (Agilent 6614C), using crocodile clips, and fixed at a distance of ~2 cm from each other in the solution. In this configuration, about two-thirds of the MoS_2 electrode was immersed in the electrolyte. In the first step, 20 mL of an aqueous 4 M KCl solution was used as the electrolyte and a negative voltage of -20 V was applied to the MoS_2 electrode for 30 min, to promote its delamination. Then, functionalization was carried out by substituting the electrolytic medium by 20 mL of iodoacetic acid solution and a negative voltage of -5 V was applied for 1 h. Although different solvents (ethanol, isopropanol, water and supporting electrolytes for iodoacetic acid were tested, the functionalization was considered to be optimal using an aqueous solution of 0.05 M iodoacetic acid and 0.15 M Na_2SO_4. After the electrochemical treatment, the most expanded part of the cathode, which roughly corresponded to the lower half of the MoS_2 piece, was recovered, thoroughly washed with water, dried overnight under reduced pressure at room temperature and finally stored in glass vials for subsequent use.

1.3. Post-processing of the functionalized products: nanosheet extraction and dispersion in water

To obtain individualized MoS_2 nanosheets (NSs) from the electrochemically treated material, the latter was first cut into smaller pieces with the aid of a scalpel and then transferred to water at nominal concentration of 2 mg mL^{-1}, where it was bath-sonicated (J.P. Selecta Ultrasons system, 40 kHz) for 3 h. After standing undisturbed for 24 h to allow sedimentation of the poorly exfoliated fraction of the material, the upper ~75% of the supernatant volume was collected from the sonicated dispersion and kept for subsequent use.

1.4. Characterization techniques

The material was characterized by UV-vis absorption spectroscopy, zeta-potential measurements, atomic force microscopy (AFM), field-emission scanning electron microscopy (FE-SEM), Raman spectroscopy, X-ray photoelectron spectroscopy (XPS), attenuated total reflection Fourier transform infrared (ATR-FTIR) spectroscopy, electron paramagnetic resonance (EPR) spectroscopy as well as by measurement of its water contact angle. UV-vis absorption (extinction) spectra were obtained for colloidal dispersions of the exfoliated MoS_2 material in a double-beam He□ios □ spectrophotometer (Thermo Spectronic) using quartz cuvettes with an optical path length of 1 cm. The average lateral size and thickness of the dispersed NSs along with their concentration in the supernatant suspension were estimated by means of UV-vis absorption (extinction) spectroscopy using the metrics developed by Backes *et al* for this 2D material [1]. Zeta-potential measurements were carried out at a temperature of 25 ºC with a Malvern Zetasizer Nano ZSP apparatus from Malvern Instruments Ltd. using ~1 mL of MoS_2 dispersion at a concentration of 0.02 mg mL^{-1}. AFM measurements were carried out with a Nanoscope IIIa Multimode apparatus (Veeco Instruments) in the tapping mode of operation, using silicon cantilevers with nominal spring constant and resonance frequency of ~40 N m^{-1} and 250–300 kHz, respectively. Samples for AFM were prepared by drop-casting a small volume (~10 □L) of a low-concentration MoS_2 NS dispersion in isopropanol (~0.03 mg mL^{-1}) onto highly oriented pyrolytic graphite and allowing it to dry under ambient conditions first and then, under vacuum at room temperature. FE-SEM images were recorded on a Quanta FEG apparatus (FEI Company) operated at 25 kV. Raman spectra were recorded on a Horiba Jobin-Yvon LabRam instrument at a laser excitation wavelength of 532 nm (green line). A low incident laser power (~0.2 mW) was employed to avoid damage to the NSs. XPS was accomplished on a SPECS system, working at a pressure below 10^{-7} Pa with a monochromatic Al K□ X-ray source (1486.7 eV) operated at 14.00 kV and 150 W. For Raman spectroscopy, XPS and contact angle measurement, specimens were prepared in the form of thin films by drop-casting MoS_2 NS dispersions (in isopropanol, in the case of the nonfunctionalized NSs and in water, in the case of the functionalized ones) onto stainless steel discs, which were allowed to dry at room temperature. ATR-FTIR spectra were registered on a Nicolet 8700 spectrometer (Thermo Scientific) with a diamond ATR crystal. Specimens for ATR-FTIR spectroscopy were prepared in the form of freestanding, paper-like films by vacuum-filtering aqueous dispersions of the functionalized MoS_2 material through silver membrane filters. EPR spectra were recorded with a X-Band (9.4 GHz) Bruker ELEXSYS E500 spectrometer using a magnetic field modulation amplitude of 1 G, a modulation frequency of 100 kHz and a microwave power of ~20 mW. Contact angles were measured by dropping 2 μL of water on the films with a pipette and immediately taking images of the droplet with a standard digital camera with an attached macro lens. Analysis of the recorded images with ImageJ software was carried out to determine the value of the contact angle.

1.5. Catalytic tests

For the catalytic tests, aqueous aliquots (2.5 mL) containing MoS_2 catalyst at concentration of 7 μg mL^{-1} and the substrate molecule (a nitroarene or an organic dye at a concentration of 0.12 or 0.06 mM, respectively) as well as a large excess of $NaBH_4$ (72–110 mM) were prepared in quartz cuvettes with an optical path length of 1 cm. Immediately after preparation, the cuvettes were transferred to an UV-vis absorption spectrophotometer and the reaction progress was monitored by recording the corresponding kinetic profiles. The latter were obtained by measuring the temporal evolution of absorbance at the wavelength of a characteristic peak of the substrate molecule, namely, at 400, 416, 380, 410, 270, 461 and 675 nm for 4-NP, 2-NP, 4-NA, 2-NA, NB, MB and MO, respectively. To check the performance of the catalyst at higher concentrations of substrate, 1.2 mM and 12 mM 4-NP aqueous solutions were reduced by $NaBH_4$ (1.1 M) in the presence of 7 µg mL^{-1} MoS_2 catalyst. To record the kinetic profiles, the absorbance of the catalytic medium was directly measured, without dilution, monitoring a wavelength different to that of the absorbance maximum (400 nm) to avoid saturation of the signal. Specifically, a wavelength of 455 nm was used for 1.2 mM 4-NP and 479 nm for 12 mM 4-NP. To test the catalyst for the reduction of mixtures of nitroarenes, a binary mixture of 0.12 mM 4-NA and 0.24 mM 2-NA and a ternary mixture of 0.06 mM 4-NP, 0.06 mM 4-NA and 0.12 mM 2-NA were reduced by $NaBH_4$ in the presence of MoS_2 catalyst at a concentration of 3.5 µg mL^{-1}. The kinetic profiles of the mixtures were followed by monitoring the absorbance at a wavelength of 400 nm. For every kinetic profile, a blank experiment, i. e., a kinetic run were no catalyst was added to the reaction medium, was recorded. To facilitate their recovery and re-use, the functionalized MoS_2 NSs were immobilized onto commercial polyurethane foam. To this end, the foam was first cut into cylinders ~1 cm in diameter and ~1 cm in height and cleaned by bath-sonication during 20 min in ethanol. After drying under vacuum, the polyurethane foam cylinders were soaked into ~10 mg L^{-1} aqueous MoS_2 dispersion and then dried at room temperature under reduced pressure. To increase the amount of loaded NSs, the soaking/drying process was carried out several times (typically three), after which the original white color of the polyurethane foam turned into an olive green tone. For the catalytic tests, the MoS_2-loaded foam cylinders were immersed into the substrate/$NaBH_4$ reaction mixture. After reaction completion, the cylinders were removed from the solution, rinsed with water and allowed to dry before being used in the next catalytic cycle.

2. Additional characterization of the functionalized MoS_2 material

2.1. Additional XPS spectra of MoS_2 nanosheets functionalized with iodoacetic acid

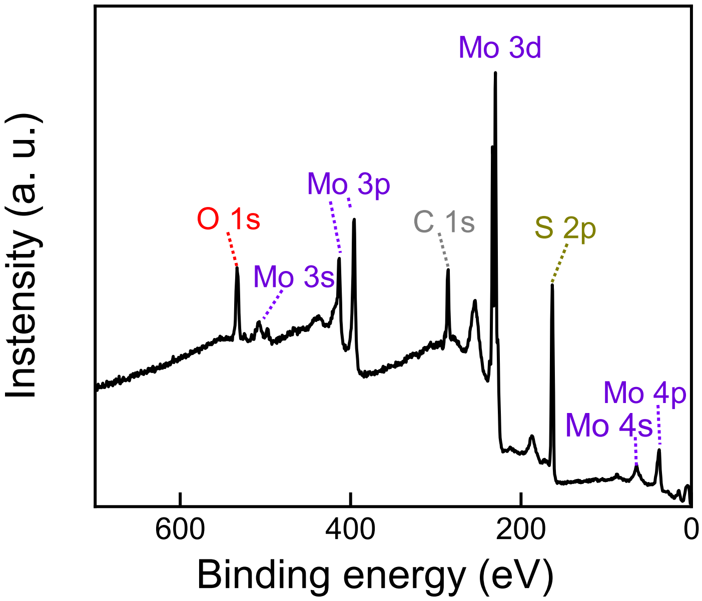

Figure S1. **XPS survey spectrum of cathodically functionalized MoS_2 nanosheets.** The main bands are labeled for clarity. The fact that no signal was detected in the 635–615 eV binding energy range, which is characteristic of the main XPS core level of iodine (I 3d) confirmed that this element was absent from the material.

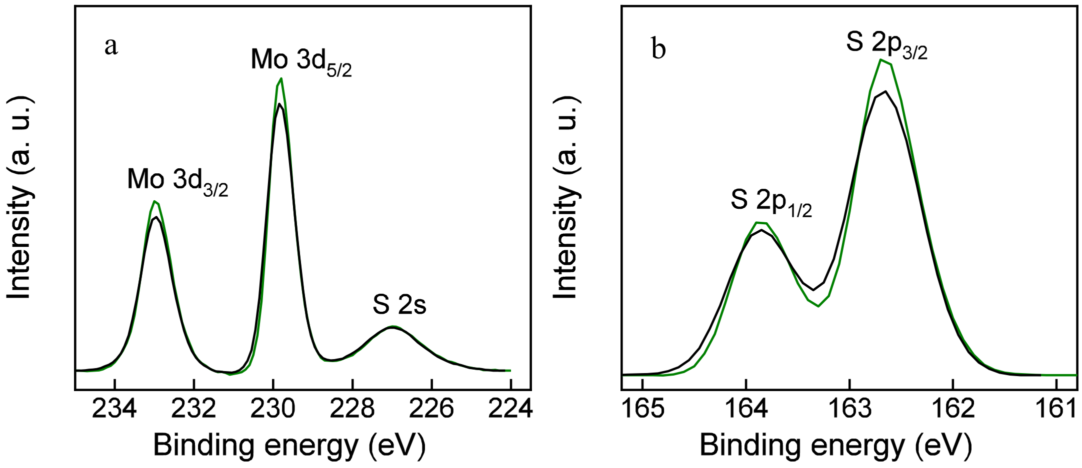

Figure S2. Background-subtracted, high resolution XPS **(a)** Mo 3d and **(b)** S 2p core level spectra of the nonfunctionalized (black trace) and functionalized (green trace) MoS_2 nanosheets. The symmetrical shape and position of the $3d_{5/2}$ and $3d_{3/2}$ components of the Mo 3d doublet band (~229.8 and 233 eV, respectively) and of the $2p_{3/2}$ and $2p_{1/2}$ components of the S 2p doublet band (~162.7 and 163.9 eV, respectively) was consistent with 2H phase-only materials. A downshift of ~0.8 eV in the position of all these components should be expected for the 1T′ phase.

2.2. Estimation from the degree of functionalization from XPS data

2.2.1. Photoelectron emission cross-section of MoS_2 for electrons from S 2p core level as a function of emission depth

When photo-emitted electrons pass through a layer of material with thickness d, the intensity of the corresponding signal, I_0, is exponentially attenuated according to the following equation, often referred to as the Beer–Lambert law or the straight-line approximation:

$$I=I_0 exp(-d/L cos\ \theta) \qquad (1)$$

where θ is the angle of emission of the electrons from the surface normal and L is the attenuation length, which gathers both elastic and inelastic scattering effects. By considering electrons that emerge at θ=90 º to the sample surface, which was the configuration used for the XPS measurements reported here, the equation simplifies to:

$$I=I_0 exp(-d/L) \qquad (2)$$

Incidentally, the approximate probe depth or information depth (ID) is defined as the sample thickness from which a specified percentage (e.g., 95%) of the detected signal originates. From eq. (2), some 95% of the signal will emanate from a depth lower than $3L$ and thus:

$$ID=3L \tag{3}$$

In earlier approaches to estimate L, the inelastic mean free path (λ) was calculated first and then, in a simplistic way, L was considered to be 10 per cent less than λ [2]:

$$L=0.9\lambda \tag{4}$$

More recently, independent universal curves for λ [3] and L [4] have been derived, which display the lowest deviations from the experimental data reported to this day amongst the different available equations [including the well-known TPM-2M equation by Tanuma, Powell and Penn [5], which is offered as an option for the calculation of λ for inorganic compounds in the NIST electron inelastic mean free path database from predictive formulae [6]. Specifically, the equation of the universal curve for L is:

$$L=\frac{(5.8+0.0041Z^{1.7}+0.088\,E^{0.93})a^{1.82}}{Z^{0.38}(1-W)}, \tag{5}$$

Apart from the energy of the photo-emitted electrons E, the only parameters involved in the calculation of L are the average atomic number Z and the average atomic size a for the corresponding material. In addition, for strongly bonded materials, such as oxides and alkali halides, a small extra term is included for the heat of formation H (where $W=0.06H$). In the case of 2H-MoS_2, H=276.14 KJ mol^{-1}.

The simplest approach to estimate Z for an inorganic compound with chemical formula G_gH_h is to calculate an average Z from the molecular formula as follows:

$$Z=\frac{gZ_g+hZ_h}{g+h} \tag{6}$$

In the case of MoS_2, Z ~24.67 Da.

The atomic size a is deduced from the relation:

$$a^3 = \frac{10^{21} M}{\rho N_A \, (g+h)} (nm^3) \qquad (7)$$

where ρ is the density in g cm^{-3}, N_A is Avogadro's number, and g and h are the stoichiometric coefficients in the molecular formula G_gH_h of a molecule with molecular mass M. In the case of 2H-MoS_2, using M=160.07 Da and ρ =5.03 g cm^{-3} yields a~0.26 nm.

The kinetic energy of the electrons photo-emitted from the S 2p core level using an Al K_α X-ray source is 1326.6 eV. Substituting E by the latter value and the aforementioned values of H, Z and a for 2H-MoS_2 in the expression for L (eq. 5) yields a value of ~2.1 nm (probe depth of ~6.3 nm by eq. 3). We note that a similar value for L (~2.2 nm) is obtained by first calculating λ by the TPM-2M equation (using the values for M and ρ specified above, number of valence electrons of 18 and a band gap of 1.2 eV), and then L through eq. 4.

2.2.2. Contribution of the outermost sulfur atoms to the total sulfur signal

Once L for the S 2p sulfur signal is calculated, eq. 2 can be used to estimate how much the outermost sulfur atoms contribute to the total sulfur signal. As mentioned above, only electrons that emerge at θ=90 ° to the sample surface are considered. The surface of the 2H-MoS_2 crystal will be constituted by its topmost (0001) basal plane, the Z axis of the crystalline structure being parallel to the photoemission. An ideal 2H-MoS_2 crystal shows sulfur planes every 3.186 Å (intra trilayer, i.e., distance between sulfur planes in a S-Mo-S sandwich) and every 2.959 Å (inter trilayer, i. e., distance between sulfur planes of adjacent S-Mo-S sandwiches) along its Z axis. To calculate the contribution of each sulfur plane to the total intensity of photo-emitted S 2p electrons, eq. 2 was used to calculate the percentage of out-coming, nonattenuated signal at the corresponding depth of each plane, except for the topmost sulfur plane, for which no attenuation was considered. The ratio of the contribution of the outer plane to that from all the sulfur planes which contribute to the signal amounts to ~14 %.

2.2.3. C1s core level XPS spectrum of bulk MoS_2 crystal functionalized with iodoacetic acid

If we consider, as explained in the main text, that all the acetic groups are grafted to the outermost sulfur atoms, then the ratio of the signal corresponding to COOH (component at ~289 eV in the C 1s core level band depicted in Fig. S3 below these lines) to that corresponding to topmost sulfur plane can be taken as an indication of the extent of functionalization. This yields a value of ~0.10 molecular groups inserted per surface sulfur atom.

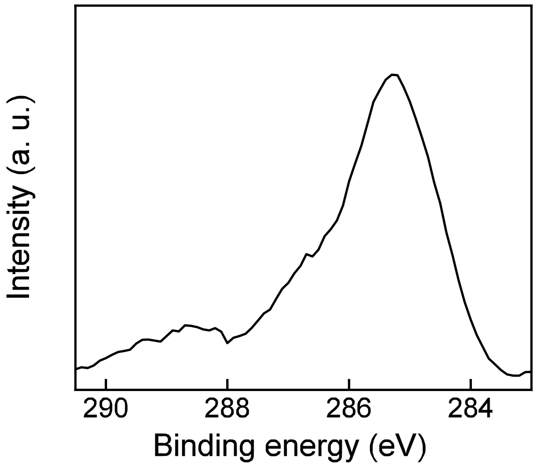

Figure S3. Background-subtracted, high resolution XPS C 1s core level spectrum of bulk MoS_2 crystal functionalized through cathodic treatment with iodoacetic acid.

2.3. XPS spectra of MoS_2 nanosheets functionalized with iodoaniline

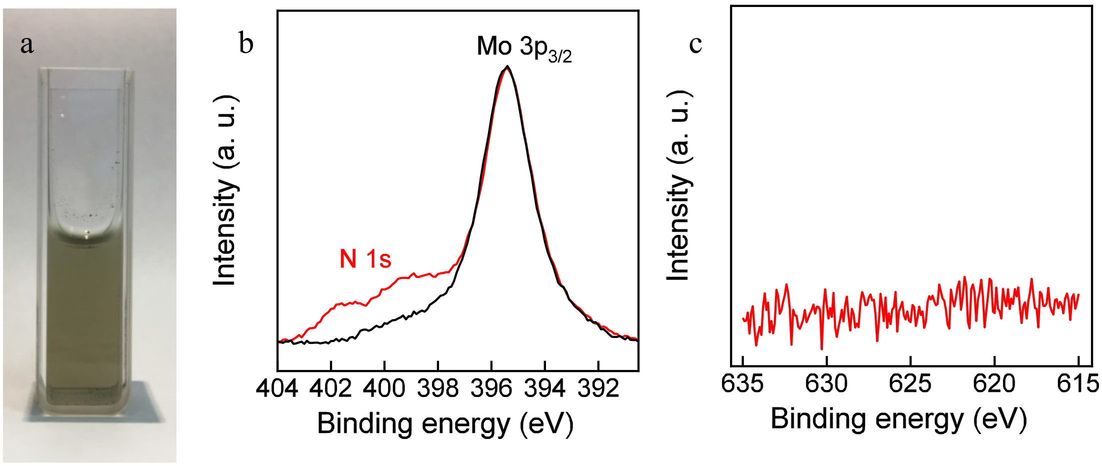

Figure S4. MoS_2 nanosheets functionalized with iodoaniline (a) Digital photograph of the aqueous dispersion obtained by sonication in water of cathodically expanded MoS_2 with a subsequent electrochemical treatment at -5 V with 0.25 M iododoaniline in ethanol. **(b)** Background-subtracted, normalized high resolution XPS spectra of the nonfunctionalized MoS_2 NSs (black trace) and MoS_2 functionalized with iodoaniline (red trace) in the binding energy range from 404 to 391.5 eV. In this range, only the main component of the Mo 3p doublet band, Mo $3p_{3/2}$, which is symmetrical and centered at 395.4 eV, was detected for the nonfunctionalized NSs (black trace). However, the functionalized material displayed two additional bands which correspond to nitrogen in aniline moieties. Specifically, the two N 1s components detected at ~399.4 and ~401.7 eV were assigned to amine in neutral and positively charged form, respectively [7]. **(c)** I 3d binding energy range for the MoS_2 nanosheets functionalized with iodoaniline. The absence of the main band of iodine in the MoS_2 NSs treated with iodoaniline that any un-reacted iodoaniline had been effectively removed from the surface by the purification process and thus confirmed that the detected aniline groups were grafted on MoS_2 surface, instead of just adsorbed on it.

2.4. Functionalization using a reducing agent as an electron source

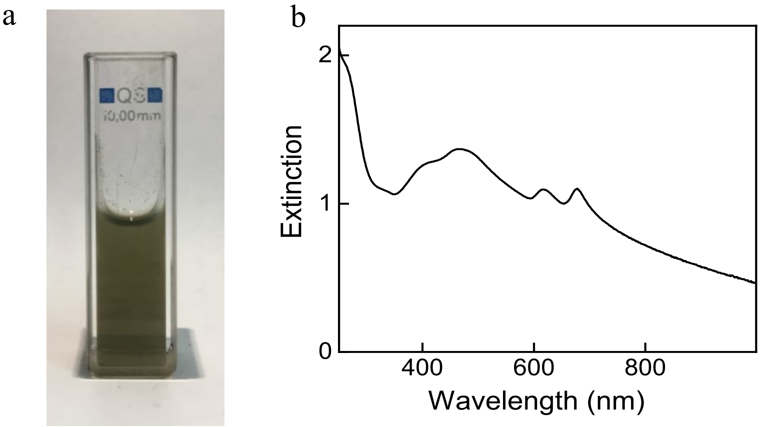

Figure S5. (a) Digital photograph and **(b)** UV-vis extinction spectrum for the dispersion obtained by sonication during 1 h of a cathodically expanded MoS_2 crystal in an aqueous solution of 0.25 M iodoacetic acid and 0.25 M sodium borohydride.

2.5. Presence of bismuth in some of the MoS_2 materials

It has been recently reported that geological MoS_2 crystals, such as the starting material in this work, contain bismuth impurities in concentrations high enough to be detected by XPS [8]. Specifically, the bismuth impurity has been found to appear mainly as the most thermodynamically stable form of bismuth oxide, Bi_2O_3. In the present work, the presence of micron-size clusters of bismuth in the MoS_2 starting material was indeed confirmed by EDX. Correspondingly, bismuth was detected in some of the samples analyzed by XPS. Bi^{3+} $4f_{5/2}$ spin-orbit component appears in a similar range to that where the S 2p component for S-C bond is expected to appear (~163-164 eV) [9,10]. Thus, special care was taken not to mistake Bi^{3+} $4f_{5/2}$ for the S-C component in S 2p spectrum, by widening the acquired range for the S 2p spectrum downwards to include Bi^{3+} $4f_{7/2}$ as well, thus confirming the presence of bismuth.

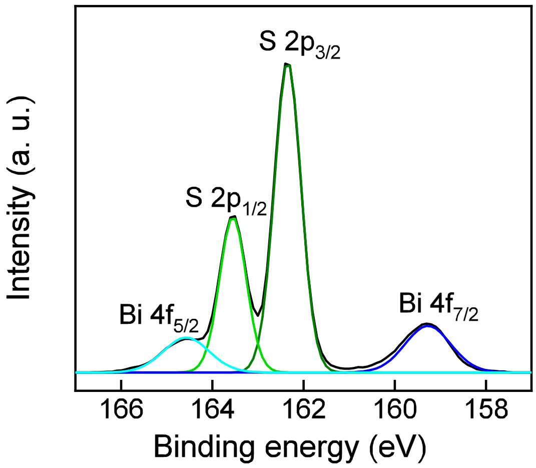

Figure S6. Background-subtracted, high resolution XPS S 2p and Bi 4f core level spectra for one of the batches where bismuth was detected. As expected for an ideal sulfur signal, the S 2p spin–orbit doublet consists of S $2p_{1/2}$ (light green trace) and S$2p_{3/2}$ (dark green trace) components with a 1:2 peak area ratio between and spin-orbit splitting constant of 1.2 eV, The position of the of S $2p_{1/2}$ and S$2p_{3/2}$ components of the S 2p doublet band (~163.9 and 162.7 eV, respectively) as well as their full width at half maximum (FWHM) of just 0.7 eV was consistent with a 2H phase-only material. The Bi 4f doublet displayed Bi $4f_{5/2}$ and Bi $4f_{7/2}$ components split apart by 5.3 eV and in 3:4 area ratio, as expected, which were centered at binding energy of 164.3 eV and 159.3 eV, respectively, which corresponded to Bi(III).

2.6. Difference C 1s spectrum of functionalized and nonfunctionalized MoS_2

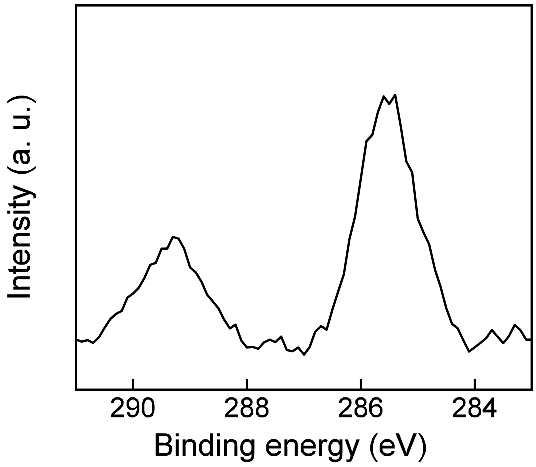

Figure S7. Difference C 1s XPS spectrum of the functionalized and the nonfunctionalized MoS_2 nanosheets (green and black traces in Figure 2g of the main text, respectively).

2.7. ATR-FTIR spectrum of functionalized MoS_2

The ATR-FTIR spectrum of functionalized MoS_2 exhibited some additional indication of functionalization.

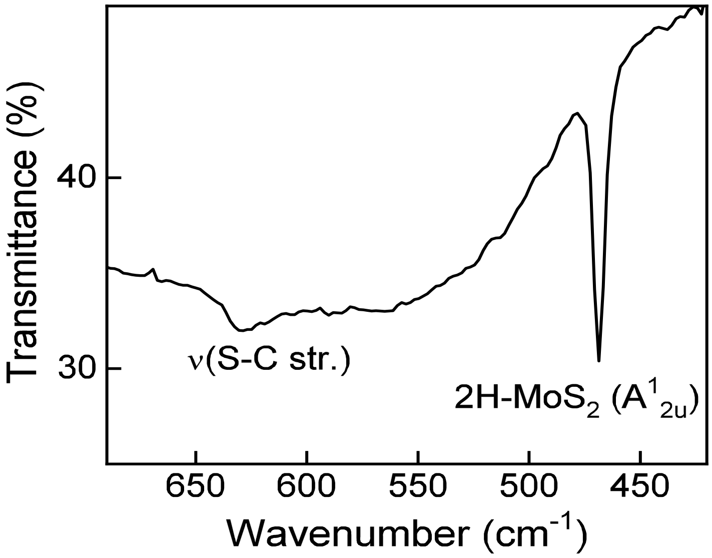

Figure S8. ATR-FTIR spectrum of the functionalized MoS_2 NSs.

Specifically, a weak band located at ~630 cm^{-1} can be ascribed to S−C stretching vibrations [9,11] arising from acetic acid groups grafted onto the NSs via sulfur atoms. This band was not very intense even in the case of functionalized 1T-phase MoS_2 monolayers, where the degree of derivatization with iodoacetic acid was ~20 percent [10]. Thus, it is expected to be weak for the current materials, where, as explained in the main text, the multi-layered nature of the MoS_2 NSs implies that the percentage of (surface) sulfur atoms that are covalently bonded to carbon must be very small.

The sharp absorption peak at ~470 cm^{-1} is due to the $A^1{}_{2u}$ phonon of 2H-MoS_2, which involves asymmetric translation of both Mo and S atoms parallel to the c axis [12]. The bands associated to the acetic group were also observed (range not shown) but they would be compatible with just adsorption (noncovalent fuctionalization) of iodoacetic acid.

2.8. EPR spectrum of functionalized MoS_2

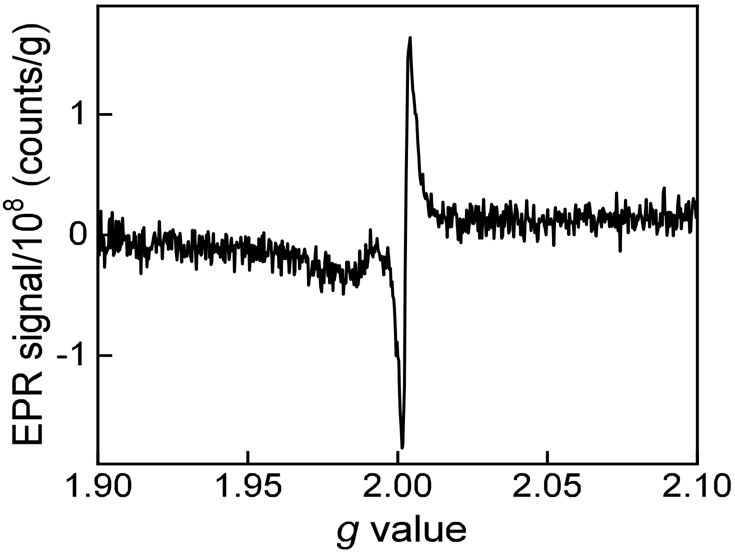

Figure S9. Representative first-derivative X-band EPR spectrum of the functionalized MoS_2 NSs. The unsaturated molybdenum atoms in edges and sulfur vacancies give rise to an EPR signal with g~2 [13,14].

3. Additional information on the performance of functionalized MoS_2 nanosheets as catalysts

3.1. UV-vis spectra of reactants and products

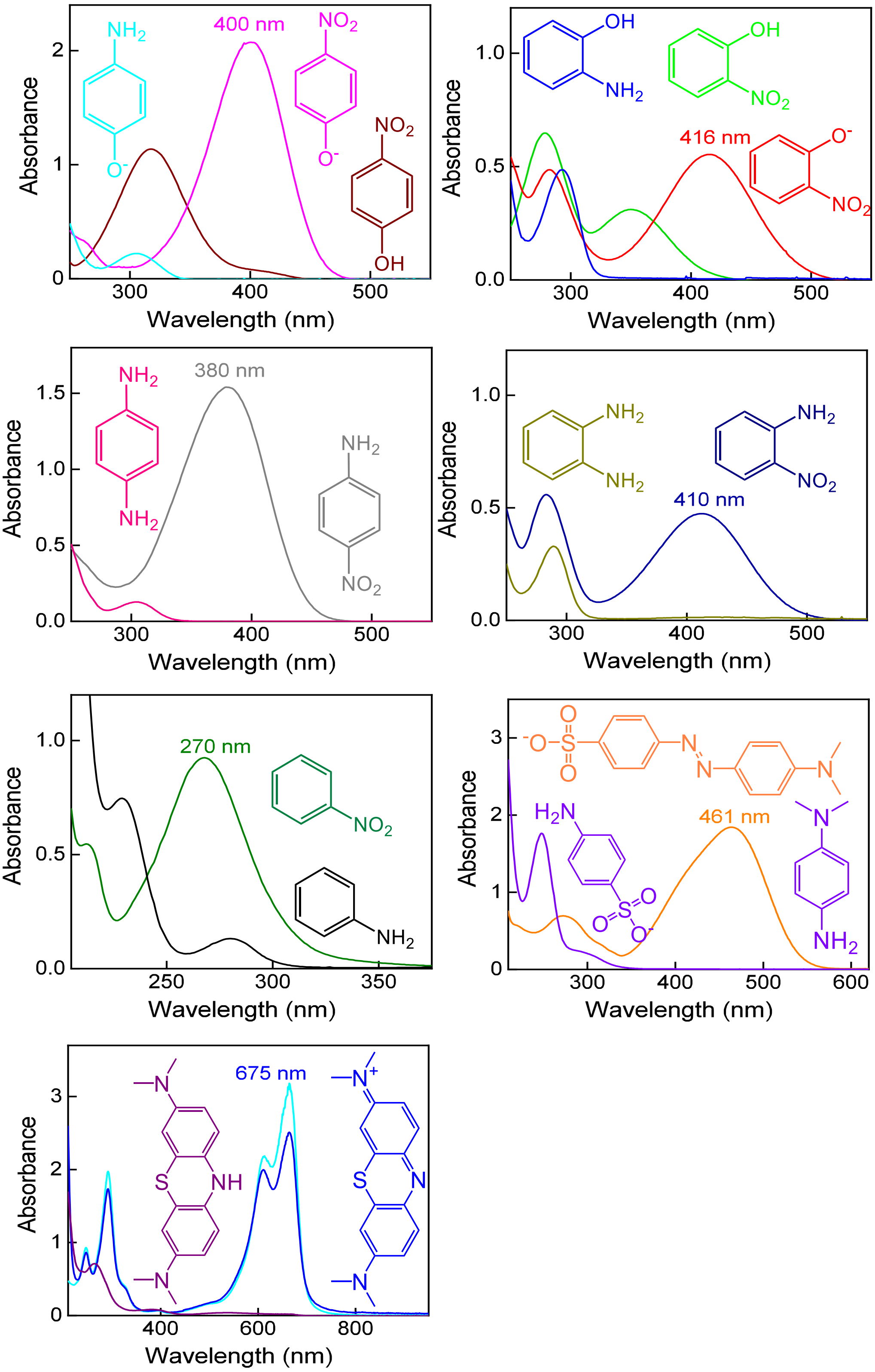

Figure S10. Chemical structure and UV-vis spectra of the reactants and products involved in the different reduction reactions where functionalized MoS_2 NSs have been tested as catalyst: **(a)** 4-NP (brown trace), 4-nitrophenolate (pink trace) and 4-aminophenol (cyan trace); **(b)** 2-NP (green trace), 2-nitrophenolate (red trace) and 2-aminophenol (blue trace); **(c)** 4-NA (gray trace) and its reduction product, *p*-phenylendiamine (fuchsia trace); **(d)** 2-NA (navy trace) and its reduction product, *o*-phenylendiamine (dark yellow trace); **(e)** nitrobenzene (olive trace) and aniline (black trace); **(f)** MO (orange trace), which is first reduced to the corresponding azo product (not shown) [15], which is followed by -HN-NH- bond dissociation to yield N,N-dimethyl-benzene-1,4-diamine and 4-amino-benzenesulfonate (both shown in violet trace) [16]; **(g)** MB (cyan trace), MB in the basic medium provided by $NaBH_4$ (blue trace) and its reduction product, leucomethylene blue (purple trace) [17,18]. The wavelength chosen to follow the kinetics of the corresponding reactions, which was in all cases the location of an absorption maximum of the reactant, is indicated for clarity.

3.2. Extinction spectrum of the catalyst

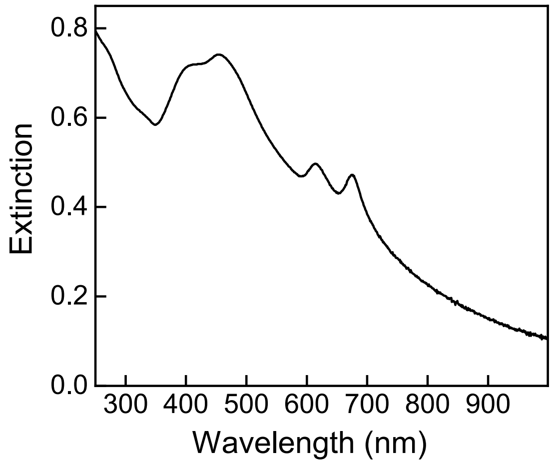

Figure S11. Extinction spectrum of the catalyst at a concentration of 7 mg L^{-1}. The extinction value for the catalyst at the wavelengths monitored for the reduction reactions of the different substrates was ~0.6 for all the substrates except for MB, for which it was 0.4 (as expected from the extinction value at $\square_{max}$~400 and ~675 nm, respectively).

3.3. Comparison of the catalytic activities of functionalized MoS_2 nanosheets with those reported in the literature for other MoS_2- and non-noble metal-based catalysts

Table S1. Catalytic activity (defined as number of moles of reactant converted per mole of catalyst used per unit time) of the functionalized MoS_2 NSs towards the reduction of 4-nitrophenol compared with that of different types of MoS_2 nanostructures, graphene-derived materials and non-noble metal-based catalysts reported in the literature.

Catalytic system	**Catalytic activity (h^{-1})**	**Ref.**
Functionalized-2H MoS_2 NSs	63	Present work
S vacancy-decorated, ultrasound-exfoliated 2H MoS_2 NSs	6.6	19
Li-exfoliated 2H-phase MoS_2 NSs	0.9	20
Li-exfoliated 1T-phase MoS_2 NSs	44.4	20
Hydrothermally synthesized 2H MoS_2 NSs supported onto Fe_3O_4 particles	2.4	21
GMP-stabilized sonicated 2H MoS_2 NSs	2.6–7.8	22
GMP-stabilized cathodically exfoliated 2H MoS_2 NSs	21.4	23
N-doped RGO foam	0.07	24
RGO NSs capped with poly(diallyldimethylammonium chloride)	0.10	25
Hydrothermally synthesized 2H MoS_2 NSs	5.4	26
Hydrothermally synthesized MoS_2 NSs intercalated in pillared montomorillonite	24	26
Hydrothermally synthesized 1T MoS_2 NSs	21	27
Bi_2Te_3-hydrothermally synthesized 1T MoS_2 heterostructure	67.2–100.8	27

Hydrogel network with embedded Co nanoparticles (NPs)	16.2	28
Ni nanoparticles on silica nanotubes	1.8	29
Hybrid Ni nanoparticles/N doping carbon on diatomite	0.85	30
Cu NPs on carbon microspheres	0.2	31
Cu and Sn sponges/dendrites	1.2–1.8	32
Co particles-decorated carbon microspheres	0.06–0.24	33
Co nanocrystals on reduced graphene oxide (RGO)	0.6	34
Ni NPs supported onto carbon black	26.4	35
Nanostructured zero-valent iron	78	36
Graphene stabilized CuNi nanocomposite	12	37
MOF-derived Ni based N-doped mesoporous carbon	2.4	38
Co NPs embedded in hierarchically porous N-doped carbon frameworks	18	39
Hexagonal Ni plates on RGO	0.44	40
Hollow porous Cu particles from silica-encapsulated Cu_2O nanoparticle aggregates	3	41
Co@BN core–shell nanoparticles	0.38	42
Co NPs embedded into ordered mesoporous carbon	7.8	43
NiO hollow nanospheres	4.2	44
Ultrafine Cu_2O nanoparticles on cubic mesoporous carbon	9.6	45
Cu NPs on oxidized boron nitride	27	46
Cu NPs immobilized by layered Ti_3C_2 MXene	51	47
Cu and Co NPs doped N-containing carbon frameworks	63	48

Table S2. Catalytic activity of the functionalized MoS_2 NSs towards the reduction of other nitroarenes and organic dyes compared with that of different types of MoS_2 nanostructures, and non-noble metal-based catalysts reported in the literature.

Catalytic system	**Catalytic activity (h^{-1})**	**Ref.**
2-nitrophenol		
Acetic acid-functionalized, cathodically exfoliated 2H MoS_2 NSs	340	Present work
N/O-doped, hydrothermnally synthesized MoS_2 NSs	0.3	49
Li-exfoliated 1T MoS_2 NS-RGO hybrid paper	3 (*)	50
NiO NSs	0.2	49
$NiMoO_4$ NPs	0.3	51
$CuFe_2O_4$ NPs	133	52
$NiFe_2O_4$ NPs	17	52
CuO NPs supported on γ-Al_2O_3	0.5	53
Carbon black-supported Ni NPs	27	54
$Fe_2(MoO_4)_3$ NPs	7	55
RGO-supported Ni NPs	176 (*)	56
Fe@SiO_2-supported Ni NPs	60.84	57
Poly(methacrylic acid)-supported Cu NPs	217	58
4-nitroaniline		
Acetic acid-functionalized, cathodically exfoliated 2H MoS_2 NSs	180	Present work
S vacancy-decorated, ultrasound-exfoliated 2H MoS_2 NSs	43	19
Li-exfoliated 1T MoS_2 NSs	83.4	20
GMP-stabilized, cathodically exfoliated 2H MoS_2 NSs	140	23
Bi_2Te_3-hydrothermally synthesized 1T MoS_2 heterostructure	106.8	27
Li-exfoliated 1T MoS_2 NS-RGO hybrid paper	6	50
Carbon-embedded Cu NPs	1	59
RGO-supported Ni NPs	0.1	60
MnO_2 NSs	0.7	61

Fe_3O_4 NPs	0.9	61
Fe@SiO_2-supported Ni NPs	179.8	57
Mesoporous polyaniline-supported Cu NPs	84	62
Pectin-capped Cu NPs	90	63
Poly(methacrylic acid)-supported Cu NPs	54	58
Fe_3O_4@Cu NPs	21	64

2-nitroaniline

Acetic acid-functionalized, cathodically exfoliated 2H MoS_2 NSs	90	Present work
Li-exfoliated 1T MoS_2 NS-RGO hybrid paper	6 (*)	50
$Bi_2O_2CO_3$/$CoFe_2O_4$ hybrid nanostructures	0.1	65
DNA-supported Ni NPs	17	66
RGO-supported Ni NPs	44(*)	56
Fe@SiO_2-supported Ni NPs	146.7	57
Pectin-capped Cu NPs	22.5	63

nitrobenzene

Acetic acid-functionalized, cathodically exfoliated 2H MoS_2 NSs	78	Present work
S vacancy-decorated, ultrasound-exfoliated 2H MoS_2 NSs	11	19
Li-exfoliated 1T MoS_2 NS-RGO hybrid paper	7.8 (*)	50
Bi_2Te_3-hydrothermally synthesized 1T MoS_2 heterostructure	960 (**)	27
Ni NP-polyvinylamine/SBA-15 hybrid	1.3	67
Fe_3O_4/β-alanine-acrylamide-Ni nanocomposite	770	68
DNA-supported Ni NPs	25	66
RGO-supported Ni NPs	59 (*)	56
Mesoporous polyaniline-supported Cu NPs	4.2	62

methyl orange

Acetic acid-functionalized, cathodically exfoliated 2H MoS_2 NSs	71	Present work
S vacancy-decorated, ultrasound-exfoliated 2H MoS_2 NSs	24	19
Li-exfoliated 1T MoS_2 NSs	150	20
Hydrothermally synthesized 2H MoS_2 NSs intercalated in pillared montmorillonite	13	69
Poly(methacrylic acid)-supported Cu NPs	35	58
Fe_3O_4@Cu NPs	10	64
Fe_3O_4-cellulose-Cu nanocomposite	0.9	70
methylene blue		
Acetic acid-functionalized, cathodically exfoliated 2H MoS_2 NSs	44	Present work
S vacancy-decorated, ultrasound-exfoliated 2H MoS_2 NSs	16	19
Fe_3O_4@Cu NPs	86	64
Spherical montmorillonite-supported MoS_2 NSs	70	71
Solvothermally synthesized, amorphous MoS_2 NPs	0.01	72
α-MnO_2 nanorods	0.2	73
Cu NPs supported onto Si nanowire array	66	74

(*) in 1:1 water/methanol solvent.

(**) in methanol solvent

3.4. Reaction mechanism

The mechanism of nitroarene and dye reduction catalyzed by the present functionalized MoS_2 is expected to be the same that we previously proposed for vacancy-decorated 2H-MoS_2 [19], i. e., a mechanism involving the catalytically active sites in the NSs, such as sulfur vacancies and edges, which possess local metallic character. The fact that the functionalization takes place near an active site of the MoS_2 NSs does not promote the deactivation or blocking of the latter. As the acetic moiety is bonded to the NSs via a sulfur atom near a sulfur vacancy, the sulfur vacancy remains “vacant”, and it is thus preserved and active. In contrast, a usual passivation method would involve filling of the vacancy with a sulfur atom provided by an external source, e.g., through chemical reaction with alkanethiols [75–77]. Indeed, the EPR signal of the functionalized MoS_2 NSs (Fig. S9) is indicative of the presence of Mo-S dangling bonds. The presence of the negatively charged acetic moiety near the active site does affect the process in some way, as discussed below and in the main text, but the reaction mechanism remains basically the same.

When nanoparticles (NPs) of certain noble metals such as gold are used as catalysts for the catalytic reduction of nitroarenes with $NaBH_4$, the BH_4^- anion readily oxidizes, injecting electrons to the NPs, which thereby become a reservoir of excess electrons [78]. Upon adsorption of the substrate molecules onto the NPs, the excess electrons trigger their reduction. In such case, the catalytic reaction is insensitive to the pH of the aqueous medium [79]. In contrast, when metallic 1T-MoS_2 NSs are used as catalyst for the same type of reaction, the reduction does not occur at pH values above ∼11 [80], which is the pH range where the spontaneous hydrolysis of BH_4^- anion becomes arrested [81,82]. This implies that, in the latter case, some product of the hydrolysis of the BH_4^- anion, rather than BH_4^- anion itself, is involved in the reduction reaction. As the active sites in 2H-MoS_2 (sulfur vacancies and edges) possess a locally metallic character, the same mechanism proposed for 1T-MoS_2 applies for 2H-MoS_2, as has been indeed reported before for vacancy-decorated 2H-MoS_2 [19].

In basic solution below pH~11 the BH_4^- anion hydrolyzes spontaneously to give molecular hydrogen and BH_3OH^- species as reaction products.

$BH_4^- + H_2O \rightarrow BH_3OH^- + H_2$ (1)

H_2 molecule undergoes dissociative adsorption at sulfur vacancies in MoS_2 [83,84]. Although the resulting adsorbed H atoms could in principle react with a nitroarene/dye molecule to trigger its reduction, such a reduction reaction is inhibited by the fast recombination of the adsorbed H atoms into H_2 molecules, which is a very favorable process at the catalytic sites of MoS_2 (i.e., the Tafel step of hydrogen evolution reaction, HER) [85,86]. Indeed, previously reported control experiments in which a H_2 gas flow several orders of magnitude larger than the hydrolysis rate of BH_4^- was passed through a nitroarene solution in the presence of MoS_2 NSs showed that no reduction of the substrate took place [20].

In addition to H_2, the spontaneous hydrolysis of $NaBH_4$ yields the BH_3OH^- anion as a rather stable intermediate. In the basic medium of the reaction, the BH_3OH^- species is oxidized at a sulfur vacancy site on the MoS_2 surface with the assistance of hydroxide anions, to release the metaborate anion (BO_2^-), water, hydrogen and electrons [reaction (1) in Fig. S12] [87]:

$2BH_3OH^- + 6OH^- \rightarrow BO_2^- + 4H_2O + 3H_2 + 6e^-$ (2)

As previously reported control experiments where $NaBH_4$ was substituted by $NaBO_2$ in the reaction medium have shown, the generated BO_2^- is inactive as a reductant and thus will not participate in the catalytic reduction [20]. Molecular hydrogen is activated by the released electrons to give a negatively charged hydride (H^-) [88], which is very unstable, and thus would not form on the surface of defect-free MoS_2, but becomes stabilized when it adsorbs at sulfur vacancies by transferring excess electron charge to their neighboring unsaturated molybdenum atoms [89] [reaction (2)]. The vacancy-anchored, negatively charged hydride should readily trigger the hydrogenation of the nitro group in the nitroarene molecules through the well-known three-step sequence [36,90]; i.e., the nitro group is first converted to the nitroso group [reaction (3)], which is then reduced to a hydroxylamine species [reaction (4)] and finally to the amino group [reaction (5)]. In the case of the dyes, the generation of highly active hydride species at the sulfur vacancy sites by way of reactions (1) and (2) in Fig. S12 would subsequently trigger hydrogenation of the substrate.

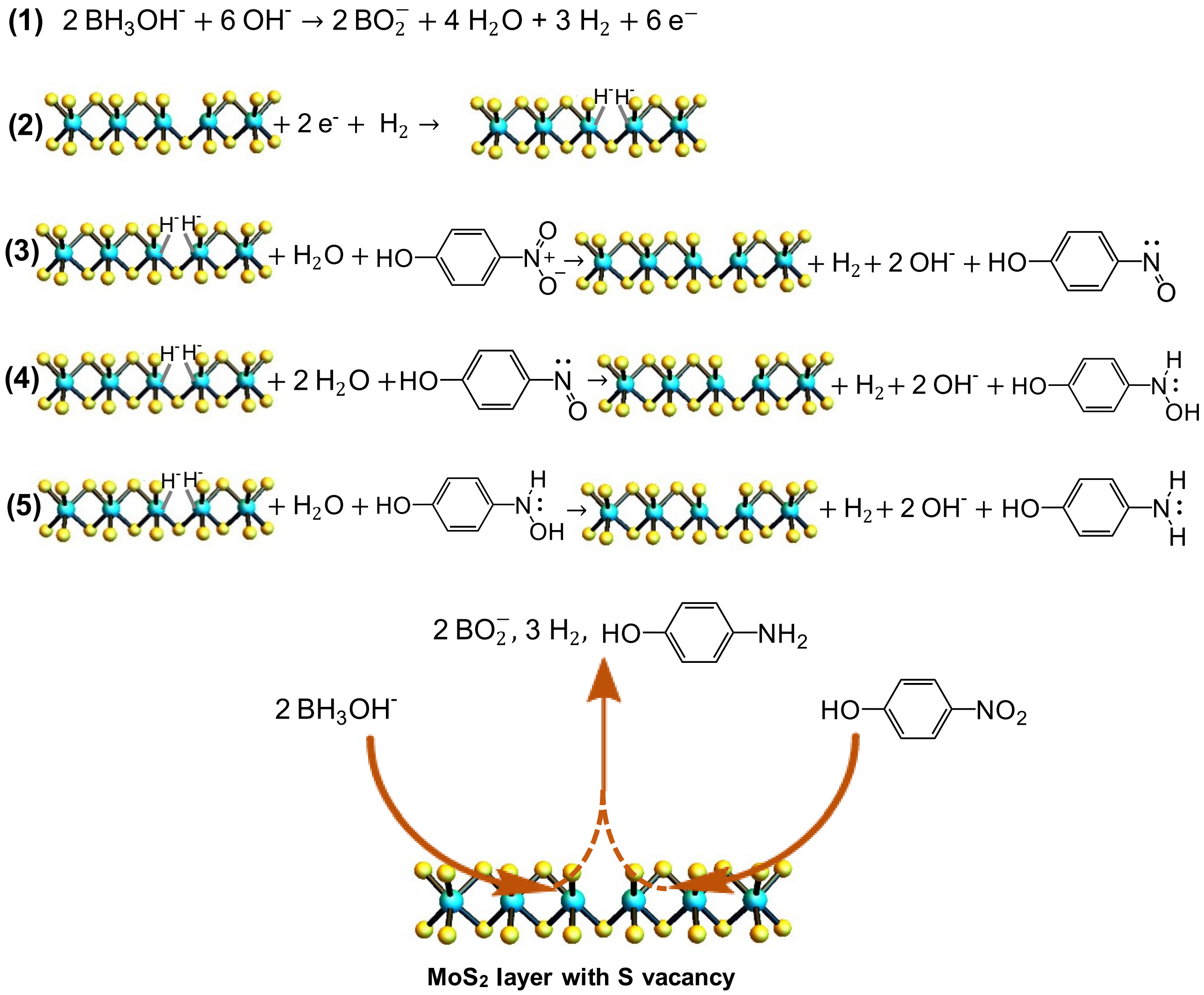

Figure S12. Proposed reaction mechanism for the reduction of 4-NP at the active sites of the MoS_2 nanosheets. Reaction (1): BH_3OH^- anion (the hydrolysis product of $NaBH_4$) is oxidized at a sulfur vacancy site on the MoS_2 surface with the assistance of hydroxide anions from the basic medium of the reaction, to release metaborate anion (BO_2^-), water, hydrogen and electrons. Reaction (2): the generated hydrogen is activated by the released electrons to give a negatively charged hydride (H^-), which adsorbs at the sulfur vacancy. The negatively charged hydride triggers the hydrogenation of the nitro group in the 4-NP molecule through the following three-step sequence: the nitro group is first converted to the nitroso group [reaction (3)], which is then reduced to a hydroxylamine species [reaction (4)] and finally to the amino group [reaction (5)]. The overall reaction is illustrated at the bottom.

As aforementioned, according to the proposed mechanism, the catalytic activity of a MoS_2 NS relies on the availability of stable adsorption sites for the H^- species, that is, unsaturated molybdenum atoms in MoS_2 edges and sulfur vacancies. Thus, the colloidal stability of the MoS_2 catalyst will have a major influence on the catalytic activity, as the adsorption sites for the H^- species in the MoS_2 layers will only be available as long as their surface remains exposed to the aqueous medium where catalysis takes place. If the layers aggregate, catalytic activity will consequently decrease.

The fact that the current materials perform better as catalysts in aqueous medium than previously reported surfactant-stabilized MoS_2 catalysts [19] could be partly related to the different way in which colloidal stabilization affects the catalytic sites in one and the other. In the present case, the covalently attached acetic group which imparts colloidal stability is grafted to a sulfur atom near the sulfur vacancy/edge, and thus the unsaturated molybdenum atoms remain available for adsorption of H^- at any time. However, in the surfactant-assisted stabilization, guanosine monophosphate (GMP) molecules adsorbed on the surface of MoS_2 by acid-base interaction between their nucleobase and some of the unsaturated molybdenum sites [22], thus blocking them. Hence, in the latter case, colloidal stability is attained at the expense of catalytic activity although not all catalytic centers will be blocked with GMP and, even those with GMP on, will be temporally available for catalysis as GMP is not irreversibly adsorbed. This was confirmed by the fact that the surfactant-stabilized MoS_2 NSs aggregated if many washing cycles were done, as washing led to their progressive removal from the NS surface and thus to a loss of colloidal stability. Thus, GMP will be desorbing and adsorbing from the surface of surfactant-stabilized MoS_2 NSs and unsaturated molybdenum sites will be available for catalysis when GMP eventually desorbs. We note that, in the case of the current functionalized MoS_2 NSs, the presence of the acetic group near the sulfur vacancy could introduce some steric impediment for the approaching substrate molecules. However, this effect will be minor in the case of diatomic vacancies, which are easily formed and stabilized [91].

References

[1] C. Backes, R.J. Smith, N. McEvoy, N.C. Berner, D. McCloskey, H.C. Nerl, A. O´Neill, P.J. King, T. Higgins, D. Hanlon, N. Scheuschner, J. Maultzsch, L. Houben, G.S. Duesberg, J.F. Donegan, V. Nicolosi, J.N. Coleman, Edge and confinement effects allow in situ measurement of size and thickness in liquid-exfoliated nanosheets, Nat. Commun. 5 (2014), 4576.

[2] J. F. Watts, J. Wolstenholme. An introduction to surface analysis by XPS and AES. Wiley, 2003.

[3] M. P. Seah. An accurate and simple universal curve for the energy-dependent electron inelastic mean free path. Surf. Interface Anal. 2012, 44, 497–533.

[4] M. P. Seah. Simple universal curve for the energy-dependent electron attenuation length for all materials. Surf. Interface Anal. 2012, 44, 1353–1359.

[5] S. Tanuma, C. J. Powell, D. R. Penn, Surf. Interface Anal. 1994, 21, 165.

[6] C. J. Powell, A. Jablonski, NIST Electron Inelastic-Mean-Free-Path Database – Version 1.2, National Institute of Standards and Technology, Gaithersburg, MD (2010). (available online at www.nist.gov/srd/nist71.cfm)

[7] E. Raymundo-Pinero, D. Cazorla-Amorós, A. Linares-Solano, J. Find, U. Wild, R. Schlögl, Structural characterization of N-containing activated carbon fibers prepared from a low softening point petroleum pitch and a melamine resin. Carbon 40 (2002) 597–608.

[8] M. G. Sales, L. Herweyer, E. Opila, S. McDonnell, MoS_2 impurities: Chemical identification and spatial resolution of bismuth impurities in geological material. Appl. Surf. Sci. 2020, 508, 145256.

[9] D. Voiry, A. Goswami, R. Kappera, C.C.C. Silva, D. Kaplan, T. Fujita, M. Chen, T. Asefa, M. Chhowalla, Covalent functionalization of monolayered transition metal dichalcogenides by phase engineering, Nat. Chem. 7 (2015), 45-49.

[10] J.I. Paredes, J.M. Munuera, S. Villar-Rodil, L. Guardia, M. Ayán-Varela, A. Pagán, S.D. Aznar-Cervantes, J.L. Cenis, A. Martínez-Alonso, J.M.D. Tascón, Impact of covalent functionalization on the aqueous processability, catalytic activity, and biocompatibility of chemically exfoliated MoS_2 nanosheets, ACS Appl. Mater. Interfaces 8 (2016), 27974-27986.

[11] G. Socrates. lnfrared Characteristic Group Frequencies: Tables and Charts,. Wiley: New York, NY, 1994, 2nd Ed.

[12] T. Livneh, J. E Spanier. A comprehensive multiphonon spectral analysis in MoS_2. 2D Mater, 2015, 2, 035003.

[13] G. Liu, H. Ma, I. Teixeira, Z. Sun, Q. Xia, X. Hong, S. C. E. Tsang, Hydrazine-assisted liquid exfoliation of MoS_2 for catalytic hydrodeoxygenation of 4-methylphenol. Chem. Eur. J. 2016, 22, 2910–2914.

[14] L. M. Martinez, C. Karthik, M. Kongara, S. R. Singamaneni, Paramagnetic defects in hydrothermally grown few-layered MoS_2 nanocrystals. J. Mater. Res. 2018, 33, 1565–1572.

[15] A. Furst, R. C. Berlo, S. Hooton, Hydrazine as a Reducing Agent for Organic Compounds (Catalytic Hydrazine Reductions). Chem. Rev. 1965, 65, 1, 51–68. DOI:10.1021/cr60233a00

[16] L.-Q. Zheng, X.-D. Yu, J.-J. Xu and H.-Y. Chen, Reversible catalysis for the reaction between methyl orange and $NaBH_4$ by silver nanoparticles. Chem. Commun., 2015, 51, 1050–1053.

[17] S. Pande, S. Jana, S. Basu, A. K. Sinha, A. Datta, T. Pal, Nanoparticle-Catalyzed Clock Reaction. J. Phys. Chem. C 2008, 112, 10, 3619-3626. DOI: 10.1021/jp7106999

[18] A. Mignani, S. Fazzini, B. Ballarin, E. Boanini, M. C. Cassani, C. Maccato, D. Barreca, D. Nanni. Mild fabrication of silica-silver nanocomposites as active platforms for environmental remediation, RSC Adv., 2015, 5, 9600–9606. DOI: 10.1039/C4RA14069A

[19] S. García-Dalí, J.I. Paredes, B. Caridad, S. Villar-Rodil, M. Díaz-González, C. Fernández-Sánchez, A. Adawy, A. Martínez-Alonso, J.M.D. Tascón, Activation of two-dimensional MoS_2 nanosheets by wet-chemical sulfur vacancy engineering for the catalytic reduction of nitroarenes and organic dyes, Appl. Mater. Today 20 (2020), 100678.

[20] L. Guardia, J. I. Paredes, J. M. Munuera, S. Villar-Rodil, M. Ayán-Varela, A. Martínez-Alonso and J. M. D. Tascón, Chemically exfoliated MoS_2 nanosheets as an

efficient catalyst for reduction reactions in the aqueous phase, ACS Appl. Mater. Interfaces, 2014, 6, 21702–21710.

[21] T. Lin, J. Wang, L. Guo and F. Fu, Fe_3O_4@MoS_2 Core–shell composites: preparation, characterization, and catalytic application, J. Phys. Chem. C, 2015, 119, 13658–13664.

[22] M. Ayán-Varela, Ó. Pérez-Vidal, J. I. Paredes, J. M. Munuera, S. Villar-Rodil, M. Díaz-González, C. Fernández-Sánchez, V. S. Silva, M. Cicuéndez, M. Vila, A. Martínez-Alonso and J. M. D. Tascón, Aqueous Exfoliation of Transition Metal Dichalcogenides Assisted by DNA/RNA Nucleotides: Catalytically Active and Biocompatible Nanosheets Stabilized by Acid−Base Interactions, ACS Appl. Mater. Interfaces, 2017, 9, 2835–2845.

[23] S. García-Dalí, J. I. Paredes, J. M. Munuera, Silvia Villar-Rodil, A. Adawy, A. Martínez-Alonso, J. M.D. Tascón. Aqueous cathodic exfoliation strategy toward solution-processable and phase-preserved MoS_2 nanosheets for energy storage and catalytic applications. ACS Appl. Mater. Interfaces 2019, 11, 40, 36991–37003.

[24] J. Liu, X. Yan, L. Wang, L. Kong and P. Jian, Three-dimensional nitrogen-doped graphene foam as metal-free catalyst for the hydrogenation reduction of *p*-nitrophenol, J. Colloid Interface Sci., 2017, 497, 102–107.

[25] J. Song, S.W. Kang, Y.W. Lee, Y. Park, J.-H. Kim and S.W. Han, Regulating the Catalytic Function of Reduced Graphene Oxides Using Capping Agents for Metal-Free Catalysis, ACS Appl. Mater. Interfaces, 2017, 9, 1692–1701.

[26] K. Peng, L. Fu, H. Yang, J. Ouyang and A. Tang, Hierarchical MoS2 intercalated clay hybrid nanosheets with enhanced catalytic activity, Nano Res., 2017, 10, 570–583.

[27] C. Nethravathi, A.D. Manganahalli, M. Rajamathi, Bi_2Te_3-MoS_2 layered nanoscale heterostructures for electron transfer catalysis, ACS Appl. Nano Mater., 2019, 2, 2005–2012.

[28] N. Sahiner, H. Ozay, O. Ozay, N. Aktas, A soft hydrogel reactor for cobalt nanoparticle preparation and use in the reduction of nitrophenols, Appl. Catal. B-Environ. 101 (2010) 137–143.

[29] S. Zhang, S. Gai, F. He, S. Ding, L. Lia, P. Yang, In situ assembly of well-dispersed Ni nanoparticles on silica nanotubes and excellent catalytic activity in 4-nitrophenol reduction, Nanoscale, 2014, 6, 11181-11188.

[30] D. B. Jiang, X. Liu, Y. Yuan, L. Feng, J. Ji, J. Wang, D. Losic, H.-C. Yao, Y. X. Zhang, Biotemplated top-down assembly of hybrid Ni nanoparticles/N doping carbon on diatomite for enhanced catalytic reduction of 4-nitrophenol, Chem. Eng. J. 383 (2020) 123156.

[31] X. Cheng, A. Fu, H. Li, Y. Wang, P. Guo, J. Liu, J. Zhang, X. S, Zhao, Sustainable Preparation of Copper Particles Decorated Carbon Microspheres and Studies on Their Bactericidal Activity and Catalytic Properties ACS Sustainable Chem. Eng. 2015, 3, 2414−2422.

[32] B. K. Barman, K. K. Nanda, Uninterrupted galvanic reaction for scalable and rapid synthesis of metallic and bimetallic sponges/dendrites as efficient catalysts for 4-nitrophenol reduction, Dalton Trans., 2015, 44, 4215–4222.

[33] X. Cheng, A. Fu, H. Li, Y. Wang, P. Guo, J. Liu, J. Zhang, X. S. Zhao, Sustainable Preparation of Copper Particles Decorated Carbon Microspheres and Studies on Their Bactericidal Activity and Catalytic Properties, ACS Sustainable Chem. Eng. 2015, 3, 2414–2422.

[34] M. Guo, Y. Zhao, F. Zhang, L. Xu, H. Yang, X. Song, Y. Bu, Reduced graphene oxide-stabilized copper nanocrystals with enhanced catalytic activity and SERS properties, RSC Adv., 2016, 6, 50587–50594.

[35] J. Xia, G. He, L. Zhang, X. Sun, X. Wang, Hydrogenation of nitrophenols catalyzed by carbon black-supported nickel nanoparticles under mild conditions, Appl. Catal. B-Environ. 180 (2016) 408–415.

[36] S. Bae, S. Gim, H. Kim, K. Hanna. Effect of $NaBH_4$ on properties of nanoscale zero-valent iron and its catalytic activity for reduction of p-nitrophenol. Appl. Catal. B-Environ. 182 (2016) 541–549.

[37] H. Fang, M. Wen, Hanxing Chen, Qingsheng Wu and Weiying Li, Graphene stabilized ultra-small CuNi nanocomposite with high activity and recyclability toward catalysing the reduction of aromatic nitro-compounds, Nanoscale. 2016, 8, 536–542.

[38] W. Zuo, G. Yu and Z. Dong, A MOF-derived nickel based N-doped mesoporous carbon catalyst with high catalytic activity for the reduction of nitroarenes, RSC Adv., 2016, 6, 11749–11753.

[39] X. Li, C. Zeng, J. Jiang, L. Ai, Magnetic cobalt nanoparticles embedded in hierarchically porous nitrogen-doped carbon frameworks for highly efficient and well-recyclable catalysis, J. Mater. Chem. A, 2016, 4, 7476–7482.

[40] Z. Ji, Y. Wang, X. Shen, H. Ma, J. Yang, A. Yuan, H. Zhou, Facile synthesis and enhanced catalytic performance of reduced graphene oxide decorated with hexagonal structure Ni nanoparticles, J. Colloid Interf. Science 487 (2017) 223–230.

[41] J. Jiang, Y. S. Lim, S. Park, S.-H. Kim, S. Yoon, L. Piao. Hollow porous Cu particles from silica-encapsulated Cu_2O nanoparticle aggregates effectively catalyze 4-nitrophenol reduction, Nanoscale, 2017, 9, 3873–3880.

[42] M. Du, Q. Liu, C. Huang, X. Qiu, One-step synthesis of magnetically recyclable Co@BN core–shell nanocatalysts for catalytic reduction of nitroarenes, RSC Adv., 2017, 7, 35451–35459.

[43] J. Liu, Z. Wang, X. Yan, P. Jian, Metallic cobalt nanoparticles imbedded into ordered mesoporous carbon: A non-precious metal catalyst with excellent hydrogenation performance, J. Colloid Interf. Sci. 505 (2017) 789–795.

[44] G. Wu, X. Liang, L. Zhang, Z. Tang, M. Al-Mamun, H. Zhao, X. Su, Fabrication of Highly Stable Metal Oxide Hollow Nanospheres and Their Catalytic Activity toward 4-Nitrophenol Reduction, ACS Appl. Mater. Interfaces 2017, 9, 18207–18214.

[45] P. C. Rath, D. Saikia, M. Mishra, H.-M. Kao, Exceptional catalytic performance of ultrafine Cu_2O nanoparticles confined in cubic mesoporous carbon for 4-nitrophenol reduction, Appl. Surf. Sci. 427 (2018) 1217–1226.

[46] X. Jiang, B. Han, C. Zhou, K. Xia, Q. Gao, J. Wu. Cu Nanoparticles Supported on Oxygen-Rich Boron Nitride for the Reduction of 4-Nitrophenol. ACS Appl. Nano Mater. 2018, 1, 6692–6700.

[47] L. Liu, Q. Zhao, R. Liu, L. Zhu. Hydrogen adsorption-induced catalytic enhancement over Cu nanoparticles immobilized by layered Ti_3C_2 MXene, Appl. Catal. B-Environ. 252 (2019) 198–204.

[48] C. Chu, S. Rao, Z. Ma, H. Han, Copper and cobalt nanoparticles doped nitrogen-containing carbon frameworks derived from CuO-encapsulated ZIF-67 as high-efficiency catalyst for hydrogenation of 4-nitrophenol, Appl. Catal. B-Environ. 256 (2019) 117792.

[49] Q. Chen, Y. Li, Q. Li, Y. Jia, X. Qiao. 3D Hierarchical N, O Co–Doped MoS_2/NiO Hollow Microspheres as Reusable Catalyst for Nitrophenols Reduction. ChemistrySelect 2019, 4, 9339 –9347.

[50] A. A. Jeffery, S. R. Rao, M. Rajamathi, Preparation of MoS_2–reduced graphene oxide (rGO) hybrid paper for catalytic applications by simple exfoliation–costacking. Carbon 112 (2017) 8–16.

[51] H. Oudghiri-Hassani, F. Al Wadaani. Preparation, Characterization and Catalytic Activitynof Nickel Molybdate ($NiMoO_4$) Nanoparticles. Molecules 2018, 23, 273.

[52] A. Goyal, S. Bansal, S. Singhal, Facile reduction of nitrophenols: Comparative catalytic efficiency of MFe_2O_4 (M [Ni, Cu, Zn) nanoferrites. International Journal of Hydrogen Energy 39 (2014) 4895-4908.

[53] S. U. Nandanwar, M. Chakraborty, Synthesis of Colloidal CuO/□-Al_2O_3 by Microemulsion and Its Catalytic Reduction of Aromatic Nitro Compounds. Chin. J. Catal., 2012, 33, 1532–1541.

[54] J. Xia, G. He, L. Zhang, X. Sun, X. Wang, Hydrogenation of nitrophenols catalyzed by carbon black-supported nickel nanoparticles under mild conditions. Appl. Catal. B 180 (2016) 408–415.

[55] H. Oudghiri-Hassani. Synthesis, characterization and catalytic performance of iron molybdate $Fe_2(MoO_4)_3$ nanoparticles. Catal. Commun. 60 (2015) 19–22.

[56] M. Karthik, P. Suresh. Greener Synthesis of Reduced Graphene Oxide-Nickel Nanocomposite: Rapid and Sustainable Catalyst for the Reduction of Nitroaromatics. ChemistrySelect 2017, 2, 6916 – 6928.

[57] J. Jiao, H. Wang, W. Guo, R. Li, K. Tian, Z. Xu, Y. Jia, Y. Wu, L. Cao. In Situ Confined Growth Based on a Self-Templating Reduction Strategy of Highly Dispersed Ni Nanoparticles in Hierarchical Yolk–Shell Fe@SiO_2 Structures as Efficient Catalysts. Chem. Asian J. 2016, 11, 3534 – 3540.

[58] M. Ajmal, M. Siddiq, H. Al-Lohedan and N. Sahiner. Highly versatile p(MAc)–M (M: Cu, Co, Ni) microgel composite catalyst for individual and simultaneous catalytic reduction of nitro compounds and dyes. RSC Adv., 2014, 4, 59562–59570

[59] Ö. Karahan, E. Biçer, A. Taşdemir, A. Yürüm, S. A. Gürsel. Development of Efficient Copper-Based MOF-Derived Catalysts for the Reduction of Aromatic Nitro Compounds. Eur. J. Inorg. Chem. 2018, 1073–1079.

[60] P. Das, S. Ghosh, M. Baskey (Sen). Heterogeneous catalytic reduction of 4-nitroaniline by RGO-Ni nanocomposite for water resource management. Journal of Materials Science: Materials in Electronics (2019) 30:19731–19737.

[61] K. Mishra, T. N. Poudel, N. Basavegowda, Y. R. Lee. Enhanced catalytic performance of magnetic Fe_3O_4–MnO_2 nanocomposites for the decolorization of rhodamine B, reduction of 4-nitroaniline, and sp C–H functionalization of 2-methylpyridines to isatins. Journal of Catalysis 344 (2016) 273–285.

[62] M. Tumma, R. Srivastava. Transition metal nanoparticles supported on mesoporous polyaniline catalyzed reduction of nitroaromatics. Catalysis Communications 37 (2013) 64–68.

[63] S. Venkatakrishnan, G. Veerappan, E. Elamparuthi, A. Veerappan. Aerobic synthesis of biocompatible copper nanoparticles: promising antibacterial agent and catalyst for nitroaromatic reduction and C–N cross coupling reaction. RSC Adv., 2014, 4, 15003–15006.

[64] U. Kurtan, E. Onus¸ Md. Amir, A. Baykal. Fe_3O_4@Hpipe-4@Cu Nanocatalyst for Hydrogenation of Nitro-Aromatics and Azo Dyes. J Inorg Organomet Polym, 2015, 25, 1120–1128.

[65] P. Zarringhadam, S. Farhadi. Hydrothermal Synthesis of Novel Magnetic Plate-Like $Bi_2O_2CO_3/CoFe_2O_4$ Hybrid Nanostructures and their Catalytic Performance for the Reduction of Some Aromatic Nitrocompounds. Acta Chim. Slov. 2018, 65, 448–461.

[66] M. Niakan, Z. Asadi. Selective Reduction of Nitroarenes Catalyzed by Sustainable and Reusable DNA-supported Nickel Nanoparticles in Water at Room Temperature. Catalysis Letters (2019) 149:2234–2246.

[67] R. J. Kalbasi, A. A. Nourbakhsh, F. Babaknezhad, Synthesis and characterization of Ni nanoparticles-polyvinylamine/SBA-15 catalystbfor simple reduction of aromatic nitro compounds. Catalysis Communications 12 (2011) 955–960.

[68] F. Zamani, S. Kianpou. Fast and efficient reduction of nitro aromatic compounds over Fe_3O_4/β-alanine-acrylamide-Ni nanocomposite as a new magnetic catalyst. Catalysis Communications 45 (2014) 1–6.

[69] K. Peng, L. Fu, H. Yang, J. Ouyang, A. Tang. Hierarchical MoS_2 intercalated clay hybrid nanosheets with enhanced catalytic activity. Nano Res., 2017, 10, 570–583.

[70] E. Kalantari, M. A. Khalilzadeh, D. Zareyee , M. Shokouhimehr, Catalytic degradation of organic dyes using green synthesized Fe_3O_4-cellulose-copper nanocomposites, Journal of Molecular Structure 1218 (2020) 128488.

[71] H. Wang, N. Wang, F. Wang, F. Xiao, D. Pan. Spherical montmorillonite-supported molybdenum disulfide nanosheets as a self-sedimentary catalyst for organic pollutants removal. Separation and Purification Technology 251 (2020) 117346.

[72] N. Saha, A. Sarkar, A. B. Ghosh, P. Mondal, J. Satra, B. Adhikary Advanced catalytic performance of amorphous MoS_2 for degradation/reduction of organic pollutants in both individual and simultaneous fashion. Ecotoxicology and Environmental Safety 160 (2018) 290–300.

[73] V. Balakumar, J. W. Ryu, H. Kim, R. Manivannan, Y.-A. Son Ultrasonic synthesis of α-MnO_2 nanorods: An efficient catalytic conversion of refractory pollutant, methylene blue. Ultrasonics Sonochemistry 62 (2020) 104870.

[74] X. Yang, H. Zhong, Y. Zhu, H. Jiang, J. Shen, J. Huang, C. Li. Highly efficient reusable catalyst based on silicon nanowire arrays decorated with copper nanoparticles. J. Mater. Chem. A, 2014, 2, 9040–9047.

[75] M. Makarova, Y. Okawa, M. Aono , Selective adsorption of thiol molecules at sulfur vacancies on MoS_2 (0001), followed by vacancy repair via S-C dissociation, J. Phys. Chem. C 116 (2012) 22411–22416.

[76] Z. Yu, Y. Pan, Y. Shen, Z. Wang, Z.-Y. Ong, T. Xu, R. Xin, L. Pan, B. Wang, L. Sun, J. Wang, G. Zhang, Y.W. Zhang, Y. Shi, X. Wang. Towards intrinsic charge trans- port in monolayer molybdenum disulfide by defect and interface engineering, Nat. Commun. 5 (2014) 5290.

[77] K. Cho, M. Min, T.-Y. Kim, H. Jeong, J. Pak, J.-K. Kim, J. Jang, S.J. Yun, Y.H. Lee, W.-K. Hong, T. Lee, Electrical and optical characterization of MoS_2 with sulfur vacancy passivation by treatment with alkanethiol molecules, ACS Nano 9 (2015) 8044–8053.

[78] P. Hervés, M. Pérez-Lorenzo, L. M. Liz-Marzán, L., J. Dzubiella, Y. Lubc, M. Ballauff. Catalysis by Metallic Nanoparticles in Aqueous Solution: Model Reactions. Chem. Soc. Rev. 2012, 41, 5577−5587.

[79] S. Carregal-Romero, N. J. Buurma, J. Pérez-Juste, L. M. Liz-Marzán, P. Hervés. Catalysis by Au@pNIPAM Nanocomposites: Effect of the Cross-Linking Density. Chem. Mater. 2010, 22, 3051−3059.

[80] J.I. Paredes, J.M. Munuera, S. Villar-Rodil, L. Guardia, M. Ayán-Varela, A. Pagán, S.D. Aznar-Cervantes, J.L. Cenis, A. Martínez-Alonso, J.M.D. Tascón, Impact of covalent functionalization on the aqueous processability, catalytic activity, and biocompatibility of chemically exfoliated MoS_2 nanosheets, ACS Appl. Mater. Interfaces 8 (2016), 27974-27986.

[81] M. Chatenet, F. Micoud, I. Roche, E. Chainet. Kinetics of Sodium Borohydride Direct Oxidation and Oxygen Reduction in Sodium Hydroxide Electrolyte: Part I. BH_4^- Electro-Oxidation on Au and Ag Catalysts. Electrochim. Acta 2006, 51, 5459−5467.

[82] J. A. Gardiner, J. W. Collat. The Hydrolysis of Sodium Tetrahydroborate. Identification of an Intermediate. J. Am. Chem. Soc. 1964, 86, 3165−3166.

[83] S.W. Han, G.-B. Cha, Y. Park, S.C. Hong, Hydrogen physisorption based on the dissociative hydrogen chemisorption at the sulphur vacancy of MoS_2 surface, Sci. Rep. 7 (2017) 7152.

[84] N.P. Rezende, A.R. Cadore, A.C. Gadelha, C.L. Pereira, V. Ornelas, K. Watanabe, T. Taniguchi, A.S. Ferlauto, A. Malachias, L.G. Campos, R.G. Lacerda. Probing the electronic properties of monolayer MoS 2 via interaction with molecular hydro- gen, Adv. Electron. Mater. 5 (2019) 1800591.

[85] C. Zhu, D. Gao, J. Ding, D. Chao, J. Wang, TMD-based highly efficient electro-catalysts developed by combined computational and experimental approaches, Chem. Soc. Rev. 47 (2018) 4332–4356.

[86] S. Jayabal, G. Saranya, J. Wu, Y. Liu, D. Geng, X. Meng, Understanding the high- -electrocatalytic performance of two-dimensional MoS_2 nanosheets and their composite materials, J. Mater. Chem. A 5 (2017) 24540–24563.

[87] D.A. Finkelstein, N. Da Mota, J.L. Cohen, H.D. Abruña, Rotating disk electrode (RDE) investigation of BH_4^- and BH_3OH^- electro-oxidation at Pt and Au: implications for BH_4^- fuel cells, J. Phys. Chem. C 113 (2009) 19700–19712.

[88] Y. Fu, T. Huang, B. Jia, J. Zhu, X. Wang, Reduction of nitrophenols to aminophenols under concerted catalysis by Au/g-C_3N_4 contact system, Appl. Catal. B: Environ. 202 (2017) 430–437.

[89] Y. Cai, Z. Bai, H. Pan, Y.P. Feng, B.I. Yakobson, Y.-W. Zhang, Constructing metallic nanoroads on a MoS_2 monolayer via hydrogenation, Nanoscale 6 (2014) 1691–1697.

[90] T. Aditya, A. Pal, T. Pal, Nitroarene reduction: a trusted model reaction to test nanoparticle catalysts, Chem. Commun. 51 (2015) 9410–9431.

[91] J. Hong, Z. Hu, M. Probert, K. Li, D. Lv, X. Yang, L. Gu, N. Mao, Q. Feng, L. Xie, J. Zhang, D. Wu, Z. Zhang, C. Jin, W. Ji, X. Zhang, J. Yuan, Z. Zhang, Exploring atomic defects in molybdenum disulphide monolayers, Nat. Commun. 6 (2015), 6293.

5.2 Exfoliación en fase líquida

Resumen de Artículo III

Two-dimensional transition metal dichalcogenides beyond MoS_2 for the catalytic reduction of nitroarenes: $MoSe_2$ exhibits enhanced performance. *Applied Catalysis B: Environmental*, 339 (2023), 123174.

A. Martínez-Jodar, S. Villar-Rodil, M.A. Salvado, D.F. Carrasco, P. Pertierra, J.M. Recio, J.I. Paredes.

Debido a las ventajas que reporta, la LPE es una de las alternativas más extendidas para la obtención de dispersiones de nanoláminas 2D de diversos TMDs. Probablemente debido a su mayor abundancia, el MoS_2 2D ha sido uno de los miembros más estudiados de esta familia en términos de su actividad (electro)catalítica. Sin embargo, esta preferencia podría no estar justificada desde el punto de vista de su desempeño como catalizador, ya que otros TMDs menos estudiados podrían ofrecer mejores resultados para esta aplicación. El objetivo del **artículo III** fue la comparación de las actividades catalíticas intrínsecas de nanoláminas 2D MoS_2 y $MoSe_2$ (obtenidas mediante LPE) en la reducción de nitroarenos. Las nanoláminas 2D de $MoSe_2$ demostraron una actividad catalítica superior a las nanoláminas equivalentes de MoS_2. Los estudios de DFT permitieron proponer un mecanismo de reducción de nitroarenos en presencia de $MoSe_2$, que implica la pasivación de los centros activos por átomos de oxígeno del grupo nitro, y su posterior reactivación con hidruro. Además, los cálculos DFT proporcionaron una explicación para la selectividad que mostraron los diferentes isómeros de nitroanilina por las nanoláminas de $MoSe_2$ durante la catálisis. De cara a la implementación práctica de estos catalizadores, se aumentó la estabilidad coloidal de las nanoláminas en medio acuoso utilizando surfactantes, sin pérdida significativa de la actividad catalítica. También se comprobó la retención de la actividad catalítica de las nanoláminas de $MoSe_2$ inmovilizadas sobre soportes poliméricos para facilitar su reutilización durante varios ciclos catalíticos.

ARTICULO III

Two-dimensional transition metal dichalcogenides beyond MoS_2 for the catalytic reduction of nitroarenes: $MoSe_2$ exhibits enhanced performance

A. Martínez-Jódar[a], S. Villar-Rodil[a,*], M.A. Salvadó[b,*], D.F. Carrasco[a], P. Pertierra[b], J.M. Recio[b], J.I. Paredes[a,*]

[a] Instituto de Ciencia y Tecnología del Carbono, INCAR-CSIC, C/Francisco Pintado Fe 26, 33011 Oviedo, Spain

[b] MALTA-Consolider Team and Departamento de Química Física y Analítica, Universidad de Oviedo, 33006 Oviedo, Spain

* Corresponding author: silvia@incar.csic.es (S. Villar-Rodil),

* Corresponding author: mass@uniovi.es (M.A. Salvadó),

* Corresponding author: paredes@incar.csic.es (J. I. Paredes)

Abstract

2D $MoSe_2$ nanosheets were investigated as a catalyst for nitroarene reduction in the context of water treatment and demonstrated to exhibit a higher activity than their more studied MoS_2 counterpart. Density functional theory (DFT) calculations disclosed a feasible nitroarene reduction pathway on 2D $MoSe_2$, which involved passivation of the active site by oxygen from the nitro group and its reactivation by a reducing hydride. DFT analysis also provided an explanation for the isomer selectivity displayed by the 2D $MoSe_2$ catalyst (towards, e.g., 2-, 3- and 4-nitroaniline). To facilitate their practical implementation, the bare $MoSe_2$ nanosheets were coated with colloidal stabilizers, and were also immobilized on polymer foam, where they could be re-used for several consecutive catalytic cycles with no significant loss of activity. Overall, the present results open the prospect of 2D transition metal dichalcogenides beyond MoS_2 as competitive nanocatalysts for the reduction of nitroarenes and other organic compounds.

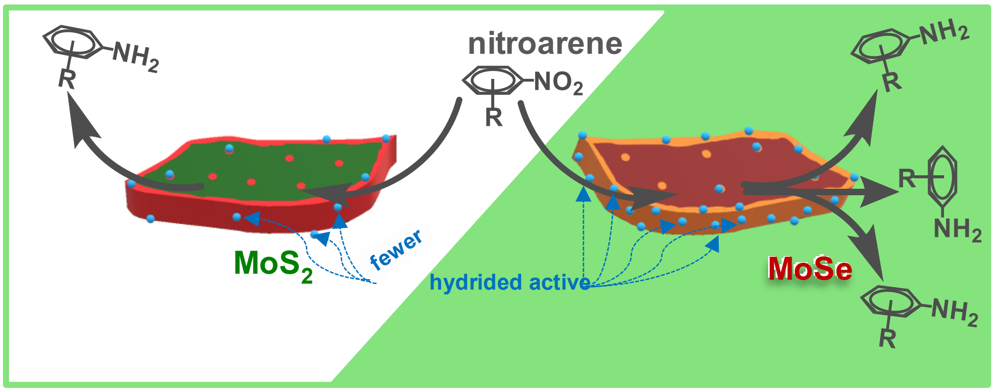

Keywords: Transition metal dichalcogenides (TMDs); nanocatalysts; $MoSe_2$; MoS_2; nitroarene reduction.

1. Introduction

Over the last decade, two-dimensional (2D) materials have been extensively investigated for their prospective use in the field of (thermo/electro/photo)catalysis, whether as catalysts themselves or in a supporting role to the catalyst proper [1-5]. Specific 2D materials of interest in this realm include graphene, phosphorene as well as other monoelemental systems, transition metal dichalcogenides (TMDs), MXenes and graphitic carbon nitride, among others [1,2]. Apart from the particular benefits that certain chemical compositions and crystal structures may bring, the attraction of 2D solids in catalysis stems from some general features of theirs, which comprise the following: (1) The large surface area (high surface-to-volume ratio) associated to their nanometric or atomic thickness implies that catalytic active sites readily accessible to the reacting substrates can be present in very high numbers, and also that 2D materials can host large numbers of nanoparticles, atomic clusters or single atoms when the former are used as a catalyst support for the latter [5,6]. (2) The electron confinement effect derived from the 2D morphology leads to changes in electronic states that can potentially alter the chemical reactivity of the active sites in the material compared to its bulk counterpart and other nanostructured forms, and thus the course and/or rate of catalytic reactions [1,6]. (3) The high mechanical flexibility of 2D solids that is derived from their large aspect ratio implies that they are very efficient at conformally coating other materials (e.g., catalytic particles). As a result, they can afford strongly confined reaction environments, where the course and/or rate of chemical reactions can be changed relative to the unconfined case ("catalysis under cover") [7]. In other cases, the conformal 2D coating provides a protective layer for catalysts that are unstable under harsh reaction conditions, such as those based on non-precious metals, so that the reaction is steered by the underlying catalyst but actually takes place on the surface of the 2D material ("chainmail for catalyst") [8].

Within the broad family of 2D materials for catalysis, TMDs and, in particular, 2D MoS_2 are currently the focus of especial interest owing to their high activity as electrocatalysts for a number of all-important chemical processes [9,10]. These electrocatalytic processes encompass the hydrogen evolution reaction (HER) first and foremost, but also the oxygen reduction reaction or the CO_2 and N_2 reduction reactions

[9,11,12]. Nonetheless, 2D TMD-based catalysts have also shown in recent years their promise in other relevant applications. This is specifically the case of the reduction of nitroarenes [13], which is of practical interest in the synthesis of fine chemicals as well as in the area of water treatment for environmental remediation. For instance, the production of some widely used pharmaceutical drugs (e.g., paracetamol), agrochemical compounds and dyes relies on the availability of certain substituted anilines as key intermediates, which can be accessed via reduction of their corresponding nitroarenes [14,15]. Likewise, many substituted nitroarenes (e.g., nitrophenols) are frequently found in industrial effluents, but the toxic and recalcitrant nature of such compounds advises against their direct release to natural water bodies. In this context, degradation of the nitroarenes by way of their reduction prior to disposal is one workable option, since the reduced products (i.e., anilines) are much more biodegradable and less hazardous than their nitroarene counterparts [16,17].

Similar to the case of the above electrocatalytic reactions, the allure of 2D TMDs as catalysts for nitroarene reduction arises from the fact that they are more affordable and earth-abundant alternatives to the noble metal-based catalysts commonly used for such reactions [14,16,18]. Here again, MoS_2 nanosheets and other nanostructures have been the TMD-based catalysts of choice in most previous studies [13,19-31]. While such a preference is very likely based on the wider availability of MoS_2 relative to other TMDs, it may not be completely justified from the perspective of catalyst performance. However, so far very little work has been carried out on the catalytic activity of other TMDs in any nanostructured form toward nitroarene reduction [32-34], let alone work directly comparing their activity with that of MoS_2. Moreover, the atomic-level understanding of the interactions between these substrate molecules and the active sites of TMD catalysts is currently very limited. Such active sites are thought to be located at coordinatively unsaturated metal centers of edges and chalcogen vacancies on the surface of the TMD lattice [25,29,33], very much like the active sites for the HER and other electrocatalytic reactions [9-12]. Having this type of physical insight would be expected to shed light on experimentally observed differences in the activity of a given TMD catalyst toward, e.g., different substituted nitroarenes. In particular, it would shed light on differences in catalyst activity toward different structural isomers of a given substituted nitroarene, which could be a priori the most difficult to rationalize.

In an effort to contribute to addressing these issues, we have investigated the use of 2D $MoSe_2$ nanosheets as a catalyst for the reduction of nitroarenes with sodium borohydride ($NaBH_4$) as the reductant, the results of which are reported here. Even though it is the closest relative of MoS_2 within the family of TMD compounds, $MoSe_2$ possesses some features that make it potentially a strong competitor of the former and thus worth exploring in the catalytic reduction of nitroarenes, as well as in other catalytic and non-catalytic applications [35,36]: (1) $MoSe_2$ is a reasonably affordable material. (2) The longer bond length and lower bond energy of $MoSe_2$ compared with those of MoS_2 render catalytically active structural defects (edges, chalcogen vacancies) easier to form [37] and, therefore, suggest that they could be intrinsically more abundant in the former TMD. (3) Due to the higher metallicity of $MoSe_2$ (lower electronegativity of selenium compared to sulfur), electronic charges taking part in reduction reactions at the catalytic active sites of this TMD could be more readily available compared to the case of MoS_2. We note that (2) and (3) would imply 2D $MoSe_2$ nanosheets to be more catalytically active in reduction reactions than their MoS_2 counterpart. In this work, we demonstrate that this is generally the case for the reduction of nitroarenes and provide some insight into the origin of such higher activity. Moreover, with the assistance of density functional theory (DFT)-based calculations, we probe into the unexpected activity trends that were observed for 2D $MoSe_2$ nanosheets toward nitroarene isomers in our experiments. The results point to differences in the adsorption configuration of the isomers as a main driver of the reported activity trends with the $MoSe_2$ catalyst. Overall, the present work opens the prospect of 2D TMDs beyond MoS_2 as competitive catalysts for nitroarene reduction for water treatment and suggests some guidelines to pinpoint the most promising candidates as well as to rationalize catalytic activity trends

2. Experimental

2.1. Materials and reagents

MoS_2 and $MoSe_2$ powder materials were purchased from Alfa Aesar, The following chemicals were acquired from Sigma-Aldrich: DMF, isopropanol, $NaBH_4$, hydrazine monohydrate, 4-nitroaniline (4-NA), 3-nitroaniline (3-NA), 2-nitroaniline (2-NA), 4-nitrophenol (4-NP), 3-nitrophenol (3-NP), 2-nitrophenol (2-NP), nitrobenzene (NB), methyl orange (MO), potassium hexacyanoferrate {$K_3[Fe(CN)_6]$}, adenosine monophosphate (AMP), [(poly(ethylene glycol)-*block*-poly(propylene glycol)-*block*-poly(ethylene glycol)] (P-123). All the materials and chemicals were used as received, without further treatment. Milli-Q deionized water (Millipore Corporation; resistivity: 18.2 MΩ cm) was used throughout the experiments.

2.2. Preparation of exfoliated $MoSe_2$ and MoS_2 nanosheets in aqueous dispersion

MoS_2 and $MoSe_2$ nanosheets (NSs) were obtained from the direct exfoliation of the corresponding bulk powders in DMF with the assistance of sonication. Specifically, TMD powder at nominal concentration of 30 g mL^{-1} in DMF was bath-sonicated (J.P. Selecta Ultrasons system, 40 kHz) for 5 h (changing from bath to bath to avoid overheating of water). The resulting suspension was centrifuged (Eppendorf 5430 microcentrifuge) at 200 *g* for 20 min to sediment the non- and poorly delaminated fractions of the material and the supernatant containing well-exfoliated flakes was collected. Then the TMD dispersion was diluted in DMF to ~0.2 mg mL^{-1} and the solvent was exchanged by water by subjecting the colloidal dispersion to four cycles of high-speed centrifugation (21,191 *g*, 25 min) to completely sediment the exfoliated flakes followed by re-suspension in deionized water by bath-sonication (~2 min). The resulting aqueous TMD suspensions were adjusted to a concentration ~0.10-0.15 mg mL^{-1}, and used in all the subsequent experiments. To determine the concentration of the TMD dispersions, the absorbance of the as-prepared dispersion was measured and a known volume was vacuum-filtered through polycarbonate filters and dried overnight under vacuum, allowed to cool down in a desiccator and finally weighed to calculate its original concentration. The extinction coefficient (ε) values derived from such measurements for MoS_2 and $MoSe_2$ were ε_{MoS2} (λ=345 nm) = 34.5 and ε_{MoSe2} (λ=365 nm) = 24.5 mg^{-1} L cm^{-1}, respectively.

2.3. Generation of selenium vacancies in $MoSe_2$ nanosheets by hydrazine treatment

To generate selenium vacancies in the exfoliated $MoSe_2$ flakes, a mixture of $MoSe_2$ aqueous dispersion with hydrazine monohydrate with a ratio of 1 mL hydrazine per 100 mg of exfoliated $MoSe_2$ was poured into a test tube, which was then capped with a rubber septum with a small orifice to allow gas release. The mixture was heated at 70 ºC for one hour, after which the reacted product was washed to remove any hydrazine monohydrate remaining in the solution by applying three consecutive cycles of sedimentation via centrifugation (21,191 *g*, 20 min), replacement of all the supernatant volume by neat water and re-dispersion of the $MoSe_2$ flakes by a brief (~2 min) sonication step.

2.4. Catalytic activity tests of $MoSe_2$ and MoS_2 nanosheets toward nitroarene reduction

For the catalytic tests, aqueous aliquots (2.5 mL) containing TMD catalyst at concentration of 14 µg mL^{-1}, 0.11-0.12 mM of nitroarene, as well as a large excess of $NaBH_4$ (112 mM) were prepared in quartz cuvettes with an optical path length of 1 cm, which were immediately transferred to an UV-Vis absorption spectrophotometer. The reaction progress was monitored by measuring the evolution of absorbance at the wavelength of the maximum of a characteristic peak of the substrate molecule versus time. The extinction coefficients of the different substrate materials at such wavelengths at the conditions of catalysis were determined by calibration in the presence of 112 mM $NaBH_4$ [ε(3-nitrophenolate, λ=390 nm) =1,456 M^{-1} cm^{-1}; ε(2-nitrophenolate, λ=416 nm)=4,643 M^{-1} cm^{-1}; ε(4-NA, λ=380 nm)=12,502 M^{-1} cm^{-1}; ε(3-NA, λ=357 nm)=1,418 M^{-1} cm^{-1}; ε(2-NA, λ=416 nm)=4,390 M^{-1} cm^{-1}; ε(NB, λ=270 nm)= 7,451 M^{-1} cm^{-1}] or, in the case of 4-NP, taken from the literature [ε(4-nitrophenolate; λ=400 nm) =17,500 M^{-1} cm^{-1} [38]]. For some selected nitroarenes (4-NP, 4-NA and 3-NA), catalytic tests were performed with a higher substrate concentration of 1 mM, as well as an excess of $NaBH_4$ (224 mM), keeping the catalyst concentration at 14 µg mL^{-1}. In such cases, the reaction progress was monitored by measuring the evolution of absorbance at a wavelength characteristic of the substrate where saturation of the signal at such higher concentration was avoided (455 nm for 4-NP [26], 445 nm for 4-NA, and 357 nm for 3-NA).

2.5. Characterization techniques

The materials were characterized by UV-Vis absorption spectroscopy, Atomic Force microscopy (AFM), Field-emission scanning transmission microscopy (FE-SEM), Scanning transmission electron microscopy (STEM), High resolution transmission electron microscopy (HR-TEM), energy dispersive X-ray spectroscopy (EDX), selected area diffraction (SAED), Dynamic light scattering (DLS), X-ray photoelectron spectroscopy (XPS), X-ray diffraction (XRD), Raman spectroscopy, Electron paramagnetic resonance (EPR) and measurement of zeta potential. UV-Vis absorption/extinction spectra of TMD dispersions were recorded with a double-beam Genesys 180 spectrophotometer (Thermo Fisher Scientific). AFM imaging was performed in a Nanoscope IIIa Multimode system in the tapping mode of operation and using rectangular silicon cantilevers with resonance frequencies of 250-300 kHz and nominal spring constant of 40 N m^{-1}. To image exfoliated TMD flakes by AFM, the delaminated material was dispersed in water (~0.01 mg mL^{-1}), drop-cast (10–20 μL) onto a freshly cleaved mica substrate and dried overnight under a vacuum at 60 °C. The recorded AFM images were analyzed with SPIP software (Image Metrology). FE-SEM and STEM imaging were carried out in a Quanta FEG apparatus (FEI Company) working at a bias voltage of 20–25 kV. Specimens for FE-SEM (melamine foam) were mounted onto the sample-holder by means of double-sided carbon adhesive tape, while those for STEM and HR-TEM were prepared by drop-casting a few microliters of the sample dispersion in water and isopropanol, respectively, onto a copper grid (200 square mesh) covered with a thin continuous carbon film (STEM) or lacey carbon (HR-TEM), and allowing it to dry under ambient conditions. HR-TEM, EDX and SAED were carried out with a JEOL JEM-2100F instrument operated at an accelerating voltage of 200 kV and equipped with Scanning transmission electron microscope (STEM) control unit (Gatan), energy dispersive X-ray (EDX) detector (Oxford Instruments, silicon drift detector (SDD) 80 mm^2), CCD camera (14-bit Gatan Orius SC600), and bright-field and high angle annular dark field (HAADF) detectors (JEOL). DLS measurements of the TMD dispersions were performed using a 3DDLS photon cross-correlation spectrometer (LS Instruments), equipped with a He-Ne laser (632.8 nm). The measurements were carried out in quintuplicate at 25 ºC and at an angle of 90º for 100 s for each measurement and using the 3D correlation mode. XPS was carried out on a SPECS system equipped with a

Phoibos 100 hemispherical electron energy analyzer. The spectra were recorded at a take-off angle of 90º, working at a pressure below 10^{-7} Pa and using a monochromatic aluminum X-ray source operated at a voltage of 14.00 kV and a power of 175 W. The photoexcited electrons were analyzed in the constant pass energy mode, using a pass energy of 50 eV for survey spectra and 10 eV for high resolution core-level spectra. CasaXPS software was used for data processing. Core level curve fitting in different components was performed using a Shirley background and a standard least squares algorithm. Each component was considered as a convolution of a Gaussian and a Lorentzian function (80:20). In the S 2p core level band, each chemical state is represented by a spin-orbit doublet with spin-orbit splitting (SOS) constant of 1.16 eV, as expected for an ideal sulphur signal, and an approximately 1:2 peak area ratio between S $2p_{1/2}$ and S $2p_{3/2}$ components, actually, relative sensitivity factor (RSF) (S $2p_{1/2}$)/RSF (S $2p_{3/2}$) =0.567/1.11=0.511 [39]. In the Mo 3d and Se 3d core level bands, each chemical state is a spin-orbit doublet with area ratio between $3d_{3/2}$ and $3d_{5/2}$ components of approximately 2:3, actually, RSF (Mo $3d_{3/2}$)/ RSF (Mo $3d_{5/2}$) = 3.88/5.62=0.69 and RSF (Se $3d_{3/2}$)/ RSF (Se $3d_{5/2}$=0.934/1.36=0.69) [39] with a SOS constant of 3.15 eV and 0.86 eV, for Mo 3d and Se 3d, respectively. XRD diffractograms were acquired on a Bruker D8 Advance diffractometer equipped with a Cu K_α anode. The data were recorded in a 2θ range of 5°–80° with a step size of 0.015° and time per step of 6 s. for XRD measurements, the starting TMD powders were used as received while the exfoliated materials were prepared in the form of films by filtering from dispersion through polycarbonate membranes with pore size of 50 µm (Nucleopore™, Whatman®). Raman spectra were acquired with a Renishaw inVia Qontor instrument, working at a laser excitation wavelength of 532 nm (green line). To avoid or minimize damage to the sample, the incident laser power was set to values below 0.5 mW. Samples for XPS and Raman spectroscopy were prepared by drop–casting the aqueous exfoliated TMD dispersions onto metallic sample holders until uniform films covered the substrate and allowing them to dry under ambient conditions. The starting TMD powders were pressed into pellets by means of a hydraulic press. EPR spectra were recorded with a X-Band (9.4 GHz) Bruker ELEXSYS E500 spectrometer using a magnetic field modulation amplitude of 2 G, a modulation frequency of 100 kHz, a time constant of 20.48 s and a microwave power of

~20 mW. The determination of the zeta potential was performed from electrophoretic mobility measurements using in a Zetasizer Nano-Z instrument (Malvern) equipped with a laser light source with a wavelength of 633 nm. The zeta potential was calculated using the Smoluchowski equation.

2.6. Computational methods

Computational calculations were performed under the density functional theory (DFT) framework using the Vienna Ab-initio Software Package (VASP) [40]. For the exchange-correlation energy term, the Perdew-Burke-Ernzerhof (PBE) functional was selected [41]. The simulation cell consisted of a 2H-$MoSe_2$ 4×4 monolayer. Periodic images along the *c* axis were separated by a vacuum slab of 18 Å. Starting from this structure, models with one ($1V_{Se}$) and four ($4V_{Se}$) selenium atom vacancies (on the same side of the layer) per supercell were built. For the adsorbed states, one nitroarene molecule per supercell was placed over one of the selenium vacancies. All the models were optimized (coordinates and the cell parameters *a* and *b*) with the *c* axis length fixed at 18 Å. Optimizations were stopped when the forces and stresses were less than 0.01 $eVÅ^{-1}$. An energy cutoff of 450 eV was used for the plane wave basis set. Due to the large size of the supercells used here, only the Γ point was sampled in the reciprocal space. Nitroarene molecules in the absence of surface were optimized using fixed cells of $18×18×18$ $Å^3$. In those reaction intermediates where the molecule was expected to be negatively charged, one sodium atom was included to maintain the electrical neutrality of the system. Structural models were built using PowderCell [42] and VESTA [43]. Structure plots were made with VESTA.

2.7. Identification of reaction intermediates

Some reaction intermediates for 3-NA reduction were identified by means of reversed-phase (RP) ultrahigh-performance liquid chromatography (UHPLC) (UltiMate™ Dionex 3000 HPLC system from Thermo Scientific) coupled to high-resolution mass spectrometry (HR-MS) (IMPACT II ESI-QTOF instrument from Bruker). 3-NA and its reaction product, 3-phenilendiamine, were also detected. The catalysis medium was prepared (2.5 mL) and the reaction was arrested after certain reaction times by removing the catalyst by syringe-filtration (Whatman® Anotop® syringe filter 0.02

μm alumina-based membrane) directly into solid phase extraction (SPE) cartridges (HLB Oasis 250cc, Waters), previously conditioned in ultrapure water (reagent grade type I, Autwomatic, Wasserlab). After sample introduction and a cleaning step with water, analytes were eluted with absolute methanol (6 mL, LC-MS grade, OPTIMA, Thermo Fisher), and collected in a glass vial. Off-line SPE eliminated $NaBH_4$, whose presence would have been detrimental to the ionization of the analytes needed for HR-MS detection. 300 μL was immediately transferred into liquid chromatography vials (300 μL insert vials, Thermo Scientific). Luna Omega Polar column (150 × 2.1 mm, 1.7 μm, Phenomex) column was used as stationary phase while the mobile phase was a mixture of: (A) ultrapure water, and (B) acetonitrile (LC-MS grade, OPTIMA, Thermo Fisher), both with 0.1 % v/v formic acid (LC-MS grade, Thermo Fisher). 5 μL was injected and separated applying the following program: 0 min 30 % B, 2 min 30 % B, 10 min 55 % B, 11 min 70% B, 13 min 70 % B. HR-MS detection was performed in full-scan (50-1500 M/Z) positive mode. CompassDataAnalysis software (V4.4, Bruker) was used for spectra analysis. A combination of exact mass and isotopic pattern was taken into consideration for molecular formula proposal of potential catalysis intermediates. In all cases, M+H ions were detected and studied.

3. Results and discussion

3.1. Preparation and physicochemical characterization of exfoliated $MoSe_2$ nanosheets

A straightforward procedure that combined liquid-phase exfoliation via sonication with an organic-to-aqueous phase transfer step was used to obtain $MoSe_2$ nanosheets or flakes from their bulk precursor that were suitable for the catalytic tests. Briefly, bulk $MoSe_2$ powder was first delaminated in *N,N*-dimethylformamide (DMF), as a well-known solvent for efficient TMD exfoliation [44], by means of bath-sonication. The resulting suspension was centrifuged at a low speed to sediment the non-delaminated and poorly delaminated fractions of the material, with the supernatant containing well-exfoliated flakes. The latter was collected and subjected to several cycles of (i) high speed centrifugation to completely sediment the exfoliated flakes and (ii) re-suspension of the flakes in deionized water by a brief sonication step. Such a procedure finally afforded a visually homogeneous aqueous suspension of $MoSe_2$ nanosheets (Fig. 1a). Indeed, UV-

Vis absorption spectroscopy (Fig. 1b) was consistent with the dispersed material being the thermodynamically stable, 2H phase of $MoSe_2$, as noticed from the characteristic excitonic peaks of this TMD located at ~720 and 815 nm [44,45]. Atomic force microcopy (AFM; Figs. 1c and d) and scanning transmission electron microscopy (STEM; Fig. 1e) imaging of the dispersed objects revealed them to exhibit an irregular polygonal profile with lateral size typically between several tens and a few hundreds of nanometers (see STEM-derived histogram in Fig. 1f) and thickness ~10 nm. Considering that the thickness of a $MoSe_2$ monolayer is ~0.6–0.7 nm [46,47], this implies that individual nanosheets in the aqueous suspension were made up of about 14–17 monolayers. The lateral size distribution determined by STEM for the $MoSe_2$ nanosheets was corroborated with dynamic light scattering (DLS) measurements. As can be seen in Fig. 1g, the hydrodynamic diameters of the $MoSe_2$ particles dispersed in water were calculated to be roughly between 70 and 400 nm by this technique. Although the hydrodynamic diameter of suspended particles is obviously correlated to their actual dimensions, such a correlation can be somewhat convoluted due to the different shapes that particles can adopt [48]. For 2D materials like graphene and TMDs, a quantitative relationship between the hydrodynamic diameter and the lateral size of dispersed nanosheets, based on approximating their shape to circular discs, has been previously demonstrated [49]. Using this relationship, the lateral size of the present $MoSe_2$ nanosheets was estimated from the DLS measurements to be approximately between 40 and 500 nm, which was in reasonably good agreement with the results obtained by direct STEM imaging (Fig. 1f). HR-TEM images (Fig. 1h and Figs. S1a–c in the SM) confirm that the exfoliated flakes were multilayer in nature. Atomic resolution images of the basal planes and the corresponding SAED patterns (Figs 1i and 1j, respectively) reveal their hexagonal symmetry and unit cell parameters.

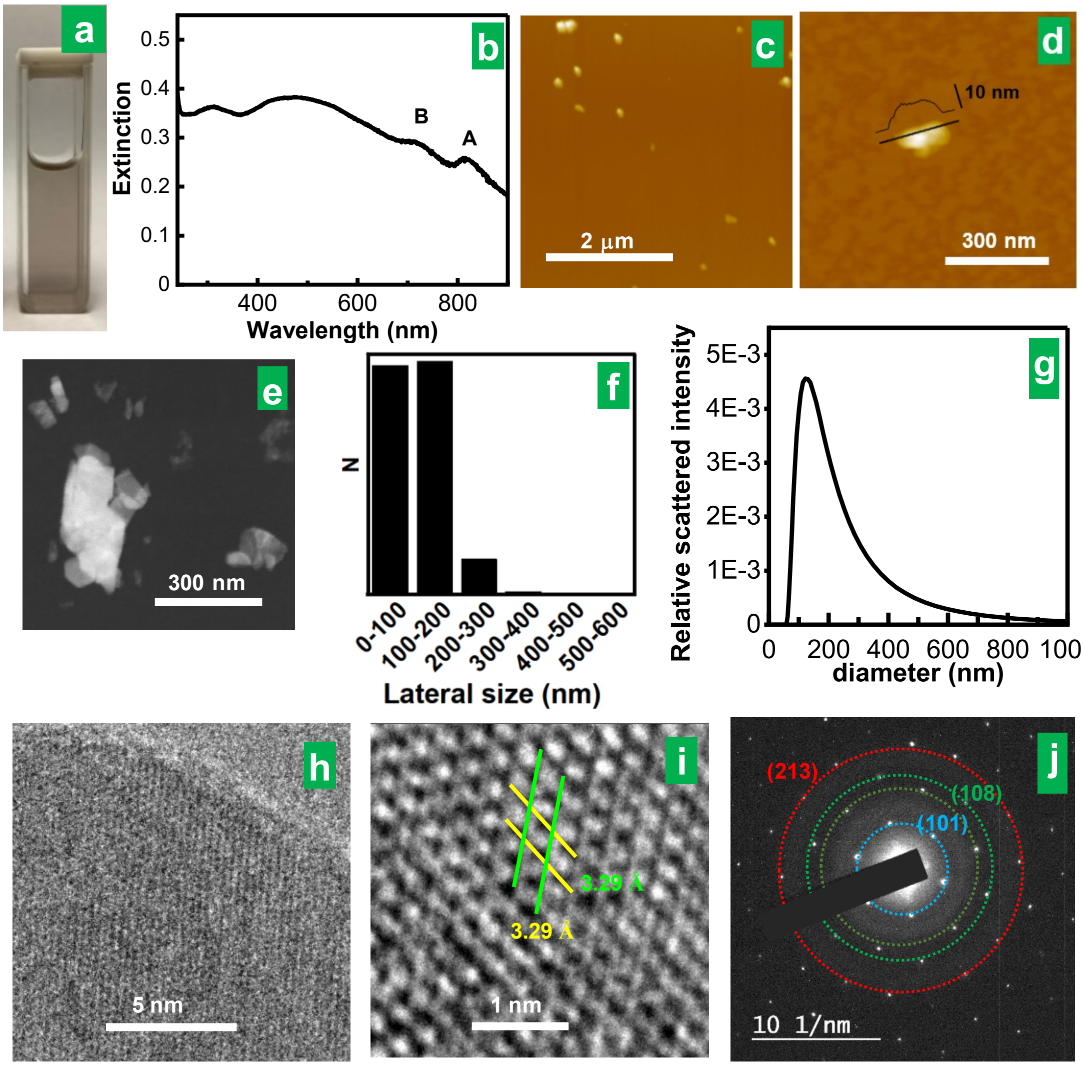

Figure 1. Characterization of MoSe$_2$ dispersions. (a) Digital photograph of the MoSe$_2$ dispersion and the corresponding **(b)** UV-Vis extinction/adsorption spectrum with indication of the characteristic excitonic peaks. Representative **(c,d)** AFM and **(e)** STEM images of the dispersed objects. **(f)** Histogram of lateral size derived from STEM imaging. **(g)** Particle size (from hydrodynamic diameter) distribution from DLS measurements. **(h,i)** Representative HR-TEM images of the MoSe$_2$ flakes at different magnifications. The parallel lines in (i) assist in visualizing *a* and *b* cell parameters in the hexagonal cell of MoSe$_2$ lattice. **(j)** SAED pattern of the MoSe$_2$ lattice with indication of the family planes involved in the observed diffractions.

The structural configuration and chemical make-up and of the exfoliated MoSe$_2$ flakes were investigated by X-ray diffraction, Raman spectroscopy, energy dispersive X-ray (EDX) mapping and X-ray photoelectron spectroscopy (XPS). XRD confirmed the crystalline structure of the exfoliated flakes to be that of 2H-$MoSe_2$, belonging to $P6_3/mmc$ space group (JCPDS card 29-0914), as in the starting $MoSe_2$ powder (see Fig. S2a). Indeed, the Raman spectra of the exfoliated flakes (Fig. 2b) displayed the characteristic features of 2H-phase $MoSe_2$ [50], i.e., an intense peak located at ~242 cm^{-1} (A_{1g} band) together with weaker bands at ~170 (E_{1g}), ~288 (E^1_{2g}) and ~352 (A^2_{2u}) cm^{-1}. The position of the A_{1g} (E^1_{2g}) band has been shown to red(blue)-shift when bulk $MoSe_2$ is downsized to the few- and single-layer level [51-53]. Hence, the spectral separation between these two bands can be taken as a fingerprint for the presence of 2D nanosheets of this material. However, such a spectral fingerprint is only sensitive to the thinnest nanosheets (<5 monolayers). Indeed, the A_{1g}-E^1_{2g} separation determined for our $MoSe_2$ flakes (~4cm^{-1}, consistently measured at many different spots of the sample) was virtually identical to that obtained for the starting bulk material (Fig. S2b in the SM). This result agreed with the AFM and HRTEM data of the exfoliated product indicating that it was made up of relatively thick nanosheets (~14–17 monolayers, Figs. 1d and S1a–c). As concluded from the EDX area mapping (Figs. 2c–e) and the XPS survey spectrum (Fig. S1d in section S1 of the SM), the material was mainly comprised of Mo and Se in approximately 1 : 2 atomic ratio (really, a little low in chalcogen, as will be explained below). Although a very small amount (<5 at%) of carbon and oxygen elements was also detected, this probably originated from the ever-present adventitious contamination in the XPS analysis chambers [54] (or, in this particular case, from residual adsorbed DMF molecules). The corresponding high resolution, core-level Mo 3d spectrum (Fig. 2f) exhibited the well-known doublet band arising from the 5/2 and 3/2 spin states of this electron energy level. Moreover, the binding energies measured for such states, namely, 229.0 eV for Mo $3d_{5/2}$ and 232.2 eV for Mo $3d_{3/2}$, were consistent with the atomic environment expected for this metal in 2H-phase $MoSe_2$ (Mo^{4+} with trigonal prismatic coordination to the chalcogen) [46,55,56]. A similar conclusion regarding the presence of 2H-phase $MoSe_2$ was reached from the high resolution core-level Se 3d spectrum (Fig. 2g), that is, the position of the Se $3d_{5/2}$ (54.5 eV) and $3d_{3/2}$ (55.4 eV) levels was also in agreement with such a structural attribution [55,56]. Both core-level spectra were essentially identical to those of the starting bulk $MoSe_2$ powder (see Fig. S2c and d in the SM), suggesting that the material was not altered to any significant extent during its exfoliation and subsequent processing. In particular, no oxidized Mo or Se species could be seen at the levels that can be detected by this technique (i.e., above a few tenths of at%), either in the starting material or its exfoliated counterpart. For instance, no doublet bands arising from MoO$_x$ (232.8 and 236 eV) or SeO$_x$ (59 and 59.8 eV) were noticed [55]. Further details on the XPS characterization of MoSe$_2$, including an explanation on the assignment of a feature observed in the Mo 3d spectral range to Se 3s core level (see Fig. 2f and Fig. S2c) are given in section S1 of the Supplementary Material (SM).

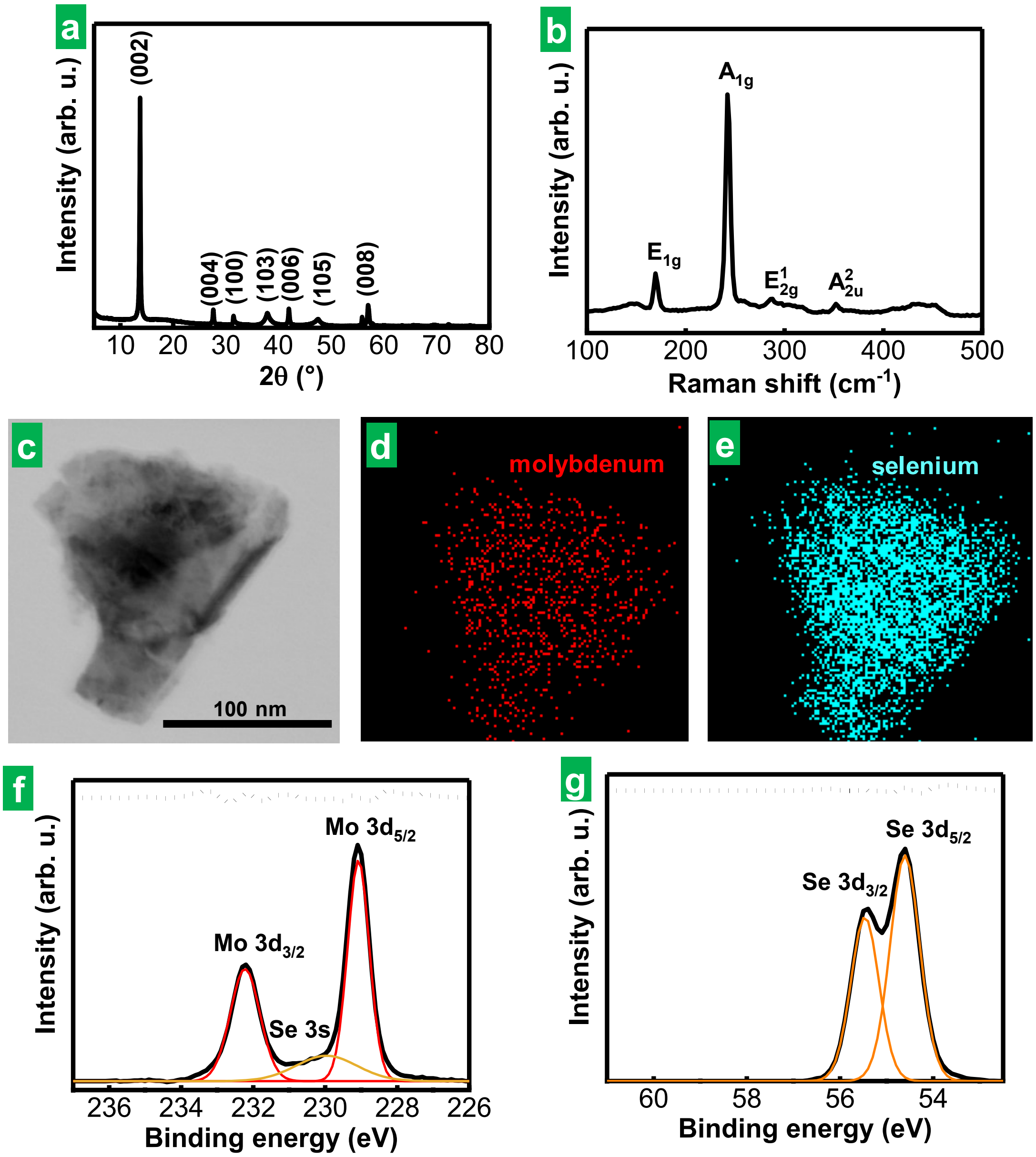

Figure 2. Structural and chemical characterization of the exfoliated $MoSe_2$ flakes. (a) XRD diffractogram of exfoliated $MoSe_2$, where peaks have been labelled according to JCPDS card 29-0914. (b) Raman spectrum for exfoliated $MoSe_2$ flakes. The main bands have been labeled for clarity. **(c)** STEM image of exfoliated $MoSe_2$ and **(d,e)** the corresponding energy dispersive X-ray (EDX) area mapping of (d) molybdenum and (e) selenium. **(f)** Background-subtracted, high-resolution XPS Mo 3d (and Se 3s) spectra and **(g)** Se 3d core level spectrum of exfoliated $MoSe_2$. The experimental data are graphed with a solid black line while the deconvoluted Mo and Se components are depicted with red and orange traces, respectively. The difference between the experimental and the fitted spectrum is graphed on top of the fitted XPS spectra (dotted traces).

The same procedure was applied to prepare aqueous dispersions of exfoliated MoS_2 flakes. Their morphological, structural and chemical characterization (Figs. S3 and S4 in section S2 of the SM) yielded very similar results to those obtained for their $MoSe_2$ counterpart, i.e., the exfoliated product was made up of submicrometer-sized nanosheets that were several layers thick and retained the original 2H phase of the starting bulk material. The only significant difference between the two exfoliated TMDs concerned their lateral size distribution. While the DLS-derived hydrodynamic diameters for the $MoSe_2$ and MoS_2 dispersions were essentially identical (see Figs. 1g and S3g), the population of the smallest flakes (< 100 nm) as determined by direct STEM imaging was noticeably larger in the $MoSe_2$ sample (compare Figs. 1e and S3f). This result was not unreasonable, considering that the Mo-Se bond in $MoSe_2$ is weaker than its Mo-S counterpart in MoS_2 [57] and, therefore, that $MoSe_2$ slabs are more likely to fragment into smaller pieces during the sonication treatment. The fact that the DLS measurements did not reflect this difference could have its origin in the relatively weaker scattering of light of the smaller particles in relation to the larger ones, which makes the former more difficult to be detected by this technique.

3.2. Catalytic performance of exfoliated $MoSe_2$ nanosheets toward nitroarene reduction and comparison with MoS_2

With a view to their use as (unsupported) catalysts for reduction reactions for water treatment and, thus, carried out in water, the colloidal stability of 2D TMD nanosheets in aqueous medium is thought to be critical [58]. The exfoliated $MoSe_2$ flakes prepared here exhibited a limited colloidal stability in such a medium. Specifically, they showed visible signs of aggregation and sedimentation after their dispersions (concentration ~0.10-0.15 mg mL^{-1}) were allowed to stand undisturbed for a few to several days. However, the material could be readily re-suspended via sonication, to give again visually homogeneous dispersions that remained stable for several hours to a few days. This behavior was not surprising, considering that bare TMDs are in general relatively hydrophobic materials and that the exfoliated $MoSe_2$ flakes were transferred to pure water without the aid of any surfactants or colloidal stabilizers [44,59-61]. Still, it is also known that different 2D materials, including TMDs like MoS_2 and $MoSe_2$, possess a small but non-negligible degree of colloidal stability by themselves (i.e., without the assistance of external dispersants) in pure water at moderate to low concentrations [62,63]. This was indeed the case of the present aqueous $MoSe_2$ dispersions, which remained stable for at least several hours before starting to sediment to any significant extent (quantitative evidence of such stability is provided in the SM, in Section S4 and Fig. S6a, as will be explained below). As a result, a sufficiently long-time window was in practice available for testing the catalytic performance of the bare flakes without the need to resort to surfactants or stabilizers that could interfere with the catalytic reactions [16,64], which allows comparing the intrinsic catalytic activities of $MoSe_2$ and MoS_2.

The ultimate cause of the non-negligible colloidal stability of some hydrophobic 2D materials in pure water is not yet well understood, but it has been ascribed to the presence of surface charges on the nanosheets [62]. The $MoSe_2$ flakes obtained here were, in fact, negatively charged in water, exhibiting a zeta potential value of -15 mV that was indicative of dispersions with incipient stability [65]. The latter was in turn consistent with the above observation of aqueous $MoSe_2$ suspensions that were only stable for several hours to a few days. A similar result was obtained regarding the stability of the aqueous MoS_2 suspensions, the zeta potential of which was measured to be -11 mV. As for the actual chemical species responsible for the negative charges in the bare TMD nanosheets, we believe (polyoxo)metalates to be very plausible candidates, and specifically (polyoxo)molybdates in the case of molybdenum-based TMDs. Small amounts of such negatively charged species are present in bulk TMD powders as a result of natural oxidation processes, although they can also be generated via purposeful oxidation. Moreover, these (polyoxo)metalates have been shown to trigger TMD exfoliation by an electrostatic repulsion mechanism upon their adsorption on the surface and at interlayer spaces of the TMD particles [66,67]. Consequently, they could furnish the bare exfoliated flakes with negative charges and, therefore, with some degree of colloidal stabilization.

The catalytic activity of the exfoliated $MoSe_2$ flakes was tested in the reduction reactions of a number of nitroarenes, which were carried out in water at room temperature with $NaBH_4$ as the reducing agent. $NaBH_4$ is the reductant of choice for nitroarene reduction [68], being comparatively more stable and safer than other reductants, such as hydrazine, and, in contrast with other hydride-based reductants, such as $LiAlBH_4$ or silanes, compatible with aqueous medium [14], which is essential for its application in water treatment. Specifically, the following substrate molecules were tested: 2-nitrophenol (2-NP), 3-nitrophenol (3-NP), 4-nitrophenol (4-NP), 2-nitroaniline (2-NA), 3-nitroaniline (3-NA), 4-nitroaniline (4-NA) and nitrobenzene (NB). Such reactions are known to be thermodynamically downhill overall, but unless a proper catalyst is used, they cannot proceed at a significant rate at room temperature due to the presence of considerable kinetic barriers [68]. Furthermore, in all these cases the reaction progress was conveniently monitored by means of UV-Vis absorption spectroscopy. This was because the substrate molecules exhibit signature absorption bands at distinct wavelengths that are absent from their reduced counterpart (see Fig. S5 in section S3 of the SM for the corresponding absorption spectra). Hence, such bands can be used to follow the substrate concentration in the reaction medium on the basis of the Lambert-Beer law, thereby affording kinetic profiles where substrate concentration is plotted against reaction time [25,26]. However, in the present case, derivation of the actual reaction kinetic profiles required applying some corrections to the raw profiles that were obtained from the UV-Vis absorption measurements, where absorbance of the reaction medium at a given wavelength vs. time was recorded. The need for such corrections arose from the observation that the $MoSe_2$ nanosheets, which contributed to the absorbance of the reaction medium just like the substrate itself, sedimented slowly in the presence of $NaBH_4$. As a result, the raw kinetic profiles included a time-dependent contribution from the slowly declining absorbance of the catalyst, which had to be removed to arrive at the actual kinetic profile of the tested reaction. Sedimentation of the $MoSe_2$ nanosheets was most likely due to waning of their colloidal stability in the high ionic strength medium created by the reducing agent (charge neutralization) [65], but it was sufficiently slow so as not to compromise the measurement of their catalytic activity. A detailed account of these effects and the applied corrections is given in section S4 and Fig. S6 of the SM.

Fig. 3 shows actual kinetic profiles (i.e., substrate concentration vs. time) for the reduction of 2-NP, 3-NP, 4-NP and NB (panel a) as well as 2-NA, 3-NA and 4-NA (panel b). These plots do not include the so-called induction period, which was an initial section of constant concentration in the profiles, as it was removed for clarity. Such an induction period is typically observed with both metal-based and MoS_2 catalysts [25,68] and was also regularly seen here with the $MoSe_2$ nanosheets (see section S4 in the SM). Its origin has been related to conversion of the reaction products (i.e., anilines) back to the starting substrates (nitroarenes) as a result of their catalytic oxidation with oxygen molecules dissolved in the reaction medium [69]. It can be seen from Fig. 3 that a plateau at substrate concentration close to zero was reached upon reaction completion in all cases, indicating that essentially full conversion of the reactants was attained. Moreover, the reaction profiles seemed to follow non-linear decay functions, which revealed information on the reaction order and thus on the kinetics of these processes. To address this question in detail, we first note that the kinetic profiles measured for the catalytic reduction of nitroarenes generally obey either a first-order or a zero-order behavior with respect to the substrate concentration [25,26,68,70]. In other words, the profiles obey one of the two following rate equations:

First-order behavior (reaction order of 1) $$d[S]/dt = -k_1[S] \tag{1}$$

Zero-order behavior (reaction order of 0) $$d[S]/dt = -k_0 \tag{2}$$

, where [S] is the substrate concentration at time *t*, and k_1 and k_0 are the apparent reaction rate constants. Equations (1) and (2) do not explicitly incorporate the concentration of the other reactant (i.e., $NaBH_4$) on their right-hand side. Because the reducing agent was used in a very large excess compared to the amount of substrate, its concentration could be reasonably assumed to remain constant during the reduction reaction, and so the corresponding term was implicitly included in the rate constants (rigorously speaking, we should use the terms pseudo-first-order and pseudo-zero-order). Further, these equations indicate that the kinetic profiles of first-order and zero-order reactions are described by exponential and linear decay functions, respectively. Therefore, to determine which of these two reaction orders best replicated the actual reduction kinetics of the substrate molecules, we fitted their measured kinetic profiles to both exponential and linear decay functions, and determined their corresponding regression coefficient (R^2) as an indicator for the quality of the fit. The results are shown in Fig. 3c and d for the exponential and linear fits, respectively. Overall, exponential decay functions reproduced the experimental profiles better than their linear counterparts, with R^2 values of 0.952-0.999 compared to 0.823-0.995 for the linear fits.

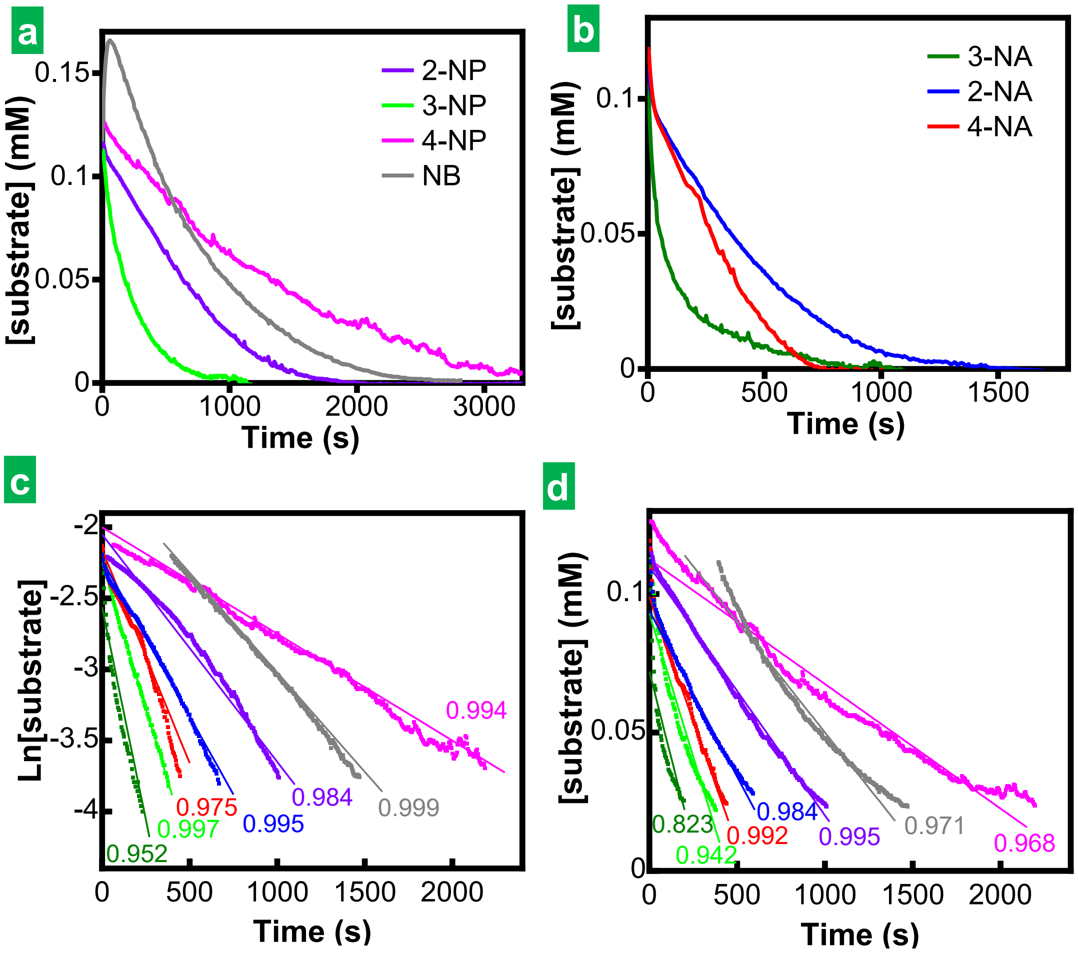

Figure 3. MoSe$_2$ nanosheets as catalysts for nitroarene reduction. (a) Substrate concentration vs. time for the reduction of 2-NP (violet trace), 3-NP (light green), 4-NP (magenta) and NB (gray) **(b)** as well as 2-NA (blue trace), 3-NA (green) and 4-NA (red) using exfoliated MoSe$_2$ as catalyst. Fitting of the kinetic profiles in (a) and (b) to **(c)** exponential and **(d)** linear decay functions using the same color code with indication of the corresponding regression coefficients (R^2).

The kinetic behaviors observed here with the 2D MoSe$_2$ catalyst differed from those recently reported for MoS$_2$ nanosheets functionalized with acetic acid groups, where a correlation between reaction order and net electric charge of the substrate in the reaction medium was noticed overall [26]. More specifically, negatively charged (electrically neutral) substrate molecules tended to exhibit first (zero) order kinetics. Such trends were rationalized by assuming that the reaction rate was heavily influenced by the rate of diffusion of the substrate molecules to the active sites on the surface of the catalyst.

Negatively charged molecules would experience a substantial electrostatic repulsion barrier when approaching the surface of the acetic acid-functionalized MoS_2 nanosheets (zeta potential of about -40 mV at a pH similar to that of the reaction medium, i.e., 10–11, and -25 mV at pH 4), and so their diffusion to the catalytic active sites would be significantly restricted. As a result, the corresponding reduction rates can be expected to be directly proportional to the substrate concentration [equation (1)], giving first-order kinetics. On the other hand, no electrostatic repulsion barriers would be in place for neutral molecules, so their unrestricted access to the catalytic active sites could easily make the latter to become saturated. Hence, the corresponding reduction rates would be essentially independent of substrate concentration [equation (2), zero-order kinetics]. However, this interpretation did not hold for the present $MoSe_2$ nanosheets, because 2-NP, 3-NP and 4-NP were negatively charged in the reaction medium (pK_a values around 7–8, i.e., these species were in the form of nitrophenolates), whereas 2-NA, 3-NA, 4-NA and NB were electrically neutral (pK_a values of the conjugate acids of the nitroanilines below 3) [71], but all the substrate molecules exhibited a similar kinetic behavior (i.e., first-order kinetics). Here, it is reasonable to argue that the overall negative charge on the $MoSe_2$ nanosheets is too small (zeta potential less negative than that of acetic acid-functionalized MoS_2) to sustain any substantial repulsion barrier against negatively charged molecules. Hence, essentially unrestricted access to the active sites would be expected with any substrate molecules, regardless of their net electrical charge. Nevertheless, this should have led to zero-order kinetics for both negatively charged and neutral substrates, but not to the first-order behavior that was actually observed with the $MoSe_2$ catalyst. Clearly, other factors should be contributing decisively to the kinetics of the latter besides the rate of diffusion of the substrate molecules to the catalytic active sites.

With the aim of shedding light on this issue, the kinetic profiles of nitroarene reduction were also recorded using, as the catalyst, the MoS_2 nanosheets prepared here in an analogous way to the $MoSe_2$ flakes. Remarkably, the measured profiles (Fig. 4a and b) were all seen to be clearly linear with this MoS_2 catalyst. Such a conclusion was quantitatively supported by the corresponding fits, which were rather good (R^2 values of 0.992-0.998) for the linear decay fits, but very poor (R^2 values of 0.962-0.988) for their exponential counterparts. This would be indeed the expected result for a MoS_2 catalyst that displays a fast diffusion of substrate molecules to the active sites, as discussed above, and therefore where such diffusion is not restricted by electrostatic barriers. Considering that the overall negative charge of the present MoS_2 flakes was substantially smaller than that of the acetic acid-functionalized nanosheets, the kinetic behaviors observed for these two types of 2D MoS_2 catalyst were totally consistent with each other. However, both the MoS_2 and $MoSe_2$ nanosheets prepared here were similarly charged in aqueous medium (similar zeta potential values), but their kinetic behaviors clearly differed. This observation suggested again that substrate diffusion to the active sites could not be the only determinant factor of the behavior noticed for the $MoSe_2$ catalyst. As discussed in the following, we believe that such kinetic discrepancies between $MoSe_2$ and MoS_2 arise from differences in the intrinsic activity of their catalytic sites.

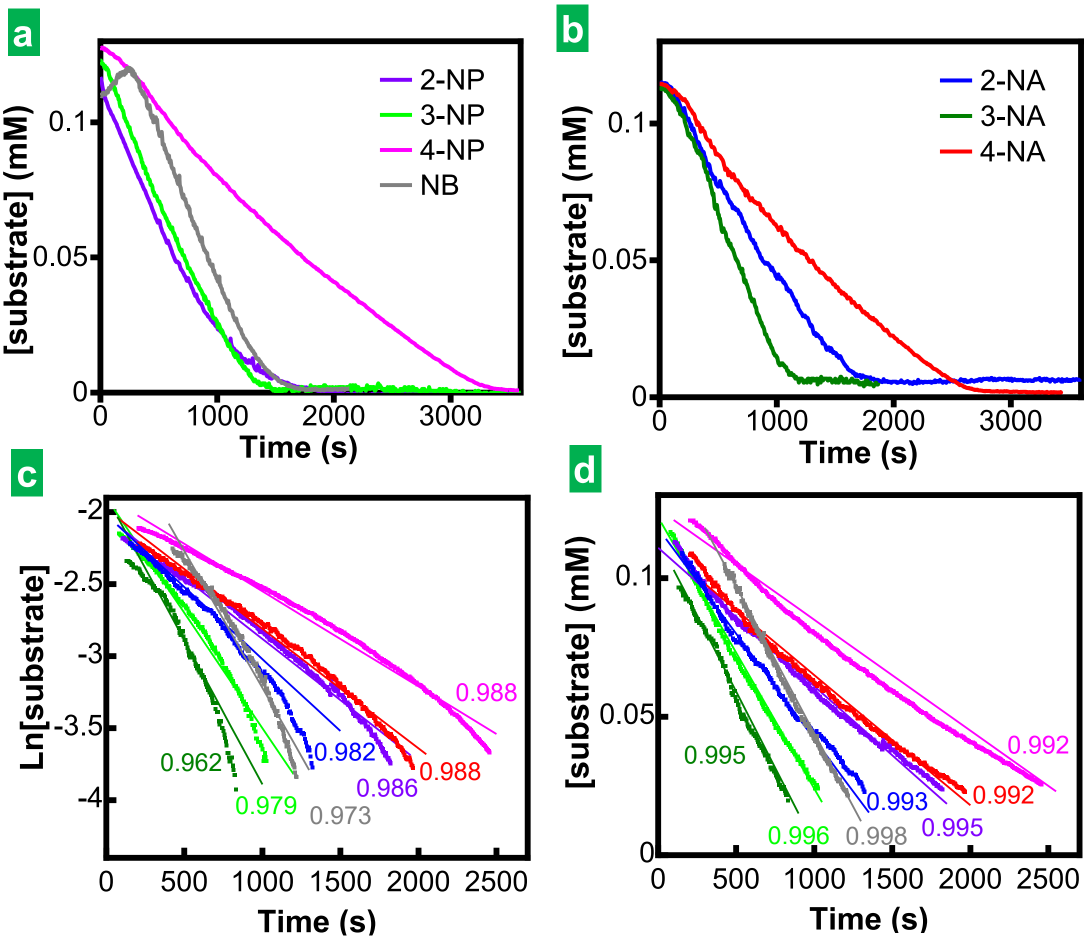

Figure 4. MoS_2 nanosheets as catalysts for nitroarene reduction. (a) Substrate concentration vs. time for the reduction of 2-NP (violet trace), 3-NP (light green), 4-NP (magenta) and NB (gray) **(b)** as well as 2-NA (blue trace), 3-NA (green) and 4-NA (red) using exfoliated MoS_2 as catalyst. Fitting of the kinetic profiles in (a) and (b) to **(c)** exponential and **(d)** linear decay functions using the same color code with indication of the corresponding regression coefficients (R^2).

3.3. Rationalizing the kinetic behavior of nitroarene reduction with $MoSe_2$ and MoS_2 catalysts

To rationalize the factors that govern the kinetic behavior of nitroarene reduction with the TMD catalysts, we note that the reaction rate (i.e., $d[S]/dt$) can be regarded to be proportional to the degree of surface coverage of the catalytic active sites by both the substrate, $\theta_s(t)$, and the reducing agent, $\theta_r(t)$, based on a Langmuir-Hinshelwood analysis [70]. Because the amount of $NaBH_4$ was much larger than that of the nitroarenes and its concentration could be assumed to remain constant throughout the reaction, to a first approximation $\theta_r(t)$ was also assumed to be constant with time. On the other hand, $\theta_s(t)$ was expected to depend mainly on two factors: (i) the rate of diffusion of the substrate molecule to the active site for adsorption, and (ii) the rate at which the substrate molecule adsorbed at the active site is converted to its corresponding product and the product is desorbed from the active site. More specifically, and for the sake of simplicity of the argument, factor (i) can be associated to a characteristic time, t_{unocc}. This can be seen as the time it takes for an active site to be occupied again by a substrate molecule after the reaction product from a previous reaction desorbs from that active site. The higher the diffusion rate of the substrate molecules to the active sites, and particularly the higher their concentration in the reaction medium, the shorter t_{unocc} should be. In turn, factor (ii) can be associated to a characteristic time t_{occ}, which would be the time it takes for the adsorbed substrate molecule to be converted to the reaction product plus the time it takes for the reaction product to desorb from the active site. Here, the higher the efficiency of the active sites in churning out reaction products, the shorter t_{occ} should be. Then, $\theta_s(t)$ would be dictated by t_{unocc} and t_{occ} through the following relation:

$$\theta_s(t) \propto \frac{t_{occ}}{t_{occ}+t_{unocc}} \qquad (3)$$

From equation (3), we can make some predictions about the determinants of the reaction order for nitroarene reduction with the different TMD catalysts. First, if access of the substrate molecules to the active sites is essentially unrestricted (i.e, very fast) and the reaction is limited by the substrate-to-product conversion and/or product desorption, then $t_{occ} \gg t_{unocc}$ for most of the reaction (this inequality could not hold anymore after most of the substrate has been consumed). Hence, $\theta_s(t)$ and the reaction rate should be largely constant in time, yielding zero-order kinetics. We infer that such a situation applied in the case of the MoS_2 flakes prepared here (Fig. 4). We note that the fitting of the kinetic profiles in Figs. 3 and 4 were done below 80 % substrate conversion, excluding the final stretch, where zero-order kinetics would not hold. Second, a different scenario could be envisaged for a MoS_2 catalyst where the value of t_{occ} was essentially the same as that of the previous case (i.e., same material and thus same type of active sites), but where t_{unocc} was comparable in magnitude to t_{occ} due to a substantial barrier to diffusion of the substrate molecules to the catalyst. In this case, $\theta_s(t)$ and the reaction rate would both decrease (in absolute value) as the reaction progressed, because t_{unocc} would become progressively larger relative to t_{occ} as the substrate was being consumed. This situation would be compatible with a first-order reaction and was that observed for the acetic-acid functionalized MoS_2 nanosheets in the reduction of negatively charged nitroarenes. Third, for the present $MoSe_2$ nanosheets it is reasonable to asume that substrate diffusion to the active sites was unrestricted, yielding t_{unocc} values similar to those of their MoS_2 counterpart (both TMDs prepared here displayed very similar zeta potential values). If t_{occ} for $MoSe_2$ were also similar to that of MoS_2, then the former catalyst would be expected to exhibit zero-order kinetics as well in the reduction of nitroarenes. However, this was not the case and first-order kinetics was observed instead (Fig. 3). In consequence, for $MoSe_2$ to exhibit first-order behavior, we have to assume that its t_{occ} values were substantially smaller than those of MoS_2, which in turn implies that the catalytic sites of $MoSe_2$ are intrinsically more active than those of MoS_2. It should be noted that in this discussion t_{unocc} and t_{occ} are not uniquely defined quantities, because the processes they describe are obviously stochastic in nature and, therefore, should be better characterized by a distribution of time intervals where such processes can occur. However, the essence of the physicochemical factors that dominate the catalyzed reactions could already be captured by this simplified treatment. Indeed, a more rigorous treatment involving the rate constants of the individual processes, i.e., substrate adsorption onto the active site, substrate conversion to product and product desorption, led to similar conclusions (see section S5 in the SM).

To test the prediction that $MoSe_2$ nanosheets are intrinsically more efficient as nitroarene reduction catalysts than their MoS_2 counterpart, their catalytic activities were quantitatively compared. Such activities were evaluated in terms of moles of substrate converted per unit time per mole of TMD catalyst. We note that the catalytic sites are thought to be associated to coordinatively unsaturated molybdenum atoms located at structural defects in the TMD lattice, such as edges and chalcogen vacancies [25,29,33].

The presence of chalcogen vacancies as an intrinsic feature of both natural and synthetic TMDs is a result of their relatively low formation energy (~2 eV [72]), while the primary cause of their formation lies in solid-gas phase thermodynamic equilibrium, which both the chalcogen and the Mo element tend to reach [72]. Owing to the higher saturated vapor pressure of the chalcogen atom, both MoS_2 and $MoSe_2$ release more chalcogen than Mo atoms into the gas phase and thus the chalcogen is prone to be deficient in the corresponding TMD [72]. In the case of MoS_2, the role of the chalcogen vacancies as catalytically active sites has been explicitly shown by purposefully generating sulfur surface vacancies in the lattice and measuring faster reaction rates in the resulting modified catalysts [25]. To demonstrate that the same behavior also applied in the case of the $MoSe_2$ nanosheets, selenium vacancies were generated in the latter via a reductive treatment with hydrazine (see Experimental section). The increased fraction of coordinatively unsaturated molybdenum atoms in the $MoSe_2$ lattice was confirmed by electron paramagnetic resonance (EPR) spectroscopy. Fig. 5a (black trace) shows the EPR spectrum of the starting bulk $MoSe_2$ powder, which already exhibited a non-negligible signal at a magnetic field of ~3150 G [73,74] that indicated the presence of a certain amount of edges and vacancies in this material. After exfoliation of the bulk powder into nanosheets, a significantly stronger EPR signal was recorded (red trace in Fig. 5a), which most likely reflected the increased fraction of edges with unsaturated atoms in the $MoSe_2$

material that resulted from its downsizing. Upon hydrazine treatment, a further increase in the EPR signal was noticed (blue trace), which could be ascribed to new unsaturated molybdenum centers generated with the selenium vacancies. As anticipated, the catalytic activity of the hydrazine-treated $MoSe_2$ nanosheets was enhanced compared to that of their untreated counterpart. Such an enhancement became apparent by comparing the corresponding kinetic profiles for different nitroarene reduction reactions (Fig. 5b; dotted traces: untreated nanosheets; solid traces: hydrazine-treated nanosheets), where the hydrazine-treated catalyst clearly afforded faster reduction rates.

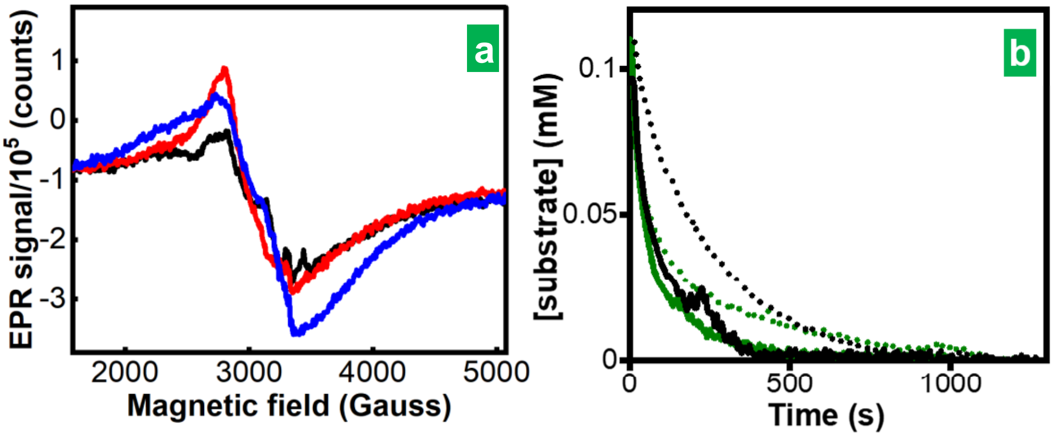

Figure 5. Characterization of the hydrazine-treated $MoSe_2$ nanosheets. (a) EPR spectrum of the starting bulk $MoSe_2$ powder (black trace), and exfoliated $MoSe_2$ as obtained (red trace), and after hydrazine treatment (blue trace). **(b)** Kinetic profiles for 3-NA (black traces) and 3-NP (green traces) reduction reactions catalyzed by untreated (dotted traces) and hydrazine-treated $MoSe_2$ flakes (solid traces).

Table 1 compares the catalytic activities of the $MoSe_2$ and MoS_2 nanosheets for the different nitroarene reduction reactions, relative to the number of moles of TMD catalyst in the reaction medium. The catalytic activity values, which were calculated at 80 % of substrate conversion, were in general substantially higher for the $MoSe_2$ nanosheets, demonstrating that this TMD outperformed MoS_2 as a nitroarene reduction catalyst. Further indication of the higher efficiency of $MoSe_2$ in these reactions was obtained from the observation of shorter induction periods with this catalyst compared to MoS_2 (see Fig. S7 in section S6 of the SM). As the induction period is related to consumption of oxygen dissolved in the reaction medium by catalytic oxidation of the reduced products (i.e., anilines) back to the starting substrates (nitroarenes) [69], a higher turnover rate of reduction products at the active sites of the TMD catalyst should imply a faster consumption of the dissolved oxygen and thus a shorter induction period.

Table 1. Comparison of the catalytic activities of the $MoSe_2$ and MoS_2 nanosheets for the different nitroarene reduction reactions relative to the number of moles of TMD catalyst in the reaction medium. The values are calculated at 80 % of substrate conversion.

substrate	$MoSe_2$ (h^{-1})	MoS_2
2-NP	6.4	2.2
3-NP	15.6	4.0
4-NP	3.0	1.7
2-NA	5.5	2.9
3-NA	15.4	4.1
4-NA	8.8	1.9
NB	4.2	3.0

While working with bare TMD flakes in water was useful to compare their intrinsic catalytic activity, this was not the optimal preparation to maximize their performance. In fact, we note that the current research was not focused on finding unprecedented catalytic activities per se, but on providing a rational framework to understand the differences between TMD catalysts. However, it is to be expected that the underlying higher intrinsic activity of $MoSe_2$ will lead to better catalytic performances than those of MoS_2 applying similar preparation protocols to both TMDs. In fact, just by a simple treatment with hydrazine (see Fig. 5b), the catalytic activities of $MoSe_2$ for 3-NP and 3-NA reduction approximately doubled (~30 h^{-1}), yielding activity values which are competitive for non-noble metal catalysts [25,26].

As regards the origin of the higher catalytic activity of $MoSe_2$, there are in principle two possibilities that could account for it. The first one concerns the adsorption of the nitroarenes on the active sites of the catalyst. For MoS_2 and other catalysts, it has been shown that the strength of adsorption of the nitroarenes and their intermediate products determines the magnitude of the reaction kinetic barriers and, therefore, the turnover rate of reduction products [75,76]. Because the adsorption strength of nitroarenes at the active sites of $MoSe_2$ and MoS_2 can be expected to differ somewhat as a result of their slightly different chemical nature, the turnover rates afforded by the two catalysts should also differ. While this possibility cannot be ruled out, we note that the higher activity of $MoSe_2$ was not restricted to the reduction of nitroarenes, but also included the reduction of species other than the nitro group. For example, the reduction of methyl orange and the hexacyanoferrate anion was faster with the $MoSe_2$ nanosheets than with their MoS_2 counterpart (Fig. S8 in section S7 of the SM), suggesting that the distinct performance of the two catalysts was dictated by more general factors that do not involve the specifics of the substrate molecules.

The second possibility is thus not related to the substrate molecule itself, but to the other reagent taking part in the reaction, namely, the reducing agent $NaBH_4$ and more specifically the hydride ion (H^-). We have recently proposed that nitroarene reduction by $NaBH_4$ with MoS_2 catalysts proceeds via hydrolytic decomposition of the BH_4^- anion to give hydride ions [25]. The generated H^- species are stabilized at coordinatively unsaturated molybdenum atoms present at sulfur vacancies and edges (but not on the pristine basal surface of the MoS_2 lattice) [77], where they become available for transfer to nitroarene molecules adsorbed at nearby sites, triggering their sequential reduction [25]. Because the stabilization of the hydride ion on the unsaturated molybdenum centers implies the reduction of such centers, it is reasonable to argue that the higher the propensity of these molybdenum centers to be reduced, the higher the abundance of hydrides on the TMD surface available for nitroarene reduction. As a result, higher turnover rates of reduction products should be expected. In turn, the reducibility of the active molybdenum centers should be modulated by their chemical environment, and particularly by the electronegativity of the chemical species bound to the molybdenum atoms. More specifically, the lower the electronegativity of such chemical species, the higher the propensity of the molybdenum centers to be reduced. Considering that selenium is less electronegative than sulfur, we infer that hydrides are more abundantly formed on the molybdenum centers of $MoSe_2$ compared to those of MoS_2, leading to a higher catalytic activity in the former TMD.

The above interpretation of the role of hydrides in nitroarene reduction with $MoSe_2$/MoS_2 catalysts is supported by very recent work on the electrocatalytic activity of molybdenum-based materials (oxides, sulfides, alloys, etc) toward the HER [78]. Such an activity was also concluded to rely on the generation of hydrides at reducible Mo^{4+} centers present on exposed locations of the material, such as sulfur vacancy defects in the case of molybdenum sulfides. Moreover, a negative correlation between the electronegativity of the chemical species bound to molybdenum and the HER activity was found, suggesting that propensity toward hydride formation is heavily influenced by the reducibility of the Mo^{4+} sites. As a proxy for electronegativity of the partner chemical species, the binding energy of Mo^{4+} 3d electrons determined by XPS was used (higher binding energy indicating higher electronegativity). In our case, the lower electronegativity of selenium in $MoSe_2$ relative to sulfur in MoS_2 was confirmed by the lower binding energy of the Mo^{4+} 3d electrons in the former TMD (compare Figs. 2a and S3a, further details are given in the text in section S1 in the SM), thus pointing to a higher propensity of the active molybdenum centers in $MoSe_2$ toward the formation of hydrides. While molybdenum selenides were not specifically included in that HER work (only sulfides were contemplated among the chalcogenides) [78], it is known from other studies that $MoSe_2$ is more active than MoS_2 as HER electrocatalyst [79,80], thus agreeing with the proposed interpretation. A schematic representation of the different propensities of $MoSe_2$ and MoS_2 to form hydrides on their active molybdenum centers, leading to different catalytic activities for nitroarene reduction, is shown in Fig. 6. We also note that this interpretation provides a rationale to understand the higher catalytic activity toward nitroarene reduction that has been reported for 1T-phase MoS_2 nanosheets relative to their 2H-phase counterpart [13,21,24]. Because the octahedral coordination of the metal in the 1T phase leads to a binding energy of the Mo^{4+} 3d electrons lower than that of the 2H phase (trigonal prismatic coordination) [13], the active molybdenum centers in the former should be more easily reducible, thus giving rise to a higher abundance of hydrides and so to a higher catalytic activity.

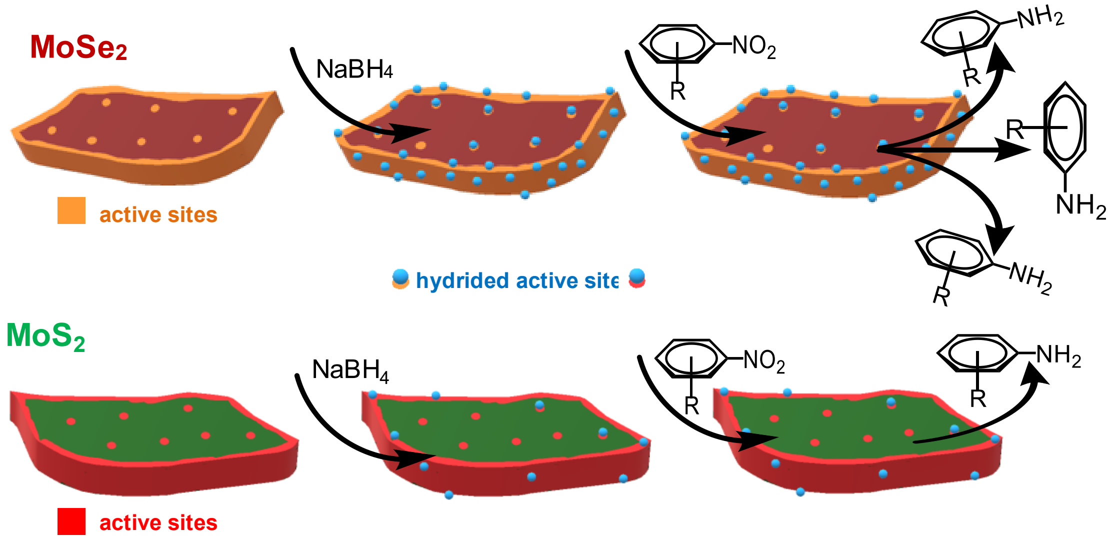

Figure 6. Different propensities of $MoSe_2$ and MoS_2 nanosheets to form hydrides. Schematic representation of $MoSe_2$ and MoS_2 nanosheets and their different propensities to form hydrides on their active sites (chalcogen vacancies and edges), leading to different catalytic activities for nitroarene reduction.

It is noteworthy that nitroarene reduction in the presence of $MoSe_2$ did not show any progress when reductants such as hydrazine monohydrate or ascorbic acid (vitamin C), which involve the generation of hydrogen rather than hydrides, were used. Most probably, as suggested by previous reports [29,31], higher hydrogen pressures would be required for catalytic transfer hydrogenation to occur in significant extent.

3.4. Computational insight into the catalytic activity trends of $MoSe_2$ toward nitroarene isomers

The observed differences in catalytic activity between $MoSe_2$ and MoS_2 toward the investigated reduction reactions were largely attributed, as discussed above, to the distinct availability of reducing hydrides on the surface of these two TMDs. However, we also observed differences in the reduction rate of different nitroarenes, and particularly different isomers of a given nitroarene, with the same TMD catalyst. This was especially the case of the nitroaniline isomers with $MoSe_2$ (Fig. 3b), where the reduction rate of 3-NA was measured to be about significantly (~2-3 times) faster than that of both 2-NA and 4-NA. Obviously, differences in hydride availability could not be invoked to explain this result, which most likely is originated from the specifics of isomer adsorption at the catalytic active sites of $MoSe_2$. Therefore, to shed light on this issue, we explored by means of DFT calculations the adsorption of 2-NA, 3-NA and 4-NA on the active sites of the catalyst, modeled as unsaturated molybdenum centers associated to selenium vacancies. Models with one selenium vacancy ($1V_{Se}$) and four selenium vacancies ($4V_{Se}$) per supercell were considered (see Experimental section for details of the calculations). In the $4V_{Se}$ model, the missing atoms were not adjacent to each other in the selenium atomic plane, but rather second nearest neighbors. Following a prior study of 3-nitrostyrene adsorption on the active sites of WS_2 [33], three configurations of adsorbed nitroanilines were analyzed, which were referred to as *vertical1* (nitro group over a vacancy), *vertical1b* (amino group over a vacancy) and *horizontal* (nitroaniline molecule parallel to the TMD surface). Each adsorption configuration was used for each of the three nitroaniline isomers. Graphical representations of the optimized geometries for 3-NA on the $1V_{Se}$ model are shown in Fig. 7 (a: *vertical1*; b: *vertical1b*; c: *horizontal*). The calculated adsorption energies, E_{ads}, for the three isomers on the $1V_{Se}$ and $4V_{Se}$ models are shown in Fig. 7d. E_{ads} values were calculated as E_{ads} = E(molecule-surface) – E(surface) – E(molecule).

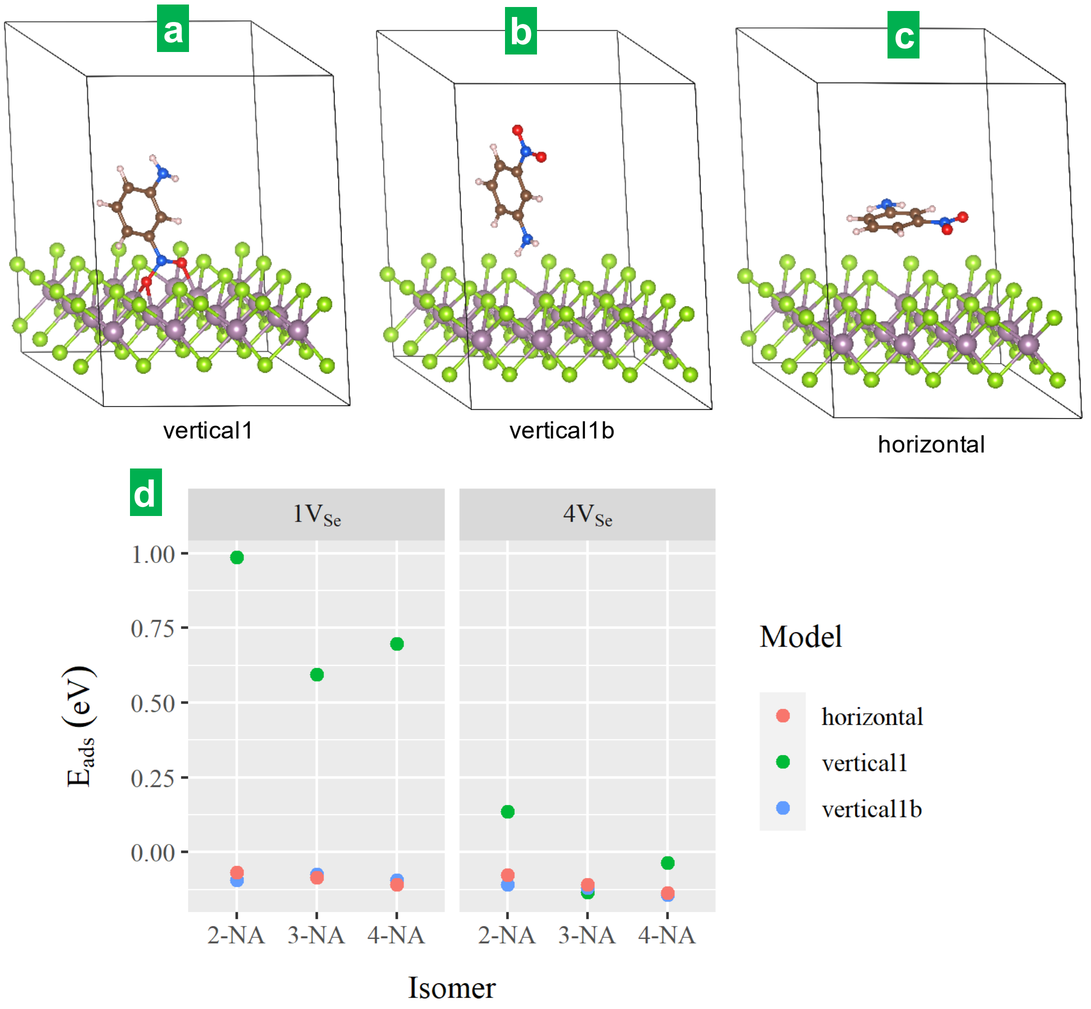

Figure 7. Energies for the adsorption of the three structural isomers of nitroaniline (NA) on $MoSe_2$ catalyst calculated for different adsorption geometries. (a-c) Graphical representation of the three studied adsorption geometries, designated as: (a) *vertical1*, (b): *vertical1b*; (c) *horizontal*. Calculated adsorption energies for the three structural isomers of nitroaniline on $MoSe_2$ catalyst with one ($1V_{Se}$) and four selenium vacancies ($4V_{Se}$) per supercell and for the three adsorption geometries shown in (a-c).

For the $1V_{Se}$ case, adsorption was favored for the *horizontal* and *vertical1b* configurations, with E_{ads} values around −0.10 eV, but not for the *vertical1* configuration (E_{ads} in the range of 0.5-1 eV). For the $4V_{Se}$ model, adsorption was favored for the three isomers in the three configurations, except in the *vertical1* configuration for 2-NA. Indeed, the most notable changes observed in this model relative to its $1V_{Se}$ counterpart corresponded to the *vertical1* configuration, which in the case of 3-NA made it to be the most energetically stable. Moreover, the *vertical1* configuration was the only one that led to $MoSe_2$-molecule distances (specifically, molybdenum-oxygen distances) short enough so as to consider the adsorption process a chemisorption. On the other hand, in the other two configurations the molecules remained practically unchanged, so the adsorption process was classified as a physisorption. In the *vertical1* configuration, one of the oxygen atoms from the nitro group bound to two unsaturated molybdenum atoms from the vacancy, while the other oxygen atom bound to a third unsaturated molybdenum, with the three metal atoms forming a triangle. The nitro group could be then considered to act as a μ_3 bridging ligand by way of μ_2 + μ oxygens. The oxygen-molybdenum and oxygen-nitrogen distances in the adsorbed complex were in the 2.13-2.31 Å and 1.31-1.41 Å range, respectively. The $4V_{Se}$ model afforded in general longer oxygen-molybdenum distances and shorter, more symmetrical oxygen-nitrogen bonds than those of the $1V_{Se}$ model. Interestingly, the carbon-nitrogen bond distance was also shorter in the $4V_{Se}$ case. That is, higher vacancy densities greatly improved the adsorption energetics of the *vertical1* configuration not because of stronger (shorter) $MoSe_2$-molecule bonds, but by allowing stronger bonding in the nitro group within the molecule. This led to a better energetic balance between the $MoSe_2$-molecule and the intramolecular interactions.

Because clustered chalcogen vacancies in TMDs are generally more stable than isolated, single vacancies [81,82], the $4V_{Se}$ model was regarded as a more realistic representation of the active sites of $MoSe_2$ than the $1V_{Se}$ model. Moreover, selenium vacancies in very close proximity to each other would be needed to secure a supply of reducing hydrides to a nitroarene molecule adsorbed at a given vacancy site. Thus, if we consider the average adsorption energies for the three configurations in $4V_{Se}$ (see Fig. 7d), we conclude that adsorption should be favored for 3-NA compared to the other two isomers. Such a preference of the active sites toward 3-NA was even more apparent when considering the *vertical1* configuration alone. The latter is expected to be the most favorable configuration for reduction of the nitroaniline, as the nitro group would be particularly accessible to nearby adsorbed hydrides. As a result of this, we would expect the reduction of 3-NA to be the fastest among the three nitroaniline isomers, which agrees with the experimental observations (Fig. 3b). We note that the slightly higher propensity of 3-NA to chemisorb at the selenium vacancies was largely due to energy differences between the nitroaniline isomers as isolated molecules, i.e., without taking their interaction with $MoSe_2$ into account. Specifically, 2-NA and 4-NA are more stable than 3-NA owing to the extra delocalization of the amino lone pair over the nitro group in the resonance hybrid, and this implied an energy penalty when the former two isomers were adsorbed on the vacancy-decorated TMD surface. Still, a difference in adsorption strength between 2-NA and 4-NA was noticed in Fig. 7d (more favorable for 4-NA), which was actually reflected in the experimental results (Fig. 3b). This difference comes from the close proximity of the nitro and amino groups in 2-NA, which provides extra stabilization of the isolated molecule resulting from intramolecular hydrogen bonding. Such an extra stabilization could in principle be compensated for upon adsorption of 2-NA if both the nitro and amino groups, and not just the nitro group, were able to efficiently interact with unsaturated molybdenum atoms from selenium vacancies. However, in the $4V_{Se}$ model the selenium vacancies were not strictly adjacent to each other, which made the simultaneous adsorption of both chemical groups difficult, due to steric hindrance. Therefore, to explore this possibility, we calculated the adsorption energy of 2-NA on a $MoSe_2$ model with adjacent vacancies, specifically, two double vacancies per supercell (to preserve a total of four missing selenium atoms as in the case of $4V_{Se}$) (see Figs. S9a and S9b, section S8, of the SM). As anticipated, the double vacancies allowed for the simultaneous adsorption of the nitro and amino groups while preserving the intramolecular hydrogen bond, with the corresponding configuration being referred to as *vertical1c* (see Fig. S9c, section S8, of the SM). The calculated E_{ads} value for this 2-NA configuration was very close to that of the *vertical1* configuration for 4-NA in the $4V_{Se}$ model (see Fig. S9d), and still lower than that of 3-NA. However, we note that, at least in the case of MoS_2, adjacent vacancies are generally unstable and transform quickly into alternating patterns of chalcogen atoms and vacancies [83]. Thus, presumably *vertical1c* configuration will be unlikely, and *vertical1* configuration will determine the reaction progress, in agreement with the experimental observations.

To clarify the role of the catalyst, we also calculated the energies associated to the reaction intermediates for the reduction of 3-NA along a mechanism similar to that proposed by Bae *et al* for 4-NP reduction by $NaBH_4$ with magnetite (111) surface as the catalyst [84]. Following their approach, we compared the energies of the different intermediates in the presence and absence of the catalyst. Initially, the following five steps were considered:

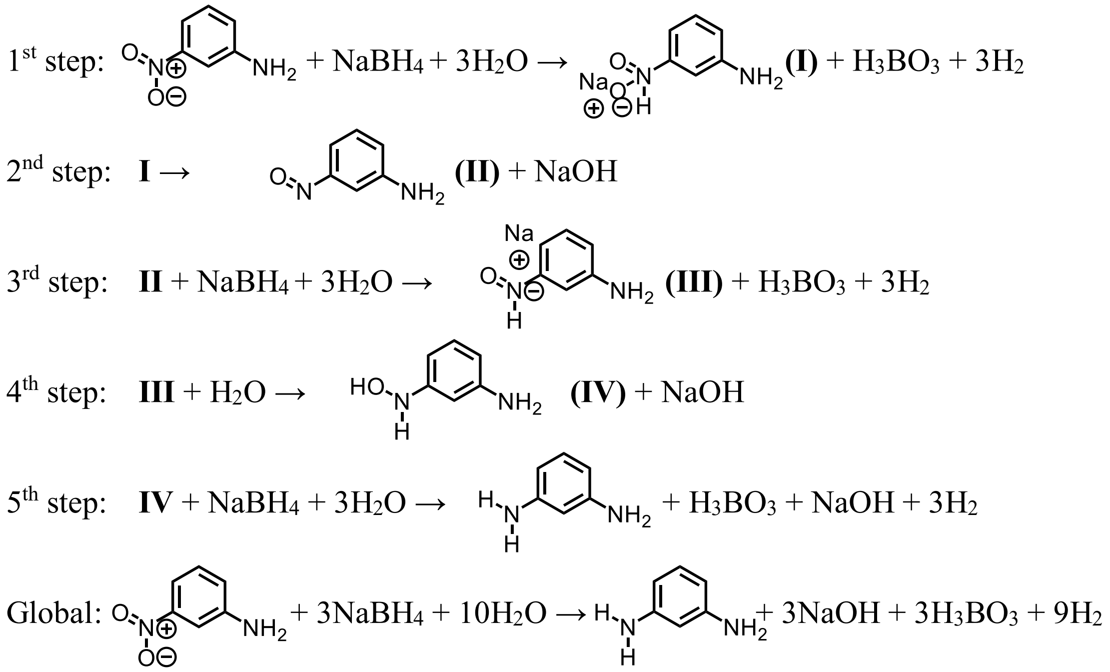

The intermediates **I-IV** described in the above equations were modeled and optimized with the same computational parameters as those of the reactant (3-NA). The energy of the other chemical species involved in the reactions ($NaBH_4$, H_2O, H_3BO_3, NaOH and H_2) was also calculated. The energies of the reactant, different intermediates and final diamine product (1,3-phenylenediamine) relative to that of the isolated 3-NA molecule that result from the above reaction steps are shown in Fig. 8a, both in the presence (red lines) and absence (blue lines) of $MoSe_2$. In this plot, the energy difference between both cases represents the adsorption energy of the different chemical species on the TMD surface. It should be noted that Fig. 8a depicts energy differences between hypothetical stable intermediates and not energy barriers associated to transition states. Likewise, although Bae *et al.* included a fifth intermediate in their calculations, which derived from attack of the hydroxylamino group in intermediate **IV** by a hydride, in our case such a fifth intermediate was not stable (neither the isolated molecule nor the $MoSe_2$-molecule complex). This could be rationalized in terms of its Lewis structure, where an octet for the nitrogen was not achievable.

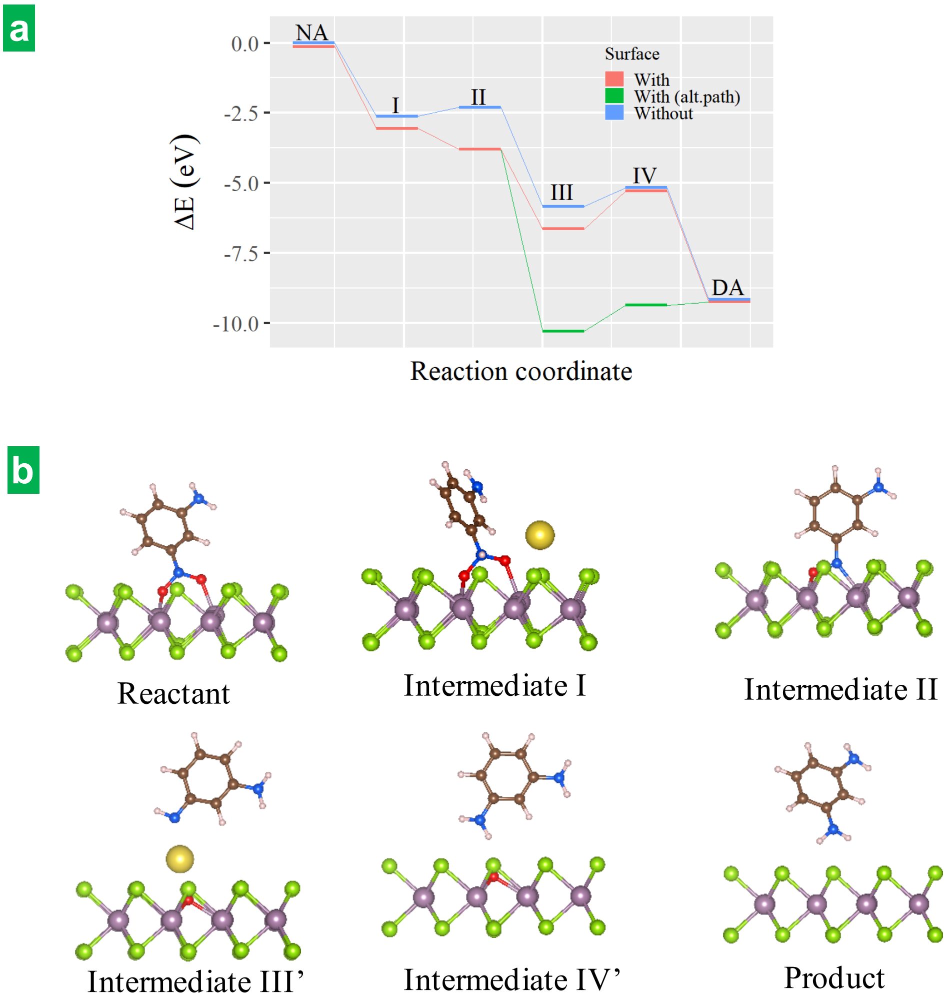

Figure 8. Energetics of the reaction in the absence and in the presence of $MoSe_2$ catalyst by different reaction mechanisms, including one originally proposed here. **(a)** Calculated energies of the reaction intermediates and the reaction product relative to that of isolated 3-NA in the presence (red lines) and absence (blue lines) of $MoSe_2$ along a mechanism similar to that proposed by Bae et al for 4-NP reduction by $NaBH_4$ with magnetite (111) surface as the catalyst [84]. Energies associated to the alternative reaction pathway suggested in this work (green lines). **(b)** Equilibrium geometries for the initial reactant, different intermediates and final diamine product along the latter reaction pathway.

In the first step of the reaction, a hydride attacked the nitrogen atom of 3-NA to give intermediate **I**, the negative charge of which was balanced by a nearby sodium cation. In the presence of $MoSe_2$, the two oxygen atoms retained their bonding to the unsaturated molybdenum atoms from a selenium vacancy, with little changes in the corresponding bond distances. However, for intermediate **II** (3-nitrosoaniline) there was a substantially increased bonding of the molecule to the TMD surface via the nitroso group, with oxygen-molybdenum and nitrogen-molybdenum distances of 2.16 and 2.12 Å, respectively. As a result, the adsorption energy for this intermediate was the greatest. Here, the selenium vacancy in $MoSe_2$ allowed for a deep vertical penetration of the nitroso group. In the third step, a second hydride attacked the nitroso group to give intermediate **III**, which led to a large overall stabilization of the system, both in the presence and absence of $MoSe_2$, and was associated to a significant adsorption energy with the TMD that mainly stemmed from interaction with the sodium cation. It is worth noting that the oxygen-molybdenum and nitrogen-molybdenum interactions disappeared in this intermediate, and it was the hydrogen atom from the NHO^- group that was pointing to the vacancy. In the fourth step, the oxygen from the NHO^- group captured a hydrogen from a nearby water molecule, yielding 3-hydroxylaminoaniline (intermediate **IV**). In this case, the stabilization of the system as a result of interaction with $MoSe_2$ was the lowest among all the intermediates, so that the corresponding adsorption energy was comparable to that of the reactant and final product. Again, interaction of unsaturated molybdenum atoms with the oxygen and nitrogen from the hydroxylamino group was stymied by its hydrogen atoms. Lastly, a third hydride attacked the hydroxylamino group, yielding the final diamine product (fifth step). The feasibility of the proposed mechanism was experimentally supported by the detection of some of the reaction intermediates, namely, 3-nitroaniline (intermediate **II**) and 3-hydroxylaminoaniline (intermediate **IV**), by means of UHPLC/HR-MS (see section S9 in the SM).

Nonetheless, while the former can be considered the classical reaction pathway for reduction of the nitro group, we noticed that an energetically competitive, alternative pathway was possible on the $MoSe_2$ surface. Specifically, when the oxygen atom from intermediate **III** was pointing to the selenium vacancy of the TMD, the molecule dissociated spontaneously, resulting in the vacancy being passivated by the oxygen atom.

This suggested an alternative pathway for the third, fourth and fifth steps of the reaction, which could take place as follows:

Alt. 3rd step: $MoSe_2 + \mathbf{II} + NaBH_4 + 3H_2O \rightarrow$ [$MoSe_2$-O + 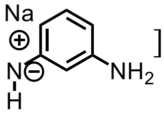] **(III′)** + H_3BO_3 + $3H_2$

Alt. 4th step: **III′** + $H_2O \rightarrow$ [$MoSe_2$-O + 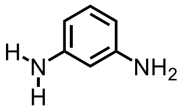] **(IV′)** + NaOH

Alt. 5th step: **IV′** + $NaBH_4 + 3H_2O \rightarrow MoSe_2$ + 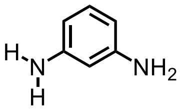 + H_3BO_3 + NaOH + $3H_2$

Here, $MoSe_2$-O denotes the TMD surface with a selenium vacancy filled by an oxygen atom. The energies associated to this alternative reaction pathway are given in Fig. 8a (green lines) and the corresponding equilibrium geometries for initial reactant, different intermediates and final diamine product are presented in Fig. 8b. In this third step, the N-O bond was broken upon hydride attack, leading to passivation of a selenium vacancy in $MoSe_2$ by the oxygen atom. In the resulting intermediate (**III′**), the sodium ion was located between the TMD surface and the negatively charged arene molecule. In the fourth step, reaction of intermediate **III′** with a water molecule yielded the final diamine product adsorbed on the passivated vacancy (intermediate **IV′**). Here, a hydrogen atom from the newly generated amino group was pointing to the vacancy-adsorbed oxygen in a plausible hydrogen bonding interaction (H-O distance of 2.18 Å). In the fifth step a hydride attacked the oxygen passivating the vacancy, which allowed regeneration of the latter. Finally, the target diamine product could readily desorb from the original, regenerated $MoSe_2$ surface. As the intermediates **III′** and **IV′** implied in this alternative mechanism are not isolable in solution, they could not be possibly detected by UHPLC/HR-MS. Their detection would probably require the use of a very sensitive, in situ characterization technique applicable to specimens in solid state, maybe even implying synchrotron radiation, which is out of the scope of this work. However, we note that the lack of experimental evidence of its intermediates does not preclude the actual occurrence of this or other energetically feasible pathways.

3.5. Colloidal stabilization and immobilization of the $MoSe_2$ nanosheet catalyst

While working with bare $MoSe_2$ flakes dispersed in water was useful to reveal their intrinsic catalytic activity, we note that the practical utility of the catalyst for water treatment under such conditions was limited due to the strictly time-bound colloidal stability of the bare flakes. To address this issue, the latter could be stabilized by means of proper dispersing agents (e.g., small molecules or polymers), but the adsorption of such chemical species on the surface of the nanosheets was likely to impact their catalytic performance, which therefore needed to be elucidated. Here, the bare exfoliated $MoSe_2$ flakes were stabilized with the aid of either a small molecule, namely, the nucleotide adenosine monophosphate (AMP), or a triblock polymer, i.e., Pluronic P123 [(poly(ethylene glycol)-*block*-poly(propylene glycol)-*block*-poly(ethylene glycol)]. Both compounds have been previously shown to be highly efficient as colloidal dispersants for TMD nanosheets [85,86]. Fig. 9a compares the reaction kinetic profiles obtained with the bare $MoSe_2$ flakes (black traces) with those recorded with the AMP- and P123-stabilized flakes (red and blue traces, respectively) for the reduction of 3-NA. As could be expected, slower reduction rates were seen for the catalyst stabilized with the (macro)molecular compounds. This was most likely the result of competitive adsorption of the reagent and the dispersant at the catalytic active sites of $MoSe_2$ [64]. However, we note that the decrease in catalytic activity of the colloidally stabilized nanosheets was not very drastic, which was positive with a view to their practical implementation. In contrast, the activity of the exfoliated MoS_2 nanosheets was seen to decrease to a larger degree after their colloidal stabilization by the same means (data not shown), resulting in much longer reduction times (as well as much longer induction periods). This highlighted once again the superiority of the 2D $MoSe_2$ catalyst over its MoS_2 counterpart.

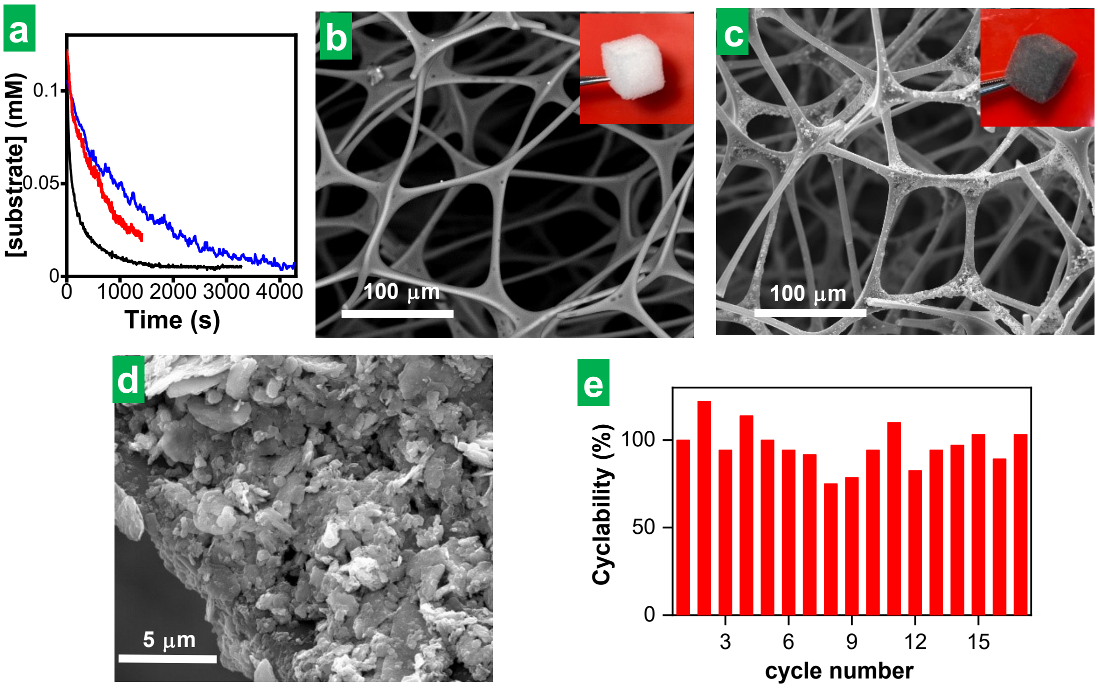

Figure 9. Colloidal stabilization and immobilization of the $MoSe_2$ catalyst (a) Kinetic profiles obtained with the bare $MoSe_2$ flakes (black traces) and with AMP- and P123-stabilized flakes (red and blue traces, respectively) for the reduction of 3-NA. FE-SEM images of **(b)** bare melamine foam and **(c,d)** $MoSe_2$-coated foam. Inset to c and d: digital photographs of the corresponding foams. **(e)** Reusability experiments of melamine foam-supported $MoSe_2$ flakes in the catalytic reduction of 3-NA with $NaBH_4$ ([3-NA] = 0.11 mM).

As an alternative to the use of colloidal dispersants, the bare $MoSe_2$ nanosheets could also be immobilized on a suitable polymeric scaffold, which facilitated the manipulation and re-use of the catalyst. For example, the nanosheets were supported onto melamine foam by a straightforward dip-coating process. Whereas the starting foam exhibited a white color together with a smooth and essentially featureless surface [see digital photograph (inset) and field emission scanning electron microscopy (FE-SEM) image in Fig. 9b], its $MoSe_2$-coated counterpart became gray-green and developed a rough surface (Fig. 9c). Closer inspection of the coated foam (Fig. 9d) revealed a film of $MoSe_2$ flakes covering the polymeric substrate. The melamine foam-supported flakes were able to catalyze the reduction of, e.g., 3-NA, as noticed from the discoloration of the reaction medium and the emergence of the signature absorption spectrum of the reaction product.

Further, they could be re-used for at least 15 consecutive reactions cycles without experiencing a substantial decline in activity (Fig. 9e), even if the foam was removed from the reaction medium, rinsed with water and finally squeezed to expel the water after each cycle. Additional information on the cycling of the catalyst is provided in section S10 of the SM. Specifically, the reaction conversion efficiency was evaluated for ten consecutive cycles and found to be consistent with ~100 % reaction conversion efficiency (Fig. S14a and accompanying text). Indeed, the characterization of the used catalyst by Raman and XPS spectroscopy (Figs. S14b-d of the SM) confirmed that its structural and chemical nature were preserved throughout the cycling process. Indeed, the Raman and XPS spectra of the cycled catalyst are very similar or even coincident within experimental error with those of the freshly prepared catalyst.

Apart from stablishing the practical utility of the $MoSe_2$ catalyst in the context of water remediation, the feasibility of its use as catalyst for synthetic applications was also confirmed by performing tests using a greater substrate concentration (1 mM) compatible with synthetic applications for some selected nitroarenes. NP was chosen as its reduction is essential in the pharmaceutical industry for the manufacture of analgesics and antipyretics, such as paracetamol [87], and other drugs, as well as for the manufacture of photographic developers, corrosion inhibitors, and anticorrosion lubricants [68]. 4-NA has also industrial relevance as a precursor to p-phenylenediamine though catalyzed reduction, which is the starting material for the synthesis of dyes [88]. As the mechanistic study in this work focuses on 3-NA reduction, testing it for synthetic applications as well was deemed necessary to offer a comprehensive study. The tests confirmed the feasibility of the use of $MoSe_2$ as a catalyst for synthesis given that the reduction of 4-NP, 4-NA, and 3-NA could be successfully carried out in larger substrate concentration as well (see Fig. S15 in section S11 of the SM).

4. Conclusions

An investigation of two-dimensional (2D) $MoSe_2$ nanosheets as a catalyst for the reduction of nitroarenes into their corresponding anilines has revealed this transition metal dichalcogenide (TMD) to be more active than its MoS_2 counterpart. This indicated that the traditional focus on the latter as the TMD catalyst of choice for such reactions is not justified from the perspective of performance, opening the prospect for a broader exploration of the family of TMD compounds toward water remediation. The experimental results indicated that nitroarene reduction was faster on the $MoSe_2$ nanosheets by a factor of about 1.5-4.5 compared to their MoS_2 counterpart. The reaction kinetic profiles recorded with different nitroarenes were also qualitatively different for the two TMDs, implying the occurrence of diverging reaction orders, more specifically, first order for $MoSe_2$ and zero-order for MoS_2 relative to the substrate molecule. A comparative analysis of the factors that can influence the kinetic behaviors observed for different TMD catalysts suggested that conversion of nitroarene molecules adsorbed at the active sites was much faster on $MoSe_2$ than it was on MoS_2. In line with recent understanding of the catalytic activity of molybdenum-based materials toward the hydrogen evolution reaction, such an outcome was interpreted to originate from the lower electronegativity of selenium relative to sulfur. This distinct electronegativity led to a higher reducibility of the catalytic active sites (unsaturated molybdenum centers) and thus to a higher availability of active reducing species (hydrides) on the active sites of $MoSe_2$ compared to MoS_2. Density functional theory studies yielded insight into the origin of the different catalytic activities that the $MoSe_2$ nanosheets exhibited toward different nitroarene isomers (e.g., 3-nitroaniline > 4-nitroaniline > 2-nitroaniline) and suggested a novel pathway for the catalyzed reduction of the nitro group that involved oxygen passivation and subsequent regeneration of the active sites of $MoSe_2$. Finally, we believe the present work provides a rational basis for the exploration and identification of TMDs beyond MoS_2 as enhanced catalysts for the reduction of nitroarenes and other organic compounds.

Acknowledgements

A. M. J. S. V.-R., J. M. M., J. I. P. gratefully acknowledge funding by the Spanish Ministerio de Ciencia e Innovación and Agencia Estatal de Investigación (MCIN/AEI/ 10.13039/501100011033) as well as the European Regional Development Fund (ERDF, A way of making Europe) through grant PID2021-125246OB-I00, and by Plan de Ciencia, Tecnología e Innovación (PCTI) 2018-2022 del Principado de Asturias and the ERDF through grant IDI/2021/000037. A. M. J. is grateful to the Spanish MINECO for his pre-doctoral contract (PRE2019-087583). The characterization of the graphene dispersions by DLS was performed at the ICTS NANBIOSIS by the Nanostructured Liquids Unit (U12) of the CIBER in Bioengineering, Biomaterials & Nanomedicine (CIBER-BBN), located at the IQAC−CSIC. M. A. S, P. P. and J. M. R. gratefully acknowledge funding by the Spanish Ministerio de Ciencia e Innovación and Agencia Estatal de Investigación (MCIN/AEI/10.13039/501100011033) as well as the European Regional Development Fund (ERDF, A way of making Europe) through grant PID2021-122585NB-C21, and by the Principado de Asturias and the ERDF through grant AYUD/2021/51036. We are very grateful to Dr. Alaa Adawy from the Laboratory of High-Resolution Transmission Electron Microscopy (Scientific and Technical Services, University of Oviedo) for her expert assistance with the HR-TEM and SAED measurements.

References

[1] D. Deng, K.S. Novoselov, Q. Fu, N. Zheng, Z. Tian, X. Bao, Catalysis with two-dimensional materials and their heterostructures, Nat. Nanotechnol. 11 (2016), 218-230.

[2] H. Jin, C. Guo, X. Liu, J. Liu, A. Vasileff, Y. Jiao, Y. Zheng, S.-Z. Qiao, Emerging two-dimensional nanomaterials for electrocatalysis, Chem. Rev. 118 (2018), 6337-6408.

[3] J. Di, J. Xiong, H. Li, Z. Liu, Ultrathin 2D photocatalysts: electronic-structure tailoring, hybridization, and applications, Adv. Mater. 30 (2018), 1704548.

[4] A. Kumar, Q. Xu, Two-dimensional layered materials as catalyst supports, ChemNanoMat 4 (2018), 28-40.

[5] L.X. Chen, Z.W. Chen, M. Jiang, Z. Lu, C. Gao, G. Cai, C.V. Singh, Insights on the dual role of two-dimensional materials as catalysts and supports for energy and environmental catalysis, J. Mater. Chem. A 9 (2021), 2018-2042.

[6] H. Yin, Y. Dou, S. Chen, Z. Zhu, P. Liu, H. Zhao, 2D electrocatalysts for converting earth-abundant simple molecules into value-added commodity chemicals: recent progress and perspectives, Adv. Mater. 32 (2020), 1904870.

[7] Q. Fu, X. Bao, Surface chemistry and catalysis confined under two-dimensional materials, Chem. Soc. Rev. 46 (2017), 1842-1874.

[8] J. Deng, D. Deng, X. Bao, Robust catalysis on 2D materials encapsulating metals: concept, application, and perspective, Adv. Mater. 29 (2017), 1606967.

[9] C. Zhu, D. Gao, J. Ding, D. Chao, J. Wang, TMD-based highly efficient electrocatalysts developed by combined computational and experimental approaches, Chem. Soc. Rev. 47 (2018), 4332-4356.

[10] X. Wu, H. Zhang, J. Zhang, X.W. Lou, Recent advances on transition metal dichalcogenides for electrochemical energy conversion, Adv. Mater. 33 (2021), 2008376.

[11] S. Jayabal, G. Saranya, J. Wu, Y. Liu, D. Geng, X. Meng, Understanding the high-electrocatalytic performance of two-dimensional MoS_2 nanosheets and their composite materials, J. Mater. Chem. A 5 (2017), 24540-24563.

[12] Z. Li, N.H. Attanayake, J.L. Blackburn, E.M. Miller, Carbon dioxide and nitrogen reduction reactions using 2D transition metal dichalcogenide (TMDC) and carbide/nitride (MXene) catalysts, Energy Environ. Sci. 14 (2021), 6242-6286.

[13] L. Guardia, J.I. Paredes, J.M. Munuera, S. Villar-Rodil, M. Ayán-Varela, A. Martínez-Alonso, J.M.D. Tascón, Chemically exfoliated MoS_2 nanosheets as an efficient catalyst for reduction reactions in the aqueous phase, ACS Appl. Mater. Interfaces 6 (2014), 21702-21710.

[14] M. Orlandi, D. Brenna, R. Harms, S. Jost, M. Benaglia, Recent developments in the reduction of aromatic and aliphatic nitro compounds to amines, Org. Process Res. Dev. 22 (2018), 430-445.

[15] A.C. Poulose, G. Zoppellaro, I. Konidakis, E. Serpetzoglou, E. Stratakis, O. Tomanec, M. Beller, A. Bakandritsos, R. Zbořil, Fast and selective reduction of nitroarenes under visible light with an earth-abundant plasmonic photocatalyst, Nat. Nanotechnol. 17 (2022), 485-492.

[16] H. Hu, J.H. Xin, H. Hu, X. Wang, D. Miao, Y. Liu, Synthesis and stabilization of metal nanocatalysts for reduction reactions – a review, J. Mater. Chem. A 3 (2015), 11157-11182.

[17] Z. Xiong, H. Zhang, W. Zhang, B. Lai, G. Yao, Removal of nitrophenols and their derivatives by chemical redox: a review, Chem. Eng. J. 359 (2019), 13-31.

[18] K. Zhang, J.M. Suh, J.-W. Choi, H.W. Jang, M. Shokouhimehr, R.S. Varma, Recent advances in the nanocatalyst-assisted $NaBH_4$ reduction of nitroaromatics in water, ACS Omega 4 (2019), 483-495.

[19] K. Peng, L. Fu, J. Ouyang, H. Yang, Emerging parallel dual 2D composites: natural clay mineral hybridizing MoS_2 and interfacial structure, Adv. Funct. Mater. 26 (2016), 2666-2675.

[20] A.A. Jeffery, S.R. Rao, M. Rajamathi, Preparation of MoS_2-reduced graphene oxide (rGO) hybrid paper for catalytic applications by simple exfoliation-costacking, Carbon 112 (2017), 8-16.

[21] K. Peng, L. Fu, H. Yang, J. Ouyang, A. Tang, Hierarchical MoS_2 intercalated clay hybrid nanosheets with enhanced catalytic activity, Nano Res. 10 (2017), 570-583.

[22] N. Meng, J. Cheng, Y. Zhou, W. Nie, P. Chen, Green synthesis of layered 1T-MoS_2/reduced graphene oxide nanocomposite with excellent catalytic performances for 4-nitrophenol reduction, Appl. Surf. Sci. 396 (2017), 310-318.

[23] Y. Li, Q. Chen, Z. Zhang, Q. Li, X. Qiao, Effects of morphology and crystallinity of MoS_2 nanocrystals on the catalytic reduction of *p*-nitrophenol, J. Nanopart. Res. 20 (2018), 327.

[24] C. Nethravathi, A.D. Manganahalli, M. Rajamathi, Bi_2Te_3-MoS_2 layered nanoscale heterostructures for electron transfer catalysis, ACS Appl. Nano Mater. 2 (2019), 2005-2012.

[25] S. García-Dalí, J.I. Paredes, B. Caridad, S. Villar-Rodil, M. Díaz-González, C. Fernández-Sánchez, A. Adawy, A. Martínez-Alonso, J.M.D. Tascón, Activation of two-dimensional MoS_2 nanosheets by wet-chemical sulfur vacancy engineering for the catalytic reduction of nitroarenes and organic dyes, Appl. Mater. Today 20 (2020), 100678.

[26] S. García-Dalí, J.I. Paredes, S. Villar-Rodil, A. Martínez-Jódar, A. Martínez-Alonso, J.M.D. Tascón, Molecular functionalization of 2H-phase MoS_2 nanosheets via an electrolytic route for enhanced catalytic performance, ACS Appl. Mater. Interfaces 13 (2021), 33157-33171.

[27] A. Ramalingam, E. Samaraj, S. Venkateshwaran, S.M. Senthilkumar, G.C. Senadi, 1T-MoS_2 catalysed reduction of nitroarenes and a one-pot synthesis of imines, New J. Chem. 46 (2022), 8720-8728.

[28] X. Pan, R.M. Sarhan, Z. Kochovski, G. Chen, A. Taubert, S. Mei, Y. Lu, Template synthesis of dual-functional porous MoS_2 nanoparticles with photothermal conversion and catalytic properties, Nanoscale 14 (2022), 6888-6901.

[29] Y. Shi, W. Zhang, J. Tan, T. Yan, Y. Jia, Z. Wang, Y. Tang, Q. Gao, Intercalation-driven defect-engineering of MoS_2 for catalytic transfer hydrogenation, Adv. Mater. Interfaces 9 (2022), 2200505.

[30] J. Tan, J. Shao, Y. Shi, W. Zhang, Q. Gao, Selective electrocatalytic hydrogenation of nitroarenes on interlayer-expanded MoS_2, ACS Sustainable Chem. Eng. 10 (2022), 13525-13533.

[31] B. Chen, Q. Zhang, P. Zhao, M. Cen, Y. Song, W. Zhao, W. Peng, Y. Li, F. Zhang, X. Fan, Coupled Co-doped MoS_2 and CoS_2 as the dual-active site catalyst for chemoselective hydrogenation, ACS Appl. Mater. Interfaces 15 (2023), 1317–1325.

[32] Y. Wen, H. Zhang, S. Zhang, One-step gas-solid reaction synthesis of W@WS_2 nanorattles and their novel catalytic activity, Nanoscale 6 (2014), 13090-13096.

[33] Y. Sun, A.J. Darling, Y. Li, K. Fujisawa, C.F. Holder, H. Liu, M.J. Janik, M. Terrones, R.E. Schaak, Defect-mediated selective hydrogenation of nitroarenes on nanostructured WS_2, Chem. Sci. 10 (2019), 10310-10317.

[34] M. Ling, B. Jiang, X. Cao, T. Wu, Y. Cheng, P. Zeng, L. Zhang, W.-C.M. Cheong, K. Wu, A. Huang, X. Wei, Phase-controllable synthesis of multifunctional 1T-$MoSe_2$ nanostructures: applications in lithium-ion batteries, electrocatalytic hydrogen evolution, and the hydrogenation reaction, ChemElectroChem 8 (2021), 4148-4155.

[35] A. Eftekhari, Molybdenum diselenide ($MoSe_2$) for energy storage, catalysis, and optoelectronics, Appl. Mater. Today 8 (2017), 1-17.

[36] Y. Deng, S. Xiao, Y. Zheng, X. Rong, M. Bai, Y. Tang, T. Ma, C. Cheng, C. Zhao, Emerging electrocatalytic activities in transition metal selenides: synthesis, electronic modulation, and structure-performance correlations, Chem. Eng. J. 451 (2023), 138514.

[37] H.-P. Komsa, J. Kotakoski, S. Kurasch, O. Lehtinen, U. Kaiser, A. V. Krasheninnikov. Two-dimensional transition metal dichalcogenides under electron irradiation: defect production and doping. Phys. Rev. Lett. 109 (2012) 035503.

[38] V. Lykourinou, A. I. Hanafy, K. S. Bisht, A. Angerhofer, L.-J. Ming. Iron(III) Complexes of metal-binding copolymers as proficient catalysts for acid hydrolysis of phosphodiesters and oxidative DNA cleavage – insight into the rational design of functional metallopolymers. Eur. J. Inorg. Chem. (2009), 1199–1207.

[39] J. H. Scofield, Hartree-Slater subshell photoionization cross-sections at 1254 and 1487 eV. J. Electon. Spectrosc. Relat. Phenom., 8 (1976) 129–137.

[40] G. Kresse, J. Furthmüller, Efficiency of ab-initio total energy calculations for metals and semiconductors using a plane-wave basis set, Comput. Mater. Sci. 6 (1996), 15–50.

[41] J.P. Perdew, K. Burke, M. Ernzerhof, Generalized gradient approximation made simple, Phys. Rev. Lett. 77 (1996), 3865–3868.

[42] W. Kraus, G. Nolze, POWDER CELL - a program for the representation and manipulation of crystal structures and calculation of the resulting X-ray powder patterns, J. Appl. Cryst. 29 (1996), 301–303.

[43] K. Momma, F. Izumi, VESTA: a three-dimensional visualization system for electronic and structural analysis, J. Appl. Crystallogr. 41 (2008), 653–65.

[44] G. Cunningham, M. Lotya, C.S. Cucinotta, S. Sanvito, S.D. Bergin, R. Menzel, M.S.P. Shaffer, J.N. Coleman, Solvent exfoliation of transition metal dichalcogenides: dispersibility of exfoliated nanosheets varies only weakly between compounds, ACS Nano 4 (2012), 3468-3480.

[45] N. Dong, Y. Li, Y. Feng, S. Zhang, X. Zhang, C. Chang, J. Fan, L. Zhang, J. Wang, Optical limiting and theoretical modeling of layered transition metal dichalcogenide nanosheets, Sci. Rep. 5 (2015), 14646.

[46] Y.-H. Chang, W. Zhang, Y. Zhu, Y. Han, J. Pu, J.-K. Chang, W.-T. Hsu, J.-K. Huang, C.-L. Hsu, M.-H. Chiu, T. Takenobu, H. Li, C. Wu, W.-H. Chang, A.T.S. Wee, L.-J. Li, Monolayer $MoSe_2$ grown by chemical vapor deposition for fast photodetection, ACS Nano 8 (2014), 8582-8590.

[47] N. Lundt, A. Maryński, E. Cherotchenko, A. Pant, X. Fan, S. Tongay, G. Sęk, A.V. Kavokin, S. Höfling, C. Schneider, Monolayered $MoSe_2$: a candidate for room temperature polaritonics, 2D Mater. 4 (2017), 015006.

[48] B.J. Berne, R. Pecora, *Dynamic light scattering, with applications to chemistry, biology and physics*, Dover Publications, Inc., New York, 2000, chapter 8.

[49] M. Lotya, A. Rakovich, J.F. Donegan, J.N. Coleman, Measuring the lateral size of liquid-exfoliated nanosheets with dynamic light scattering, Nanotechnology 24 (2013), 265703.

[50] D. Nam, J.-U. Lee, H. Cheong, Excitation energy dependent Raman spectrum of $MoSe_2$, Sci. Rep. 5 (2015), 17113.

[51] P. Tonndorf, R. Schmidt, P. Böttger, X. Zhang, J. Börner, A. Liebig, M. Albrecht, C. Kloc, O. Gordan, D.R.T. Zahn, S.M. Vasconcellos, R. Bratschitsch, Photoluminescence emission and Raman response of monolayer MoS_2, $MoSe_2$, and WSe_2, Opt. Express 21 (2013), 4908-4916.

[52] X. Lu, M.I.B. Utama, J. Lin, X. Luo, Y. Zhao, J. Zhang, S.T. Pantelides, W. Zhou, S.Y. Quek, Q. Xiong, Rapid and nondestructive identification of polytypism and stacking sequences in few-layer molybdenum diselenide by Raman spectroscopy, Adv. Mater. 27 (2015), 4502-4508.

[53] X. Lu, X. Luo, J. Zhang, S.Y. Quek, Q. Xiong, Lattice vibrations and Raman scattering in two-dimensional layered materials beyond graphene, Nano Res. 9 (2016), 3559-3597.

[54] G. Greczynski, L. Hultman. Impact of sample storage type on adventitious carbon and native oxide growth: X-ray photoelectron spectroscopy study, Vacuum 205 (2022), 111463.

[55] A. Azcatl, K.C. Santosh, X. Peng, N. Lu, S. McDonnell, X. Qin, F. de Dios, R. Addou, J. Kim, M.J. Kim, K. Cho, R.M. Wallace, HfO_2 on UV-O_3 exposed transition metal dichalcogenides: interfacial reactions study, 2D Mater. 2 (2015), 014004.

[56] M. Wu, N. Li, S. Zuo, W. Shen, G. Sun, Q. Li, M. Shi, J. Ma, Efficient charge separation via $MoSe_2$ nanosheets with tunable 1T phase contents: piezoreduction of Cr(VI) to Cr(III) and piezodegradation of RhB, Inorg. Chem. 61 (2022), 17972-17984.

[57] L.-F. Huang, Z. Zeng, Roles of mass, structure, and bond strength in the phonon properties and lattice anharmonicity of single-layer Mo and W dichalcogenides, J. Phys. Chem. C 119 (2015), 18779-18789.

[58] J.I. Paredes, J.M. Munuera, S. Villar-Rodil, L. Guardia, M. Ayán-Varela, A. Pagán, S.D. Aznar-Cervantes, J.L. Cenis, A. Martínez-Alonso, J.M.D. Tascón, Impact of covalent functionalization on the aqueous processability, catalytic activity, and biocompatibility of chemically exfoliated MoS_2 nanosheets, ACS Appl. Mater. Interfaces 8 (2016), 27974-27986.

[59] R.J. Smith, P.J. King, M. Lotya, C. Wirtz, U. Khan, S. De, A. O´Neill, G.S. Duesberg, J.C. Grunlan, G. Moriarty, J. Chen, J. Wang, A.I. Minett, V. Nicolosi, J.N. Coleman, Large-scale exfoliation of inorganic layered compounds in aqueous surfactant solutions, Adv. Mater. 23 (2011), 3944-3948.

[60] Z. Lei, W. Zhu, S. Xu, J. Ding, J. Wan, P. Wu, Hydrophilic $MoSe_2$ nanosheets as effective photothermal therapy agents and their application in smart devices, ACS Appl. Mater. Interfaces 8 (2016), 20900-20908.

[61] M.R. Uhlig, D. Martin-Jimenez, R. Garcia, Atomic-scale mapping of hydrophobic layers on graphene and few-layer MoS_2 and WSe_2 in water, Nat. Commun. 10 (2019), 2606.

[62] J. Kim, S. Kwon, D.-H. Cho, B. Kang, H. Kwon, Y. Kim, S.O. Park, G.Y. Jung, E. Shin, W.-G. Kim, H. Lee, G.H. Ryu, M. Choi, T.H. Kim, J. Oh, S. Park, S.K. Kwak, S.W. Yoon, D. Byun, Z. Lee, C. Lee, Direct exfoliation and dispersion of two-dimensional materials in pure water with temperature control, Nat. Commun. 6 (2015), 8294.

[63] V. Forsberg, R. Zhang, J. Bäckström, C. Dahlström, B. Andres, M. Norgren, M. Andersson, M. Hummelgård, H. Olin, Exfoliated MoS_2 in water without additives, PLoS ONE 11 (2016), e0154522.

[64] R.D. Neal, R.D. Hughes, P. Sapkota, S. Ptasinska, S. Neretina, Effect of nanoparticle ligands on 4-nitrophenol reduction: reaction rate, induction time, and ligand desorption, ACS Catal. 10 (2020), 10040-10050.

[65] D.H. Everett, *Basic principles of colloid science*, Royal Society of Chemistry, London, 1988, chapters 3 and 8.

[66] A. Jawaid, J. Che, L.F. Drummy, J. Bultman, A. Waite, M.-S. Hsiao, R.A. Vaia, Redox exfoliation of layered transition metal dichalcogenides, ACS Nano 11 (2017), 635-646.

[67] A.M. Jawaid, A.J. Ritter, R.A. Vaia, Mechanism for redox exfoliation of layered transition metal dichalcogenides, Chem. Mater. 32 (2020), 6550-6565.

[68] T. Aditya, A. Pal, T. Pal, Nitroarene reduction: a trusted model reaction to test nanoparticle catalysts, Chem. Commun. 51 (2015), 9410-9431.

[69] E. Menumerov, R.A. Hughes, S. Neretina, Catalytic reduction of 4-nitrophenol: a quantitative assessment of the role of dissolved oxygen in determining the induction time, Nano Lett. 16 (2016), 7791-7797.

[70] P. Hervés, M. Pérez-Lorenzo, L.M. Liz-Marzán, J. Dzubiella, Y. Lu, M. Ballauff, Catalysis by metallic nanoparticles in aqueous solution: model reactions, Chem. Soc. Rev. 41 (2012), 5577-5587.

[71] J.A. Dean, *Langés Handbook of Chemistry*, 15th edition, McGraw-Hill, New York, section 8, pages 8.24-8.72.

[72] J. Hong, Z. Hu, M. Probert, K. Li, D. Lv, X. Yang, L. Gu, N. Mao, Q. Feng, L. Xie, J. Zhang, D. Wu, Z. Zhang, C. Jin, W. Ji, X. Zhang, J. Yuan, Z. Zhang. Exploring atomic defects in molybdenum disulphide monolayers. Nat. Commun. 2015, 6, 6293.

[73] D. Xiao, D.-L. Bao, X. Liang, Y. Wang, J. Shen, C. Cheng, P.K. Chu, Experimental and theoretical investigation of the control and balance of active sites on oxygen plasma-functionalized $MoSe_2$ nanosheets for efficient hydrogen evolution reaction, Appl. Catal. B: Environ. 288 (2021), 119983.

[74] M. Wang, Z. Sun, H. Ci, Z. Shi, L. Shen, C. Wei, Y. Ding, X. Yang, J. Sun, Identifying the evolution of selenium-vacancy-modulated $MoSe_2$ precatalyst in lithium-sulfur chemistry, Angew. Chem. Int. Ed. 60 (2021), 24558-24565.

[75] Y. Zhang, Y. Gao, S. Yao, S. Li, H. Asakura, K. Teramura, H. Wang, D. Ma, Sublimation-induced sulfur vacancies in MoS_2 catalyst for one-pot synthesis of secondary amines, ACS Catal. 9 (2019), 7967-7975.

[76] F. Yang, C. Chi, C. Wang, Y. Wang, Y. Li, High graphite N content in nitrogen-doped graphene as an efficient metal-free catalyst for reduction of nitroarenes in water, Green Chem. 18 (2016), 4254-4262.

[77] Y. Cai, Z. Bai, H. Pan, Y.P. Feng, B.I. Yakobson, Y.-W. Zhang, Constructing metallic nanoroads on a MoS_2 monolayer via hydrogenation, Nanoscale 6 (2014), 1691-1697.

[78] J.A. Bau, R. Ahmad, L. Cavallo, M. Rueping, A unified theory for H_2 evolution on Mo-based electrocatalysts, ACS Energy Lett. 7 (2022), 3695-3702.

[79] H. Tang, K. Dou, C.-C. Kaun, Q. Kuang, S. Yang, $MoSe_2$ nanosheets and their graphene hybrids: synthesis, characterization and hydrogen evolution reaction studies, J. Mater. Chem. A 2 (2014), 360-364.

[80] J.D. Wiensch, J. John, J.M. Velazquez, D.A. Torelli, A.P. Pieterick, M.T. McDowell, K. Sun, X. Zhao, B.S. Brunschwig, N.S. Lewis, Comparative study in acidic and alkaline

media of the effects of pH and crystallinity on the hydrogen-evolution reaction on MoS_2 and $MoSe_2$, ACS Energy Lett. 2 (2017), 2234-2238.

[81] S. Wang, A. Robertson, J.H. Warner, Atomic structure of defects and dopants in 2D layered transition metal dichalcogenides, Chem. Soc. Rev. 47 (2018), 6764-6794.

[82] Q. Liang, Q. Zhang, X. Zhao, M. Liu, A.T.S. Wee, Defect engineering of two-dimensional transition-metal dichalcogenides: applications, challenges, and opportunities, ACS Nano 15 (2021), 2165-2181.

[83] P.-Y. Wang, B.-A. Chen,Y.-C. Lee, C.-C. Chiu. First-principles modeling of the highly dynamical surface structure of a MoS2 catalyst with S-vacancies. Phys. Chem. Chem. Phys. 24 (2022), 24166–24172.

[84] S. Bae, S. Gim, H. Kim, K. Hanna, Effect of $NaBH_4$ on properties of nanoscale zero-valent iron and its catalytic activity for reduction of *p*-nitrophenol, Appl. Catal. B: Environ. 182 (2016), 541-549.

[85] N.D. Mansukhani, L.M. Guiney, P.J. Kim, Y. Zhao, D. Alducin, A. Ponce, E. Larios, M.J. Yacaman, M.C. Hersam, High-concentration aqueous dispersions of nanoscale 2D materials using nonionic, biocompatible block copolymers, Small 12 (2016), 294-300.

[86] M. Ayán-Varela, O. Pérez-Vidal, J.I. Paredes, J.M. Munuera, S. Villar-Rodil, M. Díaz-González, C. Fernández-Sánchez, V.S. Silva, M. Cicuéndez, M. Vila, A. Martínez-Alonso, J.M.D. Tascón, Aqueous exfoliation of transition metal dichalcogenides assisted by DNA/RNA nucleotides: catalytically active and biocompatible nanosheets stabilized by acid-base interactions, ACS Appl. Mater. Interfaces 9 (2017), 2835-2845.

[87] Ellis, Frank (2002). Paracetamol: a curriculum resource. Cambridge: Royal Society of Chemistry. ISBN 0-85404-375-6.

[88] Gerald Booth (2007). Aromatic nitro compounds Ullmann's Encyclopedia of Industrial Chemistry. Weinheim: Wiley-VCH.

Supplementary Material

Two-dimensional transition metal dichalcogenides beyond MoS_2 for the catalytic reduction of nitroarenes: $MoSe_2$ exhibits enhanced performance

A. Martínez-Jódar[a], S. Villar-Rodil[a,], M.A. Salvadó[b,]*, D.F. Carrasco[a], P. Pertierra[b], J.M. Recio[b], J.I. Paredes[a,]**

[a] Instituto de Ciencia y Tecnología del Carbono, INCAR-CSIC, C/Francisco Pintado Fe 26, 33011 Oviedo, Spain

[b] MALTA-Consolider Team and Departamento de Química Física y Analítica, Universidad de Oviedo, 33006 Oviedo, Spain

*Corresponding authors' e-mail addresses:

silvia@incar.csic.es (S. Villar-Rodil),

mass@uniovi.es (*M.A. Salvadó*),

paredes@incar.csic.es (J. I. Paredes)

S1. Further characterization of bulk and exfoliated $MoSe_2$

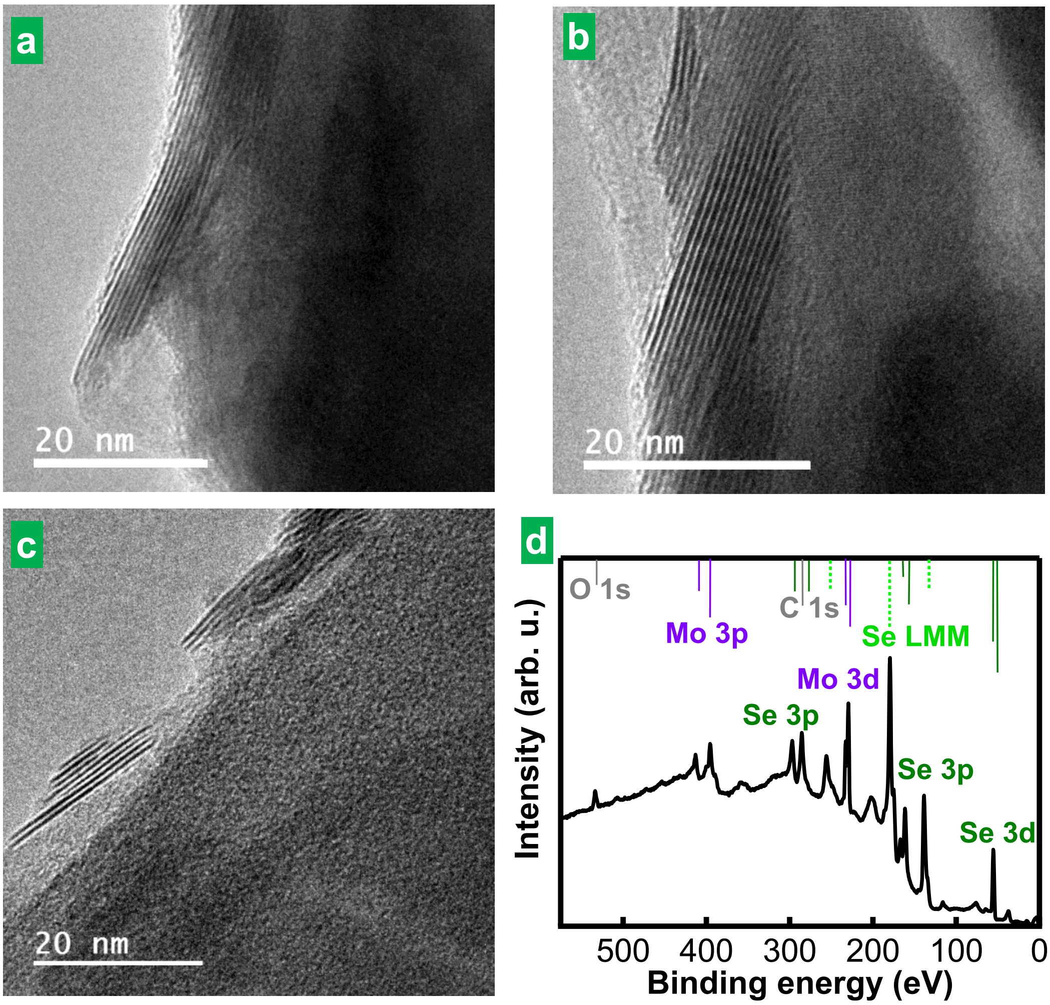

Figure S1. Additional HR-TEM and XPS characterization of exfoliated $MoSe_2$. (a–c) HRTEM images of exfoliated $MoSe_2$ where the edges of the flakes clearly reveal their multilayer nature. The number of $MoSe_2$ trilayers per flake can be directly determined by counting the dark fringes seen on the edges. **(d)** XPS survey spectrum of exfoliated $MoSe_2$. The main XPS bands and the complex, multipeak Se LMM Auger band have been labelled for clarity, and their position has been indicated in the top axis.

The binding energy (BE) values for spin-orbit levels of Mo^{4+} in 2H-$MoSe_2$, i. e., ~229.0 eV for Mo $3d_{5/2}$ and ~232.2 eV for Mo $3d_{3/2}$ lie in between those usually reported for 2H- and 1T-MoS_2 phases both for the starting $MoSe_2$ powder (Fig. S2c below) and for exfoliated $MoSe_2$ nanosheets (Fig. 2f in the main text). However, both the UV-Vis spectra of the exfoliated material (Fig. 1b in the main text) and the Raman spectra of the starting and exfoliated material (Fig. S2b and Fig. 2b, respectively) point to the presence of 2H-$MoSe_2$ exclusively. Furthermore, the fact that the XPS bands (Figs. S2c and 2f) are narrow rules out the presence of a mixture of chemical environments and/or phases. We believe that the lower BE of the Mo 3d components in 2H-$MoSe_2$ in relation with those of 2H-MoS_2 arises from the difference in the nature of the atoms bound to molybdenum. Indeed, sulfur is more electronegative than selenium and will thus pull away more electron density from molybdenum, unshielding the nucleus and rising the BE needed to eject an electron by photoemission. This BE shift is analogous to the one taking place for C 1s in the well-known case of carbon functionalities, where, for the same oxidation state of the carbon atom, more electronegative fluorine atoms induce higher BE that oxygen atoms.

The XPS weak feature at BE~230 eV, in between the Mo $3d_{5/2}$ and Mo $3d_{3/2}$ components in $MoSe_2$ (Figs. S2c and 2f), arises from none other than the Se 3s core level, although it has either passed unnoticed in the literature [1] or wrongly assigned to Mo $3d_{5/2}$ from a higher oxidation state of the molybdenum atom [2]. The wrong assignment is obvious, if only because any Mo $3d_{5/2}$ should be accompanied by the corresponding Mo $3d_{3/2}$ about 3.2 eV higher in BE. As Se 3s band for Se^0 is located at 232 eV [3], the lower BE found here must be assigned, as expected, to the selenide, i. e., the only lower oxidation state possible for Se element (-II).

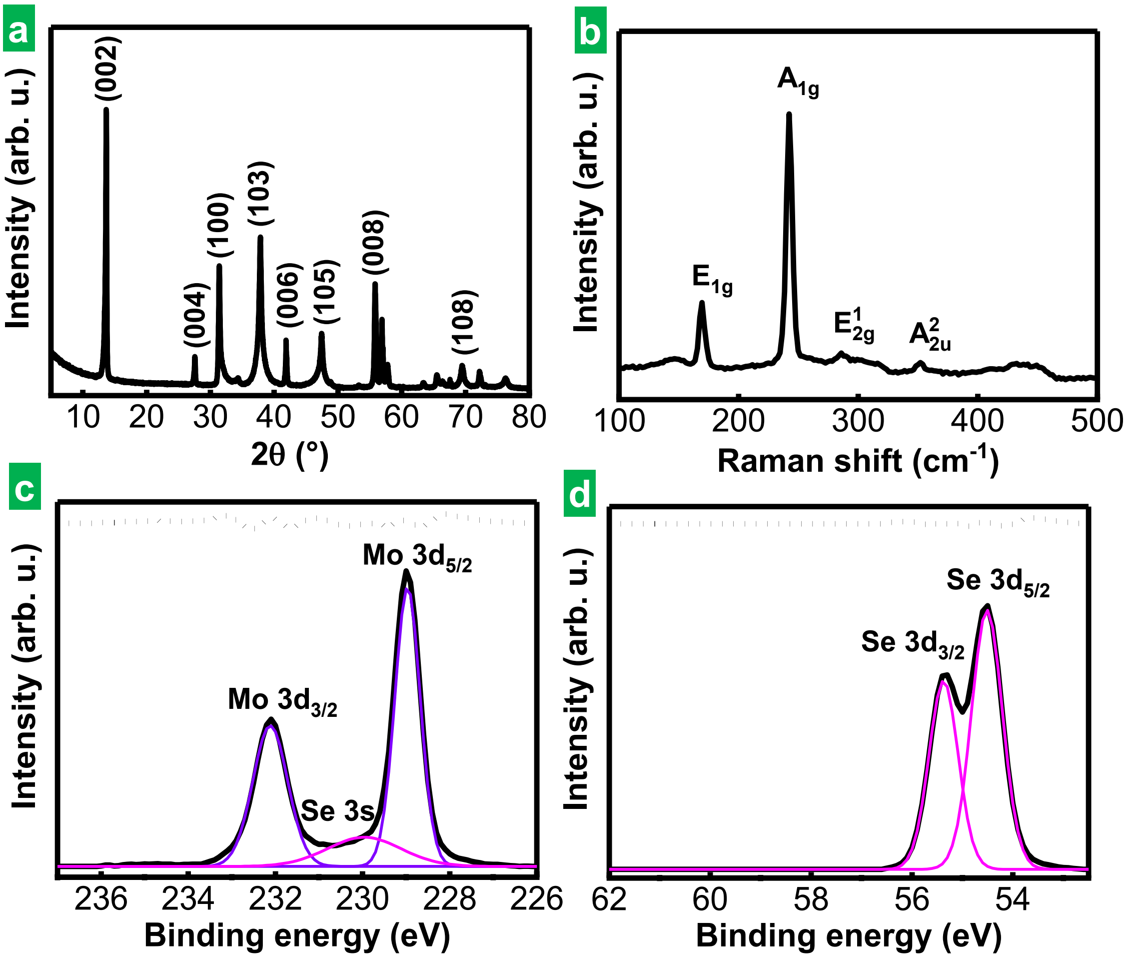

Figure S2. Characterization of bulk $MoSe_2$ powder (a) XRD diffractogram of the $MoSe_2$ starting powder, where peaks have been labelled according to JCPDS card 29-0914. **(b)** Raman spectrum of bulk $MoSe_2$, where the main bands have been labeled for clarity. Background-subtracted XPS core level spectra of **(c)** Mo 3d (and Se 3s) and **(d)** Se 3d. The experimental spectroscopic data are depicted with black solid traces while the fitted Mo and Se components are drawn with violet and pink traces, respectively. The difference between the experimental and the fitted spectrum is graphed on top of the fitted XPS spectra (black dotted line).

S2. Characterization of the exfoliated MoS_2 nanosheets

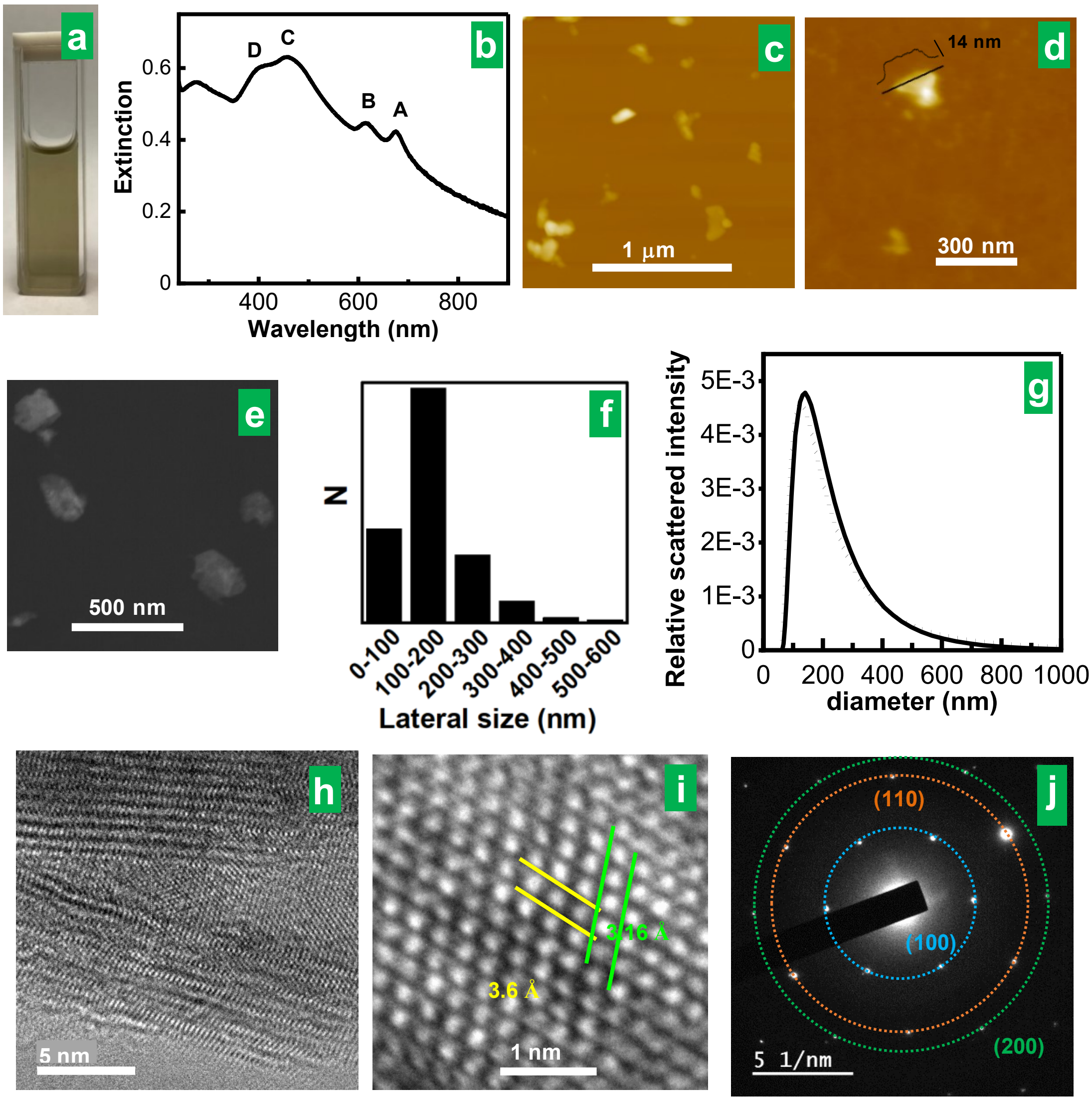

Figure S3. Characterization of MoS_2 dispersions. (a) Digital photograph of the MoS_2 dispersion and the corresponding **(b)** UV-Vis extinction/adsorption spectrum with indication of the characteristic excitonic peaks. Representative **(c,d)** AFM and **(e)** STEM images of the dispersed objects. **(f)** Histogram of lateral size and derived from STEM imaging and **(g)** DLS-derived hydrodynamic diameters distribution for MoS_2 aqueous dispersion (solid trace) and $MoSe_2$ dispersion (dotted trace). **(h,i)** Representative HR-TEM images of the MoS_2 flakes at different magnifications. The parallel lines in (i) assist in visualizing *a* and *b* cell parameters in the hexagonal cell of MoS_2 lattice. **(j)** SAED pattern of the MoS_2 lattice with indication of the family planes involved in the observed diffractions.

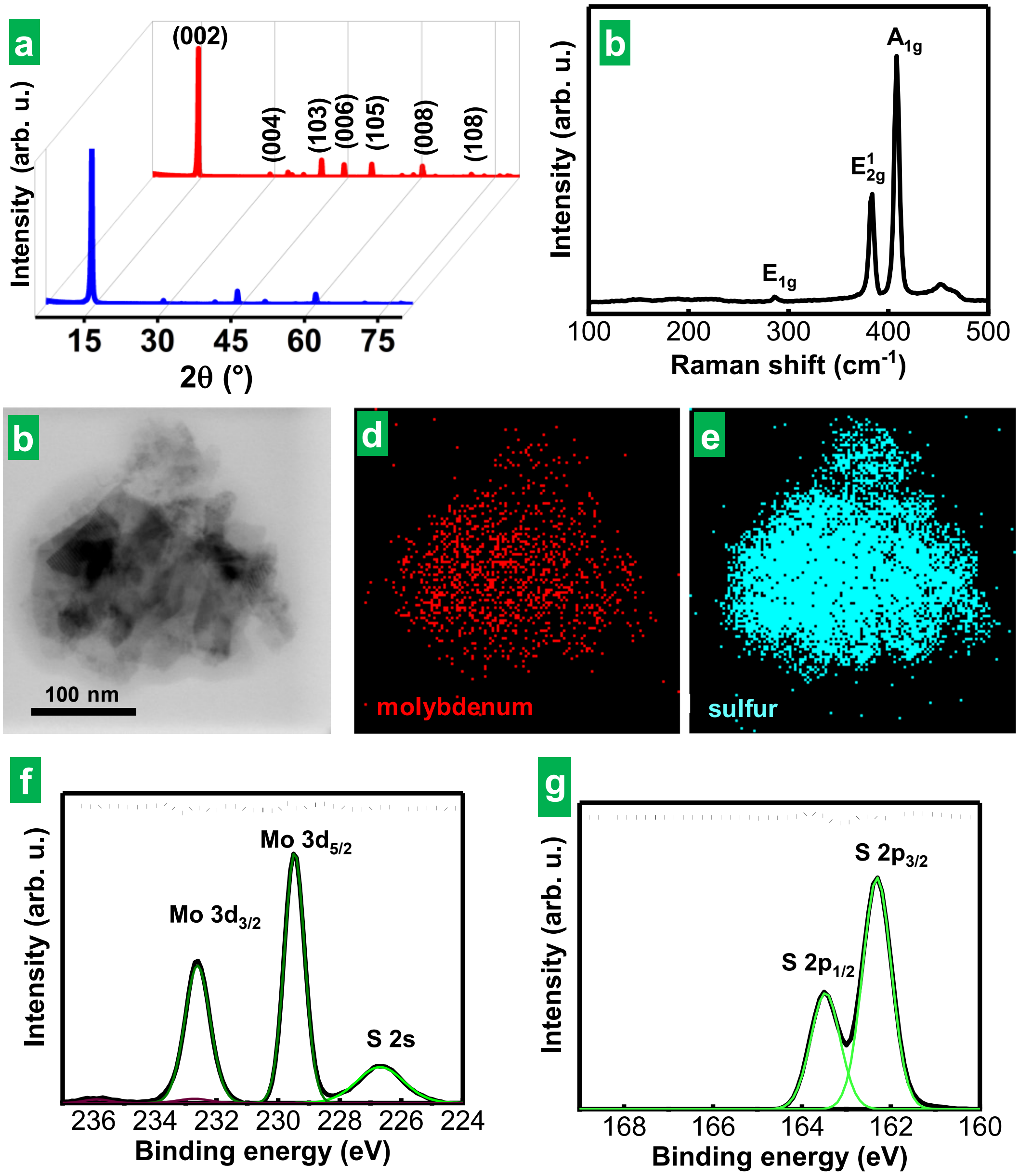

Figure S4. Structural and chemical characterizations of the exfoliated MoS_2 flakes. (a) XRD diffractogram of bulk (red trace) and exfoliated MoS_2 (blue trace), where peaks have been labelled according to JCPDS card 37-1492. **(b)** Raman spectrum for exfoliated MoS_2 flakes where the main bands have been labeled for clarity. **(c)** STEM image of exfoliated MoS_2 and the corresponding energy dispersive X-ray (EDX) area mapping of

(d) molybdenum and **(e)** sulfur. **(f)** Background-subtracted, high-resolution XPS Mo 3d (and S 2s) and **(g)** S 2p core level spectrum of exfoliated MoS_2. The experimental data are depicted with solid back trace while the fitted Mo and S components are drawn in dark and light green traces, respectively. The difference between the experimental and the fitted spectrum is graphed on top of the fitted XPS spectra (black dotted traces).

S3. UV-Vis absorption spectra of the nitroarenes and their reduced counterparts

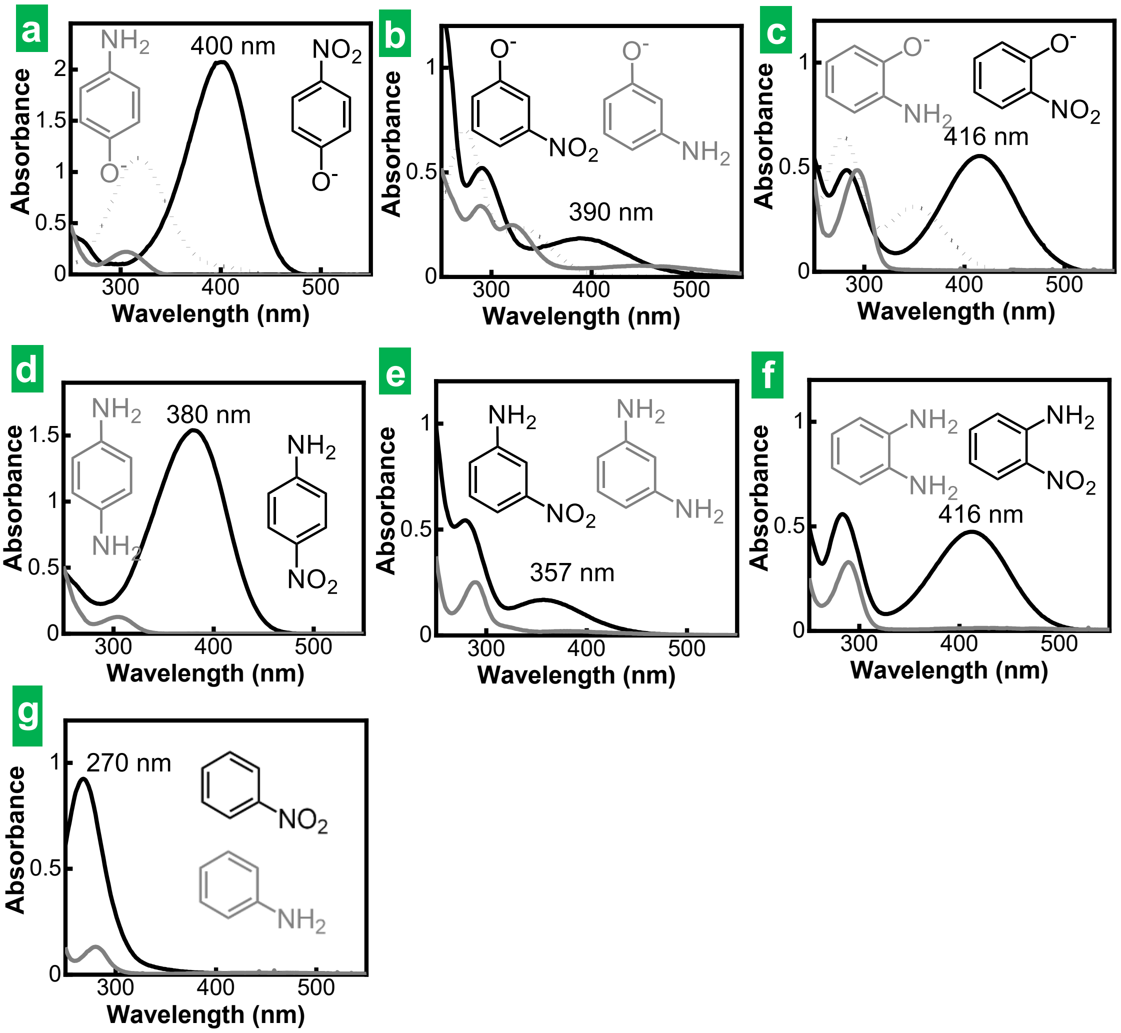

Figure S5. Chemical structure and UV-Vis absorption spectra of the nitroarenes and their reduced counterparts. Chemical structure and UV-Vis spectra of the reactants (black trace) and products (gray trace) involved in the different nitroarene reduction reactions where exfoliated $MoSe_2$ and MoS_2 have been tested as catalysts: **(a)** 4-NP (dotted trace), 4-nitrophenolate (solid trace) and 4-aminophenol; **(b)** 3-NP (dotted trace), 3-nitrophenolate (solid trace) and 3-aminophenol; **(c)** 2-NP (dotted trace), 2-nitrophenolate (solid trace) and 2-aminophenol; **(d)** 4-NA and its reduction product, p-phenylenediamine; **(e)** 3-NA and m-phenylenediamine; **(f)** 2-NA and o-phenylenediamine; **(g)** nitrobenzene and aniline. The concentrations for the reactants are those used for the corresponding catalysis experiments (see section 2.4 in the main text).

S4. Derivation of actual reaction kinetic profiles from raw profiles recorded with UV-Vis absorption spectroscopy

To determine the effect of the catalyst on the reaction profiles that were directly recorded with UV-Vis absorption spectroscopy (raw kinetic profiles), we quantitatively evaluated the colloidal stability of the $MoSe_2$ flakes in the presence of the reactants at the concentrations that would be used in the catalytic tests. To this end, the same spectroscopic technique was used (see Fig. 1b in the main text). Fig. S6a (black trace) shows the time evolution of the absorbance (A) of the exfoliated $MoSe_2$ flakes suspended in pure water (concentration of 14 μg mL^{-1}) relative to the initial absorbance of the suspension (A_0), measured at a wavelength of 380 nm. It can be noticed that the A/A_0 value was constant (~1) throughout the measurement (~2000 min), indicating that the dispersion was stable and did not precipitate to any noticeable extent. As expected, the same result was obtained using other wavelengths for the absorption measurement. In the presence of the substrate molecules (0.11-0.12 mM), A/A_0 was also seen to remain constant with time, as exemplified in Fig. S6a for 4-NP (red trace, measured at 400 nm) and 4-NA (green trace, measured at 380 nm), indicating that the stability of the dispersed $MoSe_2$ flakes was not affected by these reactants. On the other hand, a slow sedimentation of the flakes was concluded to occur when $NaBH_4$ (112 mM) was added to the aqueous $MoSe_2$ dispersion. In this case, the measured A/A_0 values followed an approximately linear decreasing trend, after a somewhat faster initial decay (Fig. S6a, gray trace). We note that only the TMD was contributing to the measured absorbance here, as $NaBH_4$ is transparent to all the benchmark wavelengths tested in the present work. Hence, the observed behavior could only be ascribed to colloidal destabilization and subsequent sedimentation of the negatively charged $MoSe_2$ flakes in the high ionic strength medium provided by $NaBH_4$, where the negative charges in the former are neutralized by positive charges from the latter (i.e., Na^+ ions) [4]. The $NaBH_4$-induced sedimentation rate derived from the A/A_0 vs. time plot (~0.7 wt.% per minute) was sufficiently low so as not to compromise the measurement of reaction kinetic profiles, as will be shown next. However, some corrections to such profiles were necessary.

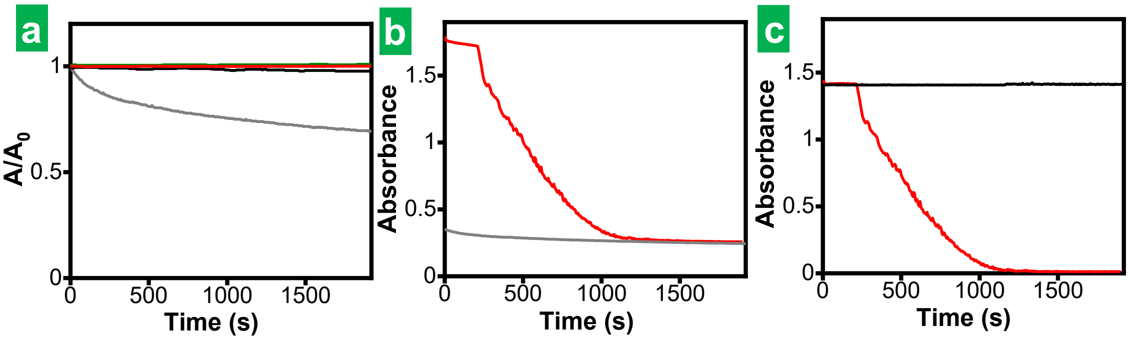

Figure S6. Correction of the time-dependent contribution from the absorbance of the catalyst to the kinetic profiles. (a) Time evolution of the absorbance (A) of the exfoliated $MoSe_2$ flakes suspended in pure water (concentration of 14 µg mL^{-1}) relative to the initial absorbance of the suspension (A_0), measured at a wavelength of 380 nm (black trace); A/A_0 vs. time, in the presence of 0.11 mM 4-NA (red trace, measured at 380 nm) and 0.12 mM 4-NP (green trace, hardly visible due to overlapping with the previous traces, measured at 400 nm); A/A_0 vs. time, in the presence of 112 mM $NaBH_4$ (gray trace). **(b)** Typical raw kinetic profile (i.e., total absorbance of the reaction medium at 380 nm vs. time) recorded for the reaction of 4-NA (0.11 mM) with $NaBH_4$ (112 mM) in the presence of $MoSe_2$ (14 µg mL^{-1}) (red trace); total absorbance of the reaction medium at 380 nm vs. time for the $MoSe_2$ flakes in the presence of only the reducing agent (gray trace). **(c)** Corrected kinetic profile of 4-NA reduction without spurious contributions from $MoSe_2$ sedimentation (red trace) obtained from the difference between the red and gray traces in Fig. S6b. of the reactant. Kinetic profile for the reaction between 4-NA and $NaBH_4$ in the absence of the $MoSe_2$ catalyst (black trace).

Fig. S6b (red trace) shows a typical raw kinetic profile (i.e., total absorbance of the reaction medium at 400 nm vs. time) recorded for the reaction of 4-NP (0.12 mM) with $NaBH_4$ (112 mM) in the presence of $MoSe_2$ (14 µg mL^{-1}), taken here as a representative nitroarene reduction. The profiles exhibited three distinctive sections: (1) an initial section, where the measured absorbance slowly declined in a more or less linear fashion, (2) a middle section that displayed a sharp drop in absorbance, and (3) a final section, where the slow decline in absorbance noticed for the initial section was resumed. Significantly, the behavior of the initial and final sections faithfully mimicked that of the

$MoSe_2$ flakes in the presence of only the reducing agent (Fig. S6b, gray trace). This suggested that both sections just reflected the slow sedimentation of the $MoSe_2$ flakes triggered by $NaBH_4$ and, therefore, that information on the kinetics of the substrate reduction was exclusively contained in the middle section of the recorded profiles. Hence, by subtracting the absorbance due to the $MoSe_2$ flakes from the raw kinetic profile (i.e., the difference between the red and gray traces in Fig. S6b), a corrected kinetic profile of 4-NP reduction without spurious contributions from $MoSe_2$ sedimentation could be obtained. Such a corrected profile is plotted in Fig. S6c (red trace). It can be seen that the initial and final sections are now constant, the former corresponding to the absorbance of 4-NP at the beginning of the reaction and the latter indicating essentially zero absorbance and thus a virtually complete conversion of the reactant. For comparison, the kinetic profile for the reaction between 4-NP and $NaBH_4$ in the absence of the $MoSe_2$ catalyst is also shown (black trace). As expected, a constant absorbance value (equal to the initial absorbance of 4-NP) was recorded throughout the whole measurement period, implying that no noticeable conversion of 4-NP was taking place. The initial constant section observed for the catalyzed reaction in Fig. S6c (red trace), where reduction of 4-NP does not appear to have yet started, can be attributed to the so-called induction time, which has been previously observed with different types of catalysts, including TMDs [5,6]. For metal catalysts, it has been shown that reduction of 4-NP does indeed occur during this period, but the reduced molecules [i.e., 4-aminophenol (4-AP)] are rapidly converted back to 4-NP by oxidation with oxygen molecules dissolved in the reaction medium, so that there is no net progress in the reduction [7]. Once the dissolved oxygen is depleted by reaction with 4-AP, a net conversion of 4-NP into 4-AP kicks in, as evidenced here by the abrupt decrease in the measured absorbance (middle section of the kinetic profile), which finally leads to a complete conversion of the substrate (zero absorbance in the final section). This interpretation was concluded to be valid for the present $MoSe_2$ catalyst, since the induction period tended to disappear from the recorded kinetic profiles when the reaction solutions were deaerated prior to the catalytic tests (data not shown).

From the corrected profile, the actual reaction kinetic profile could be finally determined after removing the initial section (induction period) and converting the absorbance values to substrate concentration by means of the Lambert-Beer law. More specifically, the absorbance measured at a given wavelength, A, can be related to the substrate concentration through the following general relation:

$$A = \varepsilon_s[S] + \varepsilon_p[P] \qquad \text{(S1)}$$

, where [S] is the molar concentration of the substrate, [P] is the molar concentration of its reduced product, and ε_s and ε_p are the molar extinction coefficients of the substrate and product, respectively, at the measured wavelength. We assume here that the nitroarene is uniquely converted to its corresponding aniline, i.e., there is not a variety of reaction products (indeed, as will be seen in section S10, the reaction conversion efficiency is ~100 %, at least for 3-NA). We also assume that the absorbance of the reaction intermediates, which will be in relatively low concentration, can be neglected. We also note that for most of the tested substrates, ε_p is zero or very close to zero, although that is not always the case. For example, ε_p was essentially zero for all the nitrophenol and nitroaniline isomers investigated here, but not for NB, the reduction product of which (aniline) exhibited non-negligible absorbance at the signature wavelength of NB, i.e., ~270 nm (see Fig. S5). Furthermore, the following relation between [S] and [P] should also hold:

$$[S] + [P] = [S]_0 \qquad \text{(S2)}$$

, where $[S]_0$ is the initial molar concentration of the substrate in the reaction medium. From equations (S1) and (S2), the reaction kinetic profile can be written as

$$[S] = \frac{A - \varepsilon_p[S]_0}{\varepsilon_s - \varepsilon_p} \qquad \text{(S3)}$$

When ε_p is zero or negligible, equation (S3) can be simplified as $[S] = A/\varepsilon_s$, which applied in practice in most cases. Plots of [S] vs. time finally afforded the actual reaction kinetic profiles, as exemplified in Fig. 3 of the main text.

S5. Analysis of reaction orders based on the rate constants of individual processes

Although the reduction of nitroarenes with $NaBH_4$ at the catalytic active sites of the TMDs is a bimolecular reaction, we note that the reducing agent was used in a very large excess relative to the substrate. Therefore, the concentration of $NaBH_4$ in the reaction medium as well as the surface coverage of this reactant on the catalytic sites of the TMD (presumably in the form of active adsorbed hydrides, as discussed in section 3.3 of the main text) can be considered to remain constant throughout the reaction. Thus, to all intents and purposes, the reduction of the nitroarene can be regarded as if it was an unimolecular reaction, where this substrate molecule is first adsorbed at the available active sites of the catalyst (i.e., those not occupied by the adsorbed hydrides), then it is converted to the corresponding aniline, and finally the latter desorbs from the catalyst, leaving the active site again available for a subsequent conversion reaction. If k_1, k_2 and k_{-1} are the rate constants for the surface adsorption, conversion and desorption steps of the reaction, respectively, C_A is the total surface concentration of active sites on the catalyst available for substrate adsorption (occupied by the substrate or not), C_{A+} is the surface concentration of active sites occupied by the substrate at any given time, and θ ($= C_{A+}/C_A$) is the surface coverage of substrate molecules on the catalyst, then the reaction rate can be written as

$$d[S]/dt = -k_2C_{A+} = -k_2\theta C_A \qquad \text{(S4)}$$

, where [S] is the substrate concentration in the reaction medium. In the steady state approximation, the surface coverage can be written as [8]

$$\theta = \frac{k_1[S]}{k_1[S]+k_{-1}+k_2} \qquad \text{(S5)}$$

If the overall reaction is limited by the conversion of the adsorbed substrate molecule at the active sites, then $k_2 << k_1[S]+k_{-1}$, so that

$$\theta \approx \frac{k_1[S]}{k_1[S]+k_{-1}} \qquad \text{(S6)}$$

In addition, if the substrate concentration is sufficiently high so that $k_1[S] >> k_{-1}$, then $\theta \approx 1$ and finally $d[S]/dt \approx -k_2C_A$, implying a zero-order reaction with respect to the substrate. We conclude that this situation applied in the case of the exfoliated MoS_2 nanosheets prepared in this work, as they led to reaction kinetic profiles that were well described by linear decay functions (see Fig. 4 in the main text), and also in the case of previously reported acetic acid-functionalized MoS_2 nanosheets with regard to electrically neutral nitroarenes (e.g., nitroanilines) [9]. In both cases, access of the substrate molecules to the active sites of the catalyst can be considered essentially unrestricted (e.g., there are no significant electrostatic barriers between substrate and catalyst), so that comparatively large k_1 (and k_{-1}) values are warranted. On the other hand, if substrate access to the catalyst is severely restricted, then k_1 should become much smaller. This appears to be the case of the acetic acid-functionalized MoS_2 nanosheets with respect to negatively charged nitroarenes (e.g., nitrophenols). Because these functionalized materials are highly negatively charged (large negative zeta potential), a strong electrostatic repulsion barrier between substrate and catalyst should be in place, and so k_2, $k_1[S] << k_{-1}$ (we assume here that the value of k_2 is essentially the same for all 2H-phase MoS_2 materials). Therefore, in this case the surface coverage can be written as $\theta \approx k_1[S]/k_{-1}$, and the rate equation as $d[S]/dt \approx -k_1k_2C_A[S]/k_{-1}$, yielding a first-order reaction with kinetic profiles described by exponential decay functions, as it was indeed observed with the acetic-acid functionalized MoS_2 catalyst and nitrophenol substrates [9].

Now, taking the kinetic behavior of these MoS_2 catalysts as a reference, we can infer some of the kinetic features of the exfoliated $MoSe_2$ nanosheets. First, because the overall electrical charge of the latter is similar to that of the exfoliated MoS_2 nanosheets (similar zeta potential values), we assume that the value of k_1 must be similar for both TMD materials. Second, if the values of k_2 and k_{-1} were also similar for both TMDs, then the inequalities $k_2, k_{-1} << k_1[S]$ discussed above for the exfoliated MoS_2 nanosheets should also hold for their $MoSe_2$ counterpart, leading again to zero-order kinetics. Considering that such a behavior was not actually observed in the kinetic profiles for the exfoliated $MoSe_2$ nanosheets (Fig. 3 of the main text), we deduce that the value of either k_2 or k_{-1} for these nanosheets must be very different to that of its equivalent in the MoS_2 nanosheets. If we assume that the difference was due to k_{-1} and this rate constant was much larger in $MoSe_2$ than in MoS_2, so that $k_2 << k_1[S] << k_{-1}$, then $\theta \approx k_1[S]/k_{-1}$ and the rate equation could be written as $d[S]/dt \approx -k_1k_2C_A[S]/k_{-1}$, yielding a first-order reaction. However, while this reaction order would be consistent with that actually observed for the exfoliated $MoSe_2$ nanosheets, we note that $\theta << 1$ in this case, compared to $\theta \approx 1$ for the MoS_2 nanosheets, implying that the reaction should be much slower with the former catalyst, which was not really the case (see Table 1 in the main text). It should be pointed out that the reduction reaction could still be faster in this case with the $MoSe_2$ catalyst if the surface concentration of available active sites, C_A, were some orders of magnitude larger with this TMD compared to MoS_2. Nonetheless, such a situation appears to be physically unrealistic for these two TMDs that were exfoliated by exactly the same method, as it would imply that the number of structural defects (unsaturated molybdenum centers) as the active sites in $MoSe_2$ would also be orders of magnitude larger than that in MoS_2. Hence, we infer that the main kinetic distinction between $MoSe_2$ and MoS_2 must not lie in the k_1 and k_{-1} values, but in the value of k_2. More specifically, the results suggest that k_2 is much larger for $MoSe_2$ than it is for MoS_2, so that for the former TMD the following inequalities would hold: $k_{-1} << k_1[S] << k_2$. Then, the surface coverage for $MoSe_2$ could be written as $\theta \approx k_1[S]/k_2$ and the rate equation as $d[S]/dt \approx -k_1C_A[S]$, giving a fist-order reaction that is consistent with the actual behavior of the $MoSe_2$ catalyst. The much higher k_2 value inferred here for $MoSe_2$ compared to MoS_2 implies that conversion of nitroarene molecules adsorbed at the catalytic active sites to anilines is much faster on the former catalyst. We believe such a distinct behavior is largely due to a higher abundance and availability of reducing hydrides on the surface of $MoSe_2$, as discussed in section 3.3 of the main text.

S6. Comparison of induction periods of nitroarene reduction in the presence of $MoSe_2$ and MoS_2 catalysts

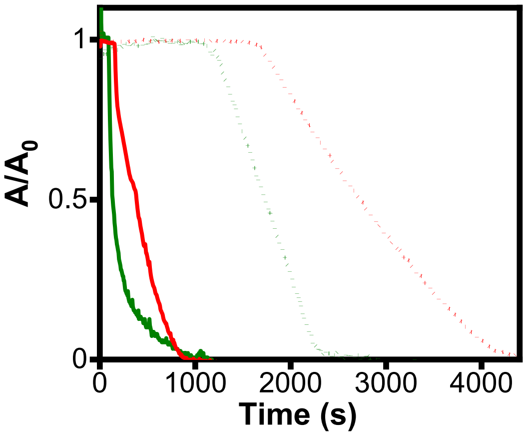

Figure S7. Comparison of the induction periods of nitroarene reduction in the presence of $MoSe_2$ and MoS_2 catalysts. Comparison of the induction periods of nitroarene reduction (3-NA, green and 4-NA, red trace, respectively) catalyzed with exfoliated $MoSe_2$ (solid) and MoS_2 (dotted trace) catalysts. The absorbance was measured at the wavelength monitored to follow the corresponding reduction reactions, i.e., 357 nm for 3-NA and 380 nm for 4-NA.

S7. Catalytic activity of $MoSe_2$ and MoS_2 nanosheets towards reduction of chemical species other than nitroarenes

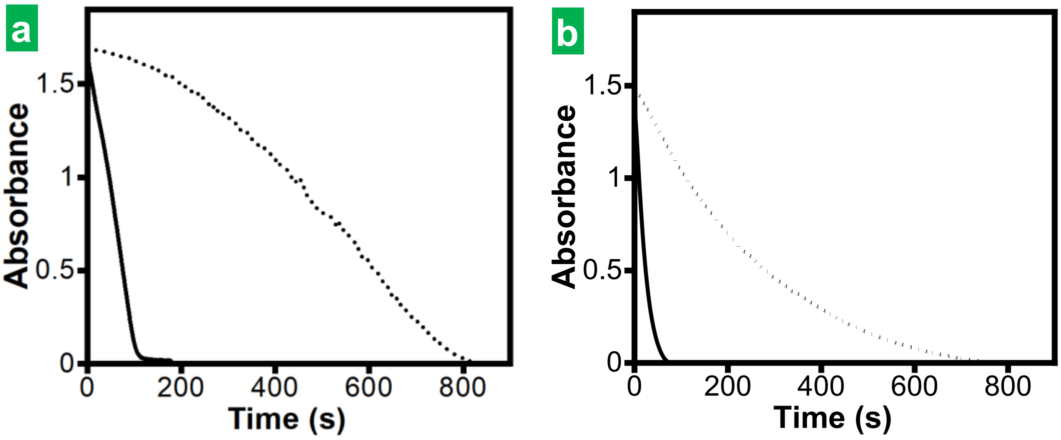

Figure S8. $MoSe_2$ and MoS_2 nanosheets as catalysts for reduction of organic compounds other than nitroarenes. (a) Absorbance at 461 nm vs. time for the reduction with $NaBH_4$ of methyl orange using $MoSe_2$ (solid trace) and MoS_2 (dotted trace) as catalysts. [TMD catalyst] = 14 μg mL^{-1}; [MO] = 0.07 mM; [$NaBH_4$] = 190 mM. **(b)** Absorbance at 417 nm vs. time for the reduction of hexacyanoferrate anion, $Fe(CN)_6^-$, with $NaBH_4$ using $MoSe_2$ (solid trace) and MoS_2 (dotted trace) as catalysts. [TMD catalyst] = 14 μg mL^{-1}; [hexacyanoferrate] = 1.5 mM; [$NaBH_4$] = 18 mM.

S8. Adsorption of 2-NA through both the nitro and amino groups on MoSe$_2$ with two double adjacent selenium (*vertical1c* configuration)

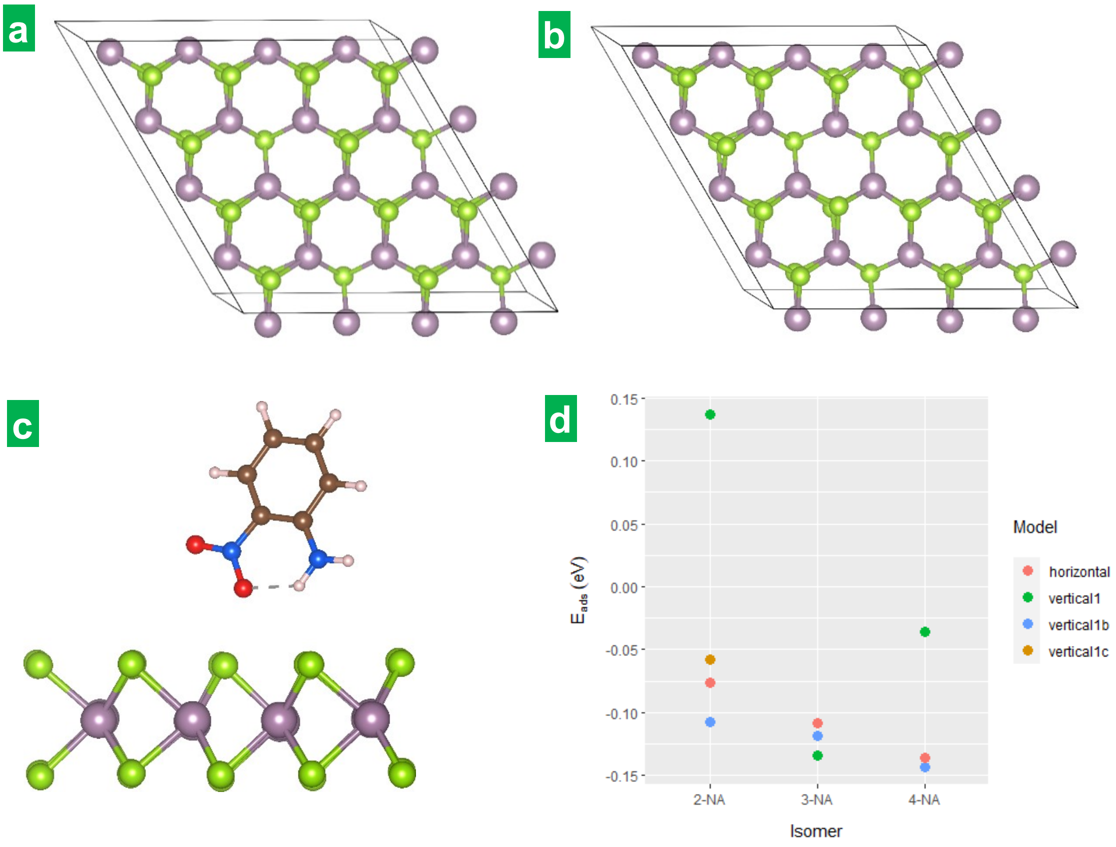

Figure S9. Energetically favorable adsorption of 2-NA on MoSe$_2$ through both the nitro and amino groups. Graphical representation of the MoSe$_2$ monolayer with four vacancies **(a)** in alternate sites, and **(b)** with two adjacent vacancies. **(c)** Graphical representation for the *vertical1c* model for the adsorption of 2-NA on MoSe$_2$ supercell shown in b. **(d)** Adsorption energies for the 4V$_{Se}$ case including the *vertical1c* model.

S9. Detection of reaction intermediates by UHPLC coupled to HR-MS.

As explained in the experimental section (section 1.7 in the main text), the catalysis medium for the reduction of 3-NA was analyzed by UHPLC/HR-MS at different reaction times, particularly, before the beginning, in the middle and near the completion of the reaction. Structural elucidation of relatively small, known molecules by mass spectrometry with a probability of 98 % is possible as long as the resolution is sufficiently high to provide accurate ion masses and isotope patterns [10]. The identification is based on a close similarity between experimental and theoretical masses (differences ≤5 ppm) and also between isotope ratios [11]. Actually, in the UHPLC/HR-MS equipment used herein, which allowed not only high resolution (≥10000) but also very accurate (internal) mass calibration of the instrument, the differences were 0.3–1.6 ppm for the identified products, as can be seen in the data shown in Figs. S11–13. As expected, 3-NA could be detected in the initial reaction medium, as shown in Fig. S11:

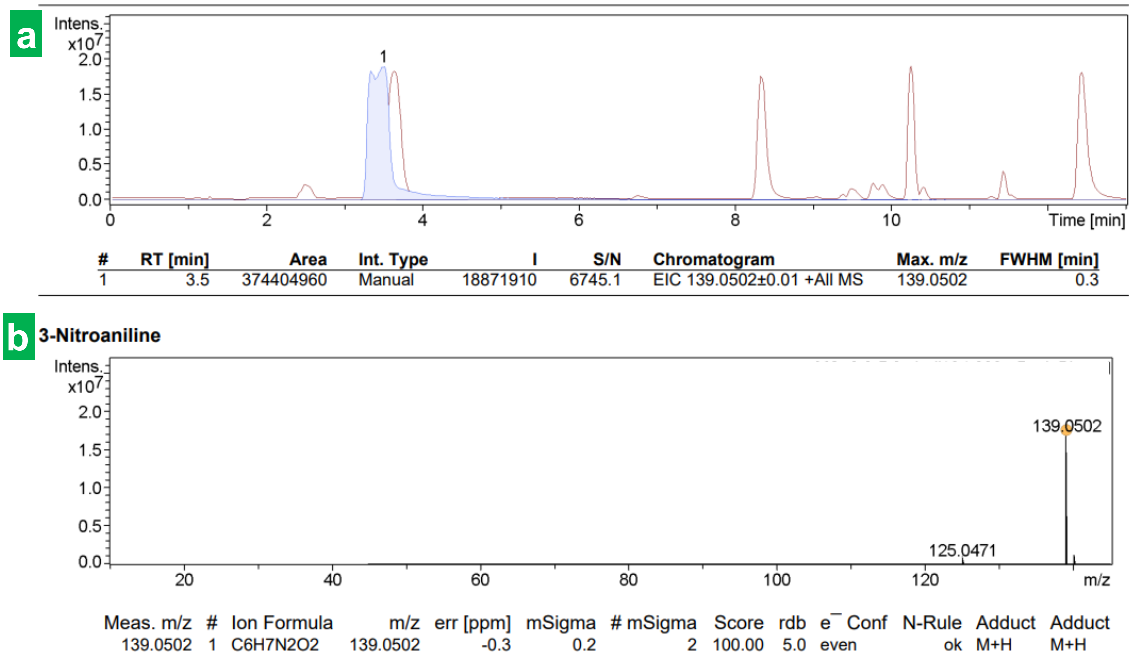

#	RT [min]	Area	Int. Type	I	S/N	Chromatogram	Max. m/z	FWHM [min]
1	3.5	374404960	Manual	18871910	6745.1	EIC 139.0502±0.01 +All MS	139.0502	0.3

Meas. m/z	#	Ion Formula	m/z	err [ppm]	mSigma	# mSigma	Score	rdb	e⁻ Conf	N-Rule	Adduct	Adduct
139.0502	1	C6H7N2O2	139.0502	-0.3	0.2	2	100.00	5.0	even	ok	M+H	M+H

Figure S11. UHPLC/MS of the initial reaction medium. (a) Chromatogram and **(b)** mass spectrum of the M+H adduct of 3-NA (peak 1 in a).

In the middle of the reaction (Fig. S12) and near its completion (Fig. S13), both the reactant (3-NA) and its reduction product (3-phenylendiamine), as well as two reaction intermediates (3-nitroaniline and 3-hydroxilamino aniline) could be detected. In fact, the experimental and theoretical masses for the intermediates differed ≤0.5 ppm, which grants identification with nearly 100 % rate. The relative intensities of the detected species show the expected trends. Indeed, the relative intensity of the reactant (3-NA) to its reduction product (3-phenylendiamine) is much higher in the middle of the reaction (Fig. S12) than near reaction completion (Fig. S13). As for the reaction intermediates, their relative intensity ratio points to a higher relative abundance of intermediate **II** (3-nitrosoaniline) in relation to intermediate **IV** (3-hydroxilamino aniline) in the middle of the reaction than near completion, which is consistent with the reaction mechanism.

a

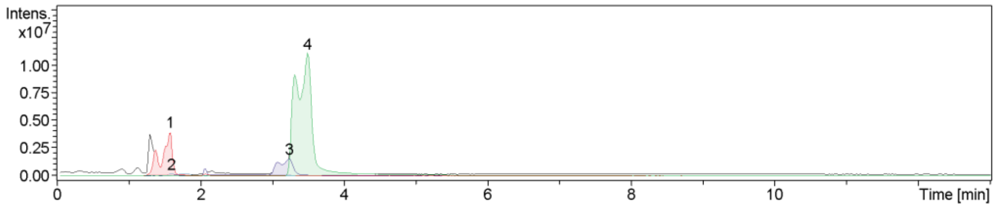

#	RT [min]	Area	Int. Type	I	S/N	Chromatogram	Max. m/z	FWHM [min]
1	1.6	37746656	Manual	4007516	1899.7	EIC 125.0709±0.01 +All MS	125.0710	0.2
2	1.6	3465689	Manual	228080	158.3	EIC 109.0760±0.01 +All MS	125.0710	0.1
3	3.2	20616180	Manual	1554055	551.9	EIC 123.0552±0.01 +All MS	123.0553	0.3
4	3.5	169790816	Manual	11037118	5166.9	3-Nitroaniline	139.0504	0.3

b **3-Hydroxialamine aniline**

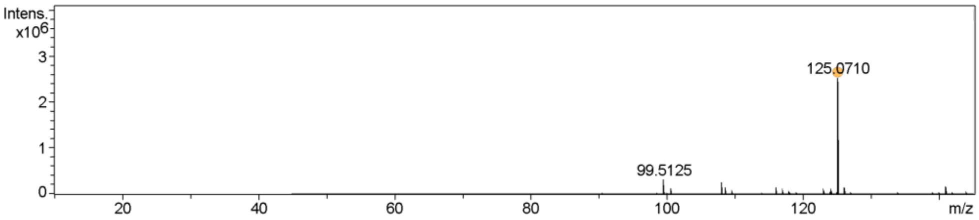

Meas. m/z	#	Ion Formula	m/z	err [ppm]	mSigma	# mSigma	Score	rdb	e^- Conf	N-Rule	Adduct	Adduct
125.0710	1	C6H9N2O	125.0709	-0.5	7.1	1	100.00	4.0	even	ok	M+H	M+H

c **3-Phenilenediamine**

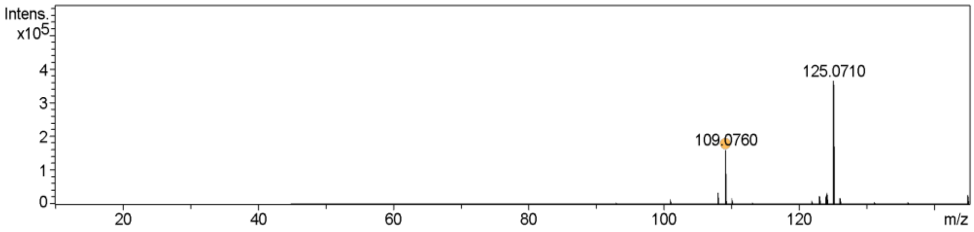

Meas. m/z	#	Ion Formula	m/z	err [ppm]	mSigma	# mSigma	Score	rdb	e^- Conf	N-Rule	Adduct	Adduct
109.0760	1	C6H9N2	109.0760	0.4	1.5	1	100.00	4.0	even	ok	M+H	M+H

d **3-Nitrosoaniline**

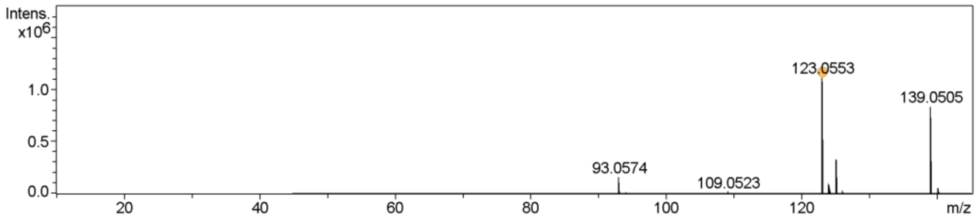

Meas. m/z	#	Ion Formula	m/z	err [ppm]	mSigma	# mSigma	Score	rdb	e^- Conf	N-Rule	Adduct	Adduct
123.0553	1	C6H7N2O	123.0553	-0.3	2.1	1	100.00	5.0	even	ok	M+H	M+H

e **3-Nitroaniline**

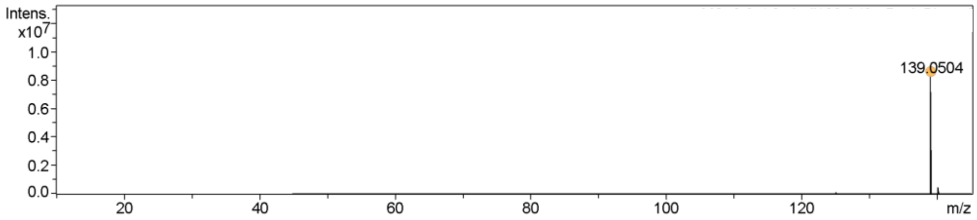

Meas. m/z	#	Ion Formula	m/z	err [ppm]	mSigma	# mSigma	Score	rdb	e^- Conf	N-Rule	Adduct	Adduct
139.0504	1	C6H7N2O2	139.0502	-1.3	8.3	2	100.00	5.0	even	ok	M+H	M+H

Figure S12. UHPLC/MS of the reaction medium in the middle of the reaction time. (a) Chromatogram and **(b–e)** mass spectra of the M+H adducts of the eluted species labelled as 1–4 in a, respectively.

a

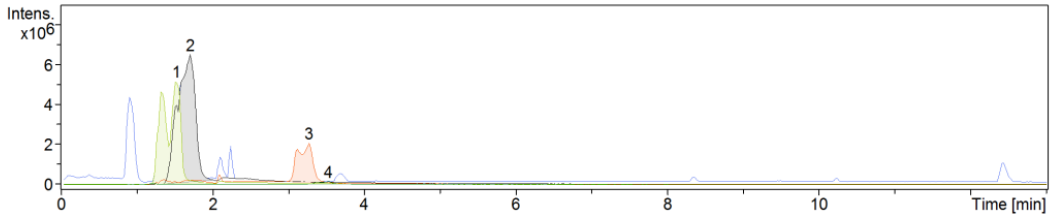

#	RT [min]	Area	Int. Type	I	S/N	Chromatogram	Max. m/z	FWHM [min]
1	1.5	78931880	Manual	5168726	1919.0	EIC 125.0709±0.01 +All MS	125.0710	0.3
2	1.7	103910928	Manual	6465674	2459.0	EIC 109.0760±0.01 +All MS	109.0760	0.3
3	3.3	27027384	Manual	2056974	569.7	EIC 123.0552±0.01 +All MS	123.0554	0.2
4	3.5	1676910	Manual	140966	81.3	EIC 139.0502±0.01 +All MS	139.0504	0.2

b **3-Hydroxilamine aniline**

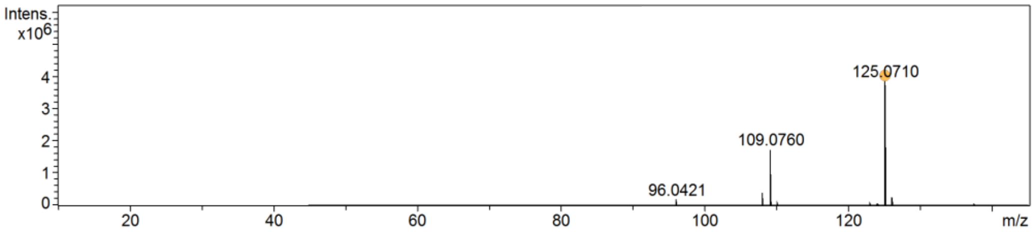

Meas. m/z	#	Ion Formula	m/z	err [ppm]	mSigma	# mSigma	Score	rdb	e^- Conf	N-Rule	Adduct
125.0710	1	C6H9N2O	125.0709	-0.4	4.9	1	100.00	4.0	even	ok	M+H

c **3-Phenilendiamine**

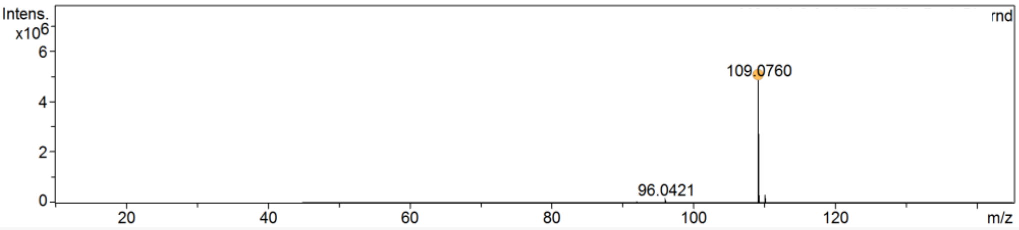

Meas. m/z	#	Ion Formula	m/z	err [ppm]	mSigma	# mSigma	Score	rdb	e Conf	N-Rule	Adduct
109.0760	1	C6H9N2	109.0760	-0.0	4.7	1	100.00	4.0	even	ok	M+H

d **3-Nitrosoaniline**

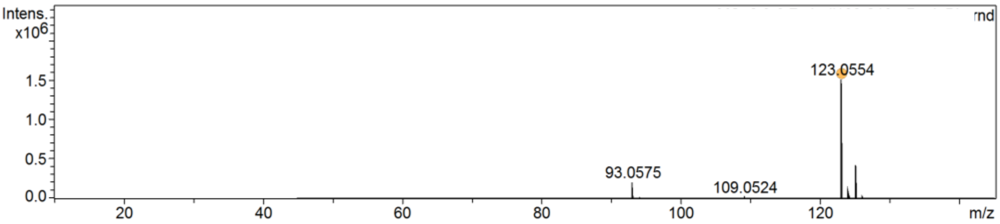

Meas. m/z	#	Ion Formula	m/z	err [ppm]	mSigma	# mSigma	Score	rdb	e^- Conf	N-Rule	Adduct
123.0554	1	C6H7N2O	123.0553	-0.6	3.6	1	100.00	5.0	even	ok	M+H

e **3-Nitroaniline**

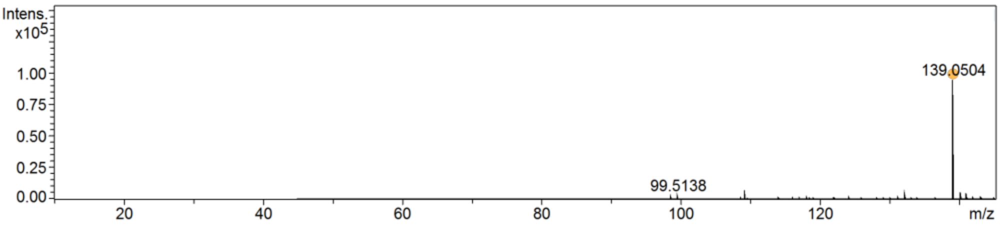

Meas. m/z	#	Ion Formula	m/z	err [ppm]	mSigma	# mSigma	Score	rdb	e^- Conf	N-Rule	Adduct
139.0504	1	C6H7N2O2	139.0502	-1.6	6.7	1	100.00	5.0	even	ok	M+H

Figure S13. UHPLC/MS of the reaction medium near reaction completion. (a) Chromatogram and **(b–e)** mass spectra of the M+H adducts of the eluted species labelled as1–4 in a, respectively.

S10. Additional information on the cyclability of the $MoSe_2$ catalyst

The reduction of 3-NA in the presence of $MoSe_2$ catalyst was carried out for ten consecutive cycles by the addition of successive amounts of substrate to the catalysis medium. To render the recovery of the catalyst easier for analysis, the flakes were not fixed on the foam (as they were in the experiments corresponding to Fig. 9c–e of the main text) but used in dispersion instead. This allowed recovering the catalyst by centrifugation and washing it with water by re-dispersion in pure water/centrifugation cycles.

Fig. S14a shows the UV-Vis spectra of the catalytic medium after the end of each consecutive cycle (corrected for the absorbance of the catalyst and for dilution). As expected for 100 % reaction conversion efficiency, the absorbance for the reaction medium after the first cycle (red trace in Fig. S14a) was that of the reduction product of 3-NA, i.e., m-phenylenediamine. Indeed, this spectrum was coincident within experimental error with that shown for 0.11 mM m-phenylenediamine in Fig. S5e (grey trace). No signs of the presence of unreacted substrate appeared in the subsequent cycles as the measured UV-Vis absorption signal was fully accounted for by the absorption spectrum of the reaction product (Fig. S5e, grey trace) while no absorption compatible with the substrate was observed (see the UV-Vis spectrum of 3-NA in Fig. S5e, black trace). The values of the cumulative absorption at the absorption maximum of the reduction product (wavelength of 290 nm) measured for the successive cycles were consistent with 100 % reaction conversion efficiency after each of them as well.

The recovered catalyst was characterized by Raman (Fig. S14b) and XPS spectroscopy (Figs. S14c and d), which confirmed that both its structural and chemical features remain unchanged throughout the cycling process, its spectra being coincident with those measured for the freshly prepared catalyst. Certainly, no sign of changes in the oxidation state of the elements constituting $MoSe_2$, i.e., Mo and Se, was detected in the XPS spectra, while both Raman and XPS analysis confirmed the preservation of its 2H phase. The fact that the structural and chemical features of the catalyst were preserved throughout the process suggested that its efficiency should remain unchanged as well, as has been already shown.

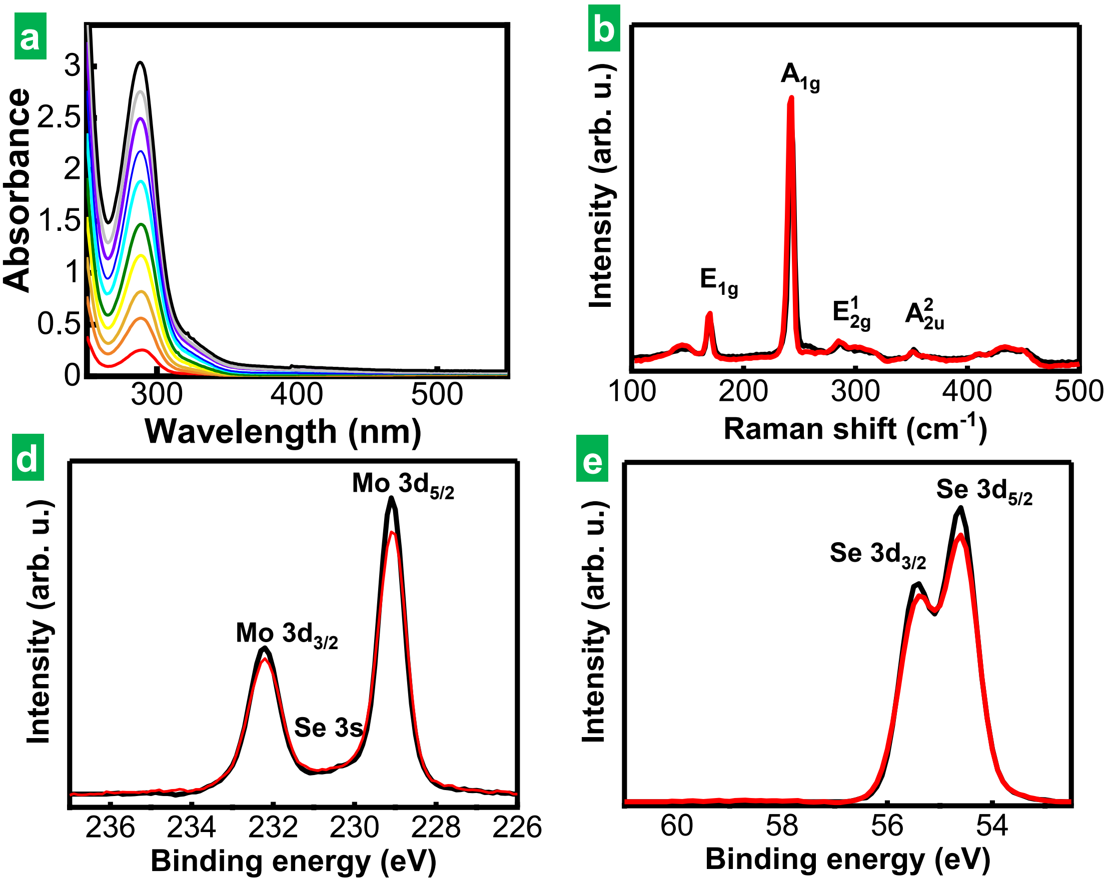

Figure S14. Cyclability of the $MoSe_2$ as catalyst for reduction of nitroarenes. (a) UV-Vis spectrum of the catalytic medium after the end of the reduction reaction for ten consecutive cycles: 1st cycle, red trace; 2nd, orange; 3rd, dark yellow; 4th, yellow; 5th, green; 6th, cyan; 7th, blue; 8th, violet; 9th, gray; 10th, black). Structural and chemical characterization of the cycled catalyst: **(b)** Raman spectra of fresh (black trace) and cycled (red trace) $MoSe_2$ catalyst. XPS spectra for **(c)** Mo 3d and Se 3s, and **(d)** Se 3d core level bands for fresh (black trace) and cycled (red trace) $MoSe_2$ catalyst.

S11. Performance of the $MoSe_2$ catalyst for synthetic applications

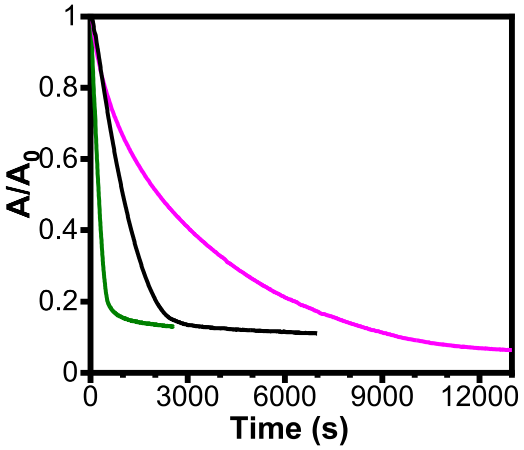

Figure S15. $MoSe_2$ nanosheets as catalyst for reduction of nitroarenes in the 1 mM concentration range. Raw kinetic profiles (as directly recorded with UV-Vis absorption spectroscopy) for the reduction of 3-NA (green trace), 4-NA (black) and 4-NP (magenta). The time-dependent contribution from the slowly declining absorbance of the catalyst (see section S4) is included in the profiles. The absorbance was monitored at wavelengths where signal saturation was avoided in such concentration range for the corresponding substrates (357 nm for 3-NA, 445 nm for 4-NA, and 455 nm for 1 mM 4-NP [9]). Catalysis conditions: [$MoSe_2$] = 14 µg mL^{-1}; [nitroarene] = 1 mM; [$NaBH_4$] = 224 mM.

References

[1] W. Li, D. Liu, N. Yang, J. Wang, M. Huang, L. Liu, Xiang Peng, G. Wang, X.-F. Yu, P. K. Chu, Molybdenum diselenide – black phosphorus heterostructures for electrocatalytic hydrogen evolution. Applied Surface Science 467–468 (2019) 328–33.

[2] B.B. Wang, K. Zheng, X.X. Zhong, D. Gao, B. Gao, Synthesis and structure of molybdenum diselenide nanosheets produced from MoO_3 and Se powders. Journal of Alloys and Compounds 695 (2017) 27–34.

[3] C. D. Wagner, W. M. Riggs, L. E. Davies, J. F. Moulder, Handbook of X-ray Photoelectron spectroscopy (Ed. G. E. Muilenberg), Perkin-Elmer corporation, Eden Prairie, Minnesota (1979).

[4] D.H. Everett, Basic principles of colloid science, Royal Society of Chemistry, London, 1988, chapter 9.

[5] S. García-Dalí, J.I. Paredes, B. Caridad, S. Villar-Rodil, M. Díaz-González, C. Fernández-Sánchez, A. Adawy, A. Martínez-Alonso, J.M.D. Tascón, Activation of two-dimensional MoS_2 nanosheets by wet-chemical sulfur vacancy engineering for the catalytic reduction of nitroarenes and organic dyes, Appl. Mater. Today 20 (2020), 100678.

[6] T. Aditya, A. Pal, T. Pal, Nitroarene reduction: a trusted model reaction to test nanoparticle catalysts, Chem. Commun. 51 (2015), 9410-9431.

[7] E. Menumerov, R.A. Hughes, S. Neretina, Catalytic reduction of 4-nitrophenol: a quantitative assessment of the role of dissolved oxygen in determining the induction time, Nano Lett. 16 (2016), 7791-7797.

[8] B. R. Puri, L. R. Sharma, M. S. Pathania, Principles of Physical Chemistry, (2013), Ch. 30, pp. 1155–1157, 46th Ed. Vishal Publishing Co., India.

[9] S. García-Dalí, J.I. Paredes, S. Villar-Rodil, A. Martínez-Jódar, A. Martínez-Alonso, J.M.D. Tascón, Molecular functionalization of 2H-phase MoS_2 nanosheets via an electrolytic route for enhanced catalytic performance, ACS Appl. Mater. Interfaces 13 (2021), 33157-33171.

[10] T. Kind, O. Fiehn, Seven Golden Rules for heuristic filtering of molecular formulas obtained by accurate mass spectrometry. BMC Bioinformatics 8 (2017), 105.

[11] B. L. Milman, General principles of identification by mass spectrometry, TrAC Trends in Analytical Chemistry, 69 (2015), 24-33.

6 Conclusiones

Tras el desarrollo de esta tesis y en relación a los objetivos descritos en la Sección 2, se pueden extraer las siguientes conclusiones:

1. Preparación de dispersiones de nanoláminas 2D de dicalcogenuros de metales de transición

La exfoliación en fase líquida asistida por ultrasonidos se ha utilizado para la preparación de dispersiones coloidales de nanoláminas 2D de MoS_2 y $MoSe_2$ en medio orgánico, con su posterior transferencia a fase acuosa.

La optimización de una estrategia basada en la exfoliación electroquímica catódica ha permitido la obtención de nanoláminas delgadas de MoS_2, usando sales de trimetilalquilamonio en medio orgánico; y de nanoláminas de MoS_2 modificadas con ácido acético, usando cloruro potásico y organoioduros en fase acuosa.

La caracterización fisicoquímica detallada de las nanoláminas obtenidas con una amplia variedad de técnicas ha posibilitado la obtención de información estructural y composicional precisa.

2. Modificación de nanoláminas 2D de dicalcogenuros de metales de transición

Se ha desarrollado con éxito y optimizado una metodología de exfoliación electroquímica catódica en fase acuosa para la obtención de nanoláminas de MoS_2 funcionalizadas covalentemente con ácido acético y otros grupos moleculares.

Se ha investigado y optimizado un tratamiento reductor para la generación superficial de vacantes de Se en las nanoláminas de $MoSe_2$ obtenidas mediante exfoliación en fase líquida.

3. Uso de nanoláminas 2D de dicalcogenuros de metales de transición en catálisis y almacenamiento de energía

La comparación de las prestaciones de las nanoláminas 2D de MoS_2 y $MoSe_2$ obtenidas mediante exfoliación en fase líquida y sin modificar como catalizadores para la reacción de reducción de nitroarenos mostró que las últimas presentan una mayor actividad catalítica intrínseca para esta aplicación. Además, las nanoláminas de $MoSe_2$

enriquecidas en vacantes de Se mostraron una mayor actividad catalítica respecto a la que presentaban las nanoláminas de partida. Se ha investigado y determinado el origen las mencionadas diferencias en actividad catalítica.

La funcionalización con ácido acético ha demostrado ser una vía eficaz para la obtención de nanoláminas de MoS_2 modificadas con una actividad catalítica superior a la de la mayoría de los catalizadores basados en MoS_2 y en metales no nobles documentados en la literatura para la reducción de ciertos nitroarenos y colorantes orgánicos.

El tratamiento electroquímico con sales de trimetilalquilamonio ha permitido obtener nanoláminas de MoS_2 exfoliadas catódicamente con un mejor desempeño, en comparación con las exfoliadas en fase líquida, en el almacenamiento electroquímico de litio en términos de capacidad gravimétrica y ciclabilidad, con vistas a su uso como ánodos en baterías de ion litio.

6 Conclusions

Upon completion of the work of this doctoral thesis and regarding the objectives described in Section 2, the following conclusions can be put forward:

1. Preparation of dispersions of 2D transition metal dichalcogenide nanosheets

Sonication-assisted liquid phase exfoliation has been successfully employed for accessing colloidal dispersions of MoS_2 and $MoSe_2$ 2D nanosheets in organic medium, with subsequent transfer to the aqueous phase.

The optimization of a cathodic electrochemical exfoliation approach allowed the obtention of thin MoS_2 nanosheets, employing trimethylalkylammonium salts in organic medium; and acetic acid-derivatized MoS_2 nanosheets, using potassium chloride and organoiodides in aqueous medium.

The detailed physicochemical characterization of the prepared nanosheets has been carried out by means of a wide range of techniques, leading to accurate structural and compositional information.

2. Modification of 2D transition metal dichalcogenide nanosheets

A cathodic electrochemical exfoliation strategy has been successfully developed and optimized to achieve covalent derivatization of MoS_2 nanosheets with acetic acid and other molecular moieties.

A reductive treatment has been investigated and optimized to trigger the generation of surface Se vacancies in $MoSe_2$ nanosheets prepared by liquid phase exfoliation.

3. Use of 2D transition metal dichalcogenide nanosheets for catalysis and energy storage applications

The comparative study of the catalytic activity of unmodified, liquid phase-exfoliated 2D MoS_2 and $MoSe_2$ nanosheets toward nitroarene reduction revealed the latter material outperforming MoS_2 in this application. Additionally, $MoSe_2$ nanosheets enriched in Se vacancies revealed a higher catalytic activity relative to that of their unmodified counterpart. The origin of such differences has been explored and rationalized.

The acetic acid functionalization has been demonstrated to be an effective route to obtain derivatized MoS_2 nanosheets with enhanced catalytic activity compared to that of most other MoS_2 catalysts and non-noble metal-based catalysts reported in the literature towards the reduction of certain nitroarenes and organic dyes.

The electrochemical treatment involving trimethylalkylammonium salts enabled the obtention of cathodically exfoliated MoS_2 nanosheets that, compared with the case of liquid phase-exfoliated MoS_2, exhibited an enhanced performance towards the electrochemical storage of lithium in terms of gravimetric capacity and cyclability, with a view to their use as anodes in lithium-ion batteries.